


Doctoral Dissertation
Doctoral Program in Aerospace Engineering (33.th cycle)

A multiscale modelling of the cardiovascular fluid dynamics for clinical and space applications

Caterina Gallo
* * * * * *

Supervisors
Prof. S. Scarsoglio, Supervisor
Prof. L. Ridolfi, Co-supervisor

Doctoral Examination Committee:
Prof. G. Pedrizzetti, Referee, Università degli Studi di Trieste
Prof. R. Verzicco, Referee, Università di Roma "Tor Vergata"
Prof. M.D. de Tullio, Politecnico di Bari
Prof. U. Morbiducci, Politecnico di Torino
Prof. J. Tiago, Instituto Superior Técnico

Politecnico di Torino
January 28th, 2021

I hereby declare that, the contents and organisation of this dissertation constitute my own original work and does not compromise in any way the rights of third parties, including those relating to the security of personal data.

. . . . . .

Caterina Gallo

Turin, January 28th, 2021

Summary

The purpose of this Thesis is two-fold: (i) developing a mathematical model of the cardiovascular system able to efficiently reproduce the human circulation behaviour of both a generic subject and specific individuals, and (ii) providing additional answers to still open questions associated to either the clinical and aerospace worlds.

A closed loop multiscale (0D-1D) mathematical model of the cardiovascular system was developed, by combining a 1D model of the systemic arterial tree, a 0D description of the microcirculation, venous return and heart-pulmonary circulation, a multiscale (0D-1D) framework of the coronary circulation, and a baroreflex model to maintain homoeostasis. By using the geometrical and mechanical properties of a healthy and young man, the resulting model was proved to properly reproduce the physiological cardiovascular behaviour, in terms of haemodynamic parameters and pressure/flow rate waveforms and mean values. The reliability of the proposed modelling solution was also tested through a patient-specific version of the general model, requiring as input data non-invasive patient-specific information only: from anthropometric and personal details (weight, height, age, sex) to common clinical measurements (time-averaged heart rate and left-ventricular contraction time - through the ECG - and beat-averaged mean/pulse brachial blood pressures - through automatic oscillometric recording). We verified that the patient-specific model is able to give accurate central blood pressure estimates for 12 specific subjects, despite it should be further tested in a larger cohort of individuals.

The model was also exploited to investigate different topics in case of atrial fibrillation and long-term microgravity exposure. In particular, we studied (i) the consequences of the sole heart rhythm variations on the systemic arterial tree in atrial fibrillation, (ii) the effects of different ventricular heart rates during atrial fibrillation on the coronary circulation performance, and (iii) the cardiovascular system response to long-duration microgravity (5/6 moths), without the application of countermeasures and with respect to a supine configuration on Earth.

Interesting insights, impossible or hard to obtain through direct experimental

approaches, were gained from these studies. These latter confirm the huge potentiality of the modelling approach in responding to clinical and space medicine questions, overcoming the principal limitations of *in-vivo* studies, which are usually invasive, expensive, time-consuming, and difficult to carry out.

*To my brother, for being my inspiration in the impossible***...*
To my husband, for his patience and love...

***

Contents

Introduction

Human circulation is an extremely complex fluid dynamic system. It is just sufficient to consider that the vasculature consists of arterial and venous tree-like structures with locally variable elastic and viscoelastic mechanical properties, and the heart, serving as pump, is an automatically-regulated engine having an intrinsic electric control of atrial and ventricular contractions. In addition, the blood is an incompressible, viscous and non-Newtonian fluid which develops in different patterns (from laminar to turbulent to single file flow), and the blood motion is not stationary but pulsatile, at least at arterial level. Finally, cardiac and vascular properties are continuously affected by short- and long-term control mechanisms, and a variety of other conditions, such as posture, exercise, age, emotions and stress, play a role in the final cardiovascular behaviour, further enriching the emerging scenario. Thus, even in physiological states, the resolution of the cardiovascular system is not trivial and the modelling of its geometrical and mechanical characteristics, as well as fluid dynamic features and regulatory systems, requires special attention when *in-silico* approaches are adopted.

Different mathematical models of the cardiovascular system have been proposed for both clinical and aerospace applications. From a clinical perspective, cardiovascular models are used to investigate the genesis of cardiac and vascular pathologies, support the design of medical devises, foresee the effects of potential therapeutic actions, and support clinicians and medicine students in decision making and learning. In the field of space medicine, mathematical models are adopted to inquire into the functioning of human circulation during hypergravity, hypogravity and microgravity exposure, in order to identify the best countermeasures to compensate for the drawbacks of altered accelerations on the physiological cardiovascular performance. Depending on the final utilization, lumped, space-dependant and multiscale models have been exploited. The latter models combine submodels of different dimensions, thus guaranteeing an adequate level of detail to each cardiovascular region at a reasonable computational cost. For this reason, multiscale models are widely appreciated in a number of sectors and employed for the majority of applications.

With the present Thesis, we developed a closed-loop multiscale mathematical model of the cardiovascular system, which was applied to different areas of research.

The model integrates a 1D description of the systemic arterial tree, a multiscale (0D-1D) model of the coronary circulation, and a 0D model of the microcirculation, venous return and heart-pulmonary circulation. It also includes a baroreflex model, which assures the automatic adjustment of the mean arterial pressure beat by beat. Despite different modelling solutions here implemented are not novel in literature, the objective of this work is not producing an entirely new mathematical model but obtaining a complete and versatile platform to be used to different aims. The proposed model, in fact, reproduces important key characteristics of the cardiovascular system, such as the propagation and reflection phenomena of pressure and flow waves along the arterial tree, the non-ideal behaviour of cardiac valves, the well-organized structure of micro-circulation groups and venous return, the haemodynamics of coronary microvasculature, and the short-term regulation mechanism. Thus, the model represents a comprehensive and versatile framework able to explore various configurations, from cardiac arrhythmias to different gravitational environments.

A simplified version of the model, reproducing the systemic arterial tree, the left heart and coronary circulation, was the starting point of this work and was exploited in two different studies applied to the area of atrial fibrillation. In particular, the first study was intended to determine the effects of the sole heart rhythm variations in atrial fibrillation on the systemic arterial tree, while the second study was aimed at analysing the role of different ventricular heart rates on the coronary function in case of atrial fibrillation. The complete version of the model (without the coronaries) was instead applied to two other studies. In the first one, the model was made patient specific through non-invasive individual data and was tested as tool to obtain central blood pressure estimates on 12 supine elderly subjects. In the second one, we used the model to simulate the cardiovascular consequences of long-term microgravity exposure after about 5/6 months in space, without the application of any countermeasure and with respect to the supine configuration on Earth.

All these studies demonstrate the huge potentiality of mathematical models in providing new insights into the cardiovascular response to a number of pathological or unusual situations. Moreover, the patient-specific version of the complete model opens the possibility to consider similar computational approaches in the future, not just to estimate central blood pressure but also to offer the complete pressure and flow rate map of the whole cardiovascular system, together with the most common haemodynamic parameters.

The Thesis is organised as follows. The physiological behaviour of the cardiovascular system is depicted in Chapter 1. An overview of the different types of cardiovascular models available in literature (from zero-dimensional to space-dependent to multiscale models) is given in Chapter 2. A complete description of

the submodels making up the global mathematical model, as well as their mathematical coupling, is provided in Chapter 3. The reliability of the proposed mathematical model for a generic healthy and young man is shown in Chapter 4. The methodology followed to make the generic global model patient-specific is explained in Chapter 5, where the testing of the same methodology to obtain central blood pressure estimates from 12 subjects is also reported. Chapters 6 and 7 are dedicated to the presentation of the model results for the studies in case of atrial fibrillation and microgravity exposure, respectively. Chapter 8 contains the conclusions of the proposed modelling approach with some of its possible future developments. Details about the resolution of the 1D model of the systemic arterial tree and the 0D model of the remaining circulatory regions, with an indication of the relative parameter settings, are illustrated in Appendixes A and B, respectively. The last one precedes Appendix C, which outlines the model parameters used in the studies described in Chapters 6 and 7, respectively. The full list of acronyms and symbols adopted throughout the text is finally reported in Appendix D.

Chapter 1

The cardiovascular system: a peculiar fluid dynamic circuit

1.1 General description

The *cardiovascular* system consists of the heart, as the word *cardio* suggests, and a network of vessels, which the term *vascular* refers to [343]. It performs five main functions essential to human life [177]: (i) provides oxygen and nutrients to tissues, (ii) removes carbon dioxide and other metabolic waste products from tissues, (iii) regulates pH and body temperature, (iv) protects against pathogenic agents, and (v) transports/produces hormones.

A simplified structure of the cardiovascular system is represented in Figure 1.1, where two main circuits can be recognised: the pulmonary (PC) and systemic (SC) circulations. PC carries deoxygenated blood from the right heart side to the lungs via the pulmonary trunk and moves oxygenated blood from the lungs to the left heart side via the two pulmonary veins (one from each lung). The pulmonary trunk bifurcates into the two pulmonary arteries (one per lung), which continue to split, finally merging into arterioles and capillaries. The latter wrap around the alveoli in the air sacs of the lungs, where the gas exchanges take place, with blood loosing carbon dioxide and acquiring oxygen. Capillaries then join into venules, which ultimately converge into the two pulmonary veins. SC transports blood rich in oxygen from the left heart side to the tissues and returns blood rich in carbon dioxide from the tissues to the right heart side. SC originates with the aorta, which branches into the systemic arteries, then leading to arterioles. As in PC, arterioles are followed by capillaries and venules. Here venules unite in groups to form the systemic veins, which converge into the superior vena cava in the upper body regions and the inferior vena cava in the lower body regions. The oxygen and nutrient supply to tissues, as well as the withdrawal of all the waste products from tissues, is carried out by capillaries [343, 349].

Based on this description, one can in general define *arteries* the vessels taking

blood away from the heart and *veins* the vessels following the opposite pattern [349]. Then, *pulmonary arteries/veins* belong to PC, while *systemic arteries/veins* belong to SC.

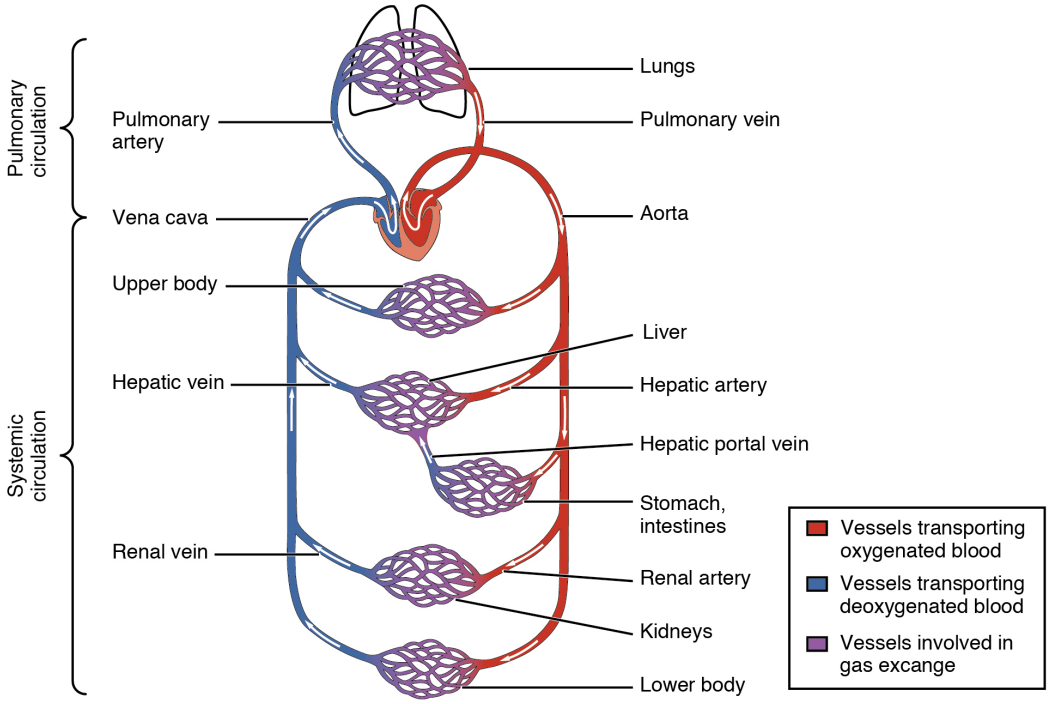

Figure 1.1: Simplified structure of the cardiovascular system. *Image extracted from* [27].

One can notice that the vasculature of both PC and SC consists of two tree-like structures, the arterial part and the venous one, which communicate through the smallest branches of each structure at capillary level [349]. Nonetheless, PC and SC differ in terms of pressure level (six-fold lower in PC), resistive action of arterioles (six-fold lower in PC), arterial thickness (reduced in PC), and capillary distribution of blood (not region-specialized in PC) [46]. In addition, the arterial and venous sides of either PC and SC show dissimilarities regarding the blood flow direction (arteries: towards capillaries, veins: towards heart), mean pressure (arteries: high, veins: low; the mean pressure difference between arteries and veins is much more marked in SC, about 85 mmHg, than in PC, about 7 mmHg), wall thickness (arteries: large for SC and small for PC, veins: small), oxygen content (arteries: high for SC and low for PC, veins: low for SC and high for PC), and valves (arteries: absent, veins: present along the limbs) [27]. A comparison between the characteristics of both arteries and veins in SC and PC is provided in Table 1.1.

Table 1.1: Characteristics of both arteries and veins in SC and PC. *Most of the data are extracted from* [46, 110].

Haemodynamic characteristics	**SC**		**PC**	
	arteries	**veins**	**arteries**	**veins**
Mean pressure [mmHg]	90-95	5-10	11-17	5-10
Pulse pressure [mmHg]	40-55	weakly pulsatile	10-17	weakly pulsatile
Vessel thickness [mm]	1	0.5	0.2	0.5
Arterial resistance [mmHg min/l]	9-20		1.25-2.5	

1.2 From physiology to fluid dynamics

The cardiovascular system can be regarded as a unique fluid dynamic circuit, whose complexity mainly depends on a number of factors.

1. Vasculature consists of tree-like structures with locally-variable elastic and viscoelastic mechanical properties.

2. The functioning of the cardiovascular circuit is dominated by two types of motion: diffusion and convection. However, differently to diffusion, convection needs metabolic energy, that imposes the presence of a powerful and sophisticated pump: the heart.

3. The heart represents an automatically-regulated machine, which requires large amounts of oxygen to properly work, and has to both receive and pump blood regularly, through the precise coordination of the contraction/relaxation of its chambers and opening/closure of its valves.

4. The fluid circulating within the system, the blood, is incompressible, viscous and non-Newtonian, with different patterns of flow developed: laminar, turbulent and single-file flow.

5. Arterial pressure and flow rate are not constant but pulsatile, with their waveforms being the result of multiple concomitant factors.

6. There are both short- and long-term control systems, which exploit a variety of mechanical and chemical mechanisms assuring the necessary oxygen supply to tissues and the best equilibrium condition within the whole circulation.

7. The cardiovascular system behaviour changes with posture, exercise condition, age, pathological situations, assumptions of medications, and even emotions and stress, thereby complicating the basic physiological response.

A more detailed presentation of each of these aspects is offered in the following sections.

1.2.1 Vascular geometry and mechanical properties

Since the mathematical model presented in this work pays special attention to the modelling of SC (see chapter 3), we here focus on the geometrical and mechanical properties of the systemic network.

It has already been observed that arteries (veins) progressively bifurcate (converge) into smaller (larger) vessels, forming the arterial (venous) tree. Moreover, the aorta and its branches taper with the distance form the heart [222, 227], creating a succession of small geometrical discontinuities along each vessel length [46]. Venous tapering, instead, is almost negligible, apart from specific vessels, like the jugular, vertebral and facial veins [222, 227].

Table 1.2: Average diameter and thickness, AD and AT, total number of vessels, TNV, total cross sectional area, TCSA, mean velocity in time and over the cross-sectional area, MAV, and Reynolds number (with MAV), Re, for the different classes of vessels in SC. Numbers in brackets (column III) represent the ratio AT/AD. *Values extracted from* [33, 46, 110].

Vessel	**AD [mm]**	**AT [mm]**	**TNV**	**TCSA [cm^2]**	**MAV [cm/s]**	**Re**
Aorta	25	2 (0.08)	1	2.5	52	3400
Large arteries	5.5	1 (0.2)	50	20	35	500
Arterioles	0.03	0.03 (1)	10^4	40	0.1	0.7
Capillaries	0.006	0.001 (0.2)	10^9	2500	0.013	$2*10^{-3}$
Venules	0.03	0.003 (0.1)	10^4	250	0.015	0.013
Veins	5	0.5 (0.1)	10^3	80	11	140
Venae cavae	30	1.5 (0.05)	2	8	42	3300

Table 1.2 shows the typical diameter range for the different vessel types in SC, with capillaries having the smallest diameter, arterioles and venules having comparable diameters, and veins and venae cavae larger than arteries and aorta, respectively. Based on Table 1.2, one can expect the highest blood flow resistance at capillaries, and progressively smaller resistances where arterial and venous diameters increase. Indeed, from the application of the Poiseuille's law[1], it emerges that resistance to blood flow depends on blood viscosity, the length and especially the calibre of the vessel through which blood flows. In particular, blood flow resistance is inversely proportional to the fourth power of the vessel radius. Nonetheless, among all the vessel types, arterioles and not capillaries generate the highest resistance to blood flow. This is due to the fact that, despite the average capillary diameter is five times smaller than the arteriolar one, the total capillary area is more than sixty times the arteriolar one [177] (see Table 1.2). One can also observe that we have a number of arterioles in parallel, each of which is followed by a number of capillaries in parallel, with more numerous capillaries than arterioles and the generic arteriolar resistance comparable with the capillary. Since the total resistance of n resistances in parallel is smaller than the single resistance, we understand why the total resistance of many capillaries in parallel is smaller than the one of fewer arterioles in parallel [153]. Thus, it is the capillary ramification to reduce the contribution of capillary resistance with respect to arterioles.

The distribution of diameters described above implies an increase in the total arterial cross sectional area from heart to tissues, and a decrease in the total venous cross sectional area from tissues to heart. Thus, blood velocity has to reduce moving away from the heart along the arterial path, and rise along the venous circuit coming back to the heart, because of the conservation of mass (see Table 1.2). These changes in the blood flow velocity are coherent with the role the different classes of vessels have to cover; while arteries and veins have to quickly move blood from and to the heart, respectively, capillaries need some time (about 3 s [110]) to transfer oxygen and extract carbon dioxide at a given site. Thus, the slowdown of blood along the capillary circuits is crucial for the cardiovascular system to succeed.

[1]Poiseuille's law can be used to study steady and laminar flows developing within rigid and cylindrical tubes when the fluid is Newtonian. It is represented by the equation $\Delta_Q = \frac{\pi \Delta_p r_v^4}{8\mu l_v}$, where Δ_Q is the mean flow rate through the tube, Δ_p is the pressure gradient between inlet and outlet of the tube, r_v and l_v are the tube radius and length, respectively, and μ is the fluid viscosity. Notice that, since the term $\frac{8\mu l_v}{\pi r_v^4}$ corresponds to the total hydraulic resistance (R), Poiseuille's law can also be written as $\Delta_p = R\Delta_Q$. Thus, based on the latter, the mean flow rate through the tube is directly proportional to the pressure difference across the tube, decreasing and increasing for higher and lower hydraulic resistances, respectively. However, blood flow does not satisfy the Poiseuille's hypotheses, being pulsatile (thus unsteady), developing along not rigid and not perfectly cylindrical channels, and involving a non-Newtonian fluid. Nonetheless, Poiseuille's theory can be applied to well approximate the functioning of human circulation along large and medium arteries, helping to identify the blood flow determinants, at least at arterial level [153].

Vascular mechanical properties are determined by the structure of walls. Apart from capillaries, all vascular walls contain three different layers [177]: the tunica intima, media and externa (or adventitia). The tunica intima is the innermost lining of the vessel walls and has no mechanical function. The tunica media is the middle layer of the vascular walls and the thickest layer for the majority of arteries. The tunica externa is the external coating of the vessel walls, is typically the thickest layer in veins, and is embedded with small blood vessels (the vasa vasorum) in large arteries and veins to provide nutrients to the tunica media [27, 177]. The thickness and percent composition of each of these tunics greatly vary within the different vessel types, determining the mechanical behaviour of each vessel class, which is strictly linked to the function it is thought for.

Large arteries (e.g., aorta and its main daughter vessels), also known as elastic arteries, have large inner diameters (from 25 to 5.5 mm) and the thickest walls (from 2 to 1 mm). The tunica media is the thickest layer of the wall and, with the other tunics, contains a large amount of elastin[2]. This allows large arteries to dilate when blood is pumped by the heart and draw back when the pumping action is terminated. In this way, peripheral sites can always receive blood and arterial pressure can be maintained at a reasonable level. In fact, if arteries were stiffer (that is what happens during ageing), arterial resistance - and thus arterial pressure - would grow, and the heart should work harder to pump the same blood volume because of the increased load [27, 177].

Medium-to-small arteries (e.g., cerebral, coronary, radial, splenic, popliteal artery, etc. . .), called muscular arteries, have thicker walls (1 mm) than elastic arteries, if one considers their lumen diameter (from 5.5 to 0.5 mm). The tunica media contains more smooth muscle and less elastin than elastic arteries, thereby avoiding collapse and limiting expansion and bleeding in case of injury. However, these arteries are unimportant for the resistance control [27, 177].

Arterioles, often defined as resistive vessels, are the main responsible for the arterial resistance. Their wall thickness (0.03 mm) is comparable to the lumen diameter (in the range 0.5-0.01 mm) and their tunica media is mainly composed of smooth muscle. This enables arterioles to actively modify their inner diameter, thus regulating resistance and altering blood flow. In particular, through *vasorelaxation* there is a reduction in resistance, through vasoconstriction there is an increase in resistance [27, 177].

One can observe that the content of elastin and smooth muscle in the arterial walls reduces and increases respectively with the distance from the heart, allowing each vascular category to accomplish a specific task. The higher the content of

[2]Elastin is a protein which returns to the original shape after having been stretched and compressed [27] and is six times more flexible than rubber [177].

elastin, the more the vessel shows a non linear elastic behaviour. The more the content of smooth muscle, the more the vessel exhibits a viscoelastic behaviour [359]. Materials with a non linear elastic behaviour have different elastic moduli or Young's moduli according to the applied stress (the stress(strain) curve is not a straight line). Materials with a viscoelastic behaviour dissipate a fraction of the applied stress because of their intrinsic viscosity [365] (distinct stress(strain) curves in loading and unloading). The double presence of elastin and smooth muscle in the walls along the arterial tree gives rise to the well known non linear viscoelastic behaviour of arteries. The strain(stress) curve of a generic viscoelastic material is depicted in Figure 1.2.

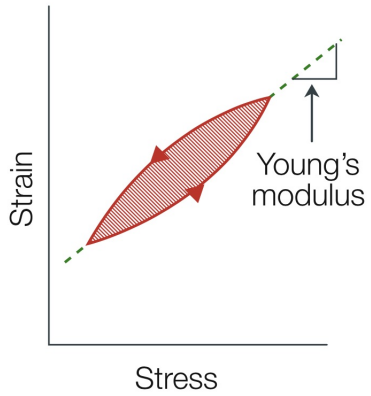

Figure 1.2: Example of a strain(stress) curve for a viscoelastic material. *Image extracted from* [365].

Capillaries are microscopic vessels both in width and length (diameters are between 0.01 and 0.005 mm, lengths are between 0.5 and 1 mm). Their walls are made of a single layer of endothelial cells (thickness is about 0.001 mm), which permits the passage of nutrients and waste products between inside (blood) and outside (cells and interstitial fluid). For this reason, capillaries are also defined exchange vessels, although gas exchanges can involve arterioles and venules too [27, 177].

Venules and veins (wall to lumen ratio: 0.1) are thinner than smaller arterioles (wall to lumen ratio: 1) and arteries (wall to lumen ratio: 0.2), respectively, with their tunica media of both collagen[3] and smooth muscle, which explain the considerable distensibility of these vessels. In fact, venules and veins accommodate 2/3 of total blood volume (see Figure 1.3), representing an important blood reservoir. The pressure impressed by the heart to the blood is dissipated along the microvasculature, thus the pressure gradient driving blood to the heart amounts to 10-15

[3]Collagen is a protein 100 times stiffer than elastin [177].

mmHg only. Such a low pressure is responsible for the common collapse of venous vessels and seems sufficient to the venous return. The latter, in fact, is facilitated by the limited venous resistance, the venous valves located along the limbs and preventing backward flow, the contracting action of leg muscles (e.g., during walking and running), and the respiration cycles [27, 177, 349].

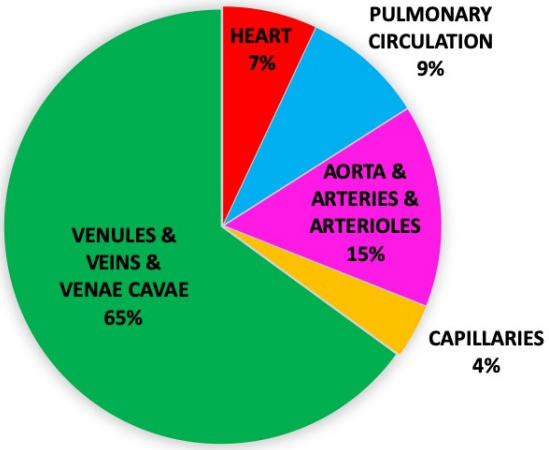

Figure 1.3: Distribution of blood volume in human circulation. *Data extracted from* [46, 120]

Capillaries, venules and veins also exhibit a viscoelastic behaviour, although this theme is largely unexplored [359]. It has been proved that venous viscoelasticity has something in common with the arterial one. In fact, viscoelastic properties of venous walls vary region by region with the histological structure, and the magnitude of wall viscosity increases with the smooth muscle content [384].

1.2.2 Diffusive and convective transport

Gas exchanges at pulmonary and tissue levels are governed by diffusion, that is an exceptionally convenient transport process: it is simply driven by a concentration gradient and does not need metabolic energy to work. However, the efficiency of this transport process is lost over large distances. In fact, according to the theory of the Brownian movement [73], the time it takes for a molecule to diffuse over a distance d is directly proportional to d^2. Therefore, diffusion is adequate at capillary level only, where distances to cover are of the order of a few micrometers. For greater distances, it is necessary a faster process to keep up with the oxygen demand of the 10^{13} cells [28] of our body [269]: the convection. The latter can transport oxygen from lungs to limb capillaries in 30 s, while diffusion would need hours to cover one centimetre [177]. The key problem with convection is that it needs metabolic energy. For this reason, we are equipped with an outstanding

pump: the heart.

It is possible to identify three main patterns of flow along human circulation: the laminar flow, turbulent flow and single file flow [177]. In arteries, arterioles, venules and veins, flow is usually laminar, with a transverse velocity profile almost flat along the ascending aorta (since the flow is not well developed) and resembling a blunted parabola further away from the heart. Flow is turbulent in the left ventricle, that is useful to mix the blood [261], and at the entrance to the aorta, where the peak Reynolds number is about 4000. Single-file flow is the special type of motion happening along capillaries, where the hypothesis of continuum is no longer valid. In fact, capillary diameters are comparable to the average width of red blood cells, which have thus to flow in single file. A theoretical study of this motion is still lacking, although it was extensively studied in the past [258]. Changes in the flow pattern at different cardiovascular sites are reflected by the values of the Reynolds number (see Table 1.2).

1.2.3 A pump for convective transport: the heart

The heart is a muscular organ weighting about 300 g (for an adult) [234] and of the size of a closed fist, looking like a blunt cone. It is located between the lungs and above the diaphragm in the rib cage, with its center 1.5 cm left the body's midline [197, 343].

Heart is contained in the pericardium, which is a sac made of two elements: the fibrous pericardium and the serous pericardium. The first one anchors the heart in its position (the mediastinum), prevents overstretch, and provides an external protection to the heart. The second one is constituted by two layers, forming the parietal cavity, with the pericardial fluid inside serving as lubricant [343].

Cardiac wall is composed of the epicardium, the myocardium and the endocardium. The epicardium is the inner layer of the pericardium and is proved to play an important role in cardiac regeneration in adulthood [68]. The myocardium, between the epicardium and endocardium, is the thickest cardiac wall and is made of cardiac muscle, which is responsible for heart contraction. The endocardium covers the internal cardiac regions and the lining of large vessels.

Heart consists of two distinct pumps: the right heart and the left heart, already identified in section 1.1 and depicted in Figure 1.4. Each pump contains two contractile chambers: one atrium and one ventricle. Atria and ventricles are separated through the interatrial septum and intraventricular septum, respectively. Chambers of each pump communicate through atrioventricular valves, called tricuspid valve for the right side and mitral valve for the left side. The edges of each atrio-ventricular valve are fastened to the opposite ventricular walls by the chordae tendinae, to prevent the cusps from being pushed into the atrium during

ventricular contraction [261]. The right heart (left heart) is linked to the pulmonary trunk (aorta) by a semilunar valve, while is directly connected to the venae cavae (pulmonary veins) without an intermediate valve. Semilunar valves are known as pulmonary valve on the right and aortic valve on the left [343, 349].

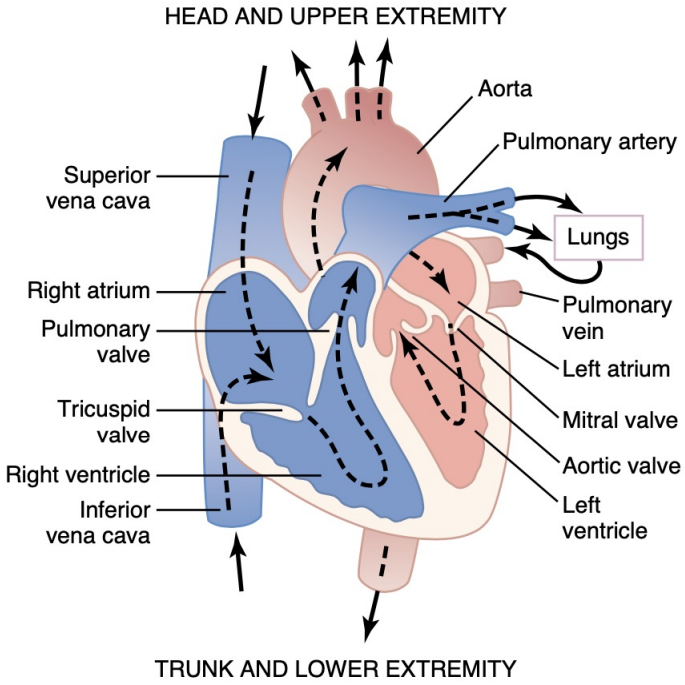

Figure 1.4: Representation of the heart and its pumps: the right heart (in blue) managing deoxygenated blood and the left heart (in pink) managing oxygenated blood. The arrows give an indication of the blood flow directions to and from cardiac chambers and through cardiac valves. *Image extracted from* [110].

All the four cardiac valves open and close passively, based on the pressure difference across them. Thus, the pressure of each chamber influences the status of the following valve, increasing during contraction and decreasing during relaxation. To ensure the proper heart functioning, atria must contract (and relax) together and ventricles must contract (and relax) together, with atria contracting before ventricles and relaxing while ventricles contract. It follows that the phases of atrial and ventricular contraction have to be absolutely coordinated [343, 349]. In physiological situations, this is possible thanks to the constitutive elements of the cardiac muscle and the presence of a special conductive system within it.

Cardiac muscle consists of two networks, the atrial one and the ventricular one. Each of these networks is constituted by individual cardiac cells, the *cardiomyocytes*. The latter are taken together through intercalated disks, which enable the

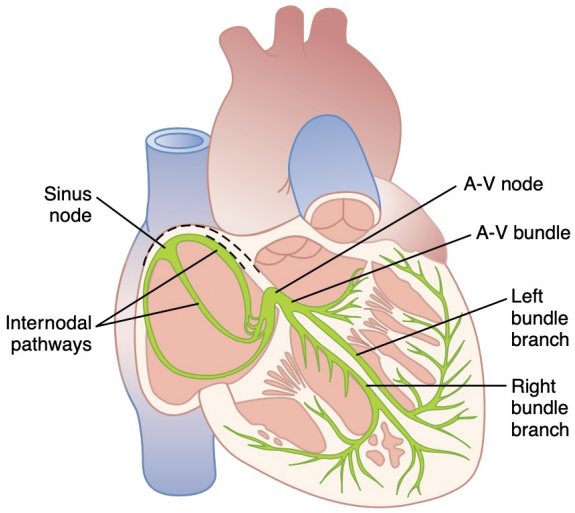

Figure 1.5: Representation of the heart conduction system. *Image extracted from* [110]

rapid convection of action potentials from one cell to all the other cells by the gap junctions. The result is that atria behave as a single cell and contract at the same time when stimulated, as well as ventricles. The initial stimulus to cardiac contraction is provided in the form of electrical impulse by the conduction system, represented in Figure 1.5. It is a system of autorhythmic cardiac cells and conducting fibres able to produce and transmit the action potentials, respectively. Characteristic components of the conduction system are the sinoatrial (SA) node, the atrioventricular (ATV) node, the bundle of His, the bundle branches and the Purkinje fibres [343, 349].

The SA node is positioned in the right atrium, close to the opening of the superior vena cava. It contains the autorhythmic cardiac cells with the highest self-excitation rate (60-100 bpm [367]) among all the other autorhythmic cardiac cells of the conductive system (ATV node: 40-60 bpm and Purkinje fibres: 20-40 bpm [367]). Thus, it is the SA node to establish the rhythm of cardiac contraction and thus the heart rate (HR). For this reason, the SA node is defined cardiac pacemaker. The action potential starting in the SA node immediately spreads to the atria (which contract rapidly and together), finally reaching the ATV node at the base of the right atrium. Because of the slow transmission of the action potential to the ATV node, atria and ventricles cannot contract at the same time, that is essential for the beat to be good developed. The action potential leaving the ATV node enters the bundle of His (following the ATV node), the bundle branches (along the intraventricular septum) and the Purkinje fibres (surrounding both the ventricles). At this point ventricles can contract almost at the same time [343, 349]. Malfunctions of the conduction system can lead to a variety of pathological

situations.

The action potentials flowing through the conductive system during each heartbeat can be recorded from the body's surface, creating the so called electrocardiogram or ECG, correlated to the cardiac cycle [343].

The term *cardiac cycle* defines the sequence of cardiac events during a normal heartbeat: first atria contract and ventricles are relaxed, then ventricles contract and atria are relaxed, finally atria and ventricles are both relaxed. The contraction phase is called systole, while the relaxation phase is called diastole [343]. We define *systole* the ventricular contraction and *diastole* the ventricular relaxation. Thus, one cardiac cycle contains one systole and one diastole.

To better describe a normal cardiac cycle, it is common to use the Wiggers diagram, shown in Figure 1.6. It actually represents the left heart dynamics. However, since atria act together and ventricles act together, the right heart dynamics is symmetrical to the left one.

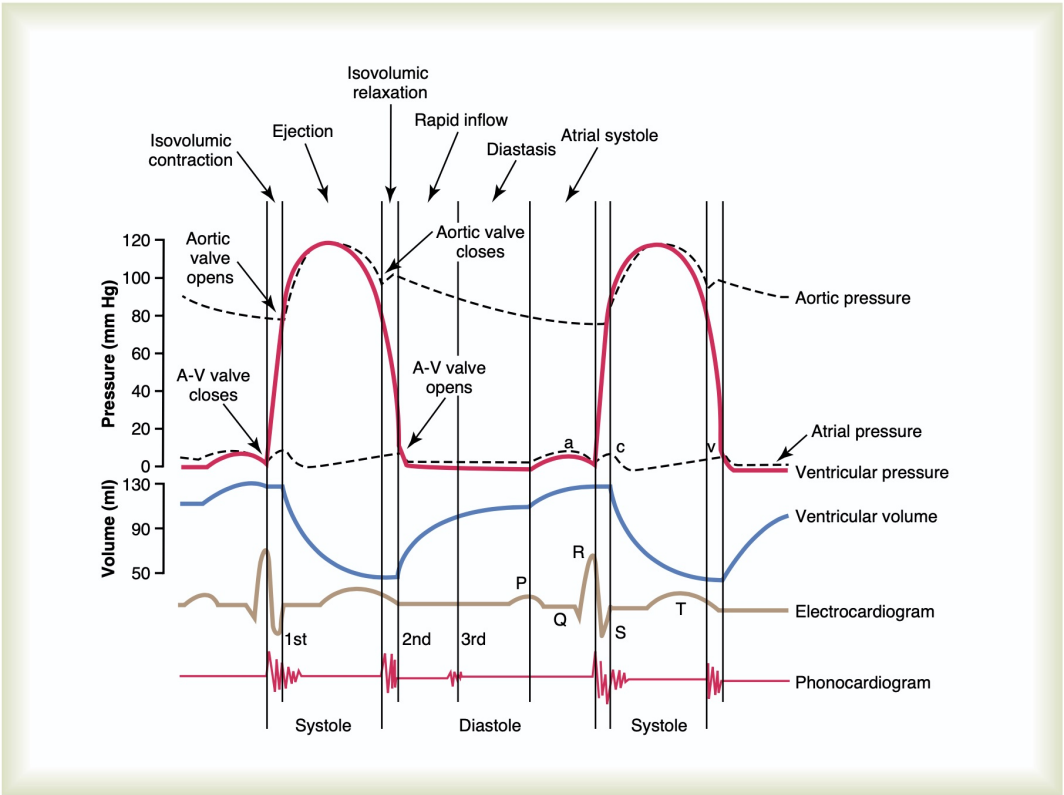

Figure 1.6: Description of the left heart dynamics during a normal cardiac cycle. Representation of the left-atrial, left-ventricular and aortic pressure signals, together with the left-ventricular volume signal, the electrocardiogram and phonocardiogram. *Image extracted from* [110].

We start considering the time when diastole begins: aortic valve has just closed and ventricular volume has reached its minimum value (the end-systolic ventricular volume). Ventricular relaxation causes an immediate decrease in ventricular pressure, while ventricular volume remains constant at its minimum value, being both the mitral and aortic valves closed. This phase is called isovolumic relaxation and is slightly anticipated in the ECG by the T wave. Before emptying, the atrium is tense with its pressure at its maximum value, while ventricular pressure is decreasing. Now atrial pressure becomes slightly higher than ventricular one, thereby causing the opening of the mitral valve and the beginning of diastolic filling. This includes three phases of equal duration: rapid inflow, diastasis and atrial systole. During rapid inflow and diastasis, ventricular volume increases, first fast then slowly, but the atrium is still relaxed. During atrial systole, instead, the atrium contracts, further augmenting the ventricular volume, which assumes the highest value (the end-diastolic ventricular volume). In any case, atrial systole contributes to 20% of ventricular filling, which happens mainly passively. Atrial contraction is due to the electrical stimulation of the atria by the SA node, which is recorded in the ECG in the form of a P wave, moderately before the atrial pressure increase. After atrial contraction, ventricular pressure overcomes atrial pressure and the mitral valve closes, concluding the diastolic period. Note that during diastole, aortic pressure gradually falls because of the blood supply to the periphery. Atrial contraction is followed by ventricular contraction, which begins when the action potential reaches the ATV node. This creates the QRS complex of waves in the ECG, immediately before the aortic valve opening. During ventricular contraction, i.e., systole, we recognize two phases: isovolumic contraction and ejection. Isovolumic contraction leads to an increase in ventricular pressure, while ventricular volume remains constant. As ventricular pressure equals aortic pressure, the aortic valve opens and ejection starts. Thus, ventricular volume starts emptying, first quickly then at a slow pace, reaching the end-systolic ventricular volume. In the meantime, aortic pressure gets larger up to its maximum value, together with ventricular pressure. After that, both pressures decrease again. When ventricle stops contracting, ventricular pressure drops below aortic pressure, aortic valve closes, systole concludes and a new cardiac cycle commences. Notice that aortic pressure starts decreasing before the end of ejection, when the rate of filling drops below the rate of blood flow along the arterial tree. One can see that, in normal conditions, diastole fills the majority of the cardiac cycle (2/3), while the remaining part is systole. Notice that the ECG lacks of a wave anticipating atrial relaxation, differently to ventricular relaxation. This is due to the fact that atrial relaxation happens together with ventricular contraction, thus the electrical activity leading to atrial relaxation is masked in the ECG by the QRS wave [343, 349].

Our heart continuously beats during the whole lifetime, performing about 10^5 cycles per day, 40 million cycles per year, and 3 billion cycles over an average life

of 80 years [97]. Thus, much more than any other organ, heart needs to be nourished by oxygenated blood. To this purpose, it is provided with its own vascular system: the coronary circulation. The main arteries of this circuit are the left and right coronary arteries, arising from the ascending aorta. Deoxygenated blood is returned from the coronary circulation to the right atrium through the coronary sinus, running along the back of the heart. Major common problems arising from a malfunctioning coronary circulation are the coronary ischaemia, which is a reduction of the coronary blood supply, and the myocardial infarction or heart attack, which is the death of a portion of the cardiac tissue due to an interruption in the regional blood supply [153, 343].

The most common haemodynamic variables associated to heart are the heart rate, HR, stroke volume, SV, stroke work, SW, ejection fraction, EF, cardiac output, CO, tension time index, TTI, and rate pressure product, RPP.

HR, as anticipated above, is the number of beats performed by heart in one minute and is provided in [bpm], standing for beats per minute. Notice that the mean heartbeat period, RR, can be calculated from HR as

$$\mathrm{RR} = 60/\mathrm{HR}. \tag{1.1}$$

SV, typically given in [ml], is the blood volume each ventricle ejects per heartbeat period and is obtained as

$$\mathrm{SV} = \mathrm{EDV} - \mathrm{ESV}, \tag{1.2}$$

where EDV, the end-diastolic ventricular volume, is the ventricular volume at the end of diastole (when tricuspid/mitral valve closes for the right/left ventricle), and ESV, the end-systolic ventricular volume, is the ventricular volume at the end of systole (when pulmonary/aortic valve closes for the right/left ventricle). EDV and ESV are both indicated in the P-V loop of Figure 1.7.

SW is the work a ventricle has to perform in order to eject a volume of blood (SV) in one heartbeat period. SW corresponds to the area of the P-V loop (see Figure 1.7), is normally represented in [ml mmHg], and is determined as

$$\mathrm{SW} = \mathrm{SV}\mathrm{x}\mathit{Force}, \tag{1.3}$$

where Force is the force acting on the ventricle and opposing to blood ejection. For the left ventricle, it is correct to assume $\mathit{Force} \simeq \mathrm{MAP}$, with MAP the mean arterial blood pressure.

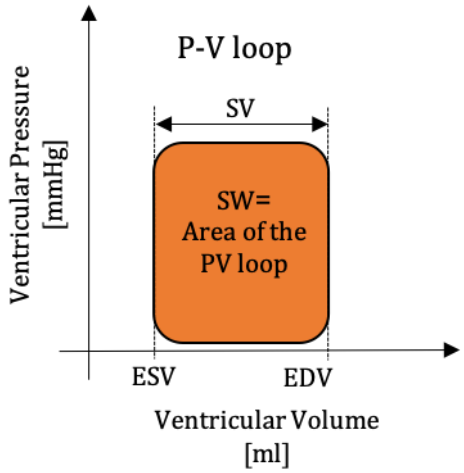

Figure 1.7: Representation of a P-V loop, with an indication of the end-diastolic, EDV, and end-systolic, ESV, volumes, together with the stroke volume, SV, and work, SW.

EF is the volumetric percentage of blood ejected by a chamber during its contraction over its total blood content. It is evaluated for the two ventricles, expressing the efficiency of pumping blood into SC and PC for the left and right ventricles, respectively. It is calculated as

$$\text{EF} = \text{SV/EDVx100\%}. \tag{1.4}$$

CO is the blood volume pumped by each ventricle per minute, generally indicated in [l/min], and is obtained as

$$\text{CO} = \text{SVxHR}. \tag{1.5}$$

It is important to note that, at steady-state, SV and CO are equal for the right and left ventricles. In other words, the volumes of blood managed by SC and PC are the same and small differences are possible in transient conditions only.

TTI ([mmHg s/min]) and RPP ([mmHg/min]) are usually considered as measures of oxygen consumption [365]. TTI corresponds to the area under the left-ventricular pressure curve during the ejection period and is obtained as

$$\text{TTI} = \bar{p}_{lv}\text{xRRxHR}, \tag{1.6}$$

with $\bar{p}_{lv}$ the mean value of the left-ventricular pressure per cardiac beat. RPP is instead defined as

$$\text{RPP} = p_{aor_{sys}}\text{xHR} \tag{1.7}$$

where $p_{aor_{sys}}$ is the aortic systolic pressure.

1.2.4 Fluid: the blood

Blood is a suspension made of a liquid called plasma and a number of cells constituting the haematocrit. Blood components are perfectly mixed during the blood movement and separate in stationary blood, for example in a test tube. Plasma and haematocrit represent the 55% and 45% of total blood volume, which approximately amounts to the 8% of the body weight, i.e., 5-6 l. Plasma mainly consists of water (93%) and proteins (7%) dissolved in it, while haematocrit contains the erythrocytes or red blood cells (4.8-5.4 million per mm^3), the leukocytes or white blood cells (5000-10000 per mm^3), and the platelets (250000-400000 per mm^3) [343, 349].

Erythrocytes appear as biconcave discs with an average diameter of 7/8 μm and incorporate a particular protein, the haemoglobin. The latter is responsible for the classical red color of blood and allows erythrocytes to transport oxygen and carbon dioxide throughout the body because of its iron content. Erythrocytes deteriorate due to the contact with capillary walls but are not able to reproduce or renew. Thus, they are periodically (every 120 days) phagocytized by specialised cells and replaced by new cells. The process leading to new erythrocytes is called erythropoiesis, is performed by the bone marrow cells, and is regulated by the erythropoietin, a hormone secreted in the kidneys. Erythropoietin stimulates the production of other erythrocytes when the number of erythrocytes reduces, the haemoglobin content per erythrocyte diminishes, the blood flow to the kidneys is limited, or the oxygen extraction at pulmonary level is impaired [343, 349].

Leukocytes are bigger in diameter than erythrocytes (8-19 μm). Their major role is to protect our body from infections or inflammation processes by phagocytosis or producing antibodies. Contrary to erythrocytes, leukocytes do not work inside the blood vessels but in the interstitial fluid, using the circulation just to reach the site of infection/inflammation. Leukocytes can destroy a limited number of foreign cells before dying. They live for a few days or a few hours in case of infection and are then substituted by new cells produced in the bone marrow [343, 349].

Platelets are disc-shaped cells with a diameter of 2-4 μm. They are essential in blood coagulation, for example, in case of injury to prevent excessive blood losses. They last 5-9 days and are then replaced by new platelets coming from the bone

marrow [343, 349].

Blood viscosity varies with tube dimension, flow rate and haematocrit ratio at a given temperature (normally around 37°). In particular, blood viscosity reduces for tube diameters below 0.3 mm, as flow rate increases, and for a diminished haematoctrit ratio (e.g., in case of severe anaemia, when haematocrit accounts for 15% only of total blood volume [110]) [153]. These changes in viscosity are due to the fact that blood is an inhomogeneous fluid, with its corpuscular elements aggregating or separating in specific conditions, thereby giving an inconstant contribution to the fluid dynamic response of the cardiovascular system.

Blood is a non-Newtonian fluid being its viscosity variable with shear rate, which grows with flow rate. However, it is proved that blood viscosity reaches an asymptotic value when the rate of shear is around 1000s^{-1} [177]. This happens in large and medium arteries, where blood can effectively be considered Newtonian.

1.2.5 Pulsatile motion: proximal to distal haemodynamics

Intravascular blood pressure (blood pressure inside the vessel) at any site in SC is given by the sum of three components: the external pressure acting on the vascular walls (p_E), the pressure that left ventricle impresses to the blood during ejection (p), and the hydrostatic pressure (p_H). p_E is typically equal to the atmospheric pressure but can be also subatmospheric, for example at chest level, because of respiration [261]. p is known as excess pressure and its gradient drives the blood throughout SC [46]. p_H depends on the blood density (ρ), the vector acceleration of gravity ($\mathbf{g}$), and the vector distance ($\mathbf{H}$) between the considered site and the hydrostatic indifference point (HIP) [126, 177, 264], i.e., $p_H = \rho\mathbf{g} \cdot \mathbf{H}$.

Transmural pressure (p_T) is the difference between the intravascular pressure and p_E, and can be expressed as $p_T = p + \rho\mathbf{g} \cdot \mathbf{H}$. Since subjects are usually assumed supine in clinical practice, it is common to write $p_T = p$. In the following, we will use the term *blood pressure* or simply *pressure* and the symbol p to refer to the excess pressure, unless otherwise indicated.

The evaluation of the pressure components in PC, especially at capillary level, is complicated, being the pulmonary pressure dependent on the inspiration and expiration cycles [261]. However, we do not treat this aspect here and will neglect the effect of respiration and the capillary contribution of PC in the modelling of human circulation (chapter 3).

The behaviour of p in SC is synthetically summarized in Figure 1.8. Arterial blood pressure is pulsatile, with its mean value progressively decreasing towards the periphery. The highest pressure gradient is localised between arterioles and capillaries, confirming that the pressure produced by the contracting activity of the heart is largely spent to push blood to distal regions [27]. Pressure gradients

are instead smaller along the arterial and venous patterns.

Arterial pressure is also pulsatile in PC, although the mean pressure level (about 16 mmHg in PC and 100 mmHg in SC [110]) and pulse pressure (about 15 mmHg in PC and 40 mmHg in SC [110]) are lower than in SC .

Since arteriolar, venular and venous blood pressures are weakly pulsatile or constant, and pulmonary arterial blood pressure is feebly pulsatile with respect to its systemic counterpart, we here focus on the blood pressure behaviour along the systemic arterial network.

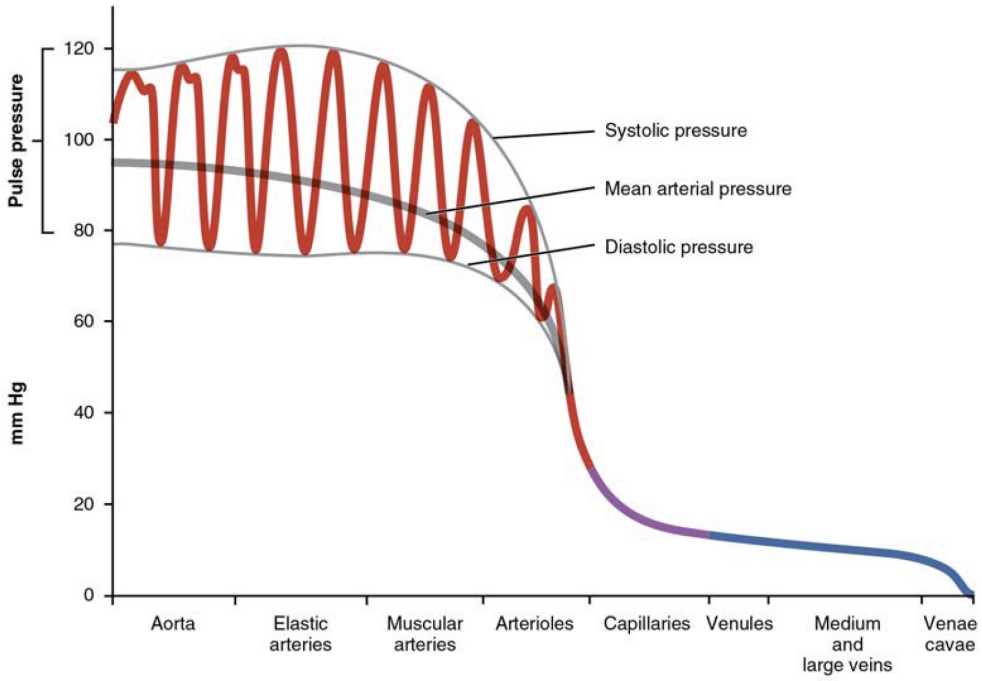

Figure 1.8: Representation of the excess pressure along the arterial (in red), capillary (in purple) and venous (in blue) circuits in SC. *Image extracted from* [27].

Being arterial pressure pulsatile, it is useful to identify characteristic pressure values over time at each arterial location. Given an aortic pressure signal (e.g., see Figure 1.6 or 1.10), one defines the systolic (p_{sys}) and diastolic (p_{dia}) pressures as the maximum and minimum pressure values, the pulse pressure (pp) as the difference $p_{sys} - p_{dia}$, and the mean pressure (p_{mean}) as the quantity $p_{dia} + 1/3pp$. One can notice that p_{mean} is not the arithmetic average between p_{sys} and p_{dia}, this to take into account the greater duration of diastole with respect to systole [349].

In normal conditions, pressure at aortic root oscillates between 120 and 80 mmHg and has a mean value around 100 mmHg, leading to the signal represented

in Figures 1.6 and 1.10. However, maximum and minimum arterial pressures, as well as arterial pressure waveforms, modify with the distance form the heart. If one was able to record a number of pressure waveforms along the aorta at the same time, something similar to what depicted in Figure 1.9 would be found. Moving away from the heart, pressure signals delay, steepen and increase in amplitude up to the third class of branches (muscular arteries) [46], with systolic pressures growing and diastolic pressures decreasing.

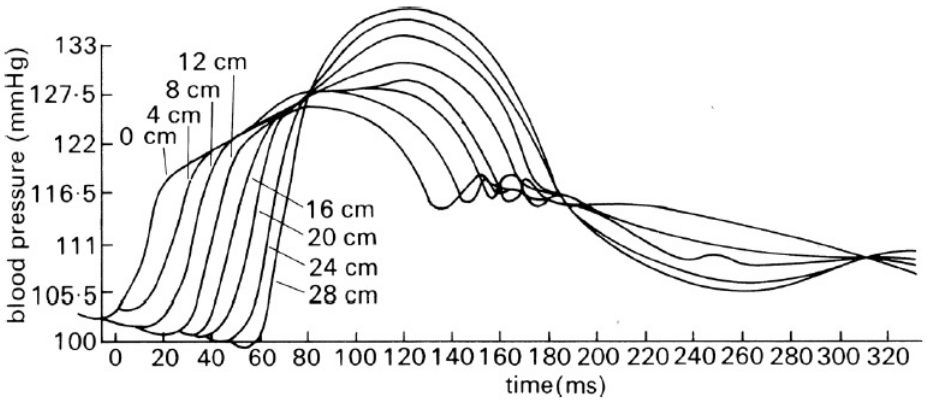

Figure 1.9: Pressure waveforms at multiple sites and at the same time along a canine aorta. *Image extracted from* [46, 253].

The delay of pressure signals along the aorta and systemic arteries is due to the fact that the pressure impulse transmitted by the heart to the blood during ejection cannot instantaneously reach the periphery because of arterial elasticity. Thus, it propagates as a wave at a finite speed, called wave speed or pulse wave velocity. The latter depends on the blood density and the vascular geometrical and mechanical properties. An approximation of the wave speed can be derived from the one-dimensional linear wave theory, which considers the propagation of pressure waves in an infinitely long elastic channel, with uniform geometrical and mechanical properties along its length, and with an incompressible inviscid fluid inside [46, 261, 365]. The one-dimensional linear wave theory leads to the Moens-Korteweg equation

$$c_{MK} = \sqrt{\frac{E_m h_w}{\rho D}}, \tag{1.8}$$

where E_m is the incremental elastic modulus of the vessel wall, h_w is the wall thickness, ρ is the blood density, and D is the internal diameter. c_{MK} well approximates the wave speed along the large and medium arteries, it is called phase velocity, and neglects the effects of both reflections and viscosity. Equation (1.8) explains why

the wave speed of large and medium arteries augments with the distance from the heart: both the ratio h_w/D (see Table 1.2) and the incremental elastic modulus increase further away from the heart.

Another way to evaluate the wave speed at a generic arterial location is using the foot-to-foot method. Basically, one has to know the distance between the heart and the generic arterial site, Δx, and the time it takes for the minimum of the pressure wave (called the *foot* of the pressure wave) to travel Δx. Therefore, $c_{FTF} = \Delta x/\Delta t$ gives an estimation of the wave speed at the chosen site. It is proved that c_{FTF} is similar to c_{MK} and, thus, could be used to get an estimation of E_m, h_w or D from the Moens-Korteweg equation [365].

The one-dimensional linear wave theory yields a good estimation of the arterial wave speed, however, it is not adequate to explain the changes in the arterial pressure waveforms from central to distal sites [46]. In fact, according to the linear theory, the shape of the arterial pressure waveforms should remain unaltered with the distance from the heart. The error committed by the one-dimensional linear wave theory in predicting the arterial pressure waveforms depends on the fact that, contrary to its hypotheses, arteries have a finite length and are not uniform in both geometry and mechanical properties, creating a succession of discontinuities. At each discontinuity, the incoming pressure wave is partly transmitted and partly reflected, leading to a forward and a backward wave [356]. Thus, the pressure signal at each arterial site is the sum of forward and backward waves, with the backward contribution justifying the pressure pulse increase with the distance from heart. Regarding the higher steepening of the arterial pressure waveforms further away from the heart, it is mainly due to the elastic and fluid dynamic nonlinearities of the arterial tree; the elastic nonlinearities derive from the mechanical behaviour of the arterial walls, while the fluid dynamic nonlinearities are due to the convective accelerations. By contrast, peripheral arterial pressures appear damped with respect to the central ones as a consequence of blood and intrinsic wall viscosity [46].

As arterial pressure signals, also flow rate signals vary in both time and space. We can first examine the shape of the flow rate waveform at the aortic root during an heartbeat period, comparing it with the simultaneous pressure waveform at the same site (see Figure 1.10). The aortic flow rate rises together with the aortic pressure early in systole. Then, this synchrony is lost, with the aortic flow rate diminishing before the aortic pressure and becoming slightly negative immediately after the closure of the aortic valve [46]. The absence of synchrony between aortic pressure and flow rate later in systole is mainly due to wave reflections. Indeed, as pressure signals, also flow rate signals can be seen as sums of forward and backward waves. However, contrary to the backward pressure wave, the backward flow rate wave is reflected upside down with respect to pressure [46, 365].

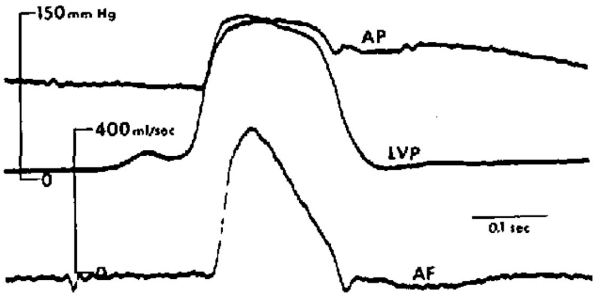

Figure 1.10: Simultaneous aortic pressure (AP), left-ventricular pressure (LVP) and aortic flow rate (AF) waveforms in a conscious dog. *Image extracted from* [238].

A representation of simultaneous cross-sectional average velocity[4] waveforms at different sites along the aorta is given in Figure 1.11. Notice that, differently to arterial pressure waveforms, flow rate waveforms experience a progressive reduction in amplitude. This phenomenon cannot be explained through the one-dimensional linear wave theory, according to which pressure and flow rate should have same waveform and phase. Instead, it is due to blood viscosity, much more important at peripheral sites, where the thickness of the boundary layer becomes comparable to the vessel radius [46, 365].

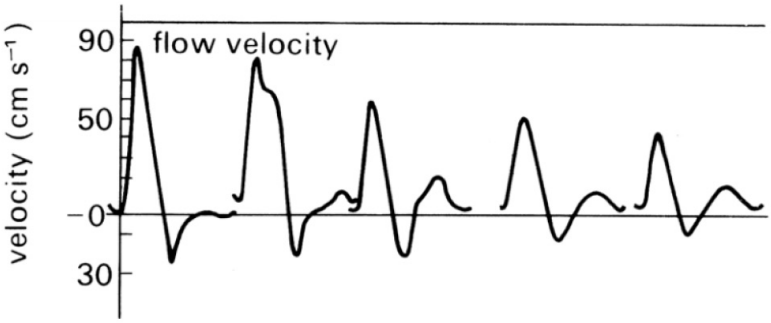

Figure 1.11: Cross-sectional averaged velocity waveforms at multiple sites and at the same time along a canine aorta. *Image extracted from* [46, 206].

To quantify the amount of reflection at any arterial site, one could use the reflection magnitude, RM, or reflection index, RI. Both these parameters require the decomposition of the total pressure signal at the chosen site (p_t) into its forward (p_f) and backward (p_b) contributions (see Figure 1.12), as proposed by Westerhof et al. [365]. In fact, RM is the ratio between the amplitudes of the backward and

[4]The cross-sectional averaged velocity has the same waveform of the corresponding flow rate but is scaled with respect to the cross-sectional area [46].

forward pressure waves (RM= $|p_b|/|p_f|$), while RI is the ratio between the amplitude of the backward pressure wave and the sum of the amplitudes of the forward and backward pressure waves (RI= $|p_b|/(|p_b| + |p_f|)$). The amount of reflection is also often quantified through the augmentation index, AI, which is calculated as the ratio between the local augmented pressure (AP) and pulse pressure (pp). AP is obtained as the difference between the second systolic shoulder and the first systolic shoulder of p_t. It is important to notice that AI depends, apart from the amount of reflection, on the time of return of the reflected wave, as well as the shapes of either the forward and backward waves [365]. It follows that, contrary to RM and RI, is not able to quantitatively describe the real magnitude of reflection at each site, despite it is widely used as a surrogate measure of RI.

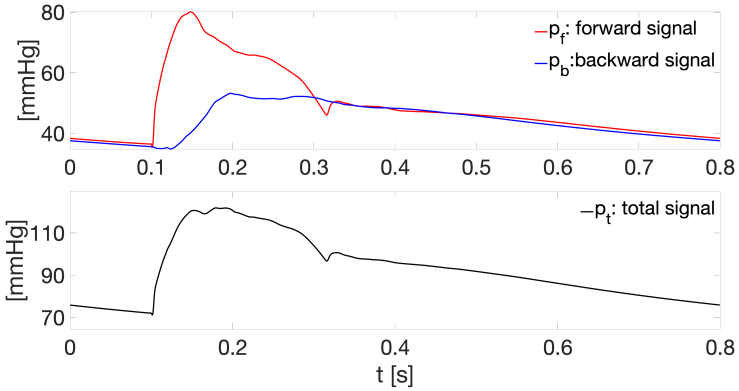

Figure 1.12: Forward (p_f) and backward (p_b) pressure waves derived from p_t.

1.2.6 The equilibrium of circulation: short- and long-term control system

The whole cardiovascular system works in order to maintain the most efficient equilibrium condition, that is minimizing the amount of energy required for an optimal functioning. This arduous task is achieved through a continuous autoregulation process, implemented through both short- and long-term control mechanisms.

The most regulated haemodynamic variable of the whole cardiovascular system is, of course, the systemic arterial pressure (p_{art}), and, in particular, its time-averaged value over the cardiac cycle ($\overline{p}_{art}$). In fact, $\overline{p}_{art}$ represents the force driving blood to tissues and back to heart [349]. It is demonstrated [177] that $\overline{p}_{art}$ mainly depends on CO and total arterial peripheral resistance (TPR [mmHg s/ml]). The latter is the total resistance associated to SC, mostly consisting of the systemic arteriolar resistances. The equation linking $\overline{p}_{art}$ to CO and TPR (having the same form of the Poiseuille's law, $\Delta_p = \Delta_Q/R$) is

$$\overline{p}_{art} - \text{CVP} = \text{CO} \cdot \text{TPR}, \tag{1.9}$$

where CVP is the central venous pressure. Referring to the atmospheric pressure, CVP is almost null and equation (1.9) can simply be written as

$$\overline{p}_{art} = \text{CO} \cdot \text{TPR}. \tag{1.10}$$

The (1.10) is considered the most important equation of cardiovascular physiology. In fact, if combined with the definition of CO (see equation (1.5)), it allows one to recognize the three main determinants of $\overline{p}_{art}$: SV, HR and TPR. Considering that each of these determinants in turn depends on other factors, one can distinguish all the variables acting on $\overline{p}_{art}$ [349].

Relationships between $\overline{p}_{art}$ and its determinants are summarized in Figure 1.13, which deserves to be commented.

SV rises with venous pressure. In fact, an increase in venous pressure, leads to an increase in venous return and, thus, in the amount of blood entering the right ventricle before ejection, called right-ventricular end-diastolic volume. Since a higher ventricular end-diastolic volume means a higher ventricular distension, and ventricular contraction swells with ventricular distension, it follows that right SV augments with venous pressure. Recalling that right and left SVs coincide, there is an increasing aortic blood volume per minute when venous pressure augments. Venous pressure in turn gets higher with the inspirations cycles, the total blood volume, the exercise of leg muscles, and the constriction of venous vessels, which is due to nervous and hormonal commands. SV also rises with cardiac contractility, which, together with HR, can change based on nervous and hormonal stimuli [349].

Regarding TPR, it alters with changes in arteriolar diameters and blood viscosity. Arteriolar diameters can modify because of nerves and hormones, as well as with the metabolic necessities of surrounding tissues and organs to which blood is supplied. In both situations, there can be vasoconstriction or vasodilatation. Blood viscosity varies with the percentage composition of blood: the higher the haematocrit (more than 45%), the higher blood viscosity and vice versa [349].

Based on this description, it appears that several factors are responsible for $\overline{p}_{art}$. However, the most impacting factors are the total blood volume and the nervous system. Control of total blood volume is more influential in long periods, while the action of the nervous system is more significant in short periods. It is on nervous system that we here focus [256].

Nervous system is able to control $\overline{p}_{art}$ through proper chemical and mechanical receptors distributed along the cardiovascular circuit. In particular, chemoreceptors

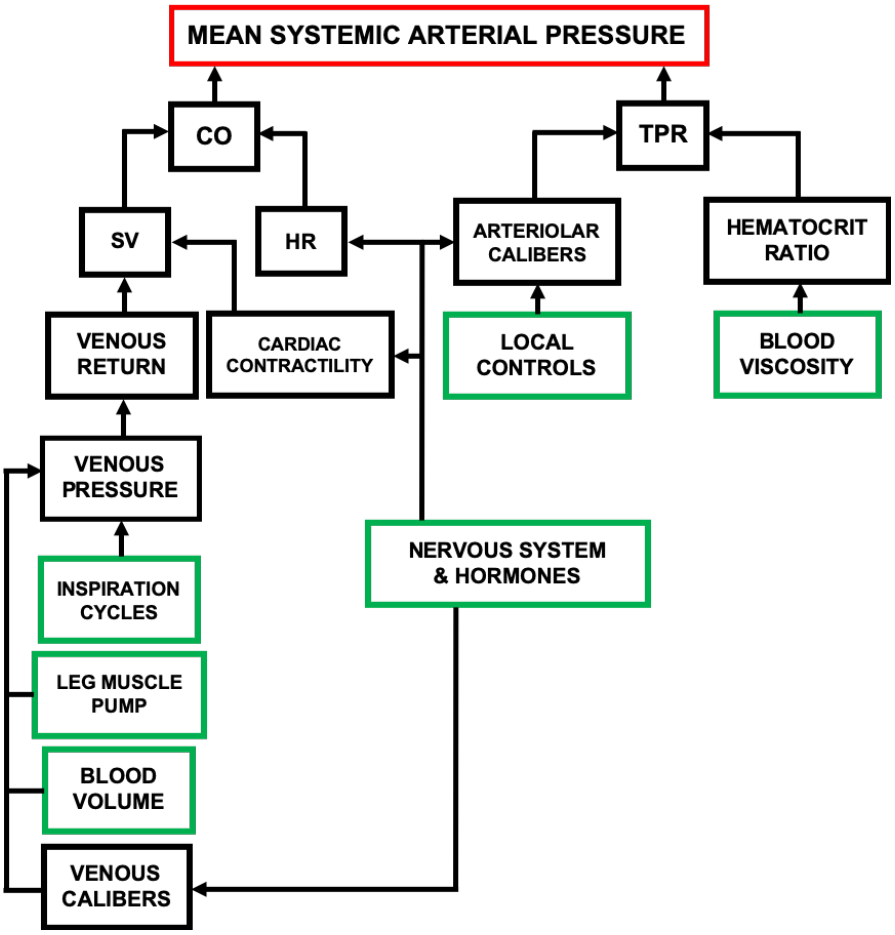

Figure 1.13: Scheme showing the cause/effect relationships between mean systemic arterial blood pressure and impacting factors. Prime determinants of arterial blood pressure are written in green rectangles [349].

respond to chemicals, such as oxygen and carbon dioxide, while baroreceptors and mechanoreceptors respond to pressure variations in high and low pressure zones, respectively. Baroreceptors are the most studied and important receptors involved in $\overline{p}_{art}$ control. A simple scheme of their functioning is reproduced in Figure 1.14. They are located at the walls of the aortic arch and carotid sinuses and consist in nerve endings. These last ones are sensitive to the degree of vascular stretching, dependent on the local blood pressure magnitude, which is similar to $\overline{p}_{art}$. In particular, a growth in $\overline{p}_{art}$ leads to an enhanced firing rate of the baroreceptors, and the opposite when $\overline{p}_{art}$ decreases with respect to its steady state normal value. Nerve endings are connected to neurons of the cardiovascular control center in the medulla. Medullary neurons generate two nervous signals, the sympathetic one and the parasympathetic or vagus one, based on the input from the baroreceptors. The sympathetic signal is directed to heart, arterioles and veins, and

increases (decreases) with a decrease (increase) in the baroreceptor firing rate. The parasympathetic signal is directed to the heart only, and decreases (increases) with a decrease (increase) in the baroreceptor firing rate. While the sympathetic signal affects heart rate, cardiac contractility and arteriolar calibres, the parasympathetic signal just affects the heart rate. The control of heart rate is called chronotropic, while the control of cardiac contractility is called inotropic effect. Thus, when $\overline{p}_{art}$ falls, the firing rate of baroreceptors reduces, causing that the sympathetic activity increases and the parasympathetic activity decreases. As a consequence, heart rate and cardiac contractility augment, while arteriolar and venous vessels constrict, provoking higher CO and TPR, and thus $\overline{p}_{art}$. The opposite happens as $\overline{p}_{art}$ rises. Considering the entire baroreceptor mechanism, baroreceptors represent the afferent part, and heart, arterioles and veins the efferent part or efferent organs [256, 349].

It should be emphasized here that the baroreceptor mechanism is efficient in maintaining normal $\overline{p}_{art}$ values in the short term only. In fact, prolonged exposure to abnormal $\overline{p}_{art}$ values can cause a change in the operative point of the cardiovascular system, which adapts to work around higher or lower $\overline{p}_{art}$. It is the case, for example, of people suffering from hypertension, who normally exhibit higher arterial pressures, despite baroreceptors are perfectly working [349].

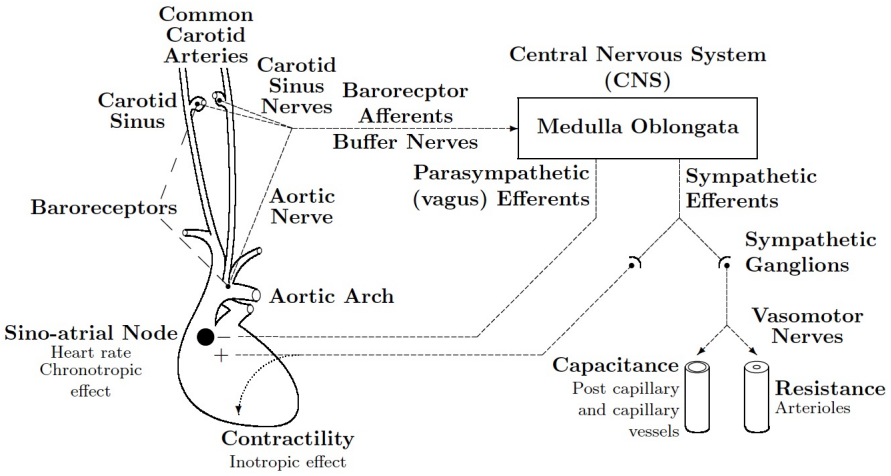

Figure 1.14: Representation of the baroreceptor mechanisms. *Image extracted from* [256].

1.2.7 A continuous evolutionary process: the effects of posture, exercise and ageing

It is not simple to define the steady-state condition of the physiological cardiovascular system, since its functioning is continuously affected by posture, amount of physical effort, age, emotional state and so on. Moreover, in presence of pathologies and assuming drugs, the analysis of the whole system is even more complex. In this section, we give more insights into the effects of posture, exercise and age on the cardiovascular system.

Posture

When lying, the hydrostatic pressure component is active on the sagittal plane and null on the longitudinal plane. Thus, the distribution of blood along the body height does not depend on the gravity vector. When standing, about 700 ml [260, 283] of blood move from the upper body to the lower body regions, causing the blood pressure increasing and decreasing in the feet and head, respectively. Arterial (venous) pressure at head and feet level is around 95 (5) mmHg at both locations in supine position, while amounts to around 50 (-40) and 195 (95) mmHg in standing position [365], respectively. The rise in the capillary and venous pressure in the legs promotes a growth in both the amount of blood migrating from capillaries to interstitial fluid and the venous distensibility. These two factors are responsible for a fall in the effective circulatory blood volume, with consequences similar to the mild haemorrhage: arterial blood pressure decays and blood flow to heart and brain drops. In this situation, arterial baroreceptors respond with a reduced parasympathetic activity and a magnified sympathetic activity, which eventually lead to a partial recovery of the arterial pressure. However, one of the most effective compensatory mechanism during standing is the contraction of leg muscles, which facilitates venous return and generates higher COs. When this compensatory mechanism is not active, for example when one stands for a long time without moving, fainting is a likely possibility [349].

Exercise

While exercising, the amount of blood required by skeletal muscle, skin and heart significantly intensifies. The higher blood flows in these areas are due to the dilation of local arterioles, partially compensated by arteriolar constriction at other cardiovascular zones. Nonetheless, it is well known that TPR globally decreases in exercise. CO, instead, remarkably increases, up to 20-25 l/min for people with a basic training, and 35 l/min for athletes, in strenuous exercise. These haemodynamic changes derive from an enhanced sympathetic activity and limited parasympathetic activity. However, variations in sympathetic and parasympathetic activities are not regulated by the arterial baroreceptors but by some brain exercise centres and the

powerful oxygen consumption by skeletal muscles. Arterial baroreceptors, in fact, oppose to the enhanced/limited sympathetic/parasympathetic activity, because of the high mean and pulse systemic arterial blood pressure during exercise. It has also been observed [90] that the reflexes active during exercise tend to elevate the mean systemic arterial pressure regulated by arterial baroreceptors. In other words, while exercising, the operative point of the mean systemic arterial pressure is shifted upward. It is important to note that during mild exercise, venous return could be limited, despite the pumping action of leg muscles, the high number of inspiration cycles, the dilated arterioles in exercising muscles (facilitating the blood movement from arteries to veins in SC), and the constriction of venous vessels by the strong sympathetic activity. This limitation to the venous return could be due to a loss in plasma volume, induced by excessive sweating and elevated capillary pressure in exercising muscles. In addition, it deserves to know that effective variations in SV, HR and CO during a given exercise depend on the individual level of physical activity, which is function of the frequency and type of exercise usually performed [349].

Age

During ageing, elastic arteries (in SC) dilate, thicken and most of all stiffen. The process leading to stiffening is due to the progressive rupture of elastic fibres because of fatigue. In fact, elastic fibres, like other materials, experience a reduction in their resistance to fatigue because of the pulsatile action of blood, and are expected to break after a fixed number of strain cycles. When broken, damaged elastin is not replaced by new elastin and is, instead, substituted by collagen and mucoid material. Thus, the basic mechanical properties of elastic arteries are progressively lost, with concomitant changes in the cardiovascular behaviour consolidated in youth. The stiffening of elastic arteries causes an increase in the local pulse wave velocities, with the consequent anticipated return of backward waves, leading to higher systolic pressures. Moreover, stiffer elastic arteries have a reduced reservoir capacity, producing a decrease in diastolic pressures [85]. Therefore, one of the most striking effect of ageing is the increase in pulse pressures, with systolic and mean pressures growing and diastolic pressures reducing along elastic arteries. Muscular arteries are less affected and their pressure signals show negligible variations in time. The central pressure pattern alteration during ageing has a lot of dramatic effects on the whole circulation. In fact, the growth in central systolic pressures provokes a rise in left-ventricular load, augmenting the risk of left-ventricular hypertrophy. Left-ventricular hypertrophy determines a lengthened systole and a shorter diastole, which, together with a smaller central diastolic pressure, can impair the coronary circulation, augmenting the risk of ischaemia. Finally, since elastic arteries are not able to effectively absorb blood flow pulsations, these can reach peripheral sites, damaging also microcirculation zones, especially at kidneys and brain [247, 246].

Chapter 2

Cardiovascular modelling

2.1 Overview on cardiovascular modelling

The key points of the cardiovascular system behaviour, summarized in the previous chapter and almost obvious nowadays, were gradually discovered and investigated over the centuries. It is sufficient to think that up to 1578 blood was believed constantly consumed and replaced by nutrients [294], and up to 1735 systemic arterial pressure was thought to be constant with time [364]. Advancing the knowledge of the circulatory system and increasing the desire to comprehend its functioning and relative mechanisms, mathematical models attempting to reproduce this complex apparatus started to be conceived. The first cardiovascular model was quantitatively defined in 1899 by Otto Frank [84, 286], who contributed to the formulation of fundamental concepts and instruments in cardio-physiology (like the Frank-Starling law and the pressure-volume loop) and introduced principles and ideas already analysed in the modern research [162]. The model by Otto Frank, known as the two-elements Windkessel model (see top model of Figure 2.1), can be considered the precursor of all the successive zero dimensional models (described in section 2.2.1). It represents the whole systemic arterial tree as an electric circuit, made of a compliance, standing for the total systemic arterial compliance, in parallel with a resistance, standing for the total systemic arterial resistance (compliances and resistances are defined later in the text). This simple model well approximates the decay of the systemic arterial pressure (p_{art}) during diastole but lacks to capture what happens in systole, where the high frequency components of p_{art} are localised [302, 364]. Starting from this basic description of the systemic arterial tree, a wealth of sophisticated and detailed mathematical models of both the whole circulation and its portions have been developed. These advanced new models, rigorously solved numerically, are currently used to answer both clinical and fluid dynamic questions, giving a substantial contribution to a great deal of applications.

From a clinical perspective, cardiovascular models are mainly adopted to shed

light on the pathogenesis of cardiac and vascular diseases [337], overcoming the main limitations of *in-vivo* studies, which are typically invasive, expensive and not easy to carry out [321]. Cardiovascular modelling has the advantage to explore the direct influence of specific pathologies, neglecting the effects of all the concomitant ones. In fact, it is not rare in cardiology that a certain number of dysfunctions coexist, making extremely difficult to isolate the role played by a single disturb. As an example, patients suffering from atrial fibrillation (AF) are usually affected by other cardiovascular disorders (e.g., hypertension [350], heart failure [74], coronary artery disease [210], valve stenosis [64], etc.), which complicate the possibility to isolate the fall-outs of AF alone from standard medical examinations. Cardiovascular models also support the design of medical devices (such as stents and valve prostheses [220]), can be used as teaching and training environments by medicine students [3], and to prognosticate the effects of potential therapeutic actions [309]. In this last case, models have to be personalised according to patient-specific data, becoming precious guides for surgeons about treatment decisions, with consequent maximization of therapy efficacy and optimization of cost, time and risk in clinical trials [220]. Thus, the modelling approach plays an important role in cardiovascular medicine, although poses challenges for the future [379]. Indeed, there is the problem to combine both physical and biological phenomena within the same framework, integrating macroscopic and microscopic scales. In addition, the more the model is complicated, the more its computational cost rises, making it arduous to run patient-specific models in real-time.

In-silico models are also adopted in the field of aerospace medicine, to inquire into unclear and unresolved cardiovascular issues caused by extreme accelerations or altered gravity conditions. Especially in case of weightlessness, questions such as orthostatic intolerance, in-flight cardiac arrhythmias, cardiovascular remodelling [175], possible visual impairment [236], and augmented risk of cardiovascular diseases due to space radiations [129] represent topics of great scientific interest. This because the genesis of these problems is not completely understood and the proposed countermeasures for their resolution are far from being definitive. To this purpose, it should be recalled that the effects of microgravity cannot be totally duplicated on Earth and are not easily measured on astronauts in space. Indeed, the reduced number of astronauts involved in medical tests per mission, the restricted time for crew members to conduct physiological measurements, and the strict operational requirements of equipments to use during spaceflight justify the difficulty in getting decisive answers from space experiments [109]. In this scenario, the use of cardiovascular models simulating microgravity effects turns out to be highly attractive.

2.2 From zero to multidimensional models

Depending on the final utilization, various cardiovascular models have been proposed, spanning from zero dimensional to multidimensional.

2.2.1 Zero dimensional models

Zero dimensional (0D) models, also known as lumped models, offer a simplified representation of the whole circulation: pressure and flow rate are taken uniform within each cardiovascular region and are simply advanced in time by solving a set of ordinary differential equations [302]. 0D models can be derived from mass and momentum conservation laws (under certain hypotheses) [81] and are represented as electric circuits by taking advantage of the hydraulic-electric analogy. Based on the latter, flow rate and pressure translate into corresponding electric current and potential, while viscous, elastic and inertial effects in the blood flow field are modelled through resistances, compliances and inertances, respectively. These last quantities are defined below.

Resistance

Resistance, R, is a measure of the force which goes against the blood flow. For a single vessel it can be obtained through the Poiseuille's law (see subsection 1.2.1). However, the application of the Poiseuille's law is not trivial, considering that it requires data often unknown, such as the exact vessel dimensions and the blood viscosity, which can be quite variable inside small vessels. Thus, the resistance of a single vessel is typically estimated as the ratio between the mean pressure gradient (Δ_p) and the mean flow rate (Δ_Q) through the vessel, i.e., $R = \Delta_p/\Delta_Q$. This is the Ohm's law if the hydraulic-electric analogy is applied [365]. The resistance associated to a group of vessel can be evaluated by combining the corresponding singular resistances in series or in parallel, as in electric circuits, depending on how the different vessels are arranged. The total resistance will be the sum of the single resistances, for resistances in series, and the inverse of the sum of the single resistances, each to the power of -1, for resistances in parallel.

Compliance and Elastance

Compliance, C, is a measure of elasticity. For a generic organ or vascular region, it can be calculated as the ratio between the variation in volume (Δ_V) experienced under a fixed variation in pressure (Δ_p) and Δ_p, i.e., $C = \Delta_V/\Delta_p$. Elastance, E, is instead defined as the inverse of compliance [365]. Notice that pressure-volume relationships are often non-linear. This means that C and thus E are typically variable within a wide pressure range and can remain constant over limited pressure intervals only.

Inertance

Inertance, L, is a measure of the variation in the pressure difference through a blood vessel (Δ_p) as mean blood velocity changes ($dQ/dt \neq 0$). It is not negligible in large/medium vessels, having a small resistance and a high blood flow pulsatility [365]. For a generic large/medium vessel, it can be evaluated as a function of blood density (ρ), vessel length (l_v) and area (A): $L = \rho l_v/A$. Inertances of different vessels are combined together as resistances.

Lumped models have the advantage to describe the entire cardiovascular system at a low computational cost, although neglect important aspects of cardiovascular mechanics, such as the propagation and reflection of pressure and flow waves. On the other hand, overdetailed models - which promise a more precise description of human circulation or a part of it - are often expensive in terms of parameter setting and computational efforts and may generate unnecessary data with respect to the prefixed goal [154]. Thus, despite its intrinsic limitations, a large number of 0D models have been formulated [302].

In general, 0D models can be divided into two groups: the mono compartment models and the multiple compartment ones [302]. In the mono compartment models, the cardiovascular apparatus or a part of it is considered as a unique block and different haemodynamic phenomena are lost in the modelling process. The multiple compartment models, instead, treat the global circulation as a combination of well-defined cardiovascular regions, each of which is properly modelled based on its fundamental characteristics.

Examples of mono compartment models are given in Figure 2.1, which depicts the two- and three-elements Windkessel models [363, 364]. The three elements Windkessel model approximates the systemic arterial behaviour through two resistances and one compliance. The entering resistance, Z_c, stands for the characteristic impedance of the arterial network, the second resistance, R_p, is such that the sum $Z_c + R_p$ corresponds to the total systemic arterial resistance, and the compliance, C, represents the total systemic arterial compliance. Notice that this model is similar to the two-elements Windkessel model, apart from the decomposition of the total systemic arterial resistance into two terms (in the two-elements Windkessel model R_p is the total systemic arterial resistance). In actual fact, this decomposition offers a better estimation of the systemic arterial pressure in systole, with respect to the two-elements Windkessel model. This is not surprising, considering that the accuracy of 0D models in general improves with the number of circuital components.

Figure 2.2 gives an example of multiple compartment model. This model has been exploited to study the impact of AF on the cardiovascular system response by Scarsoglio and co-authors [292]. In their work, the main arterial blocks (systemic and pulmonary aortic sinus and arteries) are modelled through RLC electric

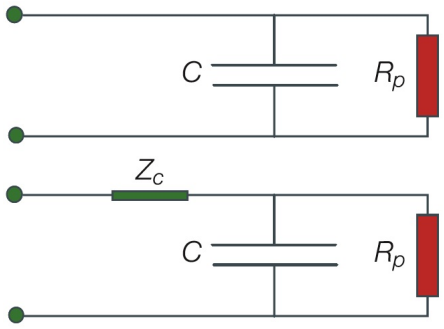

Figure 2.1: Examples of mono compartment models: the two- (top image) and three-elements (bottom image) Windkessel model. *Image extracted from* [365].

circuits, which consist in a parallel combination of a compliance and a sequence resistance-inertance. The venous blocks (systemic and pulmonary vein) are taken equal to the previous ones but lack of the inertance, the arteriolar and capillary groups (systemic and pulmonary arteriole/capillary) are represented as pure resistances, and the cardiac chambers and valves are reproduced through time-varying elastances and orifice models, respectively.

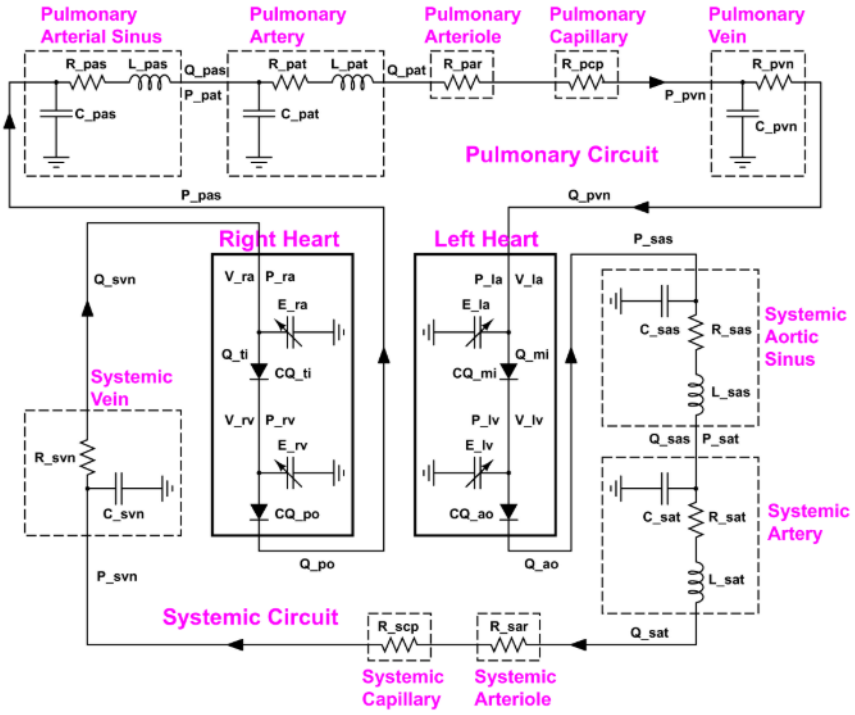

Figure 2.2: Example of multiple compartment model. *Image extracted from* [292].

Nowadays, 0D submodels of different kinds have been suggested to represent the contractility of heart chambers [325, 362], the functioning of cardiac valves [120, 156, 155, 228], the arterial, venous and pulmonary circulations [110, 348, 120], the venous valves [228, 313, 120], the distal coronary districts [226, 227], the auto- and neuro-regulation systems [256, 347, 164], and other cardiovascular features [302]. Thus, distinct 0D submodels can be put together in multiple compartment models, leading to a reasonable description of the cardiovascular apparatus. However, despite the wide availability of more or less sophisticated cardiovascular models in literature, the choice of the most appropriate solution depends on the specific physiological/pathological condition to explore [41].

2.2.2 One dimensional models

One dimensional (1D) models are typically adopted to study the haemodynamics of the systemic arterial tree and, differently to 0D models, enable to inquire into the propagation and reflection phenomena of pressure and flow rate waveforms. Nonetheless, 1D models have more recently applied to the systemic venous circuit too [222, 227, 378], despite the scarce measurements of venous diameters, their huge compliance (with respect to systemic arteries), and capability to collapse under certain transmural pressures.

1D models derive from a simplified version of the Navier-Stokes equations, resulting in a system of partial differential equations, generally coupled to some constitutive algebraic equations. These models are solved numerically in both space and time with a reasonable computational demand, although they cannot provide a complete representation of the blood flow field, which is instead produced by higher dimensional models [381].

The resolution of a generic 1D model of the arterial/venous tree usually requires the application of three types of boundary conditions: at the inlet and outlet of the tree and at each arterial/venous junction. The inlet consists in the aorta, for the arterial tree, and the two venae cavae, for the venous tree, while there are as many outlets as terminal arteries/veins. The quantities to impose at each boundary are the dependent variables in the 1D formulation (e.g., pressure and flow rate, or pressure and axial velocity, or area and flow rate, etc.). The boundary conditions at arterial/venous bifurcations usually consist in the conservation of mass and total pressure. The boundary condition at the inlet can be represented by periodic signals of the dependent variables (especially for the systemic arterial tree) or can be derived by a 0D model of the heart or a portion of it. The boundary condition at each terminal artery/vein is typically given by a more or less complex 0D model (e.g., a resistance, a two-elements Windkessel model, a sequence of RLC electric circuits, etc.). For the sake of clarity, a 1D model coupled with models of other dimensions (also 0D models) gives rise to a multiscale model, which is presented in section 2.2.4.

A large number of 1D models of the systemic arterial tree have been proposed and tested to various objectives. As already observed by other authors [279, 321], differences among these models mainly consist in the choice of domain, wall mechanical properties, velocity profile, boundary conditions and numerical methods. A schematic summary of the features of some 1D models of the systemic arterial tree is offered in Table 2.1. Based on the latter, one can guess that the accuracy of the 1D models of the systemic arterial tree has progressively improved over the years. More recent models, in fact, not only incorporate more cardiovascular elements, such as the cerebral and coronary circulations, but also refine the proximal and distal boundary conditions and the modelling of the wall mechanical properties. To this purpose, it has been documented that taking into account the viscoelastic behaviour of arterial walls and closing terminal arteries with at least a two-elements Windkessel model (rather than a simple resistance) can greatly ameliorate the peripheral pulse waveforms, damping local oscillations [205]. In addition, the accuracy in the calculation of the convective term and shear stress strongly depends on the choice of the velocity profile [356], although a number of well known 1D models have used a flat velocity profile. Notice that adopting a flat velocity profile not always implies neglecting the friction term. In fact, authors like Mynard et al. [227] employed a flat velocity profile and a velocity profile with boundary layer for the calculation of the convective and viscous friction terms, respectively.

2.2.3 Two and three dimensional models

Two (2D) and three (3D) dimensional models, both obtained from the Navier-Stokes equations, offer a more precise calculation of the pressure and flow fields with respect to the previous modelling solutions. However, these models (especially the 3D ones) require a high computational effort. For this reason, they are usually employed to accurately study the fluid dynamics of small cardiovascular regions [204, 218], such as cardiac valves, coronary arteries and ventricles [317, 380], or confined vascular areas in pathological situations, for example in presence of atheromatous plaques [38, 136] or aneurysms [16, 299].

Nowadays, 3D models are selected to perform patient-specific simulations in clinical trials, with a large number of advantages from a preventive, diagnostic and operative point of view [188, 329]. In fact, new advances in imaging techniques allow one to recreate 3D images of heart, single cardiac elements and vessels at a patient-specific level, which are used to reconstruct comprehensive model domains and accurately simulate the functioning of complex cardiovascular zones. In particular, about the heart, it has been proved of dramatic importance the modelling of its electrical function, which is strongly coupled to the mechanical one and is essential to investigate phenomena like ventricular arrythmogenesis [345]. Thus, in the last few years there has been a growing interest in integrating the electromechanical function of the heart to the haemodynamics of cardiac chambers [272, 354].

Table 2.1: Summary of the features among some 1D models of the systemic arterial tree [279]. (A) Author and year of publication, (R) corresponding reference, (HM) heart model or a portion of it as inlet boundary condition, (CeC) 1D cerebral arteries, (CoC) 1D coronary arteries, (Visc) viscoelasticity of the arterial walls. "y" means modelled, "n" means not modelled. (VeP) velocity profile for the convective term - flat: "f", Poiseuille: "p", Witzig-Womersley theory: "w", approximated: "a" -, (DB) distal boundary conditions - resistance: "r", Windkessel model: "wk", method of structured tree: "m", microcirculation districts and venous return: "c".

A (year)	**R**	**HM**	**CeC**	**CoC**	**Visc**	**VeP**	**DB**
Avolio (1980)	[20]	n	y	n	y	p	r
Stergiopulos et al. (1992)	[321]	n	n	n	n	f	wk
Olufsen et al. (2000)	[254]	n	n	n	n	a	m
Sherwin et al. (2003)	[301]	n	n	n	n	f	r
Formaggia et al. (2006)	[82]	y	n	n	n	f	wk
Matthys et al. (2007)	[205]	n	n	n	n	f	r
Liang et al. (2009)	[180]	y	n	n	n	f	c
Reymond et al. (2009)	[279]	y	y	y	y	w	wk
Blanco et al. (2013)	[30]	y	y	n	y	p	c
Müller et al. (2014)	[222]	y	y	n	n	f	c
Guala et al. (2015)	[108]	y	n	y	y	a	wk
Mynard et al. (2015)	[227]	y	y	y	y	f	c

2D and 3D models can also be used in conjunction with fluid-structure interaction and fluid-solid-growth models. The first approach is useful to take into account the reciprocal interaction between the blood and the solid elements in contact with it (vessel walls, cardiac valves, etc.) [49]. The second approach is helpful to model the progressive changes in the geometrical and mechanical properties of a cardiovascular region during an evolutionary process (e.g., when simulating the enlargement

of an aneurysm [317]). These processes are proper of the living matter, whose shape and properties continuously adapt to the applied chemical and mechanical stimuli, in turn variable with age, diseases, injuries, surgical interventions, etc. [9].

2D and 3D models can be simulated alone with measured haemodynamic signals (got through MRI or catheterisation) as boundary conditions. However, this solution is often impracticable, due to the difficulty in recording different simultaneous haemodynamic signals at both the inlet and outlet of high dimensional models. For this reason, 2D and 3D models are frequently coupled to 0D and 1D models (giving rise again to multiscale models - see section 2.2.4) to just provide the boundary conditions. The key problem with this solution is the setting of low dimensional model parameters, which have to be adapted to the specific patient to simulate through a scaling procedure.

2.2.4 Multiscale models

As stated by Formaggia et al. [81], the cardiovascular system and its constitutive elements have an inherent multiscale nature in both time and space. E.g., plaque formation depends on the stress applied by the blood to the vessel wall at each cardiac cycle, lasting less than 1s. However, the visible growing of the plaque is not appreciated in seconds but in months or years. Furthermore, dysfunctions at cellular level (like in the transmission of the action potentials among cardiomyocytes) or within small cardiovascular regions (like the regurgitation of a cardiac valve) can cause macroscopic modifications in the whole cardiovascular behaviour [81]. Taking into account these considerations, it is reasonable that some cardiovascular models combine models of different dimensions (0D-3D), making up multiscale mathematical models. In such frameworks, each single model is suitable to describe a particular cardiovascular area, based on the characteristics of the zone to study, the scope of the work and the expected computational effort. To this purpose, it is important to notice that, in cardiovascular modelling, there is not the right model and the wrong one, but all depends on what one aims at. For instance, one has to treat the blood as non-Newtonian when working at capillary level, but can rightly consider the blood as Newtonian in large-to-medium arteries, thus avoiding to detail the haemodynamics of capillaries, if an attentive investigation of molecular phenomena in them is not required.

An example of multiscale cardiovascular model is represented in Figure 2.3. This model was presented by Blanco et al. [30] and includes three modelling components: a 1D model to reproduce the systemic arterial tree, a 0D model for the microcirculation, venous return, cardiac and pulmonary circulations, and a 3D model (embedded in the 1D model) to take into account the role played by a patient-specific cerebral aneurysm. Through this global model, the authors managed to recreate the typical physiological cardiovascular behaviour, show the effects of mild and severe aortic valve regurgitation (by acting on the parameters of the 0D valvular model),

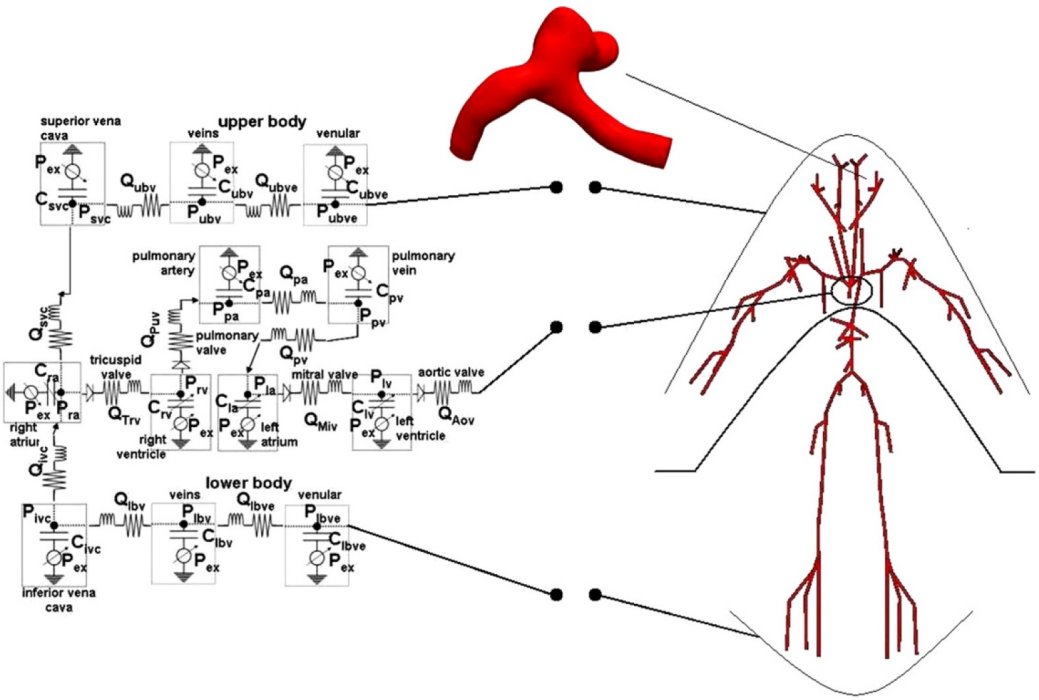

Figure 2.3: Example of multiscale cardiovascular model. *Image extracted from* [30].

and detail the pressure and flow rate time signals where the aneurysm is located. Notice that this model is closed-loop, which means that the input of each single model integrated in it depends on the output. This condition is not always the case: there are plenty of open models in literature, where inlet and outlet depend on periodic haemodynamic signals externally imposed or 0D submodels generating periodic boundary conditions.

To create a multiscale mathematical model of human circulation is sufficient to combine at least two models of different dimensions, already introduced in the previous section. However, the most difficult aspect to joint models of different dimensions is assuring they are stably coupled. To achieve this purpose, each research group chooses the most appropriate solution, depending on the numerical technique used to solve each submodel in the multiscale formulation. An overview of all the numerical solutions available in literature is out of the scope of this Thesis, but the full description of the method solving the multiscale model developed in this work will be provided in chapter 3.

Chapter 3

Closed-loop multiscale mathematical model of the cardiovascular system

Some of the contents of this chapter have been previously published in [91, 92, 291, 293].

We here present the closed-loop multiscale (0D-1D) mathematical model of the cardiovascular system developed in this work. It couples a 1D representation of the systemic arterial tree and a 0D description of the following microcirculation and venous return, together with the heart and pulmonary circulation. This model also features a multiscale (0-1D) reproduction of the coronary circulation, and a short-term baroreflex mechanism adjusting the haemodynamic response to the mean arterial pressure variations. A sketch of the entire modelling is provided in Figure 3.18, after having detailed each submodel in the following sections: the 1D model of the systemic arterial tree in section 3.1, the 0D model of the systemic microcirculation and venous return, with the heart and pulmonary circulation, in section 3.2, the multiscale model of the coronary circulation in section 3.4, the baroreflex model in section 3.5, and the mathematical approach implemented to couple 0D and 1D models in section 3.3.

3.1 1D model of the systemic arterial tree

The 1D model of the systemic arterial tree used in this work was first proposed by Guala et al. [106, 108]. It incorporates 48 large-to-medium arteries and 24 arterial bifurcations. Both left and right arm arteries are modelled because of their asymmetric distribution, while only the left leg arteries are taken into account, exploiting the symmetrical vasculature of the lower limbs. The model domain is

shown in Figure 3.1, the names of the included arteries are given in Table 3.1, and their geometrical and mechanical properties are reported in Appendix A.1.

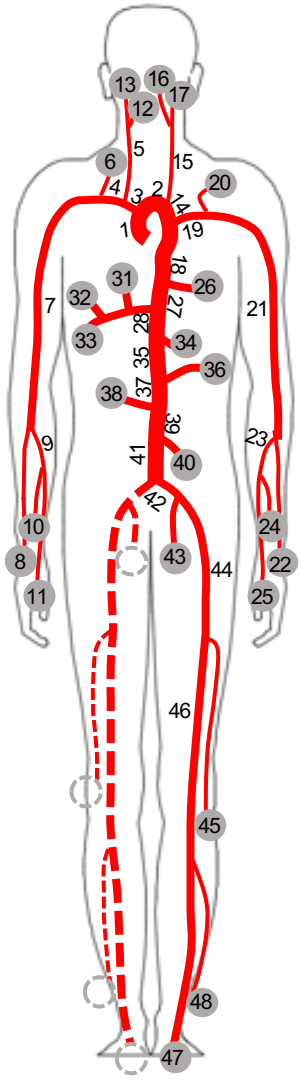

Figure 3.1: Representation of the modelled systemic arterial tree. Numbers corresponding to distal arteries are indicated in grey circles.

Table 3.1: Names of the arteries numbered in Figure 3.1.

N right/left	**Arterial tract**
1	Ascending Aorta
2	Aortic Arch A
3	Brachiocephalic
4/19	Subclavian A
5/15	Common Carotid
6/20	Vertebral
7/21	Subclavian B, Axillary, Brachial
8/22	Radial
9/23	Ulnar A
10/24	Interosseous
11/25	Ulnar B
12/16	Internal Carotid
13/17	External Carotid
14	Aortic Arch B
18	Thoracic Aorta A
26	Intercostals
27	Thoracic aorta B
28	Abdominal aorta A
29	Coeliac A
30	Coeliac B
31	Hepatic
32	Gastric
33	Splenic
34	Superior Mesenteric
35	Abdominal Aorta B
36/38	Renal
37	Abdominal Aorta C
39	Abdominal Aorta D
40	Inferior Mesenteric
41	Abdominal Aorta E
42	Common Iliac
43	Inner Iliac
44	External Iliac
45	Deep Femoral
46	Femoral
47	Anterior Tibial
48	Posterior Tibial

3.1.1 Hypotheses and mathematical formulation

The present 1D model of the systemic arterial tree solves the blood flow field within large and medium arteries under a number of hypotheses [80, 82]: (i) vascular geometry and flow field are axisymmetric, (ii) vessel lengths are time-invariant, (iii) wall motions are radial only (areas modify with time, remaining circular and perpendicular to the vessel axis), (iv) walls are impermeable, (v) viscous effects are significant just close to the walls, (vi) pressure is constant over each section, (vii) blood is incompressible and Newtonian (density, ρ=1050 kg/m^3, dynamic viscosity, μ=0.04 Pas, and kinematic viscosity, $\mu/\rho = \nu$=3.8 mm^2/s, are taken constant [237]), (viii) and flow is laminar [161, 261].

Since the resolution of this problem is based on the conservation of mass and momentum laws, the mathematical formulation derives from the Navier-Stokes equations written for an incompressible and Newtonian fluid:

$$\begin{cases} \nabla \cdot \mathbf{u} = 0, \\ \rho \dfrac{\partial \mathbf{u}}{\partial t} + \rho \mathbf{u} \cdot \nabla \mathbf{u} = -\nabla p + \mu \nabla^2 \mathbf{u} + \rho \mathbf{g}, \end{cases} \tag{3.1}$$

with t the time, $\mathbf{u}$ the velocity vector, p the pressure, and $\mathbf{g}$ the gravity vector.

Considering the generic artery as a cylinder, system (3.1) can be rewritten on a cylindrical coordinate system (r, ϕ, z), with r the radial coordinate, ϕ the azimuthal coordinate, and z the axial coordinate. Namely,

$$\begin{cases} \dfrac{1}{r}\dfrac{\partial (r u_r)}{\partial r} + \dfrac{1}{r}\dfrac{\partial u_\phi}{\partial \phi} + \dfrac{\partial u_z}{\partial z} = 0, \\ \rho \left(\dfrac{\partial u_r}{\partial t} + u_r \dfrac{\partial u_r}{\partial r} + \dfrac{u_\phi}{r}\dfrac{\partial u_r}{\partial \phi} - \dfrac{u_\phi^2}{r} + u_z \dfrac{\partial u_r}{\partial z} \right) = \\ = -\dfrac{\partial p}{\partial r} + \mu \left[\dfrac{1}{r}\dfrac{\partial}{\partial r}\left(r \dfrac{\partial u_r}{\partial r} \right) - \dfrac{u_r}{r^2} + \dfrac{1}{r^2}\dfrac{\partial^2 u_r}{\partial \phi^2} - \dfrac{2}{r^2}\dfrac{\partial u_\phi}{\partial \phi} + \dfrac{\partial^2 u_r}{\partial z^2} \right] + \rho g_r, \\ \rho \left(\dfrac{\partial u_\phi}{\partial t} + u_r \dfrac{\partial u_\phi}{\partial r} + \dfrac{u_\phi}{r}\dfrac{\partial u_\phi}{\partial \phi} + \dfrac{u_r u_\phi}{r} + u_z \dfrac{\partial u_\phi}{\partial z} \right) = \\ = -\dfrac{1}{r}\dfrac{\partial p}{\partial \phi} + \mu \left[\dfrac{1}{r}\dfrac{\partial}{\partial r}\left(r \dfrac{\partial u_\phi}{\partial r} \right) - \dfrac{u_\phi}{r^2} + \dfrac{1}{r^2}\dfrac{\partial^2 u_\phi}{\partial \phi^2} + \dfrac{2}{r^2}\dfrac{\partial u_r}{\partial \phi} + \dfrac{\partial^2 u_\phi}{\partial z^2} \right] + \rho g_\phi, \\ \rho \left(\dfrac{\partial u_z}{\partial t} + u_r \dfrac{\partial u_z}{\partial r} + \dfrac{u_\phi}{r}\dfrac{\partial u_z}{\partial \phi} + u_z \dfrac{\partial u_z}{\partial z} \right) = \\ = -\dfrac{\partial p}{\partial z} + \mu \left[\dfrac{1}{r}\dfrac{\partial}{\partial r}\left(r \dfrac{\partial u_z}{\partial r} \right) + \dfrac{1}{r^2}\dfrac{\partial^2 u_z}{\partial \phi^2} + \dfrac{\partial^2 u_z}{\partial z^2} \right] + \rho g_z, \end{cases} \tag{3.2}$$

where $(u_r,\ u_\phi,\ u_z)$ and $(g_r,\ g_\phi,\ g_z)$ are the components of $\mathbf{u}$ and $\mathbf{g}$ along the r, ϕ and z directions, respectively.

However, we are interested in a 1D formulation, thus take as main direction of the blood flow field z, simplifying system (3.2) as

$$\begin{cases} \dfrac{\partial u_z}{\partial z} = 0, \\ \rho\left(\dfrac{\partial u_z}{\partial t} + u_z\dfrac{\partial u_z}{\partial z}\right) = -\dfrac{\partial p}{\partial z} + \mu\left[\dfrac{1}{r}\dfrac{\partial}{\partial r}\left(r\dfrac{\partial u_z}{\partial r}\right)\right] + \rho g_z. \end{cases} \tag{3.3}$$

Integrating system (3.3) over the cross-sectional area, $A = \pi r^2$, one obtains the integral form of the mass balance equation [271]

$$\frac{\partial A}{\partial t} + \frac{\partial Q}{\partial z} = 0, \tag{3.4}$$

and the momentum balance equation

$$\frac{\partial Q}{\partial t} + \frac{\partial}{\partial z}\left(\int_0^{r_v} 2\pi r u_z^2 \mathrm{d}r\right) = -\frac{A}{\rho}\frac{\partial p}{\partial z} + 2\pi\nu\left[r\frac{\partial u_z}{\partial r}\right]_{r=r_v} + A|\mathbf{g}|\sin\gamma. \tag{3.5}$$

In equations (3.4) and (3.5), $Q = \int_A u_z \mathrm{d}A$ is the flow rate, r_v is the vessel radius, $|\mathbf{g}|$ is the modulus of the gravity vector (positive in the head-foot direction), and γ is the sine of the angle between the axial and horizontal directions [108]. The term $\partial A/\partial t$ in the mass balance equation is due to the wall radial motions and would disappear if blood flow developed within perfectly rigid tubes [271].

3.1.2 Velocity profile

In order to define the convective and viscous terms of equation (3.5), a velocity profile $u_z(t, r, z)$ must be assumed. The shape of the velocity profile changes in time, being the motion pulsatile, and with the distance from the heart [46]. In particular, it appears quite flat close to the heart and progressively rounded towards the periphery. In fact, arterial diameters reduce with the distance from the heart, making viscous forces increasingly important at distal sites with respect to central ones.

Flat [80, 82, 180, 181, 205, 226, 227, 301, 321], parabolic [20, 31, 30], and approximated [254, 279, 280] velocity profiles have been employed in literature. The one proposed by Guala et al. [108] is here used (see Figure 3.2). It combines an inviscid flat core with constant velocity $\overline{u}_z$ and a parabolic boundary layer of thickness δ as

$$u_z = \begin{cases} \overline{u}_z & \text{if } 0 \leq r < r_v - \delta, \\ \overline{u}_z \frac{r_v^2 - r^2}{2r_v\delta - \delta^2} & \text{if } r_v - \delta \leq r \leq r_v. \end{cases} \tag{3.6}$$

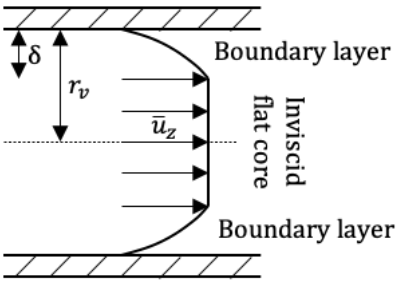

Figure 3.2: Representation of an instantaneous velocity profile, with r_v the local radius, δ the boundary layer thickness, and $\overline{u}_z$ the modulus of the uniform velocity along the axial direction within the flat core.

δ can be determined through the Womersley number, α_{WN}. It is a non-dimensional parameter, coming from the momentum balance equation of the Hagen-Poiseuille flow as a periodic pressure gradient is applied [372]. α_{WN} is typically used to characterize the unsteady nature of biological flows [190], identifying the weight of the inertial forces over the viscous ones within a period of oscillation. In this sense, it is considered as an unsteady Reynolds number [46]. Referring to arteries, α_{WN} is calculated as

$$\alpha_{WN} = r_v \sqrt{\frac{\omega}{\nu}}, \tag{3.7}$$

with ω equal to the cardiac pulsation. Notice that, in large arteries, α_{WN} is greater than 10, flow is mainly dominated by inertial forces, and the boundary layer is extremely thin with respect to the vessel radius. At microcirculation districts, instead, α_{WN} is smaller than 1, viscous effects are not negligible, and the boundary layer thickness is comparable to the vessel radius [46]. In order to calculate the boundary layer thickness is sufficient to set α_{WN}=1. In fact, the boundary layer ends at a distance from the wall such that inertial and viscous forces balance. In doing so, one finds

$$\delta = \sqrt{\frac{\nu}{\omega}} \sim 1\text{mm}. \tag{3.8}$$

However, since at distal sites r_v is comparable to δ, we define δ as

$$\delta = \min\left\{r_v, \sqrt{\frac{\nu}{\omega}}\right\}. \tag{3.9}$$

By using the definition of flow rate, $\overline{u}_z$ (in equation (3.6)) can be expressed as a function of Q, r_v and δ only. Practically,

$$\begin{aligned} Q &= \int_A u_z \mathrm{d}A, \\ &= \int_0^{r_v} 2\pi r u_z \mathrm{d}r, \\ &= 2\pi\overline{u}_z \left(\int_0^{r_v-\delta} r dr + \int_{r_v-\delta}^{r_v} \frac{r_v^2 - r^2}{2r_v\delta - \delta^2} r \mathrm{d}r \right). \end{aligned} \tag{3.10}$$

Developing integrals at second member and inverting the resultant expression, one gets

$$\overline{u}_z = \frac{2Q}{\pi\left[\delta^2 + 2r_v(r_v - \delta)\right]}. \tag{3.11}$$

Therefore, based on equations (3.8) and (3.11), δ only varies with time through ω (apart in those vessels where $r_v < \delta$, for which we impose $\delta = r_v$), while $\overline{u}_z$ is time- and space-dependent, being Q and A (and thus r_v) both time- and space-dependent.

Knowing the explicit value of $\overline{u}_z$, the calculation of the convective and viscous terms in equation (3.5) is easily obtainable [108]. The convective term is

$$\begin{aligned} \int_0^{r_v} 2\pi r u_z^2 \mathrm{d}r &= 2\pi\overline{u}_z^2 \left[\int_0^{r_v-\delta} r \mathrm{d}r + \int_{r_v-\delta}^{r_v} r \frac{r_v^4 - 2r_v^2 r^2 + r^4}{4r_v^2\delta^2 - 4r_v\delta^3 + \delta^4} \mathrm{d}r \right], \\ &= \frac{4}{3} \frac{\left(2\pi A\delta^2 + 3A^2 - 4\sqrt{\pi}A^{3/2}\delta\right)}{\left(\pi\delta^2 + 2A - 2\sqrt{\pi}\sqrt{A}\delta\right)^2} \frac{Q^2}{A}, \\ &= \beta \frac{Q^2}{A}, \end{aligned} \tag{3.12}$$

with β the Coriolis coefficient. The viscous term is

$$2\pi\nu\left[r\frac{\partial u_z}{\partial r}\right]_{r=r_v} = \frac{8\nu\sqrt{\pi}A^2}{\delta\left(-4A^{3/2}+6A\delta\sqrt{\pi}-4\sqrt{A}\pi\delta^2+\pi^{3/2}\delta^3\right)}\frac{Q}{A}, \equiv N_4\frac{Q}{A}, \tag{3.13}$$

where $\frac{\partial u_z}{\partial r}$ is

$$\frac{\partial u_z}{\partial r} = \begin{cases} 0 & \text{if } 0 \le r < r_v - \delta, \\ -\frac{2r}{2r_v\delta-\delta^2}\frac{2Q}{\pi(\delta^2+2r_v(r_v-\delta))} & \text{if } r_v-\delta \le r \le r_v. \end{cases} \tag{3.14}$$

Thus, the resulting balance equations are

$$\begin{cases} \dfrac{\partial A}{\partial t}+\dfrac{\partial Q}{\partial z}=0, \\ \dfrac{\partial Q}{\partial t}+\dfrac{\partial}{\partial z}\left(\beta\dfrac{Q^2}{A}\right) = -\dfrac{A}{\rho}\dfrac{\partial p}{\partial z}+N_4\dfrac{Q}{A}+A|\mathbf{g}|sin\gamma, \end{cases} \tag{3.15}$$

with t and z independent variables, A, Q and p dependent variables, and β, ρ, N_4, $|\mathbf{g}|$ and γ parameters. Notice that ρ is constant under the hypothesis of incompressible fluid, $|\mathbf{g}|$ is constant if one stays on the ground, γ is constant in a static posture, and $\beta(A,\delta)$ and $N_4(A,\delta)$ are time- and space-dependent for definition. However, in this work, both β and N_4 are taken constant with time. At each site, they are evaluated at a reference pressure, $p_0 = 100$ mmHg (for which A values (A_0) are the ones in Table A.1), and at a reference $\delta = \min\{r_v, 1\text{mm}\}$ [183].

3.1.3 Constitutive equation for pressure

System (3.15) is made of two equations and contains three dependent variables (A, Q and p), thus another equation has to be defined. Choosing as dependant variables A and Q, a constitutive relationship for p is introduced. p is written as a function of A through a relation which takes into account the anisotropic non-linear viscoelastic behaviour of arterial walls [108]. We set

$$p = p_e + p_{visc}, \tag{3.16}$$

where p_e is the elastic pressure component and p_{visc} the viscoelastic one.

p_e is calculated according to the theory reported by Reymond et al. [279], who evaluated the elastic component of the arterial compliance, C_A^e, as

$$C_A^e = \frac{\partial A}{\partial p_e} = C_g^e C_p^e, \tag{3.17}$$

where C_g^e is a geometric-dependent function and C_p^e is a pressure-dependent function. C_g^e provides the local compliance for a time-averaged area, $\bar{A} = \pi \bar{D}/4$, and at the reference pressure, p_0 (=100 mmHg), like

$$C_g^e = \frac{\bar{A}}{\rho PWV^2(\bar{D}, p_0)}, \tag{3.18}$$

where PWV is the pulse wave velocity. Taking as time-averaged area and diameter the ones at p_0 ($\bar{A} = A_0$ and $\bar{D} = D_0$, respectively), one gets

$$C_g^e = \frac{A_0}{\rho PWV(D_0, p_0)^2} = \frac{A_0}{\rho PWV_0^2}. \tag{3.19}$$

In equation (3.19), PWV_0 is calculated according to Reymond et al. [279], that is

$$PWV_0 = \frac{a_2}{D_0^{b_2}}, \tag{3.20}$$

with $a_2 = 13.3$ m$^{1.3}$/s and $b_2 = 0.3$. Regarding the pressure-dependent function, C_p^e, it is also expressed as in Reymond et al. [279]:

$$C_p^e = a_1 + \frac{b_1}{1 + \left(\frac{p_e - p_{maxC}}{p_w w}\right)^2}, \tag{3.21}$$

where the fitting parameters ($a_1 = 0.4$, $b_1 = 5$, $p_{maxC} = 20$ mmHg and $p_w w = 30$ mmHg) are proved to hold throughout the entire systemic arterial tree [279].

The generic arterial area can be written as

$$A = A_0 + A_p, \tag{3.22}$$

where A_0 is the area at the reference pressure and A_p is the pressure-dependent area

$$A_p = \int \frac{\partial A}{\partial p_e} \mathrm{d}p_e = \int C_A^e dp_e. \tag{3.23}$$

Exploiting equation (3.17) and recalling that C_g^e does not depend on p_e, one can write

$$\begin{aligned} A &= A_0 + C_g^e \int C_p^e \mathrm{d}p_e, \\ &= A_0 + \frac{A_0}{\rho PWV_0^2} \int C_p^e \mathrm{d}p_e. \end{aligned} \tag{3.24}$$

$\int C_p^e \mathrm{d}p_e$ is numerically integrated and fitted with the invertible function

$$\int C_p^e \mathrm{d}p_e \simeq a_3 p_e^{1/3} + a_5, \tag{3.25}$$

where $a_3 = 1914\ \mathrm{N}^{2/3}/\mathrm{m}^{4/3}$ and $a_5 = -45.35\ \mathrm{N/m}^2$ [108]. Substituting the (3.25) into the (3.24) and solving with respect to p_e, one finds

$$p_e = \left(\frac{A - A_0}{A_0} \frac{\rho PWV_0^2}{a_3} - \frac{a_5}{a_3} \right)^3, \tag{3.26}$$

that is the space-dependent (A_0 and PWV_0 vary site by site) relationship relating the elastic pressure component p_e to the corresponding vessel area A. Expanding equation (3.26) in a polynomial function of the area, one obtains the simple algebraic equation

$$p_e = B_1 + B_2 A + B 3_A^2 + B_4 A^3, \tag{3.27}$$

where the space-dependent coefficients B_i (i=1÷4) [108] contain the information related to the local mechanical properties of the arterial wall and can be calculated as follows

$$B_1 = -\frac{1}{a_3^3} \left(a_5^3 + PWV_0^6 \rho^3 + 3PWV_0^4 \rho^2 a_5 + 3a_5^2 PWV_0^2 \rho \right), \quad \left[\frac{\mathrm{N}}{\mathrm{m}^2} \right], \tag{3.28}$$

$$B_2 = \frac{3\rho PWV_0^2}{A_0 a_3^3} \left(\rho^2 PWV_0^4 + 2\rho a_5 PWV_0^2 + a_5^2 \right), \quad \left[\frac{\mathrm{N}}{\mathrm{m}^4} \right], \tag{3.29}$$

$$B_3 = -\frac{3\rho^2 PWV_0^4}{A_0^2 a_3^3} \left(a_5 + \rho PWV_0^2 \right), \quad \left[\frac{\mathrm{N}}{\mathrm{m}^6} \right], \tag{3.30}$$

$$B_4 = \left(\frac{\rho PWV_0^2}{a_3 A_0} \right)^3, \quad \left[\frac{\mathrm{N}}{\mathrm{m}^8} \right]. \tag{3.31}$$

The viscoelastic component, p_{visc}, of p is determined as suggested by Kivity et al. [147]

$$p_{visc} = \frac{K_{visc} h_{w_0}}{2\sqrt{A_0}\sqrt{A} r_{v_0}} \frac{\partial A}{\partial t}, \tag{3.32}$$

with K_{visc} the effective viscosity of the wall, and h_{w_0} and r_{v_0} the arterial wall thickness and the vessel radius at the reference pressure, p_0 (=100 mmHg), respectively. By exploiting equation (3.4), equation (3.32) can be written as

$$p_{visc} = -B_5 \frac{1}{\sqrt{A}} \frac{\partial Q}{\partial z}, \tag{3.33}$$

where B_5, equal to $(K_{visc} h_{w_0}) \,/\, \left(2\sqrt{A_0} r_{v_0}\right)$, is space-dependent ($A_0$ varies site by site) [108].

Thus, combining equations (3.16), (3.27) and (3.33), the constitutive equation for pressure becomes

$$\begin{aligned} p &= p_e + p_{visc}, \\ &= B_1 + B_2 A + B_3 A^2 + B_4 A^3 - B_5 \frac{1}{\sqrt{A}} \frac{\partial Q}{\partial z}, \end{aligned} \tag{3.34}$$

and the closed form of the momentum balance equation can be written as

$$\begin{aligned} &\frac{\partial Q}{\partial t} + \frac{\partial}{\partial z}\left(\beta \frac{Q^2}{A}\right) = \\ &= -\frac{A}{\rho}\frac{\partial}{\partial z}\left(B_1 + B_2 A + B_3 A^2 + B_4 A^3 - B_5 \frac{1}{\sqrt{A}} \frac{\partial Q}{\partial z}\right) + N_4 \frac{Q}{A} + A|\mathbf{g}|\sin\gamma. \end{aligned} \tag{3.35}$$

Notice that coefficients B_j, for $j = 1 \div 5$, result to be time-independent being evaluated at p_0 (for which A values (A_0), K_{visc} and h_{w_0} are the ones in Table A.1).

3.1.4 Conservative form of mass and momentum balance equations

Choosing A and Q as conservative variables, the mass balance equation (3.4) is already written in conservative form. The momentum balance equation (3.35), instead, not. It can be reformulated in conservative form by further developing the pressure term in the (3.35) as

$$\begin{aligned}&\frac{A}{\rho}\frac{\partial}{\partial z}\left(B_1+B_2A+B_3A^2+B_4A^3-B_5\frac{1}{\sqrt{A}}\frac{\partial Q}{\partial z}\right)=\\&\frac{A}{\rho}\frac{\partial}{\partial z}\left(B_1+B_2A+B_3A^2+B_4A^3\right)+\frac{A}{\rho}\frac{\partial}{\partial z}\left(-\frac{B_5}{\sqrt{A}}\frac{\partial Q}{\partial z}\right).\end{aligned}\tag{3.36}$$

One can verify that

$$\frac{A}{\rho}\frac{\partial}{\partial z}\left(B_1+B_2A+B_3A^2+B_4A^3\right)=\frac{\partial}{\partial z}\left(\sum_{j=2}^{4}\frac{(j-1)A^jB_j}{j\rho}\right)+\sum_{j=1}^{4}\frac{A^j}{j\rho}\frac{\mathrm{d}B_j}{\mathrm{d}z},\tag{3.37}$$

and

$$\frac{A}{\rho}\frac{\partial}{\partial z}\left(-\frac{B_5}{\sqrt{A}}\frac{\partial Q}{\partial z}\right)=\frac{\partial}{\partial z}\left(-\frac{B_5}{\rho}\sqrt{A}\frac{\partial Q}{\partial z}\right)+\frac{B_5}{\rho\sqrt{A}}\frac{\partial Q}{\partial z}\frac{\partial A}{\partial z}.\tag{3.38}$$

Therefore, adjusting signs, the conservative form of equation (3.35) becomes

$$\begin{aligned}&\frac{\partial Q}{\partial t}+\frac{\partial}{\partial z}\left(\beta\frac{Q^2}{A}+\sum_{j=2}^{4}\frac{(j-1)A^jB_j}{j\rho}-\frac{B_5}{\rho}\sqrt{A}\frac{\partial Q}{\partial z}\right)+\\&\left(\sum_{j=1}^{4}\frac{A^j}{j\rho}\frac{\mathrm{d}B_j}{\mathrm{d}z}+\frac{B_5}{\rho\sqrt{A}}\frac{\partial Q}{\partial z}\frac{\partial A}{\partial z}-N_4\frac{Q}{A}-A|\mathbf{g}|\sin\gamma\right)=0.\end{aligned}\tag{3.39}$$

Adopting a vectorial notation, the conservative form of mass and momentum balance equations can be written as

$$\frac{\partial\mathbf{U}}{\partial t}+\frac{\partial\mathbf{F}}{\partial z}+\mathbf{S}=0,\tag{3.40}$$

where $\mathbf{U}=[A,Q]^T$, while the flux vector, $\mathbf{F}$, and the source vector, $\mathbf{S}$, are

$$\mathbf{F}=\begin{bmatrix}Q\\ \beta\frac{Q^2}{A}+\sum_{j=2}^{4}\frac{(j-1)A^jB_j}{j\rho}-\frac{B_5}{\rho}\sqrt{A}\frac{\partial Q}{\partial z}\end{bmatrix},\tag{3.41}$$

and

$$\mathbf{S} = \begin{bmatrix} 0 \\ \sum_{j=1}^{4} \frac{A^j}{j\rho} \frac{\mathrm{d}B_j}{\mathrm{d}z} + \frac{B_5}{\rho\sqrt{A}} \frac{\partial Q}{\partial z} \frac{\partial A}{\partial z} - N_4 \frac{Q}{A} - A|\mathbf{g}|\sin\gamma \end{bmatrix}, \tag{3.42}$$

respectively.

3.1.5 Model resolution I

Solving the conservative form of mass and momentum balance equations (system (3.40)) means determining the conservative variables (A, Q) both in space (along the vessel axis z) and time (t).

Spatial resolution

Concerning the spatial resolution, a Discontinuous-Galerkin method is implemented [108]. The whole 1D structure, consisting in a network of 1D vessels, is subdivided in N_e elemental non-overlapping regions $\Omega_e = [z_e^l, z_e^r]$, such that $z_{e-1}^r = z_e^l$ for $e = 1 \div N_e$ and $\cup_{e=1}^{N_e} \Omega_e = \Omega$. Then, system (3.40) is written in weak form, that is each term is multiplied by a set of arbitrary test functions in Ω, ψ, and is integrated over the entire domain. Namely

$$\left(\frac{\partial \mathbf{U}}{\partial t}, \psi\right)_{\Omega} + \left(\frac{\partial \mathbf{F}}{\partial z}, \psi\right)_{\Omega} + (\mathbf{S}, \psi)_{\Omega} = 0. \tag{3.43}$$

Since $\Omega = \sum_{e=1}^{N_e} \Omega_e$, one can write

$$\sum_{e=1}^{N_e} \left[\left(\frac{\partial \mathbf{U}}{\partial t}, \psi\right)_{\Omega_e} - \left(\mathbf{F}, \frac{\mathrm{d}\psi}{\mathrm{d}z}\right)_{\Omega_e} + [\mathbf{F}\psi]_{\delta\Omega_e} + (\mathbf{S}, \psi)_{\Omega_e} \right] = 0, \tag{3.44}$$

with the flux term integrated by part (see Appendix A.3). Being this problem solved in discrete form, both the solution $\mathbf{U}$ and the test functions ψ have to be discretised.

Concerning $\mathbf{U}$, we choose an approximate solution, $\mathbf{U_h}$, over the generic elemental region Ω_e. It is defined as

$$\mathbf{U_h}(\Omega_e(\xi), t) = \begin{bmatrix} \alpha_{1A} & \alpha_{2A} \\ \alpha_{1Q} & \alpha_{2Q} \end{bmatrix} \begin{bmatrix} \phi_1 \\ \phi_2 \end{bmatrix}, \tag{3.45}$$

where $\xi \in [-1,1]$ stands for the non-dimensional form of z_e in Ω_e, subscripts 1 and 2 refer to the left and right extremes (nodes) of the element, α_{1A}/α_{1Q} and α_{2A}/α_{2Q} are the time-dependent unknown weights at 1 and 2 for A/Q, and ϕ_1 and ϕ_2 are

the space-dependent trial functions over the element. The relation linking z_e and ξ within each interval Ω_e [108] is

$$z_e(\xi) = z_e^l \frac{1-\xi}{2} + z_e^r \frac{1+\xi}{2}, \tag{3.46}$$

and its inverse is

$$\xi(z_e) = \left(z_e - \frac{z_e^r + z_e^l}{2} \right) \frac{2}{l_e}, \tag{3.47}$$

with $l_e = z_e^r - z_e^l$ the length of the element Ω_e. Taking the trial functions ϕ_1 and ϕ_2 equal to the first degree Lagrangian functions ($\phi_1 = (1-\xi)/2$ and $\phi_2 = (1+\xi)/2$), equation (3.45) becomes

$$\mathbf{U_h}(\Omega_e(\xi), t) = \begin{bmatrix} \alpha_{1A} & \alpha_{2A} \\ \alpha_{1Q} & \alpha_{2Q} \end{bmatrix} \begin{bmatrix} \frac{1-\xi}{2} \\ \frac{1+\xi}{2} \end{bmatrix}. \tag{3.48}$$

It is important to observe that the approximate solution $\mathbf{U_h}$ over Ω_e is accurate at the first order, being constructed as a linear combination of the weights (α_{1A}/α_{1Q} and α_{2A}/α_{2Q}) on the nodes of the element. Moreover, solutions at the interface between two contiguous elements are typically different, in fact, the method is said *discontinuous*. However, these discontinuities are expected to reduce as spatial discretisation improves (the number of elements Ω_e over a given vessel length rises).

Concerning ψ, we choose the discrete test functions, ψ_h, in the same discrete space of $\mathbf{U_h}$ and equal to the trial functions (ϕ_1 and ϕ_2), as usual according to the Galerkin approach. Therefore, on Ω_e, $\psi_\mathbf{h} = \left[\frac{1-\xi}{2}, \frac{1+\xi}{2}\right]$. In light of all the above, it is clear that the approximate solution over each element is calculated *a-posteriori* from equation (3.48).

Substituting the discrete form of $\mathbf{U}$ and ψ into equation (3.44), one gets

$$\sum_{e=1}^{N_e} \left[\left(\frac{\partial \mathbf{U_h}}{\partial t}, \psi_\mathbf{h} \right)_{\Omega_e} - \left(\mathbf{F}(\mathbf{U_h}), \frac{\mathrm{d}\psi_\mathbf{h}}{\mathrm{d}z} \right)_{\Omega_e} + [\mathbf{F_{LF}}(\mathbf{U_h})\psi_\mathbf{h}]_{\delta\Omega_e} + (\mathbf{S}(\mathbf{U_h}), \psi_\mathbf{h})_{\Omega_e} \right] = 0. \tag{3.49}$$

where $\mathbf{F_{LF}}$ is the boundary flux. Notice that, in case of external boundary (inlet and outlet of a vessel), $\mathbf{F_{LF}}$ is calculated using the definition of $\mathbf{F}$ and the variables at the boundary. In case of boundary between two different elements, instead, $\mathbf{F_{LF}}$ is obtained from the Lax-Friedrichs method [108] as

$$\mathbf{F_{LF}}(\mathbf{U_h}) = \frac{1}{2}\left(\mathbf{F}(\mathbf{U_h^-}) + \mathbf{F}(\mathbf{U_h^+}) - \lambda_{max}(\mathbf{U_h^+} - \mathbf{U_h^-})\right), \tag{3.50}$$

where $\mathbf{U_h^-}$ and $\mathbf{U_h^+}$ are the variables on the left and right side of the boundary, respectively, and λ_{max} is the maximum eigenvalue of the matrix $\bar{\mathbf{H}} = \frac{\partial \mathbf{F}}{\partial \mathbf{U}}$ (equation (3.70)), which appears in the quasi-linear form of the system of mass and momentum balance equations (equation (3.69)).

To practically understand how to obtain the weights of the generic element Ω_e, one can suppose that the entire domain consists in a single element Ω_e, like that shown in Fig. 3.3.

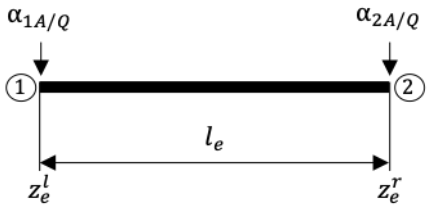

Figure 3.3: Representation of a single element Ω_e. It has length $l_e = z_e^r - z_e^l$ and weights $\alpha_{1A/Q}$ and $\alpha_{2A/Q}$ at nodes 1 and 2, respectively, for both A and Q.

In this case, equation (3.49) becomes

$$\int_{z_e^l}^{z_e^r} \frac{\partial \mathbf{U_h}}{\partial t}\psi_\mathbf{h} \mathrm{d}z_e - \int_{z_e^l}^{z_e^r} \mathbf{F}(\mathbf{U_h})\frac{\mathrm{d}\psi_\mathbf{h}}{\mathrm{d}z}\mathrm{d}z_e + \int_{z_e^l}^{z_e^r} \mathbf{S}(\mathbf{U_h})\psi_\mathbf{h}\mathrm{d}z_e + \mathbf{F_{LF}}(\mathbf{U_h})\psi_\mathbf{h}|_{z_e^l}^{z_e^r} = 0. \tag{3.51}$$

Since both $\mathbf{U_h}$ and $\psi_\mathbf{h}$ depend on the non-dimensional spatial variable ξ, it should be better to change the integration variable from z_e to ξ. This change is easily feasible, reminding that $\mathrm{d}z_e = l_e/2\mathrm{d}\xi$ (see equation (3.47)). Thus, when $z_e = z_e^l$ then $\xi = -1$, when $z_e = z_e^r$ then $\xi = 1$. Based on these expressions, equation (3.51) can be written as

$$\frac{l_e}{2}\left[\int_{-1}^{1}\left(\frac{\partial \mathbf{U_h}}{\partial t}\psi_\mathbf{h} - \mathbf{F}(\mathbf{U_h})\frac{2}{l_e}\frac{\mathrm{d}\psi_\mathbf{h}}{\mathrm{d}\xi} + \mathbf{S}(\mathbf{U_h})\psi_\mathbf{h}\right)d\xi\right] + \mathbf{F_{LF}}(\mathbf{U_h})\psi_\mathbf{h}|_{-1}^{1} = 0. \tag{3.52}$$

Using the definitions of $\psi_\mathbf{h}$, one can calculate the four terms of the (3.52) as follows

$$\begin{aligned}\frac{\partial \mathbf{U_h}}{\partial t}\psi_{\mathbf{h}} &= \frac{\partial}{\partial t}\begin{bmatrix}\alpha_{1A} & \alpha_{2A}\\ \alpha_{1Q} & \alpha_{2Q}\end{bmatrix}\begin{bmatrix}\frac{1-\xi}{2}\\ \frac{1+\xi}{2}\end{bmatrix}\left[\frac{1-\xi}{2}, \frac{1+\xi}{2}\right],\\ &= \begin{bmatrix}\frac{\mathrm{d}\alpha_{1A}}{\mathrm{d}t} & \frac{\mathrm{d}\alpha_{2A}}{\mathrm{d}t}\\ \frac{\mathrm{d}\alpha_{1Q}}{\mathrm{d}t} & \frac{\mathrm{d}\alpha_{2Q}}{\mathrm{d}t}\end{bmatrix}\begin{bmatrix}\frac{1+\xi^2-2\xi}{4} & \frac{1-\xi^2}{4}\\ \frac{1-\xi^2}{4} & \frac{1+\xi^2+2\xi}{4}\end{bmatrix},\end{aligned} \tag{3.53}$$

$$\begin{aligned}\mathbf{F}(\mathbf{U_h})\frac{2}{l_e}\frac{\mathrm{d}\psi_{\mathbf{h}}}{\mathrm{d}\xi} &= \mathbf{F}(\mathbf{U_h})\frac{2}{l_e}\left[-\frac{1}{2}, \frac{1}{2}\right],\\ &= \mathbf{F}(\mathbf{U_h})\left[-\frac{1}{l_e}, \frac{1}{l_e}\right],\\ &= \begin{bmatrix}\mathbf{F_A}\\ \mathbf{F_Q}\end{bmatrix}\left[-\frac{1}{l_e}, \frac{1}{l_e}\right],\\ &\equiv \begin{bmatrix}F_{1A} & F_{2A}\\ F_{1Q} & F_{2Q}\end{bmatrix},\end{aligned} \tag{3.54}$$

$$\begin{aligned}\mathbf{S}(\mathbf{U_h})\psi_{\mathbf{h}} &= \mathbf{S}(\mathbf{U_h})\left[\frac{1-\xi}{2}, \frac{1+\xi}{2}\right],\\ &= \begin{bmatrix}\mathbf{S_A}\\ \mathbf{S_Q}\end{bmatrix}\left[\frac{1-\xi}{2}, \frac{1+\xi}{2}\right],\\ &\equiv \begin{bmatrix}S_{1A} & S_{2A}\\ S_{1Q} & S_{2Q}\end{bmatrix},\end{aligned} \tag{3.55}$$

and

$$\begin{aligned}\mathbf{F_{LF}}(\mathbf{U_h})\psi_{\mathbf{h}}|_{-1}^{1} &= \mathbf{F_{LF}}(\mathbf{U_h})\left[\frac{1-\xi}{2}, \frac{1+\xi}{2}\right]\Bigg|_{-1}^{1},\\ &= \begin{bmatrix}\mathbf{F_{LF_A}}\\ \mathbf{F_{LF_Q}}\end{bmatrix}[-1, 1],\\ &\equiv \begin{bmatrix}F_{LF_{1A}} & F_{LF_{2A}}\\ F_{LF_{1Q}} & F_{LF_{2Q}}\end{bmatrix}.\end{aligned} \tag{3.56}$$

We recall that $\mathbf{F}$ (equation (3.41)), $\mathbf{S}$ (equation (3.42)) and $\mathbf{F_{LF}}$ - which is function of $\mathbf{F}$ - (equation (3.50)) are all vectors. Since the first component of these vectors

refers to the dependent variable A, while the second component to the dependent variable Q (see conservative formulation (3.40)), we identify the first component with the subscript A and the second component with the subscript Q. It follows that subscripts $1A$ and $2A$ are calculated with the first component of vectors $\mathbf{F}$, $\mathbf{S}$ and $\mathbf{F_{LF}}$, and refer to the left and right extremes of the element Ω_e, respectively. Subscripts $1Q$ and $2Q$, instead, are calculated with the second component of vectors $\mathbf{F}$, $\mathbf{S}$ and $\mathbf{F_{LF}}$, and refer to the left and right extremes of the element Ω_e, respectively.

Integrating expressions (3.53), (3.54) and (3.55), one has

$$\begin{aligned}\int_{-1}^{1}\frac{\partial \mathbf{U_h}}{\partial t}\psi_{\mathbf{h}}\mathrm{d}\xi &= \int_{-1}^{1}\begin{bmatrix}\frac{\mathrm{d}\alpha_{1A}}{\mathrm{d}t} & \frac{\mathrm{d}\alpha_{2A}}{\mathrm{d}t}\\ \frac{\mathrm{d}\alpha_{1Q}}{\mathrm{d}t} & \frac{\mathrm{d}\alpha_{2Q}}{\mathrm{d}t}\end{bmatrix}\begin{bmatrix}\frac{1+\xi-2\xi}{4} & \frac{1-\xi^2}{4}\\ \frac{1-\xi^2}{4} & \frac{1+\xi^2+2\xi}{4}\end{bmatrix}\mathrm{d}\xi,\\ &= \begin{bmatrix}\frac{\mathrm{d}\alpha_{1A}}{\mathrm{d}t} & \frac{\mathrm{d}\alpha_{2A}}{\mathrm{d}t}\\ \frac{\mathrm{d}\alpha_{1Q}}{\mathrm{d}t} & \frac{\mathrm{d}\alpha_{2Q}}{\mathrm{d}t}\end{bmatrix}\int_{-1}^{1}\begin{bmatrix}\frac{1+\xi-2\xi}{4} & \frac{1-\xi^2}{4}\\ \frac{1-\xi^2}{4} & \frac{1+\xi^2+2\xi}{4}\end{bmatrix}\mathrm{d}\xi,\\ &= \begin{bmatrix}\frac{\mathrm{d}\alpha_{1A}}{\mathrm{d}t} & \frac{\mathrm{d}\alpha_{2A}}{\mathrm{d}t}\\ \frac{\mathrm{d}\alpha_{1Q}}{\mathrm{d}t} & \frac{\mathrm{d}\alpha_{2Q}}{\mathrm{d}t}\end{bmatrix}\begin{bmatrix}2/3 & 1/3\\ 1/3 & 2/3\end{bmatrix},\end{aligned} \tag{3.57}$$

$$\begin{aligned}\int_{-1}^{1}\mathbf{F}(\mathbf{U_h})\frac{2}{l_e}\frac{\mathrm{d}\psi_{\mathbf{h}}}{\mathrm{d}\xi}\mathrm{d}\xi &= \int_{-1}^{1}\begin{bmatrix}F_{1A} & F_{2A}\\ F_{1Q} & F_{2Q}\end{bmatrix}\mathrm{d}\xi,\\ &\equiv \begin{bmatrix}i'_{1A} & i'_{2A}\\ i'_{1Q} & i'_{2Q}\end{bmatrix},\end{aligned} \tag{3.58}$$

and

$$\begin{aligned}\int_{-1}^{1}\mathbf{S}(\mathbf{U_h})\psi_{\mathbf{h}}\mathrm{d}\xi &= \int_{-1}^{1}\begin{bmatrix}S_{1A} & S_{2A}\\ S_{1Q} & S_{2Q}\end{bmatrix}\mathrm{d}\xi,\\ &\equiv \begin{bmatrix}i''_{1A} & i''_{2A}\\ i''_{1Q} & i''_{2Q}\end{bmatrix},\end{aligned} \tag{3.59}$$

with integrals (3.58) and (3.59) numerically calculated through a Gauss-Legendre quadrature method [330].

Substituting terms (3.56), (3.57), (3.58) and (3.59) in the (3.52), one obtains

$$\begin{aligned}\begin{bmatrix}\frac{\mathrm{d}\alpha_{1A}}{\mathrm{d}t} & \frac{\mathrm{d}\alpha_{2A}}{\mathrm{d}t}\\ \frac{\mathrm{d}\alpha_{1Q}}{\mathrm{d}t} & \frac{\mathrm{d}\alpha_{2Q}}{\mathrm{d}t}\end{bmatrix}\begin{bmatrix}2/3 & 1/3\\ 1/3 & 2/3\end{bmatrix} &= \begin{bmatrix}i'_{1A} & i'_{2A}\\ i'_{1Q} & i'_{2Q}\end{bmatrix} - \begin{bmatrix}i''_{1A} & i''_{2A}\\ i''_{1Q} & i''_{2Q}\end{bmatrix} - \frac{2}{l_e}\begin{bmatrix}F_{LF_{1A}} & F_{LF_{2A}}\\ F_{LF_{1Q}} & F_{LF_{2Q}}\end{bmatrix}\\ &\equiv \begin{bmatrix}G_{1A} & G_{2A}\\ G_{1Q} & G_{2Q}\end{bmatrix},\end{aligned} \tag{3.60}$$

which is equivalent to

$$\begin{bmatrix} 2/3 & 1/3 \\ 1/3 & 2/3 \end{bmatrix} \begin{bmatrix} \frac{\mathrm{d}\alpha_{1A}}{\mathrm{d}t} & \frac{\mathrm{d}\alpha_{1Q}}{\mathrm{d}t} \\ \frac{\mathrm{d}\alpha_{2A}}{\mathrm{d}t} & \frac{\mathrm{d}\alpha_{2Q}}{\mathrm{d}t} \end{bmatrix} = \begin{bmatrix} G_{1A} & G_{1Q} \\ G_{2A} & G_{2Q} \end{bmatrix}. \tag{3.61}$$

Vectorial system (3.61) enables the calculation of the time derivatives of the weights for the element of interest as

$$\begin{aligned} \begin{bmatrix} \frac{\mathrm{d}\alpha_{1A}}{\mathrm{d}t} & \frac{\mathrm{d}\alpha_{1Q}}{\mathrm{d}t} \\ \frac{\mathrm{d}\alpha_{2A}}{\mathrm{d}t} & \frac{\mathrm{d}\alpha_{2Q}}{\mathrm{d}t} \end{bmatrix} &= \begin{bmatrix} 2/3 & 1/3 \\ 1/3 & 2/3 \end{bmatrix}^{-1} \begin{bmatrix} G_{1A} & G_{1Q} \\ G_{2A} & G_{2Q} \end{bmatrix} \\ &= \begin{bmatrix} 2 & -1 \\ -1 & 2 \end{bmatrix} \begin{bmatrix} G_{1A} & G_{1Q} \\ G_{2A} & G_{2Q} \end{bmatrix}. \end{aligned} \tag{3.62}$$

The result reported above refers to a single element. However, the more frequent case is the one in which the whole 1D structure is divided in N_e elements, like in this work and in Figure 3.4. In this last case, equation (3.62) transforms into

$$\begin{bmatrix} \frac{\mathrm{d}\alpha_{1,1,A/Q}}{\mathrm{d}t} \\ \frac{\mathrm{d}\alpha_{1,2,A/Q}}{\mathrm{d}t} \\ \frac{\mathrm{d}\alpha_{2,1,A/Q}}{\mathrm{d}t} \\ \frac{\mathrm{d}\alpha_{2,2,A/Q}}{\mathrm{d}t} \\ \frac{\mathrm{d}\alpha_{3,1,A/Q}}{\mathrm{d}t} \\ \frac{\mathrm{d}\alpha_{3,2,A/Q}}{\mathrm{d}t} \\ \frac{\mathrm{d}\alpha_{e,1,A/Q}}{\mathrm{d}t} \\ \frac{\mathrm{d}\alpha_{e,2,A/Q}}{\mathrm{d}t} \\ \cdots \\ \frac{\mathrm{d}\alpha_{N_e,2,A/Q}}{\mathrm{d}t} \end{bmatrix} = \begin{bmatrix} 2 & -1 & 0 & 0 & 0 & 0 & 0 & 0 & 0 & 0 \\ -1 & 2 & 0 & 0 & 0 & 0 & 0 & 0 & 0 & 0 \\ 0 & 0 & 2 & -1 & 0 & 0 & 0 & 0 & 0 & 0 \\ 0 & 0 & -1 & 2 & 0 & 0 & 0 & 0 & 0 & 0 \\ 0 & 0 & 0 & 0 & 2 & -1 & 0 & 0 & 0 & 0 \\ 0 & 0 & 0 & 0 & -1 & 2 & 0 & 0 & 0 & 0 \\ 0 & 0 & 0 & 0 & 0 & 0 & 2 & -1 & 0 & 0 \\ 0 & 0 & 0 & 0 & 0 & 0 & -1 & 2 & 0 & 0 \\ 0 & 0 & 0 & 0 & 0 & 0 & 0 & 0 & 2 & -1 \\ 0 & 0 & 0 & 0 & 0 & 0 & 0 & 0 & -1 & 2 \end{bmatrix} \begin{bmatrix} G_{1,1,A/Q} \\ G_{1,2,A/Q} \\ G_{2,1,A/Q} \\ G_{2,2,A/Q} \\ G_{3,1,A/Q} \\ G_{3,2,A/Q} \\ G_{e,1,A/Q} \\ G_{e,2,A/Q} \\ \cdots \\ G_{N_e,2,A/Q} \end{bmatrix}, \tag{3.63}$$

where the first subscript refers to the element, while the second one indicates the node of the element (1 for the left node and 2 for the right one). Equation (3.63) can be synthetically written as

$$\frac{\mathrm{d}}{\mathrm{d}t}\alpha = \overline{\mathbf{M}}\mathbf{G}, \tag{3.64}$$

with $\overline{\mathbf{M}}$ the mass matrix, α the vector of A/Q weights, and $\mathbf{G}$ the vector of known terms corresponding to the A/Q weights. It should be noted that equation (3.64) is a system of ordinary differential equations, with independent variable: t. Thus, this system has to be solved in time.

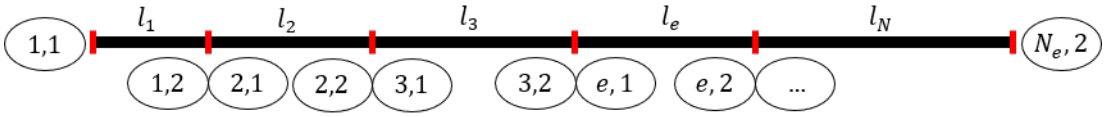

Figure 3.4: Representation of a multiple sequence of elements Ω_e. Each element has length l_e for $e = 1 \div N_e$. Each node is defined by two numbers; the first one refers to the element it belongs to, the second one is 1 for the left node and 2 for the right one.

Temporal resolution

Vector of weights α has to be updated in time. To this purpose, it is first necessary to discretise the time vector, $\mathbf{t}$. In this work, the sequence of heartbeat durations, $\mathbf{T_H}$, is provided in input. Therefore, $\mathbf{t}$ can be obtained from $\mathbf{T_H}$ at the beginning of the simulation as follows. Each heartbeat duration, which is first made multiple of the time step (ΔT), is divided by ΔT to obtain the number of intervals to simulate the whole heartbeat period. The sum of all the time intervals to simulate for all the heartbeat durations is equal to N_t. Hence, starting from the initial time, e.g., $t = 0$, the whole time vector $\mathbf{t}$ can be constructed as $\mathbf{t} = [0, n\Delta T, ...]$, with $n = 1 \div N_t$.

Advancing in time is implemented through a two steps Runge-Kutta explicit scheme. This means that, starting from the initial weight vector, α^0, an intermediate weight vector, $\alpha^{n+1/2}$, is calculated at each half time step, before obtaining α^{n+1}. In particular, the first time step leads to

$$\alpha^{n+1/2} = \alpha^n + \frac{\Delta T}{2}\frac{\mathrm{d}\alpha^n}{\mathrm{d}t}, \tag{3.65}$$

while the second time steps to

$$\alpha^{n+1} = \alpha^n + \Delta T\frac{\mathrm{d}\alpha^{n+1/2}}{\mathrm{d}t}. \tag{3.66}$$

General procedure

In light of all the above, one can now summarize the essential guidelines to follow in order to solve the mass and momentum balance equations (system (3.40)) for the 1D network through a two steps Runge-Kutta Discontinuous-Galerkin scheme.

1. Evaluation of the time vector $\mathbf{t}$, given the sequence of heartbeat durations to simulate $\mathbf{T_H}$.
2. Discretisaton of the whole space domain, with each vessel divided in a number of segments of constant length[1].
3. Imposition of the initial conditions (as explained in Appendix A.2) and determination of the weights (values of A and Q) at the nodes of each segment, to make up the vector of initial weights $\alpha^{\mathbf{0}}$ at time $t_0 = 0\Delta T$.
4. Determination of constant coefficients appearing in the equations (B_1, B_2, B_3, B_4, B_5, β, N_4, γ, dB_1/dz, dB_2/dz, dB_3/dz, dB_4/dz, dB_5/dz) at the nodes of each vascular segment.
5. Calculation of the time-dependent vector $\mathbf{G^n}$ with the solution $\mathbf{U}^n$ at time $t_n = n\Delta T$ and the vector of weights $\alpha^{\mathbf{n+1/2}}$ at the end of the first time step $t_{n+1/2} = (n + 1/2)\Delta T$.
6. Resolution of the boundary conditions.
7. Calculation of the time-dependent vector $\mathbf{G^{n+1/2}}$ with the solution $\mathbf{U}^{n+1/2}$ at time $t_{n+1/2}$ and the vector of weights $\alpha^{\mathbf{n+1}}$ at the end of the second time step $t_{n+1} = (n + 1)\Delta T$.
8. Resolution of the boundary conditions.
9. Substitution of variables at step n-th with variables at step $(n + 1)$-th and repetition of points 5.-8. ΔT by ΔT until the whole time vector is simulated.

Concerning the boundary conditions, these are defined by a combination of physical and compatibility equations, introduced in section 3.1.6 and 3.1.7, respectively.

3.1.6 Physical boundary conditions

Physical boundary conditions have to be set at the edges of the 1D structure, that are: entrance to the aorta, distal arteries and arterial junctions.

[1]The number of segments for each vessel depends on its mechanical characteristics. For example, if a vessel is extremely tapered, the number of segments increases.

Entrance to the aorta and distal arteries

The entrance to the aorta receives its physical boundary condition by the 0D model of the aortic valve (system (3.100)), while the i-th distal artery, represented in Figure 3.5, by the relationship linking flow rate and pressure drop across the closing characteristic impedance, $Z_{c,i}$ (calculated through the (A.1) and reported in Table A.1). This relationship is

$$Q_{ter\_art,i} = \frac{p_{ter\_art,i} - p_{art,i}}{Z_{c,i}}, \tag{3.67}$$

with $p_{ter\_art,i}$ and $Q_{ter\_art,i}$ the pressure and flow rate at the i-th distal artery, and $p_{art,i}$ the pressure at the entrance of the the following arteriole, defined by the relative 0D model (system (3.95)).

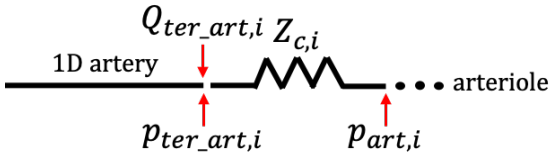

Figure 3.5: Representation of the i-th 1D distal artery with the following characteristic impedance, $Z_{c,i}$. $p_{ter\_art,i}$ and $Q_{ter\_art,i}$ are the pressure and flow rate at the distal artery, while $p_{art,i}$ is the pressure at the entrance of the successive arteriole.

Arterial junctions

As Formaggia and co-workers [80] have observed, flow at the bifurcations is intrinsically three-dimensional. However, one can treat arterial junctions as single points when solving a 1D model. In this case, bifurcation details, such as the angles between the vessels making up the bifurcation, are neglected. Approximating the generic junction in Figure 3.6 as a single point, the local physical boundary condition is represented by the conservation of mass and total pressure as

$$\begin{cases} Q_1 = Q_2 + Q_3, \\ p_1 + \frac{1}{2}\rho\bar{u}_1^2 = p_2 + \frac{1}{2}\rho\bar{u}_2^2, \\ p_1 + \frac{1}{2}\rho\bar{u}_1^2 = p_3 + \frac{1}{2}\rho\bar{u}_3^2, \end{cases} \tag{3.68}$$

where subscript 1 refers to the parent artery, subscripts 2 and 3 to the daughter arteries, and $\bar{u}_i$ $(i = 1:3)$ stands for the mean blood velocity (Q/A) [108].

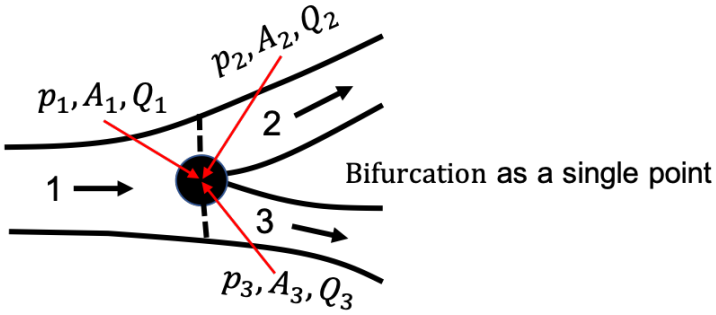

Figure 3.6: Representation of a generic bifurcation, mathematically treated as a single point. Numbers 1, 2 and 3 are used to indicate the parent and daughter arteries, respectively.

3.1.7 Compatibility conditions

Since the 1D model of the systemic arterial tree is solved in two dependent variables (A, Q), both A and Q have to be provided at each boundary. Thus, together with a physical condition, a so called compatibility condition per boundary has to be imposed.

A compatibility condition in this problem is a relationship linking A and Q, and is extracted from the quasi-linear form of mass and momentum balance equations, that is

$$\frac{\partial \mathbf{U}}{\partial t} + \bar{\mathbf{H}}\frac{\partial \mathbf{U}}{\partial z} + \mathbf{S_2} = 0, \tag{3.69}$$

where

$$\bar{\mathbf{H}} = \frac{\partial \mathbf{F}}{\partial \mathbf{U}} \begin{bmatrix} 0, & 1 \\ \sum_{j=1}^{3} \frac{jA^j B_{j+1}}{\rho} - \frac{\beta Q^2}{A^2}, & \frac{2\beta Q}{A} \end{bmatrix}, \tag{3.70}$$

and

$$\mathbf{S_2} = \begin{bmatrix} 0 \\ \sum_{j=1}^{4} \frac{A^j}{\rho} \frac{\mathrm{d}B_j}{\mathrm{d}z} - N_4 - A|\mathbf{g}|sin\gamma \end{bmatrix}. \tag{3.71}$$

This expression can be obtained by rearranging system (3.15) and equation (3.34), with the viscoelastic term $(-B_5 \frac{1}{\sqrt{A}} \frac{\partial Q}{\partial z})$ neglected [108].

Imposing $\det\left(\bar{\mathbf{H}} - \mathbf{\Lambda}\bar{\mathbf{I}}\right) = 0$ - with $\bar{\mathbf{I}}$ the identity matrix -, one can calculate the eigenvalues of matrix $\bar{\mathbf{H}}$ (see Appendix A.4), which represent the slopes of the two

characteristic lines at the generic arterial location and are equal to

$$\lambda_{1,2} = \frac{\beta Q}{A} \pm c. \tag{3.72}$$

In the latter, c, which is the local pulse wave velocity in resting blood, is determined as

$$c = \sqrt{\frac{A}{\rho}\left(B_2 + 2B_3 A + 3B_4 A^2\right) + \frac{Q^2}{A^2}\beta(\beta - 1)}. \tag{3.73}$$

Notice that, at each site, blood velocity, $\frac{\beta Q}{A}$, is smaller than c, and both $\frac{\beta Q}{A}$ and c are positive. Thus, $\lambda_1 < 0$ and $\lambda_2 > 0$, with λ_1 associated to the backward characteristics and λ_2 to the forward one. Moreover, since λ_1 and λ_2 have opposite signs, the problem is strictly hyperbolic.

The row eigenvector related to each eigenvalue is calculated through the vectorial equation

$$[k1_{\lambda_1}, k2_{\lambda_1}] \det\left(\bar{\mathbf{H}} - \lambda_1 \bar{\mathbf{I}}\right) = [0, 0] \tag{3.74}$$

for λ_1, and

$$[k1_{\lambda_2}, k2_{\lambda_2}] \det\left(\bar{\mathbf{H}} - \lambda_2 \bar{\mathbf{I}}\right) = [0, 0] \tag{3.75}$$

for λ_2. Developing equations (3.74) and (3.75) as done in Appendix A.5 and A.6, respectively, one finds the row eigenvector corresponding to λ_1, $\mathbf{l_1} = [-\lambda_2, 1]$, and the row eigenvector corresponding to λ_2, $\mathbf{l_2} = [-\lambda_1, 1]$. Thus, based on the above, one can define the matrix of the eigenvalues

$$\bar{\mathbf{\Lambda}} = \begin{bmatrix} \lambda_1, & 0 \\ 0, & \lambda_2 \end{bmatrix}, \tag{3.76}$$

and the matrix of the eigenvectors

$$\bar{\mathbf{L}} = \begin{bmatrix} -\lambda_2, & 1 \\ -\lambda_1, & 1 \end{bmatrix}, \tag{3.77}$$

which verify the relationship $\bar{\mathbf{L}}\bar{\mathbf{H}} = \bar{\mathbf{\Lambda}}\bar{\mathbf{L}}$.

At each boundary, two compatibility conditions (one per characteristic line) are available. These conditions are provided by system (3.69) itself, projected along the characteristics [80] as

$$\bar{\mathbf{L}}\frac{\partial \mathbf{U}}{\partial t} + \bar{\mathbf{L}}\bar{\mathbf{H}}\frac{\partial \mathbf{U}}{\partial z} + \bar{\mathbf{L}}\mathbf{S_2} = 0, \tag{3.78}$$

that is equivalent to

$$\bar{\mathbf{L}}\frac{\partial \mathbf{U}}{\partial t} + \bar{\mathbf{\Lambda}}\bar{\mathbf{L}}\frac{\partial \mathbf{U}}{\partial z} + \bar{\mathbf{L}}\mathbf{S_2} = 0. \tag{3.79}$$

Notice that, if $\mathbf{S_2}$=$\mathbf{0}$, system (3.79) would correspond to

$$\frac{\partial \mathbf{W}}{\partial t} + \bar{\mathbf{\Lambda}}\frac{\partial \mathbf{W}}{\partial s} = 0, \tag{3.80}$$

with $\mathbf{W} = [W_1, W_2]^T$, the vector of the characteristic variables, satisfying relation [81]

$$\frac{\partial \mathbf{W}}{\partial \mathbf{U}} = \bar{\mathbf{L}}. \tag{3.81}$$

Thus, if $\mathbf{S_2}$=$\mathbf{0}$, compatibility conditions would be the equations of the characteristic variables W_1 and W_2, which have the property to remain constant along the corresponding characteristic lines (the characteristics with slope λ_1 for W_1 and λ_2 for W_2). However, in the problem we are solving, $\mathbf{S_2} \neq \mathbf{0}$. As a consequence, we do not have the characteristic variables but pseudo-characteristic variables, which are obtained by developing equation (3.79) as follows.

Exploiting the identities

$$\frac{\partial}{\partial t}\left(\bar{\mathbf{L}}\mathbf{U}\right) = \bar{\mathbf{L}}\frac{\partial \mathbf{U}}{\partial t} + \frac{\partial \bar{\mathbf{L}}}{\partial t}\mathbf{U} \tag{3.82}$$

and

$$\bar{\mathbf{\Lambda}}\frac{\partial}{\partial z}\left(\bar{\mathbf{L}}\mathbf{U}\right) = \bar{\mathbf{\Lambda}}\frac{\partial \bar{\mathbf{L}}}{\partial z}\mathbf{U} + \bar{\mathbf{\Lambda}}\bar{\mathbf{L}}\frac{\partial \mathbf{U}}{\partial z}, \tag{3.83}$$

equation (3.79) can be rewritten as in [108]:

$$\frac{\partial}{\partial t}\left(\bar{\mathbf{L}}\mathbf{U}\right) - \frac{\partial \bar{\mathbf{L}}}{\partial t}\mathbf{U} + \bar{\mathbf{\Lambda}}\frac{\partial}{\partial z}\left(\bar{\mathbf{L}}\mathbf{U}\right) - \bar{\mathbf{\Lambda}}\frac{\partial \bar{\mathbf{L}}}{\partial z}\mathbf{U} + \bar{\mathbf{L}}\mathbf{S_2} = 0. \tag{3.84}$$

Then, introducing the total derivative D/Dt [108], the latter becomes

$$\frac{D}{Dt}\left(\bar{\mathbf{L}}\mathbf{U}\right) - \frac{\partial \bar{\mathbf{L}}}{\partial t}\mathbf{U} - \bar{\mathbf{\Lambda}}\frac{\partial \bar{\mathbf{L}}}{\partial z}\mathbf{U} + \bar{\mathbf{L}}\mathbf{S_2} = 0. \tag{3.85}$$

Discretising time as $\Delta T = t_{n+1} - t_n$ [108], one can approximate the total derivative as

$$\begin{aligned}\frac{D}{Dt}\left(\bar{\mathbf{L}}_{\mathbf{n+1}}\mathbf{U}_{\mathbf{n+1}}\right) &\approx \frac{\bar{\mathbf{L}}_{\mathbf{n+1}}\mathbf{U}_{\mathbf{n+1}} - \bar{\mathbf{L}}^*_{\mathbf{n}}\mathbf{U}^*_{\mathbf{n}}}{\Delta T} \\ &= \frac{\bar{\mathbf{L}}_{\mathbf{n+1}}\mathbf{U}_{\mathbf{n+1}} + \bar{\mathbf{L}}_{\mathbf{n}}\mathbf{U}_{\mathbf{n+1}} - \bar{\mathbf{L}}_{\mathbf{n}}\mathbf{U}_{\mathbf{n+1}} - \bar{\mathbf{L}}^*_{\mathbf{n}}\mathbf{U}^*_{\mathbf{n}}}{\Delta T} \\ &= \frac{\bar{\mathbf{L}}_{\mathbf{n}}\mathbf{U}_{\mathbf{n+1}} - \bar{\mathbf{L}}^*_{\mathbf{n}}\mathbf{U}^*_{\mathbf{n}}}{\Delta T} + \frac{\bar{\mathbf{L}}_{\mathbf{n+1}} - \bar{\mathbf{L}}_{\mathbf{n}}}{\Delta T}\mathbf{U}_{\mathbf{n+1}},\end{aligned} \tag{3.86}$$

where the superscript $*$ refers to the point located at a distance $c\Delta T$ from the boundary, $\bar{\mathbf{L}}_{\mathbf{n+1}} = \bar{\mathbf{L}}(\mathbf{U}_{\mathbf{n+1}})$, $\bar{\mathbf{L}}_{\mathbf{n}} = \bar{\mathbf{L}}(\mathbf{U}_{\mathbf{n}})$, and $\bar{\mathbf{L}}^*_{\mathbf{n}} = \bar{\mathbf{L}}(\mathbf{U}^*_{\mathbf{n}})$. Being

$$\frac{\bar{\mathbf{L}}_{\mathbf{n+1}} - \bar{\mathbf{L}}_{\mathbf{n}}}{\Delta T}\mathbf{U}_{\mathbf{n+1}} \approx \frac{\partial \bar{\mathbf{L}}}{\partial t}\mathbf{U}, \tag{3.87}$$

equation (3.85) simplifies [108]. It is discretised as

$$\frac{\bar{\mathbf{L}}_{\mathbf{n}}\mathbf{U}_{\mathbf{n+1}} - \bar{\mathbf{L}}^*_{\mathbf{n}}\mathbf{U}^*_{\mathbf{n}}}{\Delta T} = \bar{\mathbf{\Lambda}}^*_{\mathbf{n}}\frac{\partial \bar{\mathbf{L}}^*_{\mathbf{n}}}{\partial z}\mathbf{U}^*_{\mathbf{n}} - \bar{\mathbf{L}}^*_{\mathbf{n}}\mathbf{S}^*_{\mathbf{2_n}}, \tag{3.88}$$

with $\bar{\mathbf{\Lambda}}^*_{\mathbf{n}} = \bar{\mathbf{\Lambda}}(\mathbf{U}^*_{\mathbf{n}})$ and $\mathbf{S}^*_{\mathbf{2_n}} = \mathbf{S_2}(\mathbf{U}^*_{\mathbf{n}})$. Thus, one gets

$$\bar{\mathbf{L}}_{\mathbf{n}}\mathbf{U}_{\mathbf{n+1}} = \bar{\mathbf{L}}^*_{\mathbf{n}}\mathbf{U}^*_{\mathbf{n}} + \Delta T\left(\bar{\mathbf{\Lambda}}^*_{\mathbf{n}}\frac{\partial \bar{\mathbf{L}}^*_{\mathbf{n}}}{\partial z}\mathbf{U}^*_{\mathbf{n}} - \bar{\mathbf{L}}^*_{\mathbf{n}}\mathbf{S}^*_{\mathbf{2_n}}\right). \tag{3.89}$$

In the end, since the pseudo characteristics are null at the initial state, equation (3.89) is balanced by subtracting the initial condition to the dependent variables as

$$\bar{\mathbf{L}}_{\mathbf{n}}(\mathbf{U_{n+1}} - \mathbf{U_i}) = \bar{\mathbf{L}}^*_{\mathbf{n}}(\mathbf{U}^*_{\mathbf{n}} - \mathbf{U}^*_{\mathbf{i}}) + \Delta T \left(\bar{\mathbf{\Lambda}}^*_{\mathbf{n}} \frac{\partial \bar{\mathbf{L}}^*_{\mathbf{n}}}{\partial z}(\mathbf{U}^*_{\mathbf{n}} - \mathbf{U}^*_{\mathbf{i}}) - \bar{\mathbf{L}}^*_{\mathbf{n}}(\mathbf{S}^*_{\mathbf{2_n}} - \mathbf{S}^*_{\mathbf{2_i}}) \right), \tag{3.90}$$

with $\mathbf{S}^*_{\mathbf{2_i}} = \mathbf{S_2}(\mathbf{U}^*_{\mathbf{i}})$ [108].

Working on equation (3.90) as described in Appendix A.7, one obtains the two compatibility conditions at the generic site

1.
$$Q_{n+1} = \lambda_{2_n} A_{n+1} + tn_1, \tag{3.91}$$

2.
$$Q_{n+1} = \lambda_{1_n} A_{n+1} + tn_2. \tag{3.92}$$

In the latter, A_{n+1} and Q_{n+1} are the values of A and Q at a generic boundary and at time t_{n+1}. λ_{2_n} and λ_{1_n} are the slopes of the second and first characteristic lines at the boundary and at time t_n. tn_1 and tn_2 are the known terms, which depend on time t_n and are defined in equation (A.2).

Since time is solved through a two-steps Runge-Kutta method, time discretisation of equation (3.85) changes depending on the time step one has to solve. It is discretised as

$$\frac{\bar{\mathbf{L}}_{\mathbf{n}}\mathbf{U_{n+1/2}} - \bar{\mathbf{L}}^{\mathbf{1*}}_{\mathbf{n}}\mathbf{U}^{\mathbf{1*}}_{\mathbf{n}}}{\Delta T} = \bar{\mathbf{\Lambda}}^{\mathbf{1*}}_{\mathbf{n}} \frac{\partial \bar{\mathbf{L}}^{\mathbf{1*}}_{\mathbf{n}}}{\partial z}\mathbf{U}^{\mathbf{1*}}_{\mathbf{n}} - \bar{\mathbf{L}}^{\mathbf{1*}}_{\mathbf{n}}\mathbf{S}^{\mathbf{1*}}_{\mathbf{2_n}}, \tag{3.93}$$

when solving the first time step ($t_{n+1/2}$), and as

$$\frac{\bar{\mathbf{L}}_{\mathbf{n}}\mathbf{U_{n+1}} - \bar{\mathbf{L}}^{\mathbf{2*}}_{\mathbf{n}}\mathbf{U}^{\mathbf{2*}}_{\mathbf{n}}}{\Delta T} = \bar{\mathbf{\Lambda}}_{\mathbf{n+1/2}} \frac{\partial \bar{\mathbf{L}}_{\mathbf{n+1/2}}}{\partial z}\mathbf{U_{n+1/2}} - \bar{\mathbf{L}}_{\mathbf{n+1/2}}\mathbf{S}_{\mathbf{2_{n+1/2}}}, \tag{3.94}$$

when solving the second time step (t_{n+1}). In these two equations, superscripts $1*$ and $2*$ refer to the points located at a distance from the boundary equal to $c\Delta T/2$ and $c\Delta T$, respectively. Then, subscripts n, $n+1/2$ and $n+1$ refer to times $t_n = n\Delta T$, $t_{n+1/2} = (n+1/2)\Delta T$ and $t_{n+1} = (n+1)\Delta T$, respectively. Thus, depending on the time step one is solving, terms tn_1 and tn_2 in the two compatibility equations modify. They are given for the first time step in equation (A.3) and for the second time step in equation (A.4).

At each boundary, one uses the compatibility condition related to the characteristic line from where the last 1D information is coming. Therefore, for a left boundary (e.g., the entrance to the aorta), one uses compatibility equation 1. (3.91), which is associated to the characteristic line with negative slope (λ_1). For a right boundary (e.g., distal arteries), one uses compatibility equation 2. (3.92), which is associated to the characteristic line with positive slope (λ_2). One follows the same criteria when solving arterial bifurcations (always made of one parent artery and two daughter arteries in this problem): parent artery has a right boundary and is represented by compatibility equation 2. (3.92), daughter arteries have a left boundary and are represented by compatibility equation 1. (3.91).

Thus, the entrance to the aorta is solved by combining the equation associated to the local characteristic line λ_1 with the physical condition of the aortic valve (system (3.100)), as in Figure 3.7. Distal arteries are solved by combining the equation associated to the local characteristic line λ_2 with the physical condition of the on-site characteristic impedance (equation (3.67)), as in Figure 3.7. Arterial bifurcations are solved by combining the equations associated to the local characteristic line λ_1 at daughter arteries, the equation associated to the local characteristic line λ_2 at parent artery, and the physical condition of the bifurcation (system (3.68)), as in Figure 3.8. The complete resolution of the entrance to the aorta and the generic distal artery is provided by the (B.2) and (B.3), respectively, after having introduced the 0D models of both cardiac valves and arterioles. The complete resolution of the generic arterial bifurcation is provided by the (A.5).

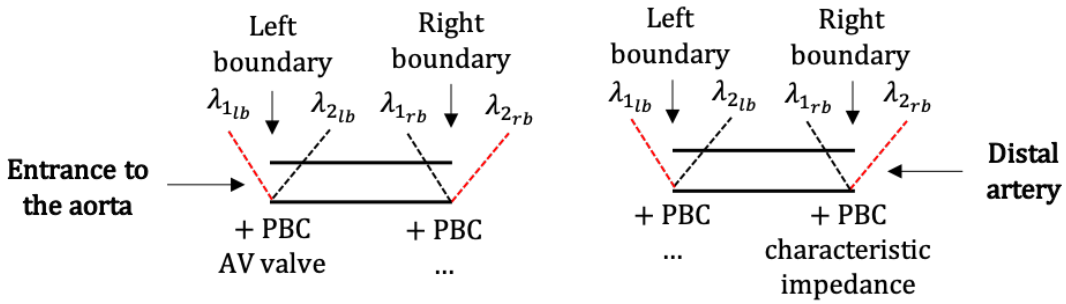

Figure 3.7: Representation of the left (subscript "lb") and right boundaries (subscript "rb") for the first aortic tract and the generic distal artery, with an indication of the characteristic to use at each boundary: the red one. PBC stands for physical boundary condition.

Based on the above, one can define the vector of the variables at the boundary of the complete 1D model, $V_{b,1D} = [Q_{aor}, A_{aor}, Q_{ter\_art,i}, A_{ter\_art,i}]$, made of flow rate and pressure at the entrance to the aorta (Q_{aor} and A_{aor}) and flow rate and pressure at distal arteries ($Q_{ter\_art,i}$ and $A_{ter\_art,i}$, for i from 1 to the number of distal arteries). $V_{b,1D}$ will be used in the coupling between the 1D model of

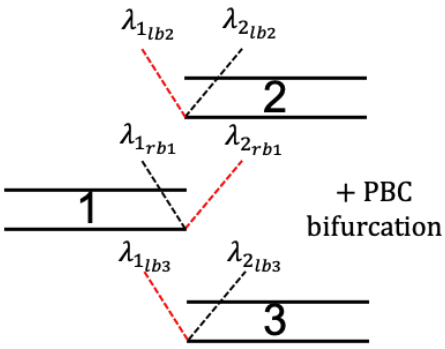

Figure 3.8: Representation of the left (subscript "lb") and right boundaries (subscript "rb") for the daughter arteries (vessels 2 and 3) and the parent artery (vessel 1) of an arterial bifurcation, respectively, with an indication of the characteristic to use at each boundary: the red one. PBC stands for physical boundary condition.

the systemic arterial tree and the 0D model of the systemic microcirculation and venous return, with the heart and pulmonary circulation (see section 3.3).

3.2 0D model of the systemic microcirculation and the venous return, with the heart and pulmonary circulation

The present 0D model includes the systemic microcirculation (arterioles, capillaries and venules) and venous return, together with the heart and pulmonary circulation. This model is represented in Figure 3.9, with its legend in Table 3.2 and each submodel described in the following.

3.2.1 0D model of arterioles, capillaries, venous return and pulmonary circulation

Arterioles, capillaries, venules, veins, pulmonary arteries and veins are all reproduced through RLC electric circuits [180, 181]. For the j-th compartment, the RLC electric circuit is described by system

$$\begin{cases} \dfrac{\mathrm{d}p_j}{\mathrm{d}t} = \dfrac{Q_{j-1} - Q_j}{C_j}, \\ \dfrac{\mathrm{d}Q_j}{\mathrm{d}t} = \dfrac{p_j - R_j Q_j - p_{j+1}}{L_j}, \\ V_j = p_j C_j + V_{j_0}. \end{cases} \tag{3.95}$$

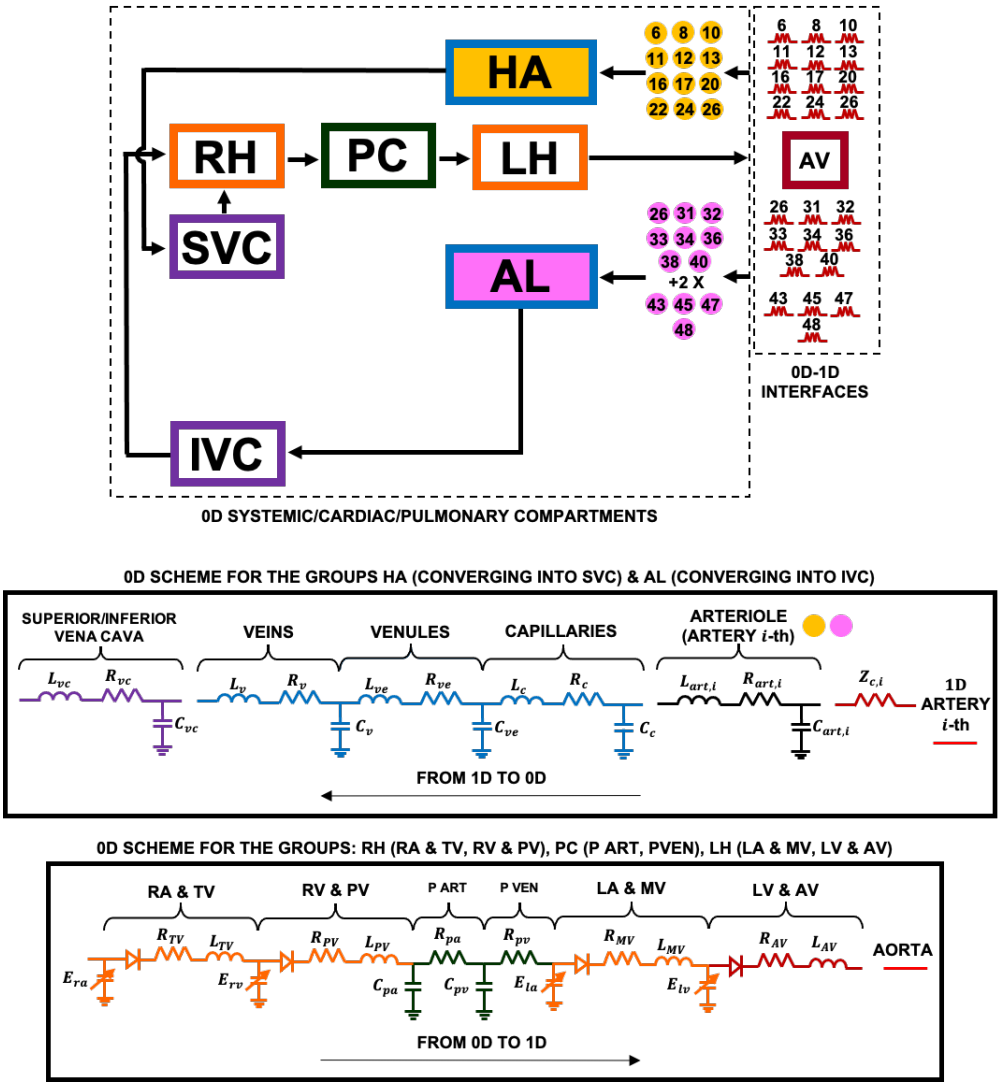

Figure 3.9: Representation of the 0D model of the systemic microcirculation and venous return, together with the heart and pulmonary circulation. The top panel includes the structure of the 0D systemic/cardiac/pulmonary compartments on the left and the 0D-1D interface (the characteristic impedances of distal 1D arteries and the aortic valve, AV) on the right. The 0D model, with details in the bottom panels, is divided into upper body (head and arms arterioles, yellow bullets; head and arms microcirculation and venous return, HA; superior vena cava, SVC; right heart, RH; pulmonary circulation, PC; left heart, LH) and lower body (arterioles of abdomen and legs, pink bullets; microcirculation and venous return of abdomen and legs, AL; inferior vena cava, IVC). The complete legend is provided in Table 3.2.

Table 3.2: Legend of the 0D model of the systemic microcirculation and venous return, with the heart and pulmonary circulation, schematically depicted in Figure 3.9. Variables followed by the symbols (+), (∗) and (/) are used in Figures 3.11, 3.18 and 7.2 respectively.

Name	**Significance**	**Name**	**Significance**
HA	Head and Arms	E_{rv}	Right-ventricular elastance
AL	Abdomen and Legs	E_{la}	Left-atrial elastance
SVC	Superior Vena Cava	E_{lv}	Left-ventricular elastance
IVC	Inferior Vena Cava	R_{TV}	Tricuspid valve resistance
RH	Right Heart	L_{TV}	Tricuspid valve inertance
PC	Pulmonary Circulation	R_{PV}	Pulmonary valve resistance
LH	Left Heart	L_{PV}	Pulmonary valve inertance
RA	Right atrium	C_{pa}	Pulmonary arteries compliance
TV	Tricuspid valve	R_{pa}	Pulmonary arteries resistance
RV	Right Ventricle	C_{pv}	Pulmonary veins compliance
PV	Pulmonary valve	R_{pv}	Pulmonary veins resistance
P ART	Pulmonary arteries	R_{MV}	Mitral valve resistance
P VEN	Pulmonary veins	L_{MV}	Mitral valve inertance
LA	Left atrium	R_{AV}	Aortic valve resistance
MV	Mitral valve	L_{AV}	Aortic valve inertance
LV	Left Ventricle	p_{aor} (+)	Aortic pressure
AV	Aortic valve	Q_{aor} (+)	Aortic flow rate
$Z_{c,i}$	Characteristic impedance of i-th artery	$Q_{ter\_art,i}$ (+)	Flow rate entering the i-th arteriole
$C_{art,i}$	Arteriolar compliance i-th artery	$*_{svc}$ (+)	which refers to the superior vena cava
$R_{art,i}$	Arteriolar resistance i-th artery	$*_{ivc}$ (+)	which refers to the inferior vena cava
$L_{art,i}$	Arteriolar inertance i-th artery	$*\__{HA}$ (+)	Belonging to HA
C_c	Capillary compliance	$*\__{AL}$ (+)	Belonging to AL
R_c	Capillary resistance	$\overline{p}_{acs}$ (∗)	aortic and carotid sinuses pressure
L_c	Capillary inertance	n_s (∗)	sympathetic signal
C_{ve}	Venular compliance	n_p (∗)	parasympathetic signal
R_{ve}	Venular resistance	HR (∗)	heart rate
L_{ve}	Venular inertance	$E_{A,rv}$ (∗)	Amplitude right-ventricular elastance
C_v	Venous compliance	$E_{A,lv}$ (∗)	Amplitude left-ventricular elastance
R_v	Venous resistance	$V_{0,ve}$ (∗)	Venular unstressed volumes
L_v	Venous inertance	$V_{0,v}$ (∗)	Venous unstressed volumes
C_{vc}	Vena cava compliance	VIP (/)	Volume indifference point
R_{vc}	Vena cava resistance	U ABD (/)	Upper abdomen
L_{vc}	Vena cava inertance	L ABD (/)	Lower abdomen
E_{ra}	Right-atrial elastance	LEGS (/)	Legs

In system (3.95), V_j and V_{j_0} are the total and unstressed volumes associated to the compartment, Q_{j-1} and Q_j are the flow rates entering and exiting the compartment, and p_j and p_{j+1} are the pressures at the inlet and outlet of the compartment (each compartment is characterised by pressure p_j). Resistance, R_j, inertance, L_j, and compliance, C_j, indicated in Appendix B.1, are proper of each compartment and chosen according to Liang et al. [181] with adjustments (compensating for the differences in ours and Liang's modelling architecture). Total and unstressed volumes of all compartments at the initial time, also provided in Appendix B.1 with initial conditions (Q_j^0 and p_j^0), are assigned in order to make a total blood volume

of 5.7 l and respect the physiological distribution of blood within both the vascular and body regions for a healthy and supine man.

For normal male subjects, total blood volume is supposed to be in the range 75-80 ml/kg [120]. Choosing a total blood volume of 76 ml/kg and referring to a male subject of 75 kg, we set total blood volume to 5.7 l. Total unstressed volume is instead taken equal to 70% of total blood volume [195]. Thus, total stressed (total blood volume minus total unstressed volume) and unstressed volumes are 1710 ml and 3990 ml, respectively. Total stressed and unstressed volumes are first distributed within the vascular regions as expected in literature, that is 10% to systemic arteries, 5% to arterioles, 7% to heart, 9% to pulmonary circulation, and 69% to capillaries, venules and veins [120]. Total and unstressed volumes of the different vascular regions are further divided among the body regions (i.e., head and arms, thorax, abdomen and legs) in accordance to literature data for a supine subject [119, 176].

3.2.2 0D model for heart chambers and valves

Similarly to what proposed by [30, 180, 181], dynamics of cardiac chambers is mimicked through a time-varying elastance model as

$$p_{ch} = E_{ch}(V_{ch} - V_{0,ch}), \tag{3.96}$$

which links the pressure into the chamber, p_{ch}, to the relative stressed volume, $(V_{ch} - V_{0,ch})$, through the elastance function,

$$E_{ch} = E_{A,ch} e_{ch} + E_{B,ch}. \tag{3.97}$$

V_{ch} and $V_{0,ch}$ are the total and unstressed volume of the chamber, $E_{B,ch}$ and $E_{A,ch} + E_{B,ch}$ are the minimal and maximal values of the elastance, and e_{ch} is a normalized time-varying function of the elastance, with different shapes for atria and ventricles. In accordance to [30, 180, 181], atrial, e_a, and ventricular, e_v, e_{ch} functions are determined like

$$e_a = \begin{cases} \frac{1}{2}\left[1+\cos\left(\pi\frac{(t+RR-t_{ar})}{T_{ar}}\right)\right] & 0 \le t \le t_{ar}+T_{ar}-RR, \\ 0 & t_{ar}+T_{ar}-RR < t \le t_{ac}, \\ \frac{1}{2}\left[1-\cos\left(\pi\frac{(t-t_{ac})}{T_{ac}}\right)\right] & t_{ac} < t \le t_{ac}+T_{ac}, \\ \frac{1}{2}\left[1+\cos\left(\pi\frac{(t-t_{ar})}{T_{ar}}\right)\right] & t_{ac}+T_{ac} < t \le RR, \end{cases} \tag{3.98}$$

and

$$e_v = \begin{cases} \frac{1}{2}\left[1-\cos\left(\pi\frac{t}{T_{vc}}\right)\right] & 0 \le t \le T_{vc}, \\ \frac{1}{2}\left[1+\cos\left(\pi\frac{(t-T_{vc})}{T_{vr}}\right)\right] & T_{vc} < t \le T_{vc}+T_{vr}, \\ 0 & T_{vc}+T_{vr} < t \le RR, \end{cases} \tag{3.99}$$

where RR is the heartbeat period, T_{ac}/T_{ar} and T_{vc}/T_{vr} are the periods of contraction/relaxation for atria and ventricles, while t_{ac} and t_{ar} are the times when atria start contracting and relaxing, respectively. Characteristic times of the e_a and e_v functions, $E_{A,ch}$, $E_{B,ch}$, initial V_{ch} (V^0_{ch}) and $V_{0,ch}$ values are set according to [30, 120, 180, 181] with some variations and listed in Appendix B.2, together with initial conditions (p^0_{ch}). Functions e_a and e_v are shown in Figure 3.10 for the chosen characteristic times and RR =0.8 s.

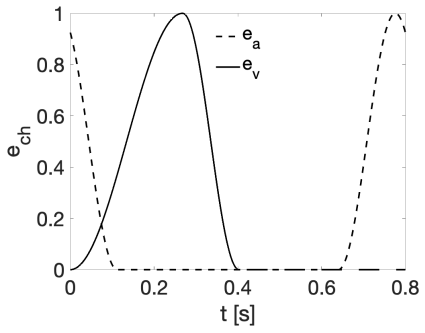

Figure 3.10: Functions e_a and e_v for an heartbeat period RR of 0.8 s and the characteristic times in Table B.2.

Cardiac valves are adequately reproduced through the pressure-flow relation

adopted by Blanco et al. [31, 30], coupled to the valve model presented by Korakianitis et al. [156]. Namely,

$$\begin{cases} L_{va}\dfrac{\mathrm{d}Q_{va}}{\mathrm{d}t} + R_{va}Q_{va} + B_{va}|Q_{va}|Q_{va} = \dfrac{(1-\cos(\theta_{va}))^4}{(1-\cos(\theta_{max}))^4}\left(p_{1va} - p_{2va}\right), \\ I_{ao}\dfrac{\mathrm{d}^2\theta_{va}}{\mathrm{d}t^2} = F_{pr} + F_{bm} - F_{fr} - F_{vo}. \end{cases} \tag{3.100}$$

This system leads to the calculation of the valvular flow rate, Q_{va}, based on the fluid inertance, L_{va}, the viscous resistance, R_{va}, the turbulent flow separation coefficient, B_{va}, the pressure difference across the valve, $p_{1va} - p_{2va}$, and the degree of the valve opening angle, θ_{va}, which is between 0 and θ_{max}=75°. θ_{va} is calculated according to the momentum of inertia of the valve, I_{ao}, and the forces applied on the valve leaflets, which are the pressure gradient ($F_{pr} = k_p(p_{1va} - p_{2va})$), the dynamic action of the blood pushing on the blood leaflets ($F_{bm} = k_q Q_{va}\cos(\theta_{va})$), the frictional effects caused by the tissue resistance ($F_{fr} = k_f \frac{\mathrm{d}\theta_{va}}{\mathrm{d}t}$), and the role of the vortexes downstream of the valve ($F_{vo} = k_v Q_{va}\sin(2\theta_{va})$ if $p_{1va} \geq p_{2va}$, and $F_{vo} = 0$ if $p_{1va} < p_{2va}$). Parameters are set as in [30] and indicated in Appendix B.3, with initial conditions (Q^0_{va} and θ^0_{va}).

3.2.3 Model resolution II

The complete circuit corresponding to the whole 0D model of the systemic microcirculation, venous return, heart and pulmonary circulation is shown in Figure 3.11, with the relative legend in Table 3.2. It is solved by the system of ordinary differential equations (B.1), deriving from the application of system (3.95) to arteriolar, capillary, venular, venous and pulmonary compartments, of equations (3.96)-(3.99) to cardiac chambers, and of system (3.100) to cardiac valves.

Based on system (B.1), one defines the vector of the dependent variables for the whole 0D model, $\mathbf{V_{0D}}$, and the vector of the variables at the boundaries of the 0D model, $\mathbf{V_{b,0D}}$, both indicated in Appendix B.4. $\mathbf{V_{0D}}$ is advanced in time as the weight vector α in the 1D model, following a two steps Runge-Kutta explicit scheme (equations (3.65) and (3.66)). Therefore, at each ΔT, one gets the intermediate solution

$$\mathbf{V_{0D}}^{n+1/2} = \mathbf{V_{0D}}^{n} + \frac{\Delta T}{2}\frac{\mathrm{d}\mathbf{V_{0D}}^{n}}{\mathrm{d}t}, \tag{3.101}$$

at the end of the first time step, and the final solution

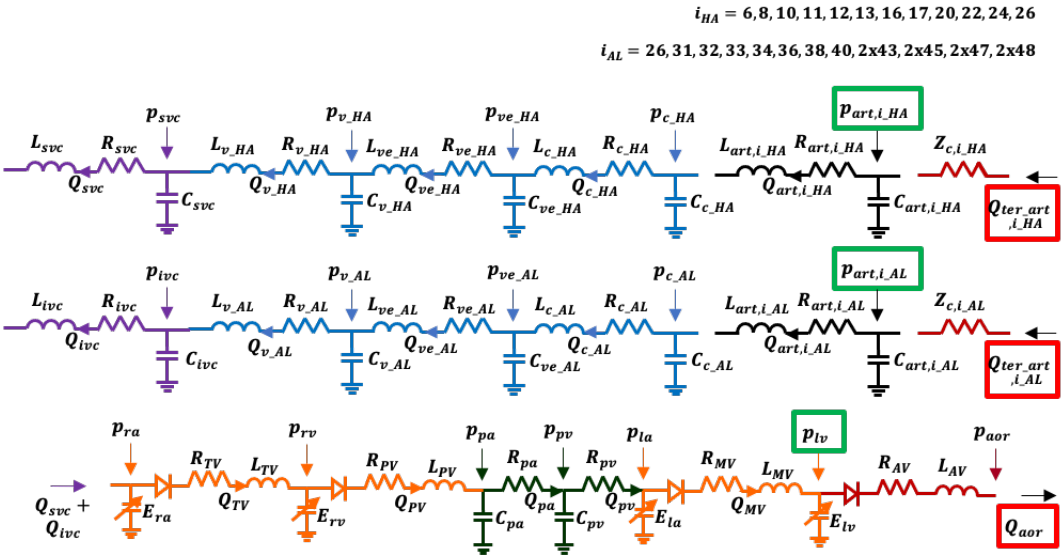

Figure 3.11: Representation of the electric circuit corresponding to the whole 0D model of the systemic microcirculation and venous return, with the heart and pulmonary circulation. Legend is shown in Table 3.2. Variables in red boxes are provided by the boundary resolution to the 0D model, and the opposite for variables in green boxes.

$$\mathbf{V_{0D}}^{n+1} = \mathbf{V_{0D}}^{n} + \Delta T \frac{\mathrm{d}\mathbf{V_{0D}}^{n+1/2}}{\mathrm{d}t}, \tag{3.102}$$

at the end of the second time step. $\mathbf{V_{b,0D}}$, instead, is advanced in time by solving at each half time step the 1D-0D boundary conditions. A detailed explanation of the coupling between the 0D and 1D models is provided in section 3.3.

3.3 Coupling 1D and 0D models

The coupling between the complete 1D and 0D models when solving the $(n+1)$-th ΔT is shown in Figure 3.12. One starts from the n-th values of the vector of weight, α^n, the vector of the complete 0D system, $\mathbf{V_{0D}}^n$, and the vector of the boundary variables ($\mathbf{V_b}^n$) for the 1D model, $\mathbf{V_{b,1D}}^n$, and the 0D model, $\mathbf{V_{b,0D}}^n$. Vectors $\mathbf{V_{0D}}^n$, $\mathbf{V_{b,1D}}^n$ and $\mathbf{V_{b,0D}}^n$ are indicated in Appendix B.4, while vector α^n is defined in the (3.64). Then, the numbered operations in Figure 3.12 have to be followed in chronological order. Namely,

1. $\alpha^{n+1/2}$ is obtained from α^n and $\mathbf{V_{b,1D}}^n$ through equations (3.64)-(3.66).

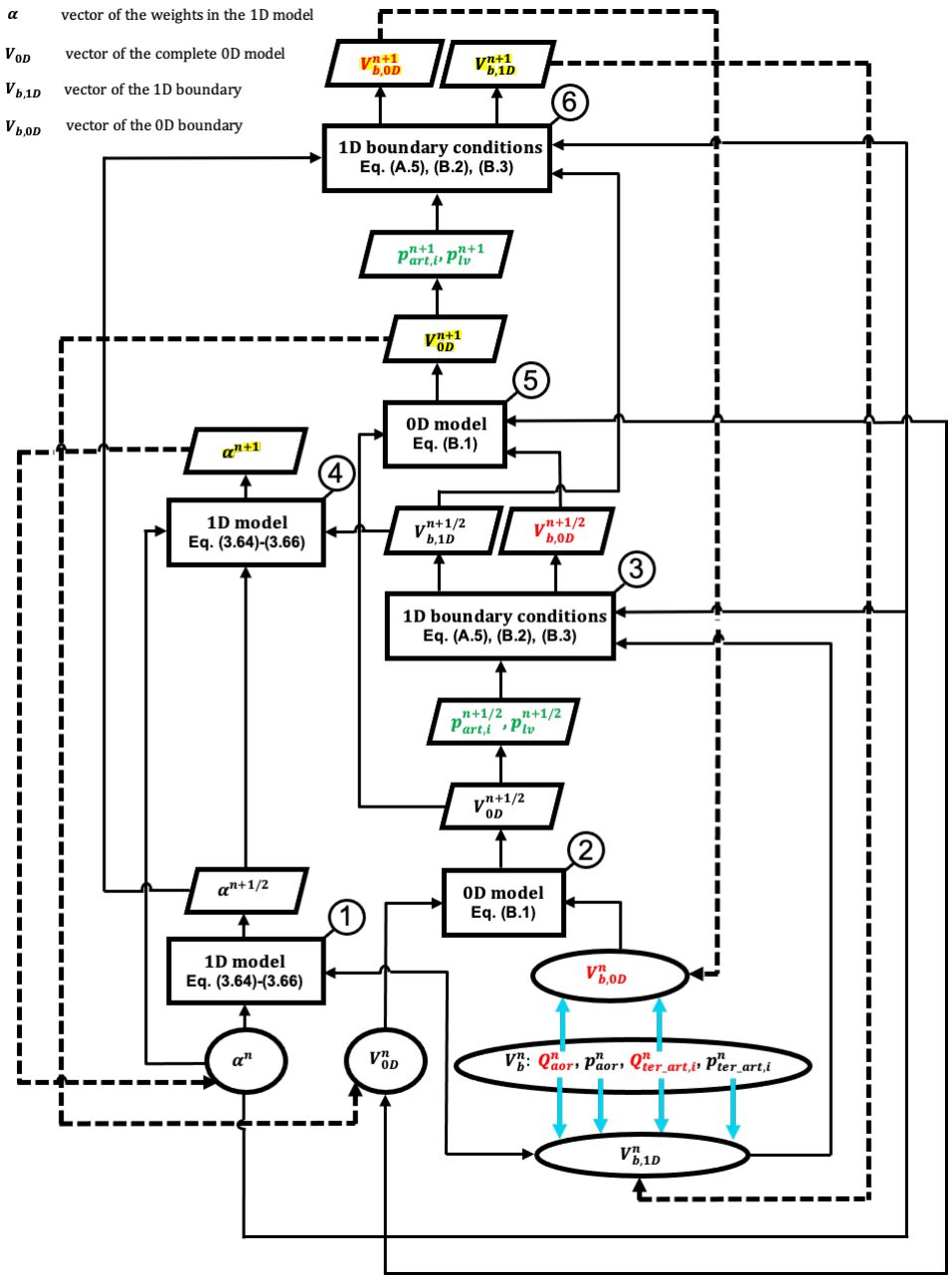

Figure 3.12: Scheme representing the chronological sequence of operations to follow at each n-th ΔT (cycle) in order to couple the 0D and 1D models. Variables in red (green) are the ones provided by the boundary resolution (0D model) to the 0D model (boundary resolution). Initial variables are enclosed in circles, while variables at the end of the cycle are highlighted.

2. $\mathbf{V_{0D}}^{n+1/2}$ is calculated from $\mathbf{V_{0D}}^{n}$ and $\mathbf{V_{b,0D}}^{n}$ by exploiting the system of

equations (B.1), from which variables at the 1D-0D interface ($p_{art,i}^{n+1/2}$ and $p_{lv}^{n+1/2}$) are extracted.

3. $\mathbf{V_{b,1D}}^{n+1/2}$ and $\mathbf{V_{b,0D}}^{n+1/2}$ are determined from the variables provided by the 0D model ($p_{art,i}^{n+1/2}$ and $p_{lv}^{n+1/2}$), α^n and $\mathbf{V_{b,1D}}^n$ by solving the boundary conditions between the 1D and 0D models. The latter are the ones at the entrance to the aorta through system (B.2) and at distal arteries through system (B.3). Notice that in this phase boundary conditions at arterial bifurcations (A.5) are also solved.

4. Points 1., 2. and 3. are repeated in the same order but with different input variables. In fact, the 1D model is solved with α^n, $\alpha^{n+1/2}$ and $\mathbf{V_{b,1D}}^{n+1/2}$, the 0D model with $\mathbf{V_{0D}}^n$, $\mathbf{V_{0D}}^{n+1/2}$ and $\mathbf{V_{b,0D}}^{n+1/2}$, and the 1D boundary conditions with $p_{art,i}^{n+1}$, p_{lv}^{n+1}, α^n, $\alpha^{n+1/2}$ and $\mathbf{V_{b,1D}}^{n+1/2}$. It is important to notice that, when solving the second time step, the 1D model also requires α^n (see equation (3.66)), the 0D model also requires $\mathbf{V_{0D}}^n$ (see equation (3.102)), and the boundary conditions also require α^n (see equations (3.91) and (3.92)).

5. Variables at step n-th are replaced by the same variables at step $(n+1)$-th and points 1., 2., 3. and 4. are performed again.

3.4 Multiscale model of the coronary circulation

Left and right coronary circulations originate from the aortic root and include 9 and 5 large-medium arteries, respectively. The latter form the networks shown in Figure 3.13, with the relative legend in Table 3.3 and the corresponding geometrical and mechanical properties in Table A.2.

Each terminal coronary artery ($k = 52 \div 57{,}59{,}61 \div 62$) is closed by a proper microvascular distal district, schematically represented in Figure 3.14, as proposed by Mynard et al. [226, 227]. This district is identified at the entrance by the characteristic impedance, Z_{ca}, and compliance, C_{ca}, of the corresponding coronary artery and contains j transmural layers: the subepicardium, SEP ($j = 1$), the midwall, MW ($j = 2$), and the subendocardium, SEN ($j = 3$). Each layer is forced by an intramyocardial pressure, p_j^{im}, and is divided into two compartments, the arterial one ($i = 1$) and the venous one ($i = 3$), with each compartment containing one resistance, R, and one compliance, C. In particular, R_{1j} and C_{1j} are the arterial resistances and compliances, while R_{3j} and C_{3j} are the venous resistances and compliances. An intermediate resistance, $R_2 j$, links the arterial and venous compartments. Characteristic impedances and compliances are constant in time, while all resistances are time-dependent, based on the instantaneous volume of each layer. The venous compartments of the microcirculation model converge into

a venula, which is characterized - as the entrance - by a specific impedance, Z_{cv}, and compliance, C_{pv}. Pressure at the outlet, p_{out}, is set at 5 mmHg.

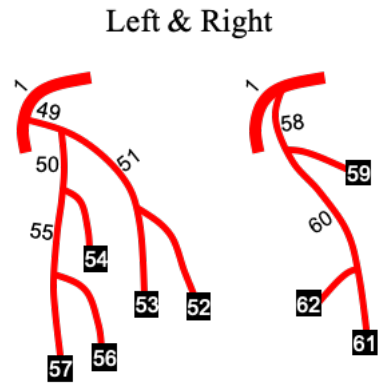

Figure 3.13: Representation of the modelled left and right coronary circulations. Terminal arteries are indicated in black squares.

Table 3.3: Names of the arteries numbered in Figure 3.13. LAD stands for Left Anterior Descending.

N right/left	**Arterial tract**
49	Left Main Coronary Artery
50	LAD Coronary Artery I
51	Circumflex Artery I
52	Marginal Artery
53	Circumflex Artery II
54	Diagonal Artery
55	LAD Coronary Artery II
56	Septal Artery
57	LAD Coronary Artery III
58	Right Coronary Artery I
59	Acute Marginal Artery I
60	Right Coronary Artery II
61	Acute Marginal Artery II
62	Right Coronary Artery III

All the parameters representing the k-th microvascular distal district are detailed in the following, as first proposed by Mynard et al. [226, 227] and in accordance with other authors [107, 290].

3.4.1 Intramyocardial compliances and unstressed volumes

Arterial, $C_{1j,k}$, and venous, $C_{3j,k}$, compliances of the k-th terminal coronary artery are evaluated based on the total arterial, $C_{1,T} = 0.026$ ml/(mmHg*hg), and venous, $C_{3,T} = 0.127$ ml/(mmHg*hg), compliances of all the coronaries (from Mynard et al. [226, 227]), respectively, the weight of the myocardial region the k-th terminal coronary artery contributes to feed, and the terminal radii of all the arteries feeding the same region.

Exploiting Murray's law[2], myocardial weights and conductances (the inverse of resistances) can be divided among the different myocardial regions proportionally to the inverse cube of the 1D penetrating artery radii [226, 227]. Based on this,

[2]Murray's law states that the cube of the radius of a parent vessel should be equal to the cubes of the radii of the daughter vessels [300].

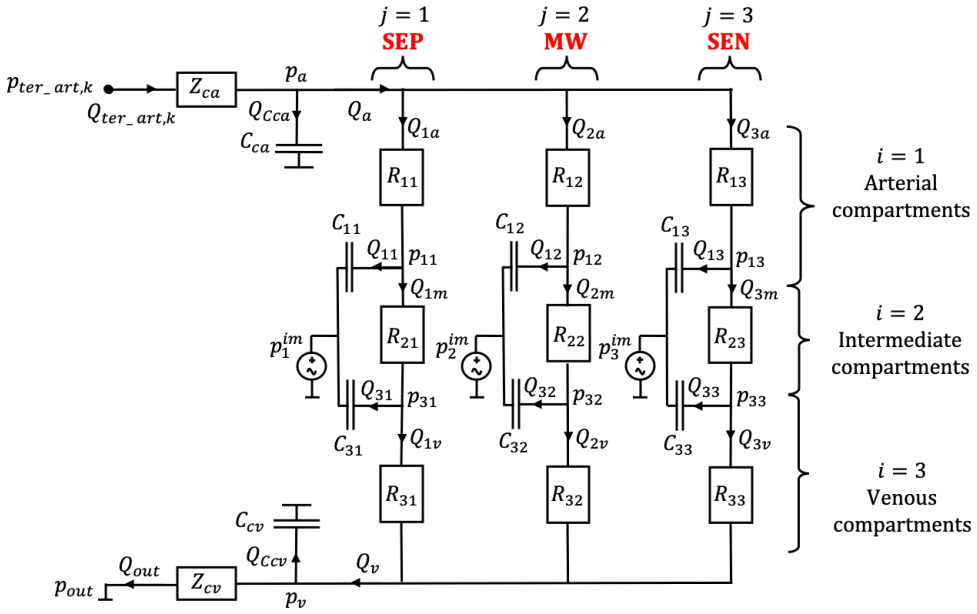

Figure 3.14: Representation of the microvascular distal district closing the k-th terminal coronary artery. It is presented in the above section and detailed below.

we impose that the portion of the myocardium weight fed by the k-th terminal coronary artery, w_k, is proportional to the cube of its radius, $r_{v,k}$, as

$$w_k = M_w r_{v,k}^3, \tag{3.103}$$

with M_w a constant [290]. Since left ventricle ($w_{LV} = 1.04$ kg [189]), septum ($w_S = 0.54$ kg [189]) and right ventricle ($w_{RV} = 0.46$ kg [189]) are fed by the groups of vessels $G_{LV} = \{52 \div 54,57\}$, $G_S = \{56,62\}$ and $G_{RV} = \{59,61\}$, respectively, one obtains different constants M_w for the distal coronaries associated to the left ventricle ($M_{w,LV}$), septum ($M_{w,S}$) and right ventricle ($M_{w,RV}$). Namely,

$$M_{w,LV} = w_{LV}\left(\sum_{G_{LV}} r_{v,k}^3\right)^{-1}, M_{w,S} = w_S\left(\sum_{G_S} r_{v,k}^3\right)^{-1}, M_{w,RV} = w_{RV}\left(\sum_{G_{RV}} r_{v,k}^3\right)^{-1}. \tag{3.104}$$

Thus, we get the total arterial and venous compliances of the k-th terminal coronary artery ($C_{1,k}$ and $C_{3,k}$, respectively) as

$$\begin{cases} C_{1,k} = C_{1,T} M_{w,LV/S/RV} r_{v,k}^3, \\ C_{3,k} = C_{3,T} M_{w,LV/S/RV} r_{v,k}^3, \end{cases} \tag{3.105}$$

where M_w assumes different values based on the region the k-th terminal coronary artery belongs to ($M_{w,LV}$ for the left ventricle, $M_{w,S}$ for the septum and $M_{w,RV}$ for the right ventricle) [290]. $C_{1,k}$ and $C_{3,k}$ are then distributed to the layers of the k-th microvascular compartments imposing a subendocardial-to-subepicardial ratio, $\gamma_{C,j}$, of 1.14 [226, 227]. Hence, $C_{1j,k}$ and $C_{3j,k}$ are

$$\begin{cases} C_{1j,k} = C_{1,k} \gamma_{C,j}, \\ C_{3j,k} = C_{3,k} \gamma_{C,j}. \end{cases} \tag{3.106}$$

Similarly, the unstressed volumes, $V_{0,1/3j,k}$, of the k-th terminal coronary artery are determined as

$$\begin{cases} V_{0,1j,k} = V_{0,1,T} M_{w,LV/S/RV} r_{v,k}^3 \gamma_{V_0,j}, \\ V_{0,3j,k} = V_{0,3,T} M_{w,LV/S/RV} r_{v,k}^3 \gamma_{V_0,j}, \end{cases} \tag{3.107}$$

where $V_{0,1,T} = 25$ ml and $V_{0,3,T} = 8$ ml are the total arterial and venous unstressed volumes of all the coronaries, respectively, and $\gamma_{V_0,j} = \gamma_{C,j}$ [226, 227].

3.4.2 Intramyocardial resistances

Intramyocardial arterial, $R_{1j,k}$, and venous, $R_{3j,k}$, resistances of the k-th terminal coronary artery vary with time through the instantaneous intramyocardial stressed volumes of the arterial, $V_{1j,k}(t)$, and venous, $V_{3j,k}(t)$, compartments, respectively, in accordance to the Poiseuille's law [226, 227]. Namely,

$$\begin{aligned} R_{1j,k} &= R_{0,1j,k} \left[\frac{V_{0,1j,k}}{V_{1j,k}(t)} \right]^2, \\ R_{3j,k} &= R_{0,3j,k} \left[\frac{V_{0,3j,k}}{V_{3j,k}(t)} \right]^2, \end{aligned} \tag{3.108}$$

where $R_{0,1j,k}$ and $R_{0,3j,k}$ are the reference resistances of the arterial and venous compartments. Middle resistances ($R_{2j,k}$), instead, are supposed to depend on the volumes of both the arterial and venous compartments as

$$R_{2j,k} = R_{0,2j,k} \left[0.75 \frac{V_{0,1j,k}^2}{V_{1j,k}(t)^2} + 0.25 \frac{V_{0,3j,k}^2}{V_{3j,k}(t)^2} \right], \tag{3.109}$$

with $R_{0,2j,k}$ the reference resistances of the middle compartment [226, 227]. In these expressions, instantaneous volumes, $V_{1/3j,k}(t)$, are calculated in accordance to Mynard et al. [226, 227]:

$$V_{1/3j,k}(t) = V_{0,1/3j,k} + \int_0^t C_{1/3j,k} \frac{\mathrm{d}}{\mathrm{d}t}(p_{1/3j,k}(t) - p_j^{im}(t))\mathrm{d}t, \tag{3.110}$$

where compliances, $C_{1/3j,k}$, and unstressed volumes, $V_{0,1/3j,k}$, are chosen as explained in section 3.4.1, while intramyocardial pressures, p_j^{im}, will be defined in section 3.4.4.

Reference resistances of the j-th layer for the k-th terminal coronary artery feeding a given myocardial region ($R_{0,1j,k}$, $R_{0,2j,k}$ and $R_{0,3j,k}$) depend on the terminal radii of all the arteries associated to the same myocardial region, and the total resistance of the j-th layer for the chosen myocardial region (left ventricle/septum/right ventricle), $R_{j,T,LV/S/RV}$. In fact, the sum of the reference resistances of the j-th layer for the k-th terminal coronary artery, $\sum_{i=1}^{3} R_{0,ij,k} = R_{s,j,k}$, is taken inversely proportional to the cube of $r_{v,k}$ (i.e., conductance $1/R_{s,j,k}$ is proportional to the cube of $r_{v,k}$, exploiting Murray's law, as done for myocardial weights in section 3.4.1) [290]. Namely,

$$R_{s,j,k} = \frac{M_R}{r_{v,k}^3}, \tag{3.111}$$

with M_R a constant of the chosen layer. Since $\sum_{G_{LV/S/RV}} R_{s,j,k} = R_{j,T,LV/S/RV}$, M_R is calculated for the vessels belonging to the groups G_{LV} ($M_{R,LV}$), G_S ($M_{R,S}$) and G_{RV} ($M_{R,RV}$) as

$$M_{R,LV} = \frac{R_{j,T,LV}}{\sum_{G_{LV}} r_{v,k}^{-3}}, \quad M_{R,S} = \frac{R_{j,T,S}}{\sum_{G_S} r_{v,k}^{-3}}, \quad M_{R,RV} = \frac{R_{j,T,RV}}{\sum_{G_{RV}} r_{v,k}^{-3}}, \tag{3.112}$$

with $R_{T,LV} = [2631.1, 1117.1, 500.1]$ mmHg/ml, $R_{T,S} = [2421.2, 931.6, 457.8]$ mmHg/ml and $R_{T,RV} = [2903.2, 2363.8, 2029.7]$ mmHg/ml, from the subepicardium ($j = 1$) to the subendocardium ($j = 3$), based on the parameters by Mynard et al. [226, 227] with modifications. Thus, $R_{s,j,k}$ are obtained as

$$R_{s,j,k} = \frac{M_{R,LV/S/RV}}{r_{v,k}^3}. \tag{3.113}$$

Reference resistances are expressed as functions of $R_{s,j,k}$, by imposing the following conditions [226, 227]:

$$\begin{cases} R_{0,1j,k} = 1.2R_{0,2j,k}, \\ R_{0,3j,k} = 0.5R_{0,2j,k}, \\ R_{s,j,k} = R_{0,1j,k} + R_{0,2j,k} + R_{0,3j,k}. \end{cases} \tag{3.114}$$

Hence, one gets

$$\begin{cases} R_{0,2j,k} = \dfrac{R_{s,j,k}}{2.7}, \\ R_{0,1j,k} = 1.2R_{0,2j,k}, \\ R_{0,3j,k} = 0.5R_{0,2j,k}. \end{cases} \tag{3.115}$$

3.4.3 Impedances and compliances at the inlet and outlet

$Z_{ca,k}$, calculated through equation (A.1), corresponds to the characteristic impedances of the k-th terminal coronary artery. For all terminal coronary arteries, Z_{ca} values are reported in Table A.1. $Z_{cv,k}$ is determined as $Z_{ca,k}$, assuming a radius 40% higher than the one used for $Z_{ca,k}$ [290]:

$$Z_{cv,k} = \frac{Z_{ca,k}}{1.4^2}. \tag{3.116}$$

$C_{ca,k}$ and $C_{cv,k}$ are calculated as

$$\begin{aligned} C_{ca,k} &= \frac{1}{10} C_{1,k}, \\ C_{cv,k} &= \frac{1}{10} C_{3,k}, \end{aligned} \tag{3.117}$$

where $C_{1j,k}$ and $C_{2j,k}$, defined in the (3.106), are the arterial and venous compliances of the k-th terminal coronary artery [226, 227].

3.4.4 Intramyocardial pressure

Intramyocardial pressures, p_j^{im}, are due to the sum of two contributions, the cavity-induced extracellular pressure, CEP, and the shortening-induced intracellular pressure, SIP. For the left/right ventricle, CEP was confirmed to be approximately equal to p_{lv}/p_{rv} in the subendocardium, linearly decreasing up to the subepicardium [226, 227]. Accordingly, CEP is calculated as

$$CEP = p_{lv}/p_{rv}\gamma_{CEP,j}, \tag{3.118}$$

for the left/right ventricle, with $\gamma_{CEP} = [0.2, 0.6, 1]$ (from the subepicardium to the subendocardium). Based on [226, 227], CEP is instead distributed between p_{rv} (on the subepicardium) and p_{lv} (on the subendocardium) for the ventricular septum. For the left ventricle and septum/right ventricle, SIP was found to have the same shape of the left/right-ventricular elastance function [226, 227]. Thus, it is approximated as

$$SIP = \phi_{SIP}E_{lv}/E_{rv}, \tag{3.119}$$

with $\phi_{SIP} = 8.9$ ml. The latter parameter is chosen in order to have, as expected [226, 227], peak p_j^{im} equal to 20% of peak p_{lv} in the subendocardium.

3.4.5 Resolution of large-medium coronary arteries

Large-medium coronary arteries are solved as the systemic arterial tree, by imposing the conservation of mass and momentum balance equations (see section 3.1). Terminal coronary arteries are resolved as distal arteries of the arterial tree, by combining a physical boundary condition and a compatibility condition. The physical boundary condition derives from the constitutive equation of the characteristic impedance, $Z_{ca,k}$, closing the k-th terminal coronary artery

$$Q_{ter\_art,k} = \frac{p_{ter\_art,k} - p_{a,k}}{Z_{ca,k}}, \tag{3.120}$$

with $Q_{ter\_art,k}$ and $p_{ter\_art,k}$ the flow rate and pressure at the outlet of the k-th terminal coronary artery, and $p_{a,k}$ the arterial pressure of the k-th microvascular distal district (see Figure 3.14). The compatibility condition here adopted is the one used for each right boundary (equation (3.92)). The complete resolution of the k-th terminal coronary artery is given in the (B.4). Notice that the boundary conditions of all the terminal coronary arteries are resolved in parallel with the ones of the other distal 1D arteries.

3.4.6 Resolution of coronary microvascular distal districts

The microvascular distal district of each terminal coronary artery (whose circuit is shown in Figure 3.14) is mathematically represented through a system of ordinary differential equations, which arises from the combination of the constitutive

equations for resistances, compliances and characteristic impedances, together with the application of the Kirchhoff law at the circuital nodes [290]. The constitutive equations for resistances, compliances and characteristic impedances are

$$\begin{cases} Q_{ja} = \dfrac{p_a - p_{1j}}{R_{1j}}, \quad j = 1 \div 3, \\ Q_{jm} = \dfrac{p_{1j} - p_{3j}}{R_{2j}}, \quad j = 1 \div 3, \\ Q_{jv} = \dfrac{p_{3j} - p_v}{R_{3j}}, \quad j = 1 \div 3, \\ Q_{C_{ca}} = C_{ca} \dfrac{\mathrm{d}p_a}{\mathrm{d}t}, \\ Q_{1j} = C_{1j} \dfrac{\mathrm{d}(p_{1j} - p_j^{im})}{\mathrm{d}t}, \quad j = 1 \div 3, \\ Q_{3j} = C_{3j} \dfrac{\mathrm{d}(p_{3j} - p_j^{im})}{\mathrm{d}t}, \quad j = 1 \div 3, \\ Q_{C_{cv}} = C_{cv} \dfrac{\mathrm{d}p_v}{\mathrm{d}t}, \\ Q_{out} = \dfrac{p_v - p_{out}}{Z_{cv}}, \end{cases} \tag{3.121}$$

excluding the one at Z_{ca}, already used to solve the boundary condition for the relative terminal coronary artery. The equations deriving from the applications of the Kirchhoff law at the circuital nodes are

$$\begin{cases} Q_{ter\_art,k} = Q_{C_{ca}} + Q_a, \\ Q_v = Q_{C_{cv}} + Q_{out}, \\ Q_a = \displaystyle\sum_{j=1}^{3} Q_{ja}, \\ Q_v = \displaystyle\sum_{j=1}^{3} Q_{jv}, \\ Q_{ja} = Q_{1j} + Q_{jm}, \\ Q_{jm} = Q_{3j} + Q_{jv}. \end{cases} \tag{3.122}$$

Combining systems (3.121) and (3.122), one obtains a single system of ordinary differential equations, that is

$$\begin{cases} C_{ca}\dfrac{\mathrm{d}p_a}{\mathrm{d}t} = Q_{ter\_art,k} - \displaystyle\sum_{j=1}^{3}\frac{pa - p_{1j}}{R_{1j}}, \\ C_{1j}\dfrac{\mathrm{d}p_{1j}}{\mathrm{d}t} = \dfrac{p_a - p_{1j}}{R_{1j}} - \dfrac{p_{1j} - p_{3j}}{R_{2j}} + C_{1j}\dfrac{\mathrm{d}p_j^{im}}{\mathrm{d}t}, \quad j = 1 \div 3, \\ C_{3j}\dfrac{\mathrm{d}p_{3j}}{\mathrm{d}t} = \dfrac{p_{1j} - p_{3j}}{R_{2j}} - \dfrac{p_{3j} - p_v}{R_{3j}} + C_{3j}\dfrac{\mathrm{d}p_j^{im}}{\mathrm{d}t}, \quad j = 1 \div 3, \\ C_{cv}\dfrac{\mathrm{d}p_v}{\mathrm{d}t} = -\dfrac{p_v - p_{out}}{Z_{cv}} + \displaystyle\sum_{j=1}^{3}\frac{p_{3j} - p_v}{R_{3j}}. \end{cases} \tag{3.123}$$

It includes 8 equations for 8 different unknowns (p_a, p_{11}, p_{12}, p_{13}, p_{31}, p_{32}, p_{33}, p_v), with $Q_{ter\_art,k}$ provided by the resolution of the boundary condition at the k-th terminal coronary artery (B.3). This system is solved with a two-steps Runge-Kutta explicit scheme, in parallel with the resolution of the other 0D compartments. Notice that to couple the 1D coronary arteries with the 0D microvascular distal districts, one follows the same technique exposed in section 3.3, with some changes in the vectors $\mathbf{V_{b,1D}}$, $\mathbf{V_{0D}}$ and $\mathbf{V_{b,0D}}$, in the variables provided by the 0D to the boundary resolution (indicated in green in Figure 3.12), and in the equations representing the 0D modelling and the boundary conditions. For the multiscale model of the coronary circulation, vector $\mathbf{V_{b,1D}}$ is replaced by vector $\mathbf{V_{b,1Dc}} = [Q_{ter\_art,k}, A_{ter\_art,k}]$, vector $\mathbf{V_{0D}}$ is replaced by the array of vectors $\mathbf{V_{0Dkc}} = [p_{a,k}, p_{11,k}, p_{12,k}, p_{13,k}, p_{31,k}, p_{32,k}, p_{33,k}, p_{v,k}]$ (there are as many vectors $[p_a, p_{11}, p_{12}, p_{13}, p_{31}, p_{32}, p_{33}, p_v]$ as terminal coronary arteries), vector $\mathbf{V_{b,0D}}$ is replaced by vector $\mathbf{V_{b,0Dc}} = [Q_{ter\_art,k}]$, and the variables provided by the 0D to the boundaries are replaced by $p_{a,k}$. In addition, the equations representing the 0D modelling and the boundary conditions are (3.123) and (3.120), respectively. Based on these changes, the coupling between the 1D and 0D counterparts in the multiscale model of the coronary circulation when solving the $(n+1)$-th ΔT is shown in Figure 3.15.

Notice that, when the coronary model is simulated together with the remaining 1D-0D model, p_{out} is imposed equal to the pressure within the right atrium, p_{ra}, and the sum of the flow rates from all the terminal coronary arteries, $\sum_k Q_{out,k} = \sum_k \frac{p_{v,k} - p_{ra}}{Z_{cv,k}}$, is added to the flow rates entering the right atrium (see system (B.1)).

3.5 Model of the baroreflex system

A short-term regulation of the arterial pressure is guaranteed by the baroreflex model presented by Ottesen et al [256] and schematically shown in Figure 3.16.

At the end of each heartbeat, the mean aortic-carotid sinus pressure ($\bar{p}_{acs}$) is

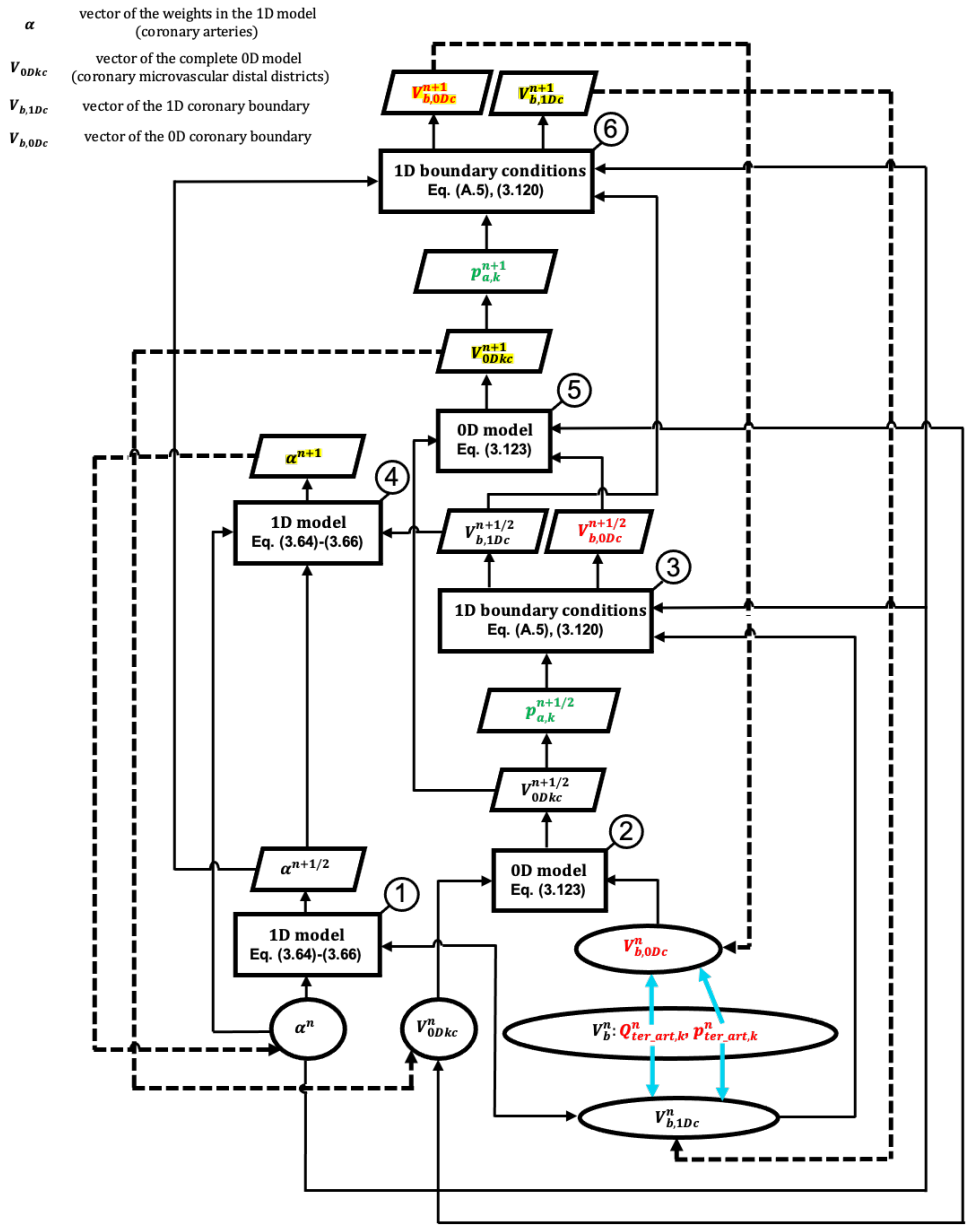

Figure 3.15: Scheme representing the chronological sequence of operations to follow at each n-th ΔT (cycle) in order to couple the 0D and 1D modelling portions in the multiscale model of the coronary circulation. Variables in red (green) are the ones provided by the boundary resolution (0D model) to the 0D (boundary resolution) model. Initial variables are enclosed in circles, while variables at the end of the cycle are highlighted.

evaluated as the arithmetic average of the aortic (p_{aor}), right- ($p_{cs,dx}$) and left-carotid sinus ($p_{cs,sx}$) pressures, each averaged over the previous heartbeat duration

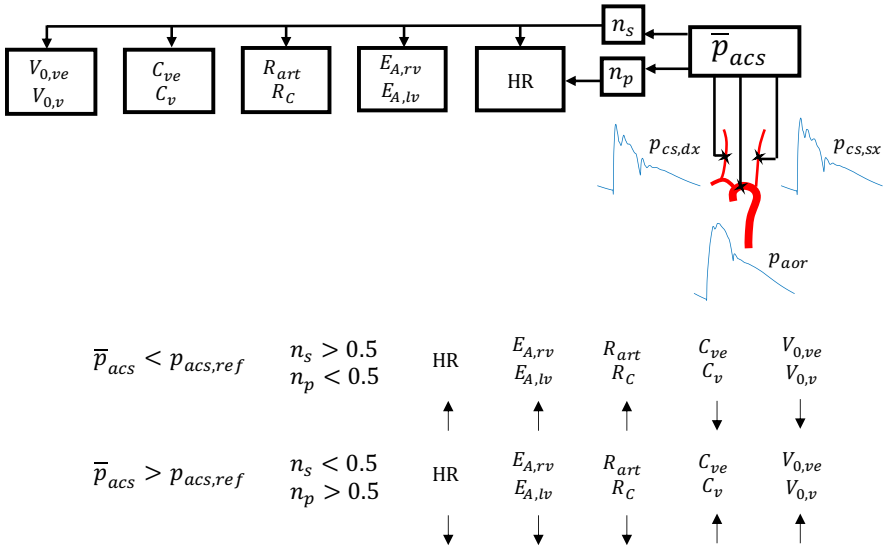

Figure 3.16: Scheme representing the functioning of the baroreflex system. p_{aor}, $p_{cs,dx}$ and $p_{cs,sx}$ are the aortic, right- and left-carotid sinus pressures, $\bar{p}_{acs}$ is the mean aortic-carotid sinus pressure, $p_{acs,ref}$ is the reference $\bar{p}_{acs}$, n_s and n_p are the sympathetic and parasympathetic activities, HR is the heart rate, $E_{A,lv/rv}$ are the amplitude values of left- and right- ventricular elastance, $R_{art/c}$ are the arteriolar and capillary resistances, and $C_{ve/v}$ and $V_{0,ve/v}$ are the compliances and unstressed volumes of venules and veins.

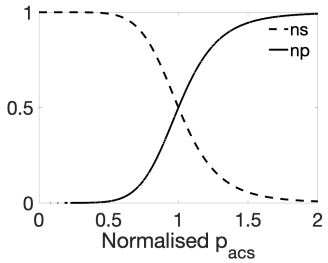

Figure 3.17: Representation of the functions n_s and n_p in the range 0-2 of the normalised aortic-carotid sinus pressure.

(RR_{-1}), as suggested by [31]. Namely,

$$\bar{p}_{acs} = \frac{1}{3RR_{-1}} \left(\int_{RR_{-1}} p_{aor}(t)\mathrm{d}t + \int_{RR_{-1}} p_{cs,dx}(t)\mathrm{d}t + \int_{RR_{-1}} p_{cs,sx}(t)\mathrm{d}t \right). \quad (3.124)$$

Sympathetic, n_s, and parasympathetic, n_p, activities are calculated as sigmoid functions:

$$n_s(\bar{p}_{acs}) = \frac{1}{1+\left(\frac{\bar{p}_{acs}}{p_{acs,ref}}\right)^{\nu_b}}, \qquad n_p(\bar{p}_{acs}) = \frac{1}{1+\left(\frac{\bar{p}_{acs}}{p_{acs,ref}}\right)^{-\nu_b}}, \tag{3.125}$$

with $\nu_b = 7$ [256] determining the steepness of the sympathetic and parasympathetic signals and $p_{acs,ref} = 93$ mmHg equal to the reference aortic-carotid sinus pressure. The shapes of n_s and n_p are given in Figure 3.17.

Reactions of the efferent organs are advanced in time through the ordinary differential equation

$$\frac{\mathrm{d}x_m}{\mathrm{d}t} = \frac{1}{\tau_m}\left(-x_m + \alpha_m n_s(\bar{p}_{acs}) - \beta_m n_p(\bar{p}_{acs}) + \gamma_m\right), \tag{3.126}$$

with x_m the m-th efferent organ, τ_m the time it takes for the efferent response to fully act, α_m and β_m the weights of the sympathetic and parasympathetic activities, and γ_m equal to x_m when n_s=n_p ($\bar{p}_{acs} = p_{acs,ref}$) [256]. Efferent organs are the heart rate (HR), the amplitude values of left- and right-ventricular elastances ($E_{A,lv/rv}$), arteriolar and capillary resistances ($R_{art/c}$), compliances and unstressed volumes of venules and veins ($C_{ve/v}$ and $V_{0,ve/v}$). Parameters of the baroreflex model are reported in Table B.4 according to [256].

Notice that the sum $n_s + n_p$ is always one and $n_s = n_p = 0.5$ when the homoeostasis is reached. Two disequilibrium conditions are possible for the baroreflex system: when $\bar{p}_{acs} < p_{acs,ref}$ and when $\bar{p}_{acs} > p_{acs,ref}$. In the first case, baroreceptors react with an increase in n_s and a decrease in n_p, which lead to a rise in HR, $E_{A,rv/lv}$ and $R_{art/c}$ and a reduction in $C_{ve/v}$ and $V_{0,ve/v}$. In the second case, instead, beroreceptors produce a decrease in n_s and an increase in n_p, causing a fall in HR, $E_{A,rv/lv}$ and $R_{art/c}$ and a rise in $C_{ve/v}$ and $V_{0,ve/v}$.

3.6 The global model

The global model presented so far in chapter 3 is schematically shown in Figure 3.18. As one can see from the top panels of the latter, it includes the 1D model of the systemic arteries, the structure of the 0D systemic/cardiac/pulmonary compartments, the 0D-1D interface (the characteristic impedances of distal 1D arteries and the aortic valve, AV), the 0D-1D coronary model, and the baroreflex model. The circuital components of the 0D systemic/cardiac/pulmonary compartments are shown in the bottom panels, while the complete legend is provided in Table 3.2.

The global model has been implemented in MATLAB, starting from the model of the systemic arterial tree developed by Guala et al. [108] with modifications. Time step is equal to 10^{-4} s, and convergence is reached after about 10 beats, as the baroreflex action is not active, and 20 beats, as the baroreflex action is active.

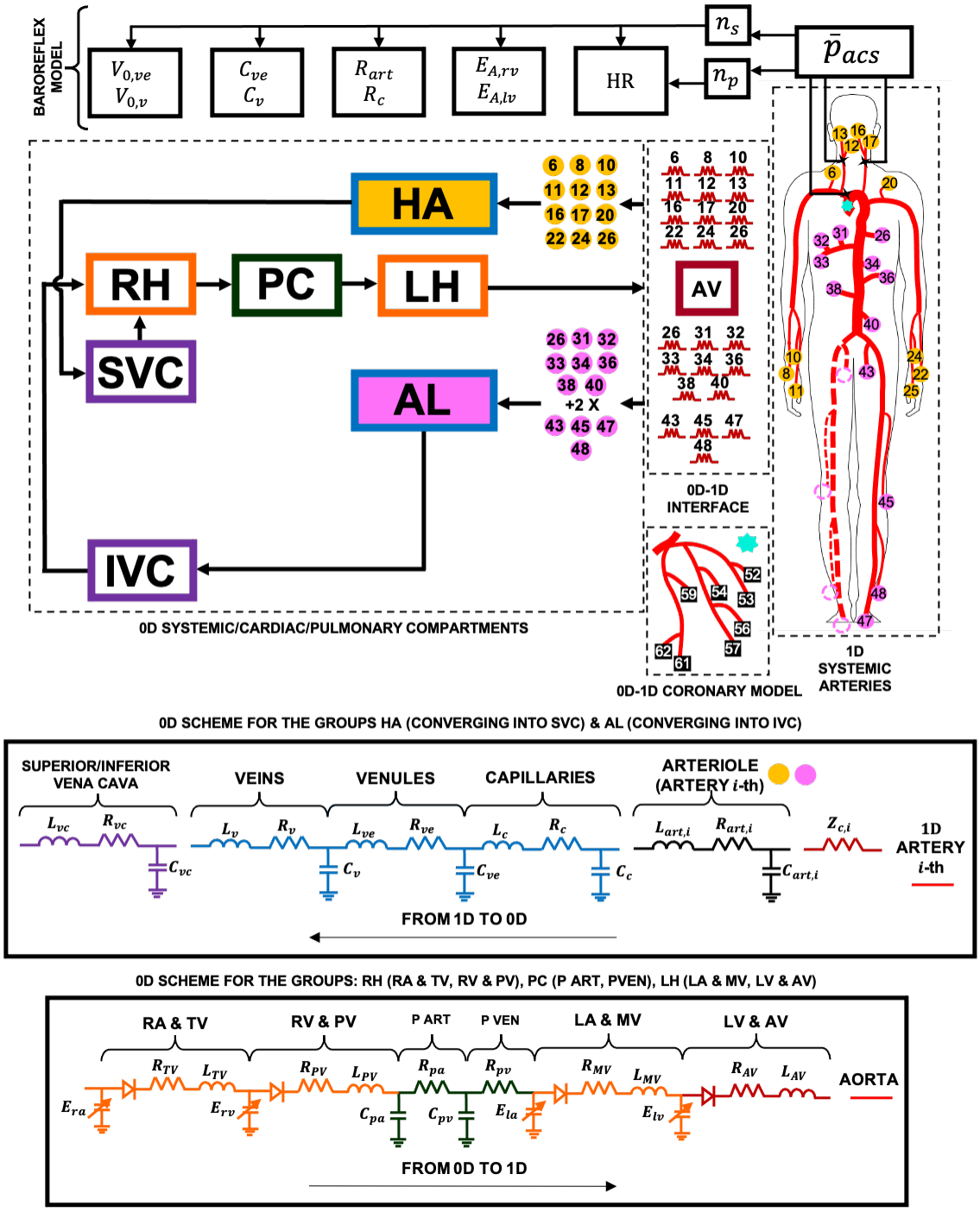

Figure 3.18: Representation of the complete closed-loop multiscale model of the cardiovascular system. Legend is provided in Table 3.2.

Chapter 4

Reliability of the global model

Some of the contents of this chapter have been previously published in [91].

The reliability of the closed-loop multiscale mathematical model presented in the previous chapter is proved in the following sections, where the computational haemodynamic signals and cardiovascular parameters throughout the model domain are compared with the corresponding measurements available in literature. In order to test a benchmark case, the geometry and mechanical properties associated to a generic healthy and young man are considered. Computer simulations are here run at a constant heart rate of 75 bpm, corresponding to a heartbeat duration of 0.8 s. Results provided by (i) the 1D model of the systemic arterial tree, (ii) the 0D model of the systemic microcirculation and venous return, and (iii) the 0D model of the heart and pulmonary circulation, together with the multiscale model of the coronary circulation, are given in sections 4.1, 4.2 and 4.3, respectively. The efficacy of the short-term baroreflex mechanism, also integrated in the multiscale framework, is demonstrated in section 4.4, where the heart pacing and open loop aortic-carotid sinus control are tested.

4.1 The systemic arterial tree

Figure 4.1 depicts pressure and flow rate signals at different sites along the systemic arterial tree, which are reproduced through the 1D model in section 3.1. These results allow one to recognize some key haemodynamic aspects already analysed in chapter 1.

- The shapes of pressure and flow rate signals at the ascending aorta (Figure 4.1A) follow the expected patterns (see Figures 1.6 and 1.11), with the typical dicrotic notch in pressure and backflow in flow rate occurring with the closure of the aortic valve [110].

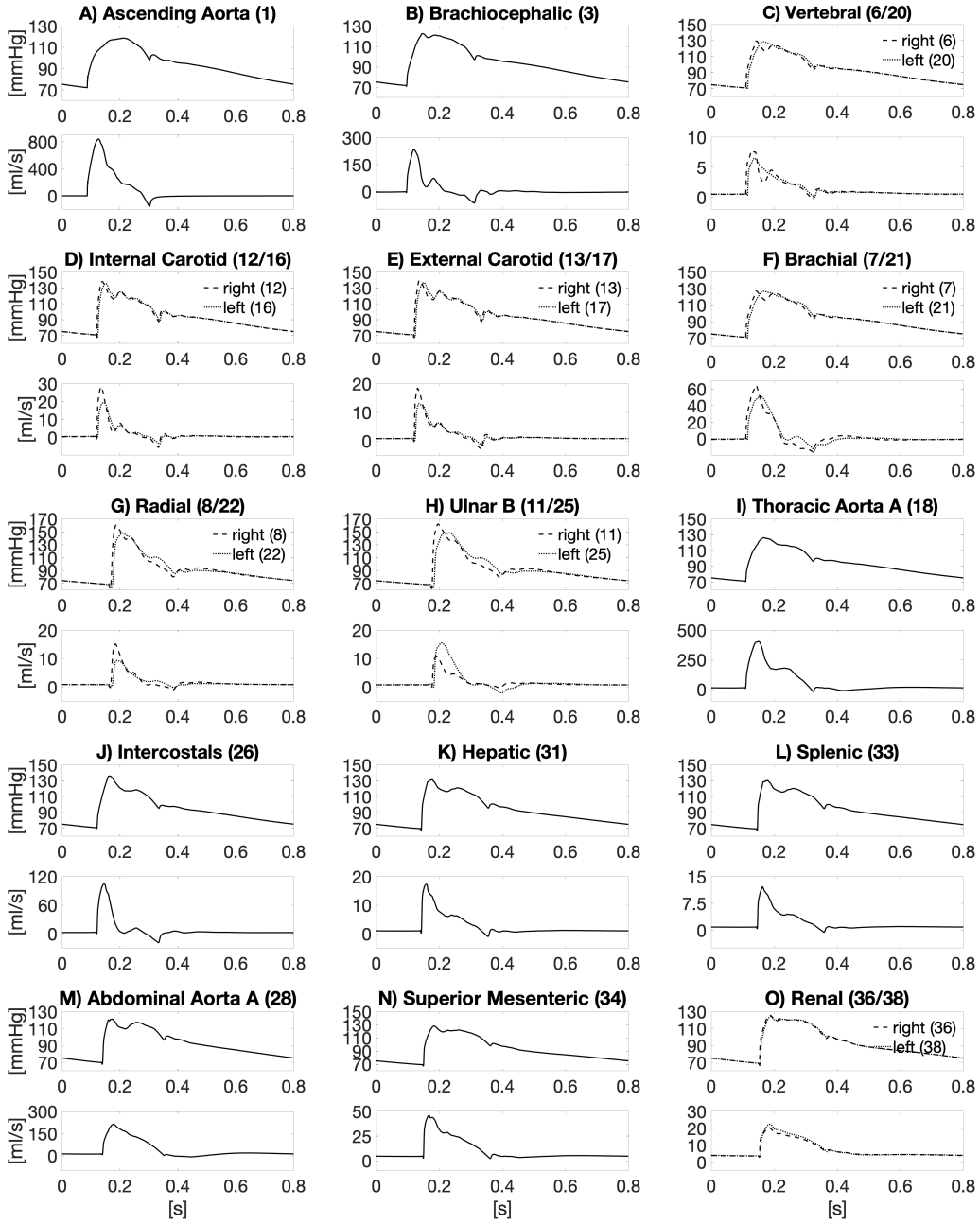

Figure 4.1: Pressure and flow rate signals at different sites along the systemic arteries for a healthy and young man with a heartbeat period of 0.8 s (HR=75 bpm). Each artery is associated to its number in brackets according to Figure 3.1. This figure continues on the next page.

- Moving from the ascending aorta to the periphery, the amplitude of both

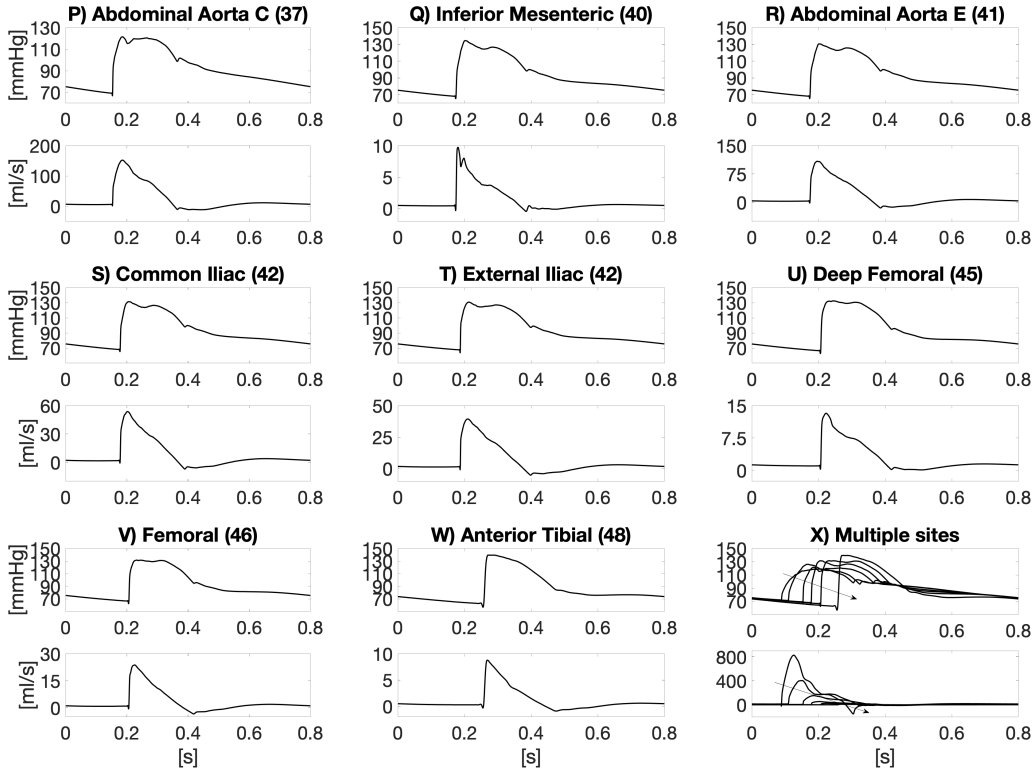

Figure 4.1: This figure begins on the previous page. Pressure and flow rate signals at different sites along the systemic arteries for a healthy and young man with a heartbeat period of 0.8 s (HR=75 bpm). Each artery is associated to its number in brackets according to Figure 3.1. The last panel on the left puts together the pressure and flow rate signals in panels A-I-P-S-V-W, with the arrows going in the direction of the more distant sites from the heart.

pressure and flow rate signals progressively increases and decreases, respectively. In addition, pressure signals steep and delay and flow rate signals loose the magnitude of the regurgitant flow [46] with the distance from the heart. These aspects are apparent in Figure 4.1 X, which puts together the simultaneous pressure and flow rate signals along the ascending aorta, thoracic aorta, abdominal aorta, common iliac, femoral and anterior tibial arteries. However, it is possible to notice from the latter figure that there is a fall in mean pressure between thoracic and abdominal arteries, since systolic pressure reduces instead of increasing. We have verified that this aspect depends on the choice of the arterial tree geometry. These results, in fact, have been obtained by adopting the arterial diameters and lengths proposed by Reymond et al. [279] (Table A.1), with slight adjustments in some diameters in order to minimize forward wave reflections at bifurcations [279]. If we used

the arterial diameters and lengths by Liang et al. [180] (in Table A.3) with all the other settings maintained, the mean pressure reduction between thoracic and abdominal areas would disappear. To this purpose, a comparison between the changes in the aortic pressure signals with the arterial diameters and lengths by Reymond et al. [279] and Liang et al. [180] is provided in Figure 4.2. Thus, it seems that the typical rise in systolic pressure from central to peripheral sites can be discontinuous throughout the aorta, depending on the arterial geometry, which in any case is patient-specific.

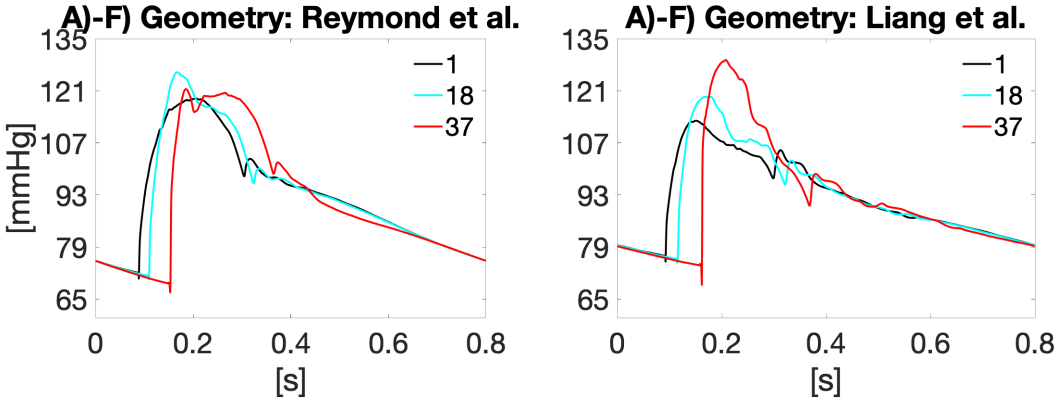

Figure 4.2: Computed pressure signals along the ascending aorta (vessel 1), thoracic aorta (vessel 18) and abdominal aorta (vessel 37) obtained by using the arterial diameters and lengths by Reymond et al. [279] (Table A.1), left panel, and by Liang et al. [180] (Table A.3), right panel.

For all simulated arteries, systolic (p_{sys}), diastolic (p_{dia}), mean ($p_{mean} = p_{dia} + (p_{sys} - p_{dia})/3$) pressures and mean flow rates (Q_{mean}) over the heartbeat duration by the 1D model are indicated in Table 4.1. Corresponding values from available measurements in literature are also reported in Table 4.1, providing a quantitative validation of computed arterial pressures and flow rates. The experimental conditions and the population data associated to the chosen references in literature are given in Table 4.2.

From Table 4.1, one observes how computed central pressure is between 118.66 and 72.07 mmHg, producing a pulse pressure of 46.59 mmHg and a mean pressure of 87.60 mmHg, which are within the expected ranges for a healthy young man in physiological conditions [110, 160, 223]. Pressures adequately evolve from central to peripheral sites, as demonstrated by the comparison in Figure 4.3 between systolic/diastolic pressures by the model and from invasive measurements in literature [160] along the brachial, radial and femoral arteries. Figure 4.3 also offers a comparison between model-generated mean flow rates and measured data reported in literature at the level of head, thorax, abdomen and legs. We find that model

Table 4.1: Systolic, p_{sys}, diastolic, p_{dia}, mean, p_{mean}, pressures and mean flow rates, Q_{mean}, by the model for HR=75 bpm (in black) and from available measurements in literature (in red with references in square brackets) along the systemic arterial tree. The experimental conditions and the population data of the chosen references are given in Table 4.2.

(N) **Arterial tract** (right/left)	p_{sys} [mmHg]	p_{dia} [mmHg]	p_{mean} [mmHg]	Q_{mean} [ml/s]
(1) Ascending Aorta	118.66	72.07	87.60	79.43
	113-146 [160, 223]	71-90 [160, 223]		
(2) Aortic Arch A	120.42	71.01	87.48	65.96
(3) Brachiocephalic	122.67	71	88.22	8.61
(4/19) Subclavian A	128.11/127.91	70.70/70.31	89.84/89.51	4.78/4.99
(5/15) Common Carotid	129.11/124.34	70.70/70.83	90.17/88.66	3.70/3.67
(6/20) Vertebral	129.57/128.74	69.73/69.73	89.67/89.41	1.35/1.34
				0.51-1.63 [250]
(7/21) Brachial	126.96/126.89	69.61/69.62	88.73/88.71	3.48/3.63
	114.13-172.28 [160]	63.9-90 [160]		
(8/22) Radial	160.17/147.45	65.87/66.32	94.72/91.37	1.84/1.66
	115.26-179.58 [160]	62.48-89.10 [160]		
(9/23) Ulnar A	161/144.49	61.77/63.15	94.85/90.26	1.64/1.97
(10/24) Interosseous	165.75/151.02	62.27/63.64	96.76/92.77	0.11/0.11
(11/25) Ulnar B	161.92/148.61	62.30/63.71	95.51/92.01	1.53/1.87
(12/16) Internal Carotid	137.93/135.79	67.31/68	90.85/90.59	1.77/1.73
				2.72-6.27 [250]
(13/17) External Carotid	139.41/136.74	67.26/67.94	91.31/90.87	1.94/1.87
(14) Aortic Arch B	121.56	70.85	87.75	62.32
(18) Thoracic Aorta A	125.98	70.33	88.88	57.39
				48.33-103.33 [383]
(26) Intercostals	136.01	69.73	91.83	7.93
(27) Thoracic aorta B	132.92	69.65	90.74	49.46
				38.33-58.33 [50]
(28) Abdominal aorta A	121.24	67.77	85.59	39.96
(29) Coeliac A	130.76	67.74	88.75	9.47
(30) Coeliac B	129.29	67.44	88.06	7
(31) Hepatic	131.43	67.56	88.85	2.45
(32) Gastric	126.28	66.35	86.33	5.16
(33) Splenic	130.40	67.07	88.18	1.85
(34) Superior Mesenteric	128.06	67.32	87.57	9.76
				5.83-13.33 [215, 314, 332]
(35) Abdominal Aorta B	121.12	67.33	85.26	30.28
(36/38) Renal	125.74/124.37	66.62/66.24	86.32/85.62	7.06/7.36
				5.17-11.87 [61, 72]
(37) Abdominal Aorta C	121.46	66.73	84.97	23.23
(39) Abdominal Aorta D	122.78	66.32	85.14	15.88
				8.33-21.67 [50]
(40) Inferior Mesenteric	134.50	65.36	88.40	1.26
(41) Abdominal Aorta E	130.59	65.44	87.16	14.56
(42) Common Iliac	131.41	65.17	87.25	7.30
(43) Inner Iliac	132.87	63.71	86.76	1.72
(44) External Iliac	130.72	63.51	85.91	5.57
				4.9-11 [149, 182]
(45) Deep Femoral	132.41	62.49	85.80	2.52
(46) Femoral	131.48	64.62	85.32	3.05
	117.52-173.74 [160]	63.90-87.30 [160]		1.85-5.22 [182]
(47) Anterior Tibial	138.76	56.48	83.91	2.03
(48) Posterior Tibial	139.54	56.60	84.25	1.01

Table 4.2: Experimental condition and population data of the references adopted in Table 4.1 and indicated in Figure 4.3. M/W: Men/Women, HR: heart rate, BSA: body surface area, BMI: body mass index, B-M: B-Mode, C: Catheterisation, C D: Color Doppler, C-M: Catheter-Manometer, E D: Echo Doppler, MR PC: MR phase-contrast imaging, P D: Pulse Doppler.

References (year)	**Technique**	**M/W**	HR [bpm]	Age [years]	BSA [m^2]	BMI [kg/m^2]
[CH]Cheng et al. [50] (2003)	MR PC	6/5	73±6.2	20-28	NA	NA
[CO]Cox et al. [61] (2017)	MR PC	33/0	NA	25±4	NA	23±2
[E]Eckerbom et al. [72] (2019)	MR PC	13/0	NA	24.5±6.9	1.89±0.19	22.6±2.5
[KL]Klein et al. [149] (2003)	MR PC	25/0	NA	26-80	NA	NA
[KR]Kroeker et al. [160] (1955)	C-M	12/0	64±8	32±5.27	1.98±0.12	NA
[L]Liang et al. [182] (2020)	C D	60/0	NA	NA	NA	NA
[MO]Moneta et al. [215] (1988)	B-M+P D	5/2	NA	28-38	NA	NA
[MU]Murgo et al. [223] (1980)	C	5/2	69±3	40±4	1.97±0.03	NA
[O]Oktar et al. [250] (2006)	C D	9/21	NA	33.67±7.98	NA	NA
[S]Someya et al. [314] (2008)	P D+E D	7/6	57±2	24±1	NA	≃20.68
[S]Someya et al. [332] (2008)	P D+E D	7/6	57±2	24±1	NA	≃20.68
[T]Takayama et al. [383] (1965)	Ultrasound+P D	24/0	59.6±9.31	31.2±6.9	NA	NA
[Z] Zitnik et al.	C-M	5/0	75.83±6.65	26-34	1.91±0.13	NA

results are in accordance with literature measurements at each analysed site apart from at the internal carotid arteries, where mean flow rate is 1.77/1.73 ml/s by the model and in the range 2.72-6.27 ml/s based on literature [250]. The reason seems to be due to the lack of the cerebral circulation, just approximated by the 0D model at the boundary of the 1D head arteries.

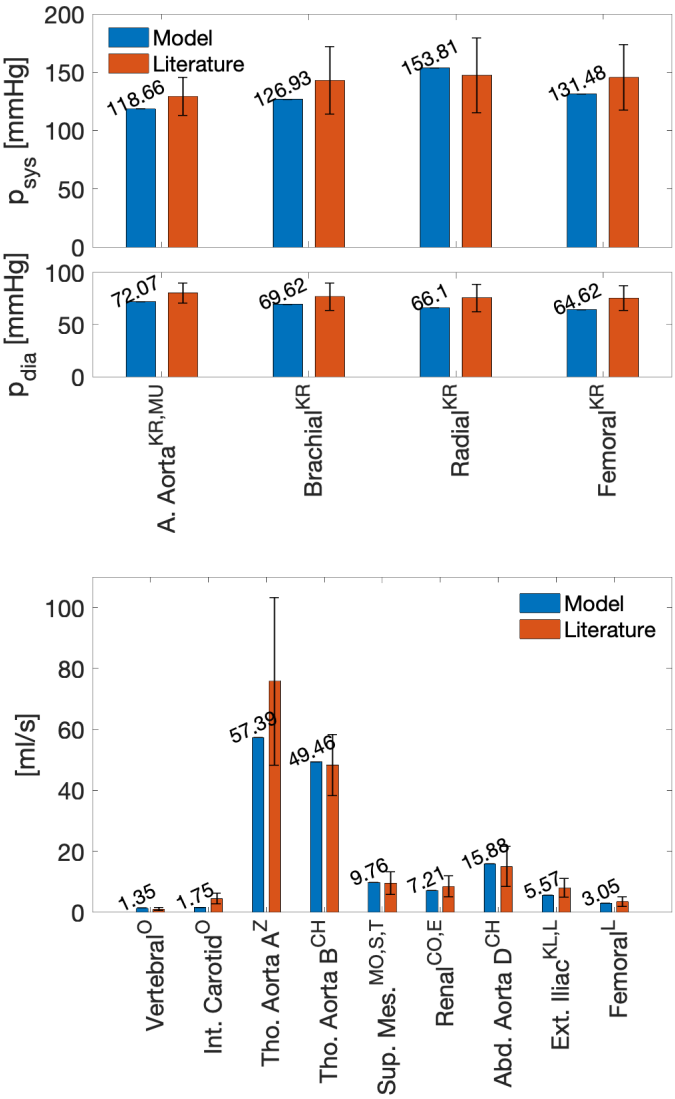

Figure 4.3: Comparison between systolic/diastolic arterial pressures (top) and mean flow rates (bottom) at the indicated sites (Ascending Aorta: A. Aorta, Thoracic Aorta: Tho. Aorta, Abdominal Aorta: Abd. Aorta, Brachial, Radial, Femoral, Vertebral, Internal Carotid: Int. Carotid, Superior Mesenteric: Sup. Mes., Renal, External Iliac: Ext. Iliac) by the model and from measurements available in literature. Vertical lines on red bars show the range of possible values found in literature. Superscripts of the arterial sites stand for the references in Table 4.2.

4.2 The systemic microcirculation, venous return and pulmonary circulation

Figure 4.4 depicts pressure and flow rate signals along the systemic microcirculation, venous return and pulmonary circulation, which are all mimicked through the 0D model in section 3.2. These results remark some key haemodynamic aspects already analysed in chapter 1.

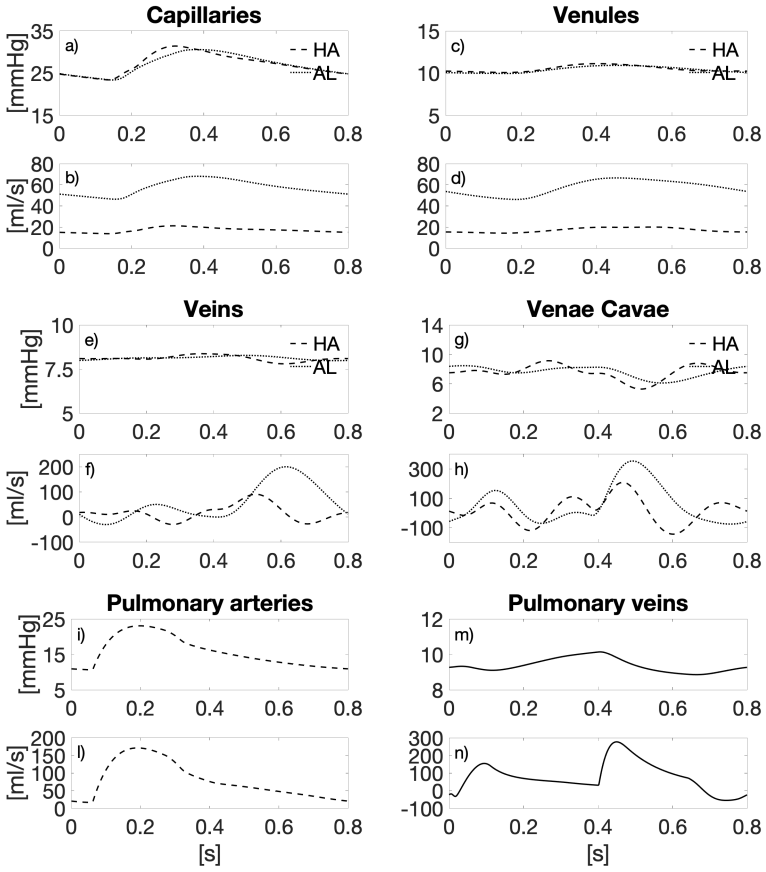

Figure 4.4: (a-h) Pressure and flow rate signals along the systemic microcirculation and venous return for the head and arms (HA) and abdomen and legs (AL) compartments, pressure and flow rate signals for the pulmonary (i-l) arteries (P ART) and (m-n) veins (P VEN) compartments. These signals are obtained for a healthy and young man with a heartbeat period of 0.8 s (HR=75 bpm).

- Mean capillary (27.12 mmHg), venular (10.47 mmHg), venous (8.12 mmHg) and venae cavae (7.61 mmHg) pressures belong to the expected ranges, that are 30-10 mmHg for capillaries, 15-5 mmHg for venules, and 10-3 for veins and venae cavae [110, 27].

- As one can see from panels i and m of Figure 4.4, while pulmonary arterial pressure is pulsatile, pulmonary venous pressure is weakly pulsatile, with similar mean pressures for the systemic and pulmonary veins [27]. Systolic, diastolic and mean pulmonary arterial pressures are 23.06, 10.62 and 14.77 mmHg, respectively, that means within the expected intervals (18-25 mmHg for systolic pressure, 8-15 mmHg for diastolic pressure and 11-17 mmHg for mean pressure [110, 169, 235]).

4.3 The heart and coronary circulation

Figure 4.5 represents pressure and volume signals within cardiac chambers, flow rate signals through cardiac valves, and P-V loops of left and right ventricles, with cardiac chambers and valves reproduced by the lumped models in section 3.2. These images depict important cardiac features recalled in chapter 1.

- Transvalvular flows (see panel c of Figure 4.5) are in accordance with literature [156], with reversal flows accompanying the closure of cardiac valves and complicating the patterns of volume signals for cardiac chambers (see panel b of Figure 4.5). Reversal flows through tricuspid and mitral valves make atrial volumes rise and ventricular volumes decrease. Reversal flows through pulmonary and aortic valves, instead, are just responsible for a slight increase in ventricular volumes.

- Left and right ventricular stroke volumes are equal, despite the right ventricle works within a pressure range considerably smaller than the left ventricle (see panel d of Figure 4.5).

Table 4.3 summarises some cardiac parameters provided by the model, together with the corresponding expected ranges. We find that all parameters are in agreement with experimental data.

Figure 4.6 depicts pressure and flow rate signals along the systemic coronary arteries, which are reproduced through the multiscale model in section 3.4. The shapes of flow rate signals as well as mean flow rate values per cardiac cycle along the main coronary arteries are also in accordance with the limited set of coronary blood flow rates in humans available in literature [226, 316]. Based on model results, the mean flow rate received by the coronary circulation per cardiac cycle is 4.90 ml/s, that is acceptable in resting conditions, corresponding to about the 5% of CO [110, 273].

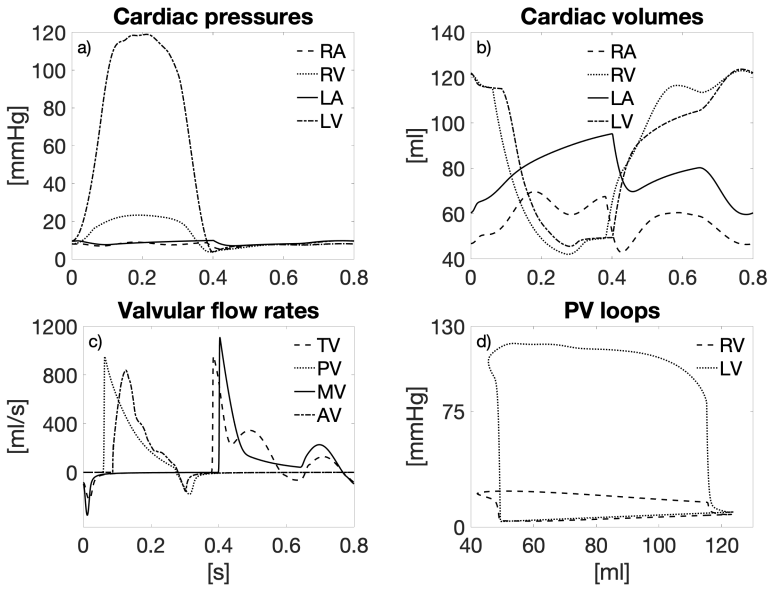

Figure 4.5: (a-b) Pressure and volume signals within cardiac chambers (right atrium, RA, right ventricle, RV, left atrium, LA, left ventricle, LV), (c) flow rate signals at cardiac valves (tricuspid valve, TV, pulmonary valve, PV, mitral valve, MV, aortic valve, AV), (d) P-V loops for right and left ventricles. These signals are obtained for a healthy and young man with a heartbeat period of 0.8 s (HR=75 bpm).

4.4 Baroreflex response

The efficacy of the baroreflex model introduced in section 3.5 has been tested by analysing the (i) heart pacing and (ii) open-loop response [91]. In heart pacing, a fixed value of HR is imposed, with its effects on the remaining effector organs quantified through the baroreflex mechanism. Instead, in the open-loop case, it is the pressure sensed by the baroreceptors, here expressed as the ratio $\bar{p}_{acs}/p_{acs,ref}$, to be imposed as independent variable, while the other effector organs respond accordingly [254]. We have simulated the heart pacing through seven HRs (35, 55, 75, 95, 115, 135 and 155 bpm) and the open-loop case through seven ratios $\bar{p}_{acs}/p_{acs,ref}$ (from 0.625 to 1.375).

Figure 4.7 depicts the results of the heart pacing simulation. Panel 4.7a shows the behaviour $\bar{p}_{acs}$(HR) with and without baroreceptors, proving the capability of the baroreflex action to limit arterial pressure variations when cardiac frequency changes with respect to its reference value (75 bpm). Figures 4.7b-c represent the behaviour of the non-dimensional stroke volume, SV', and cardiac output, CO', with the non-dimensional HR' (apex indicates non-dimensional quantities), together with the experimental data by [239, 212, 318]. Normalisation is done with respect to the baseline values at 75 bpm for the results by the model, and

Table 4.3: Stroke volume, SV, cardiac output, CO, left ventricular end-diastolic volume, V_{edlv}, left-ventricular end-systolic volume, V_{eslv}, ejection fraction, EF, and left atrial pressure by the model for HR=75 bpm (in black) and by available measurements in literature (in red with references in square brackets). Cardiac parameters are defined in chapter 1.1.

Parameters	Left heart
SV [ml]	68.84
	59-119 [41]
CO [l/min]	5.16
	4-8 [41]
V_{edlv} [ml]	116.72
	83-218 [128]
V_{eslv} [ml]	47.88
	18-82 [128]
EF [%]	58.98
	55-63 [41]
Left atrial pressure	7.58
	5.8-10.8 [41]

with respect to the indicated baseline values for the experimental results. As reported in literature [25], SV falls with HR, while CO rises at low HRs, reaching a maximum value for HRs between 90 and 180 bpm, and reducing for further HR increases. These trends are reproduced in Figure 4.7b-c, where one observes an overall agreement between simulated and experimental data. However, the maximum CO predicted by the model (between 135 and 155 bpm) is located at HRs higher than the experimental measures shown in the Figure. This could depend on the techniques adopted to modify HR in the experiments (ventricular pacing, atrial pacing, pharmacological agents, exercise, etc.) as well as the experimental conditions (e.g., conscious or anaesthetized subjects). Moreover, the fact that experimental results are often published in dimensional form limits the possibility to effectively compare results from different sources.

Figure 4.8 shows the results for the open-loop analysis. The behaviours of HR, mean arterial pressure (MAP), arterial and capillary resistances (R_{art} and R_c), and compliances of venules and veins (C_{ve} and C_v) with $\bar{p}_{acs}$ are provided in non-dimensional form for both simulated and experimental results [35, 62, 306], with normalization done as in the case of heart pacing. Apart from the general correspondence between numerical and experimental results, same discrepancies emerge, mainly because experimental results consider the contribution of carotid

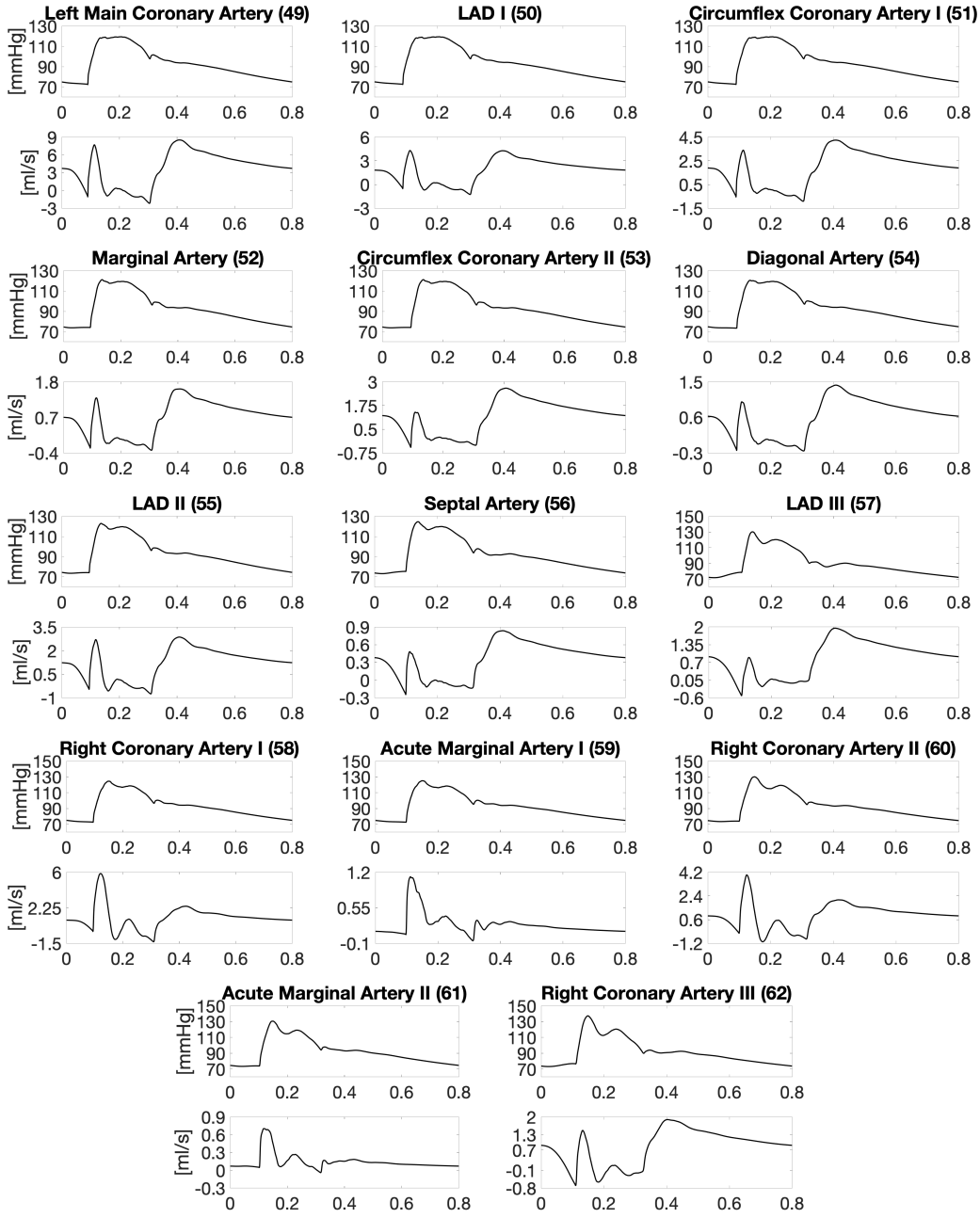

Figure 4.6: Pressure and flow rate signals along the systemic coronary arteries for a healthy and young man with a heartbeat period of 0.8 s (HR=75 bpm). Each artery is associated to its number in brackets according to Figure 3.13.

sinus pressure only in the baroreflex action [256]. By contrast, in our model, pressure triggering the baroreflex action is a combination of both aortic arch and carotid sinus pressures.

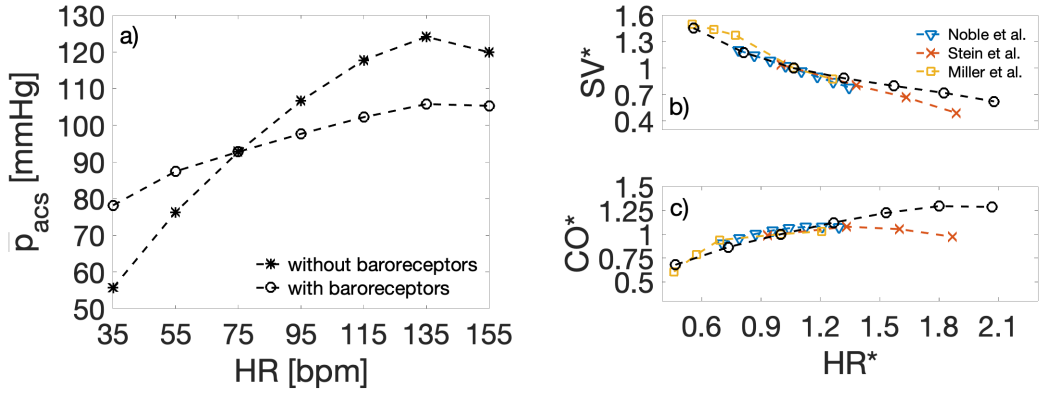

Figure 4.7: Heart pacing case. (a) Behaviours of the average aortic-sinus carotid pressure with HR. Dependence of the stroke volume (b) and cardiac output (c) on HR, with a comparison with experimental data. Variables marked with an apex are non-dimensional. Data by Stein et al. [318] refer to human subjects, while data by Noble et al. [239] and Miller et al. [212] are measured on dogs.

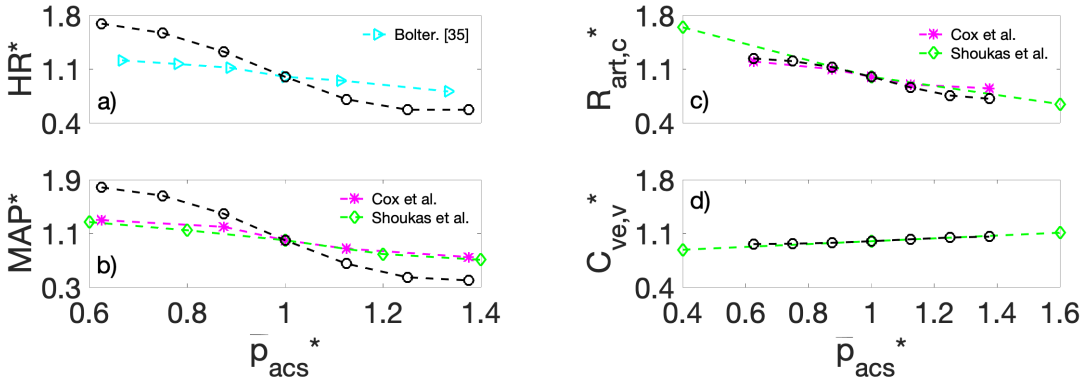

Figure 4.8: Open-loop case. Non-dimensional open-loop responses for the (a) heart rate, (b) mean arterial pressure, (c) arterial and capillary resistances, and (d) compliances of venular and venous compartments, with a comparison with experimental data. Variables marked with an apex are non-dimensional. All experimental data (Bolter et al. [35], Cox et al. [62] and Shoukas et al. [306]) refer to dogs.

Based on the above, one recognises how the baroreflex model here presented works well over a wide range of heart rates and aortic-carotid sinus pressures, and is able to guarantee homoeostasis in accordance with the limited set of data available in literature.

Chapter 5

Making the model patient-specific and testing

Some of the contents of this chapter have been submitted for publication [94].

Nowadays, it is common to develop personalised models of the cardiovascular system or limited portions of it, mainly to support clinicians in diagnostics and decision-making, and transform average treatments into individual therapies [101]. Cardiovascular models are typically made patient-specific by using for each patient the exact cardiac/vascular geometry derived from his/her scans. However, alternative approaches have been proposed by other authors [108, 259], who adopted empirical rules (extracted from large cohort of individuals) to introduce patient-specific personal and anthropometric data.

In this context, we propose a patient-specific model of the entire cardiovascular system, obtained from the general model presented in chapter 3, which is relative to a reference healthy subject. The transition from general to patient-specific model has been implemented by (i) imposing the individual mean heart rate, left ventricular contraction time and brachial blood pressure (BP), and (ii) adjusting some key model parameters of the reference subject, based on noninvasive data routinely measured during standard clinical examinations, through validated empirical rules reported in literature. In this process, we have neglected the coronary circulation.

This chapter is organised in two sections. Section 5.1 contains a description of how the model has been made patient-specific, with a summary of the rules applied to adapt the reference geometrical and mechanical properties of the general model domain (see chapter 3) to a specific subject. Section 5.2 is instead dedicated to prove the reliability of the patient-specific model.

5.1 Patient-specific adaptation

To make the general model patient-specific, we have defined as model input data the following subject information: heart rate (HR), left-ventricular contraction time (T_{vc}), weight (w), height (h), age (age), sex (s), mean (p_{mb}) and pulse (pp_b) noninvasive brachial BPs. Depending on the explicit or implicit occurrence of the different model input data in the general model, patient-specific values of HR, T_{vc} and p_{mb} have been directly introduced in the model, while individual values of w, h, age, s and pp_b have been used in empirical relationships to adapt the arterial geometry and cardiac/vascular mechanical properties of the reference healthy subject (HR_{ref}=75bpm, $T_{vc_{ref}}$=0.27s, w_{ref}=75kg, h_{ref}=175cm, age_{ref}=25y, s_{ref}=man, $p_{mb_{ref}}$=88mmHg, $pp_{b_{ref}}$=67mmHg) to the patient-specific characteristics. In particular, we have considered the following dependencies: arterial lengths (l_{art}) from h, age and s, arterial diameters (d_{art}) from age, h, w and s, arterial compliances (through the pulse wave velocities, PWV_{art}) from age, pp_b and p_{mb}, arterial thickness (h_{art}), cardiac ($E_{A/B,ch}$) and venous compliances (C_v) from age, and reference BP sensed by the baroreceptors from p_{mb}. The rationales of these dependencies and the adopted empirical rules are reported in the following sections.

Special attention has been paid to the choice of the regression models, which can sometimes lead to controversial results, being extracted from heterogeneous cohorts of individuals. To justify the differences in regression models linking the same parameters, one could just take into account the following considerations.

- The clinic profiles of people from who regression models are derived vary according to the author's purpose and may have a role on the resultant trends. For instance, if data are taken from potential living organ donors, final regression models will be associated to a low risk population. Otherwise, if data come from people who are recovering from cardiovascular surgery, regression models will be related to higher risk subjects.

- The number of individuals involved per study, as well as the distribution of patient characteristics among the participants, is responsible for the closing results. For example, if the number of women is significantly larger than the number of men, or the amount of underweight people is huge compared with that of the obese ones, results could become increasingly specific to the group under study and cannot be interpreted as general behaviours.

- Cardiovascular properties of people coming from different countries are not always comparable. As a matter of fact, regression models extracted from Chinese people or American people or a mix of them could lead to contrasting empirical relationships between cardiovascular parameters and impacting factors.

- The different techniques to measure arterial diameters and lengths, as well as cardiovascular mechanical properties, could have a role on the ultimate outcomes.

In this complex scenario, we have opted for regression models representative of white people affected by cardiovascular or cardiovascular-related problems, such as hypertension, diabetes, atrial fibrillation, etc.. This choice has been intended to obtain a patient-specific model of the cardiovascular system to be tested with pre-existing invasive BP signals, which were recorded on white, old and not perfectly healthy patients.

5.1.1 Arterial lengths

It is quite accepted in literature that the arterial path length depends on h and influences the resultant haemodynamic behaviour [166, 167, 187, 312]. In fact, in shorter people, the earlier arrival of the reflected waves to the heart during systole leads to a rise in central systolic and pulse BPs, which are responsible for an increase in the left-ventricular work and stress at the same mean BP.

To take into account the relationship between body height and vessel lengths, all arterial lengths have been scaled according to the specific subject h [108]. Namely, arterial lengths have been multiplied for the ratio between the h to simulate and h_{ref}.

Some arterial lengths also elongate with *age*. Thus, a dependence of these arterial tracts from *age* has been considered. Parametric relationships linking the length of the aorta to *age* are available in literature [282, 326]:

- Rylski et al. [282] evaluated aortic lengths at 4 locations, from the aortic valve to the iliac bifurcation, in 195 patients between the ages of 20 and 96. Subjects underwent electrocardiogram-gated computed tomography angiography and were affected by hypertension, diabetes mellitus and smoking. They documented that the absolute values of aortic lengths are higher in men than women. However, after adjustments for BSA, lengths of ascending, descending thoracic and abdominal aorta are slightly longer in women than in men. Aortic lengths rise in both women and men with age, with a greater degree of increase in women than in men along the ascending aorta and aortic arch segments;

- Sugawara et al. [326] measured the lengths of aorta, carotid and iliac arteries on 256 healthy subjects, in the age range 19-79 years, through 3D transverse magnetic resonance imaging arterial tracing. They found that the ascending aorta length increases with age, while the lengths of descending aorta, carotid and iliac arteries are not associated to age.

We have modified aortic lengths with *age* according to the regression coefficients by Rylski et al. [282], reported in Table 5.1, while have maintained the other arterial lengths constant with *age*. Notice that Rylski's coefficients, which are sex-dependent, are expressed for a change in mm per year and m^2 of body surface area, BSA[1]. Thus, coefficients are multiplied for the patient-specific BSA, which we have calculated from h and w through the Du Bois's formula [34]: BSA=$0.20247h^{0.725}w^{0.425}$ (h and w are expressed in m and kg, respectively).

Table 5.1: Regressions coefficients for women ($c_{1,w}$) and men ($c_{1,m}$) expressing the variations (in mm) in aortic lengths with age (per year) according to the regression models by Rylski et al. [282]. Results are given for 4 different aortic tracts; 1: from the aortic valve to the origin of the brachiocephalic artery, 2: from the end of tract 1 to the the origin of the left subclavian artery, 3: from the end of tract 2 to the origin of coeliac artery, and 4: from the end of tract 3 to the aortic bifurcation. The numbers of the 1D arteries (see Table 3.1) included in each aortic tract are indicated in brackets. *Table extracted from* [94].

Aortic tract (vessels)	$c_{1,w}$ [mm/y/m^2]	$c_{1,m}$ [mm/y/m^2]
1 (1)	0.22	0.21
2 (2, 14)	0.11	0.09
3 (18, 27)	0.45	0.55
4 (28, 35, 37, 39, 41)	0.19	0.19

Thus, considering the effects of h, *age* and s, arterial lengths are modified starting from those of the reference subject ($l_{art,ref}$, indicated in Table A.1) as

$$l_{art} = l_{art,ref}\frac{h}{h_{ref}} + c_{1,w/m}\text{BSA}(age - age_{ref}), \tag{5.1}$$

where coefficients c_1, both space- and sex-dependent, are shown in Table 5.1.

[1]BSA is typically used to determine drug dosage in many medical fields, such as cancer chemotherapy, transplantology, toxicology, etc. [277]. Different formulas are available in literature to calculate BSA, each of which with its own specificity. Among the most used formulas, we recall the Du Bois's one [34]: $0.20247h[\text{m}]^{0.725}w[\text{kg}]^{0.425}$ and the Mosteller's one [221]: $\sqrt{\frac{h[\text{cm}]w[\text{kg}]}{3600}}$, with h and w the body height and weight, respectively.

5.1.2 Arterial diameters

It is well known that diameters of elastic arteries enlarge while muscular arteries remain almost unaltered during normal ageing [198]. However, if the age-induced rise in aortic and common carotid arterial diameters is widely accepted, there is some controversy regarding the impact of *age* on diameters of muscular arteries such as the brachial, radial and common femoral arteries. In fact, some authors sustain the diameters of these last arteries reduce [40], while others report the opposite result [103]. This controversy could be imputed to a transitional elastic-muscular behaviour at more peripheral zones, as proved by Bjarnegard et al. [29], who evaluated the variations in the brachial artery diameter with *age* along the arm length. Based on the contrasting trends observed at more distant locations, we have introduced the effects of *age* on aortic and carotid diameters only.

Arterial diameters also alter with both w and h, whose combined effect can be taken into account by either the body mass index (BMI[2]) or BSA. We have here used BSA as body size variable, since it was demonstrated to be better associated to some aortic diameters than BMI [370]. We have modelled the effects of BSA at aortic and carotid level only, where the role of BSA has been mostly analysed.

Concerning the behaviour of aortic diameters with *age* and BSA, we have considered a number of regression models in literature [66, 76, 111, 282, 370]:

- Davis et al. [66] measured aortic diameters at three locations, from ascending to abdominal aorta, through cardiovascular magnetic resonance at 1.5 T. They analysed 447 subjects aged between 19 and 70 and without identifiable cardiovascular risk factors. They found that aortic diameters increase with BSA and age for both women and men. The amount of dilatation does not depend on sex as the BSA increases. The rate of dilation with advancing age, instead, is not gender-specific at proximal level but becomes larger for men than women at abdominal level. Moreover, the increase in aortic diameters with BSA is modest, since people affected by hypertension and other cardiovascular risk factors were excluded in this study;

- Fleischmann et al. [76] focused on the abdominal aortic diameters of 77 potential living renal donors aged between 19 and 67. Image-data were acquired with contrast-enhanced helical computed tomography angiography. They reported that men always have larger diameters than women. Aortic diameters progressively reduce from proximal to distal sites, and the degree of dilation

[2]BMI is adopted to determine the degree of overweight, even if, in some circumstances, it appears to be a poor indicator of body fatness [245]. In fact, it does not discriminate between lean and fat mass, making it look like athletes and body builders overweight, while they are not [44]. BMI is calculated as $\frac{w[\mathrm{kg}]}{h[\mathrm{m}]^2}$.

in diameters with age progressively decreases moving down along the abdominal aorta. Finally, the effect of BSA does not change site by site and is equal for both men and women;

- Hager et al. [111] measured aortic diameters from the aortic valve to the thoracic aorta at the level of diaphragm by helical computed tomography. Data were obtained from 70 individuals, with age between 17 and 89, without any sign of cardiovascular disease. They indicated no influence of height, weight and BSA, while recognised the impact of both sex and age on aortic diameters. In particular, men have always larger diameters than women and age is responsible for an increase in aortic dimensions at all intrathoracic levels;

- Rylski et al. [282] evaluated aortic diameters, together with aortic lengths, as explained in section 5.1.1. They documented that the absolute values of aortic diameters are always higher in men than women. However, after adjustments for BSA, women have larger ascending aorta and aortic arch diameters than men. Aortic diameters rise in women and men with age, with a greater degree of increase in women than in men along the ascending aorta and aortic arch segments. They concluded that, in the elderly, aortic diameters are similar in men and women because of the faster growth in the ascending aorta for women;

- Wolak et al. [370] measured ascending and descending thoracic aorta diameters in a low-risk population of 4883 individuals in the 26-92 age range. Assessments were based on gated non contrast computed tomography scans for coronary calcium measurements. They reported that men and women have similar diameters in the youth, while aortic diameters become greater in men than women in the elderly. Furthermore, the rate of increase in aortic diameters with BSA is almost equal between young men and women, and greater in old men than women.

Notice that results coming from the empirical rules proposed by the authors above are not perfectly comparable. For instance, according to Davis et al. [66], the rate of age-dependent increase in proximal aortic diameters is not gender-specific, while, for Rylski et al. [282], aortic diameters grow more in women than in men at proximal level because of age. This type of dissimilarities can be explained based on the differences in the characteristics of the cohorts analysed, with Davis et al. excluding people with identifiable cardiovascular risk factors and Rylski et al. including them.

Changes in carotid arterial diameters with *age* and BSA were determined by different authors [114, 139, 159]. However, not only results coming from these

authors are not coherent but also the influence of different determinants on changes in carotid dimensions was considered:

- Kamenskiy et al. [139] were interested in quantifying the changes in carotid geometry with ageing. Variations in carotid diameters with age were evaluated on 15 healthy individuals, aged between 15 and 64 years, and on 17 patients with unilateral carotid artery disease, in the age range 49-86 years. Geometry was investigated through 3D reconstructions of thin-section computed tomography angiography scans. It was found that, in absence of carotid artery disease, the right common carotid artery diameter is the most prone to increase with age, while the left common carotid artery diameter and the left/right internal carotid artery diameters slightly increase with age;

- Krejza et al. [159] measured the diameters of the common carotid (left and right) and internal carotid arteries (left and right) on 500 patients, aged between 14 and 103, through ultrasound examinations. People involved were affected by hypertension, diabetes, atrial fibrillation, heart and cerebrovascular diseases, and hypercholesterolaemia. They found correlations between carotid diameters and sex, BSA, neck length, age and systolic arterial BP. In particular, carotid diameters are larger for men than women and grow with the BSA, neck length and systolic arterial BP. Women have the right common carotid artery slightly larger than the left one, while there are not side-to-side effects in the common carotid arteries of men and in the internal carotid arteries of both women and men. It also emerged that, in contrast with other studies, the relationship between carotid diameters and age is not significant. Authors justified this conclusion with the fact that the population under study was relatively young (mean age: 51.6 years for women and 52.8 years for men).

We have reproduced the role of *age* through the regression coefficients c_2, given in Table 5.2, by Rylski et al. [282] along the aorta and by Kamenskiy et al. [139] for the common carotid arteries, respectively. All these coefficients are sex-dependant, and express a change in mm per year and per m^2 of BSA by Rylsky et al., and a change in mm per year by Kamenskiy et al.. Since an explicit dependence of the aortic diameters with BSA is considered, age-dependant coefficients by Rylsky et al. are multiplied for the reference BSA, BSA_{ref}, which - calculated through the Du Bois's formula - is equal to 1.90 m^2. The role of BSA on the aortic and common carotid arteries diameters has been instead quantified through the regression coefficients c_3 by Davis et al. [66] and Krejza et al. [159], respectively, both indicated in Table 5.2 and expressing different changes depending on sex.

Thus, including the effects of *age*, h and w (through BSA), and s, arterial diameters, d_{art}, are modified from the corresponding reference values ($d_{art_{ref}}$, indicated in Table A.1) as

Table 5.2: Regressions coefficients for women ($c_{2,w}/c_{3,w}$) and men ($c_{2,m}/c_{3,m}$) expressing the variations in aortic and carotid diameters with age/BSA. Dependences with age are expressed according to Rylski et al. [282] (in [mm/y/m^2]) and Kamenskiy et al. [139] (in [mm/y]) for the aortic and carotid tracts, while dependences with BSA according to Davis et al. [66] and Krejza et al. [159] (both in [mm/m^2]) for the aortic and carotid tracts, respectively. Results are given for 6 different arterial tracts; 1: from the aortic valve to the origin of the brachiocephalic artery, 2: from the end of tract 1 to the the origin of the left subclavian artery, 3: from the end of tract 2 to the origin of coeliac artery, 4: from the end of tract 3 to the aortic bifurcation, 5: along the right common carotid artery, and 6: along the left common carotid artery. The numbers of 1D arteries (see Table 3.1) included in each aortic tract are indicated in brackets. *Table extracted from* [94].

Arterial tract (vessels)	c_{2w}, c_{3w}	$c_{2,m}, c_{3w}$
1 (1)	0.11, 5.6	0.08, 7.6
2 (2, 14)	0.08, 2.8	0.06, 5.5
3 (18, 27)	0.08, 3.1	0.08, 3.8
5 (28, 35, 37, 39, 41)	0.05, 3.1	0.06, 3.8
5 (5)	0.017, 1.13	0.018 1.21
6 (15)	0.006, 1.13	0.006 1.21

$$d_{art} = d_{art_{ref}} + c_2(age - age_{ref}) + c_3(\mathrm{BSA} - \mathrm{BSA_{ref}}), \tag{5.2}$$

with coefficients c_2 and c_3, both space- and sex-dependent, in Table 5.2.

5.1.3 Arterial thicknesses

Aortic and common carotid arteries thicken with *age* [127, 198, 274], while there are contrasting results at other arterial locations. Thus, patient-specific arterial thickness values, h_{art}, have been modified along the aorta and common carotids only with respect to the reference values ($h_{art_{ref}}$, indicated in Table A.1). Namely,

$$h_{art} = h_{art_{ref}} + c_4(age - age_{ref}), \tag{5.3}$$

with coefficient c_4 differently determined for aorta and common carotids.

Along the aorta, we have adopted the regression coefficients derived from a widely used work: the one by Virmani et al. [355]. They measured aortic intimal and medial thickness at 4 fixed locations (ascending aorta, descending thoracic aorta, suprarenal abdominal aorta and subrenal abdominal aorta) on a population of 302 subjects, with ages between 19 and 104 years. Subjects were all dead because of different causes, from trauma to cerebrovascular accidents. They found that medial thickness variations with age are negligible with respect to the age-related intimal thickness increases. Moreover, the highest growth in intimal thickness is localised at abdominal level. Relationships between intimal thickness and age are linear at each aortic site, with the following regression coefficients (c_4): 0.0040 mm/years for the ascending aorta, 0.0092 mm/years for the descending thoracic aorta, 0.0085 mm/years for the suprarenal abdominal aorta, and 0.0144 mm/years for the subrenal abdominal aorta.

Concerning common carotids, instead, numerous works treating variations in carotid intima-media thickness with *age* [193, 274, 127, 318, 334, 344] have been considered:

- Ma et al. [193] analysed left and right carotid intima-media thickness of both women and men by B-mode ultrasonography. Population under exam included 2402 subjects with age in the range 35-64 years. They found that there is a linear correlation between carotid intima-media thickness and age in the age range 35-64 years, with some differences between men and women, right and left side. They reported a rate of increase in carotid intima-media thickness between 0.0051 and 0.0057 mm per year;

- Rashid et al. [274] evaluated carotid intima-media thickness in 140 people, aged from 20 to 88 years, by B-mode ultrasonography. Selected subjects were free from previous ischaemic heart diseases and strokes. They found that intima-media thickness of all carotid arteries highly increases with age. They indicated a mean rate of increase of about 0.011 mm/year, with the highest variation at carotid bifurcation rather than at common and internal carotid arteries. Moreover, they concluded that there are not significant differences between left and right side, as well as between women and men;

- Rashid's results are in accordance with the ones by Howard et al. [127], who reported that the averaged age-related increases in wall thickness are about 0.015/0.018 mm/year for women/men at carotid bifurcation, 0.010/0.014 mm/years for women/men at internal carotid artery, and 0.010 mm/years for both women and men at common carotid artery;

- Stein et al. [318] measured carotid intima-media thickness on 519 black and white adults, in the age range 20-38 years, through B-mode carotid ultrasound

images. They documented that carotid intima-media thickness increases with age, without important age-related differences between females and males, black and white subjects.

- Tanaka et al. [334] determined carotid intima-media thickness on 129 individuals from 18 to 77 years. Population included sedentary and active people, who were all normotensive, nonobese and without chronic heart diseases. Measurements of carotid intima-media thickness were done on images obtained from an ultrasound machine, with a high-resolution linear array. The primary finding is that carotid intima-media thickness grows in the elderly, being 50% higher in old people (mean age 65 years) than among young people (mean age 27 years);

- Tosetto et al. [344] analysed the influence of age on the carotid intima-media thickness of 2484 individuals with age>40 years by ultrasonic scans. Some of the subjects involved had suffered from cardio or cerebrovascular disease and were subjected to drug medications. It was found that carotid intima-media thickness constantly increases with age both in women and men, with negligible gender-related differences.

To the purpose of our model, we have imposed that common carotid intima-media thickness linearly grows with *age* within the whole age spectrum. In particular, in accordance with the age-related increases indicated by Rashid et al. [274] and Howard et al. [127], we have used a rate of increase of 0.010 mm/years (c_4) for common carotid arteries. We have not taken into account side-to-side and sex differences in the growth rate of common carotid intimal-media thickness with advancing *age*. Moreover, we have neglected any age-modification along internal carotids.

5.1.4 Arterial compliances

It is well known how aorta stiffens during ageing [211, 246, 295, 320], leading to a decrease in arterial compliances. It was discussed that arterial stiffening is greatly caused by the fatigue and successive rupture of the median elastic lamellae, which typically break after about $8e^8$ cycles (e.g., 30 years with a mean HR of 70 bpm) [247, 248]. Carotid-femoral pulse wave velocity (PWV) is nowadays taken as the gold standard for aortic stiffness evaluation [37], with a great deal of data available in literature [22, 39] about its variations with ageing. However, as Hickson et al. [125] observed, carotid-femoral PWV doesn't take into account the influence of proximal aorta, which has the highest elastic content and plays an important role in buffering BP pulsations produced by the contracting activity of heart. Therefore, to better map the stiffening process along the aorta with *age*, one should refer to

the regional PWVs.

Different authors have quantified the variations in PWVs with *age* along the aorta [125, 249, 276, 284]:

- Hickson et al. [125] measured regional PWV in 4 segments, from the aortic valve to the iliac bifurcation, by cine phase contrast magnetic resonance imaging. Measurements were done on 162 subjects, with age between 18 and 77 years, who didn't exhibit cardiovascular diseases and were free from medications. The highest increase in aortic stiffening, expressed through a growth in PWV, was localised along the abdominal artery (+0.9 m/s per decade), then along the thoracic-descending region (+0.7 m/s per decade), the mid-descending region - at the level of the diaphragm - (+0.6 m/s per decade), and the ascending aorta (+0.4 m/s per decade). By contrast, the most important changes in aortic diameters because of age were identified in the ascending aorta (0.96 mm per decade), then along the mid-descending region (0.85 mm per decade), the thoracic-descending region (0.78 mm per decade), and the abdominal artery (from 0.64 to 0.37 mm per decade depending on the site). Moreover, the effect of ageing on aortic stiffness was proved to increase exponentially with age. In fact, curves linking regional PWVs to age are second-order polynomials regardless of the aortic position;

- O'Rourke et al. [249] recorded BP waves from proximal aorta to iliac artery in 39 patients, with ages in the interval 6-69 years, through diagnostics catheterisation. They observed that there is a decrease in the transmission time of BP signals with age, reflecting a rise in PWV during ageing. They also noticed that the greatest changes are localised along the distal aorta and iliac artery, with negligible variations along the thoracic artery;

- Redheuil et al. [276] evaluated the aortic arch PWV and the carotid-femoral PWV by tonometry in 111 asymptomatic subjects in the age range 20-84. They concluded that both aortic and carotid-femoral PWVs increase with age of about 1.60 and 1.56 m/s per decade, respectively. In addition, the relationship between aortic PWV and age was found not linear, with a more marked rise in aortic PWV among individuals older than 50 years;

- Rogers et al. [284] determined PWV in 3 aortic segments and carotid-femoral PWV. Measurements were done on 24 volunteers between 21 and 72 years by phase-contrast magnetic resonance imaging and applanation tonometry. It was verified that the age-related increases in PWV are higher at proximal level than at distal level. Moreover, at each aortic site, the growth in PWV is more significant on subjects older than 55 years.

Results by Hickson et al. [125] and Rogers et al. [284] are contrasting. In fact, according to Hickson et al., PWV mainly grows at distal aortic sites, while, according to Rogers et al., the greatest variations in PWV are localised along the ascending and proximal descending aorta. Although Hickson's results are not perfectly in accordance with those by Rogers et al., they were derived from the largest cohort of individuals. Furthermore, Hickson et al. justified their conclusion of a higher distal rise in PWV with age. They observed that proximal aortic diameters grow more than distal diameters with age. Thus, since PWV is directly proportional to the square-root of wall thickness and inversely proportional to the square root of the radius, increases in vessel diameter in absence of corresponding increases in vessel wall thickness could limit PWV growth at proximal level.

The changes in carotid PWV with *age* have been determined by other authors [36, 357]:

- Borlotti et al. [36] calculated PWV at carotid and femoral arteries in 1774 healthy individuals of 35-55 years, through direct measurements of local flow velocity and diameter. They concluded that carotid PWV linearly rises with age, with not statistically significant differences between men and women. Femoral PWV, instead, is not associated to age and is higher in men than women;
- Vriz et al. [357] compared carotid-femoral PWV with one-point carotid PWV, which were evaluated for 160 individuals (age range 17-78 years), both healthy and affected by cardiovascular problems, such as hypertension, aortic valve disease and ventricular dysfunction. They found that both carotid-femoral PWV and one-point carotid PWV linearly correlate with age, but one-point carotid PWV is always lower than carotid-femoral PWV. Thus, the relationship between carotid-femoral PWV and age cannot be applied to one-point carotid PWV.

When making the model patient-specific, we have maintained the reference compliances of the arterial areas where age alteration in PWVs were found negligible or absent. Instead, we have adapted patient-specific carotid and aortic compliances through the relative patient-specific PWVs. In fact, mechanical properties of 1D arteries are specified through coefficients $B_1 - B_5$ of the constitutive equation for BP, which are functions of the local PWVs (see equations (3.27-3.31)). In particular, aortic PWVs have been calculated from reference values ($PWV_{art_{ref}}$, obtained from the (3.20)) through the quadratic relationship $PWV(age)$:

$$PWV = PWV_{art_{ref}} + [c_5(age - age_{ref}) + c_6(age^2 - age_{ref}^2)]a + b, \tag{5.4}$$

with c_5 and c_6, provided in Table 5.3, by Hickson et al. [125]. Carotid PWVs, instead, have been evaluated from reference values through the linear relationship $PWV(age)$:

$$PWV = PWV_{art_{ref}} + c_7(age - age_{ref})a + b, \tag{5.5}$$

with $c_7 = 0.0538$ m/s/year given by Vriz et al. [357]. Coefficients a and b in equations (5.4-5.5) allow one to include the role of the BP level (pp_b and p_{mb}) in the patient-specific arterial compliances.

Table 5.3: Linear and quadratic regressions coefficients expressing the variations in aortic PWVs with age according to Hickson et al. [125]. Results are given for 4 different aortic tracts; 1: ascending aorta, 2: descending thoracic aorta, 3: suprarenal abdominal aorta, 4: subrenal abdominal aorta. The numbers of the 1D arteries (see Table 3.1) included in each aortic tract are indicated in brackets. *Table extracted from* [94].

Aortic tract (vessels)	c_5 [mm/y]	c_6 [mm/y^2]
1 (1)	$1.8986\ 10^{-4}$	0.0266
2 (2, 14)	$8.1551\ 10^{-4}$	0.0016
3 (18, 27)	$6.3056\ 10^{-4}$	0.0109
4 (28, 35, 37, 39, 41)	$5.0331\ 10^{-4}$	0.0674

5.1.5 Cardiac compliances

Since ventricular stiffening increases with *age* [275], we have corrected patient-specific amplitude, $E_{A,ch}$, and minimum, $E_{B,ch}$, values of left-ventricular elastance, starting from the corresponding reference values ($E_{A,ch_{ref}}$ and $E_{B,ch_{ref}}$, indicated in Table B.2), as

$$E_{A,ch} = E_{A,ch_{ref}} + c_8(age - age_{ref}) \tag{5.6}$$

and

$$E_{B,ch} = E_{B,ch_{ref}} + c_9(age - age_{ref}). \tag{5.7}$$

Coefficient c_8 has been set to have an increase of 1% and 0.5% per year for women and men, respectively, according to Redfield et al. [275]. c_9, instead, has been reasonably taken equal to $c_8 E_{B,ch_{ref}}/E_{A,ch_{ref}}$.

5.1.6 Venous compliances

Venous compliances, as arterial ones, reduce with *age* [102, 214, 252]. We have evaluated patient-specific venous compliances, C_{ven}, through the

$$C_{ven} = C_{ven_{ref}} + c_{10}(age - age_{ref}), \tag{5.8}$$

with $C_{ven_{ref}}$ reported in Table B.1 and c_{10} chosen in order to have a linear reduction in $C_{ven_{ref}}$ of 50% from 25 to 80 years [252].

5.1.7 Reference status of the baroreceptors

In order to reach the mean BP level of the generic subject patient-specific, we have set the reference BP of the baroreceptors equal to the specific mean brachial BP p_{mb}. In this fashion, the comparison between reference and effective BP sensed by the baroreceptors at the end of each heartbeat is done at brachial level rather than at aortic-carotid level.

5.1.8 Sensitivity analysis

In order to quantify the role of the different patient-specific input data to the individual central BP values, we have performed a sensitivity analysis. Considering the input parameter X and the output parameter Y, the sensitivity of Y to X is defined as

$$Sens = \left(\frac{Y' - Y}{Y}\right)\left(\frac{X}{X' - X}\right), \tag{5.9}$$

where Y' is the modified output parameter obtained with the modified input parameter X' [224]. According to this definition, negative values of $Sens$ imply that an increase in X causes a decrease in Y and a decrease in X causes an increase in Y. In addition, if $|Sens|>1$ (<1), the input variability introduced through X is amplified (damped) in Y. Here, we have applied an increase of 25% to all the patient-specific input data: $X' = X + 0.25X$.

Figure 5.1 shows the sensitivities of central systolic (sys), diastolic (dia), mean (mean) and pulse (pp) BPs to *age*, w, h, HR, T_{vc}, p_{mb} and pp_b for a male subject.

Very similar results have been obtained for a female subject. From Figure 5.1, it emerges that p_{mb} is the only input parameter having a not negligible impact on all the output parameters, and h and pp_b are the input parameters with the greatest impact on central pp. The sensitivity of central pp to H is negative (-0.94), while the sensitivity of central pp to pp_b is positive (1.40). The other input parameters (age, w, HR and T_{vc}) result to be less effective on the output parameters, with the smallest sensitivities for central mean and the highest for central pp. Also from Figure 5.1, it appears that the variability introduced through p_{mb} is amplified in central dia and mean (and damped in central sys and pp), and the variability introduced through pp_b is amplified in central pp (and damped in central sys, dia and mean). The variability associated to all the other input parameters results to be damped. Thus, according to Figure 5.1, specific brachial BPs and h measurements are the most influential input data on the model outputs, although the majority of the chosen patient-specific input data are proven to be important to match central pp.

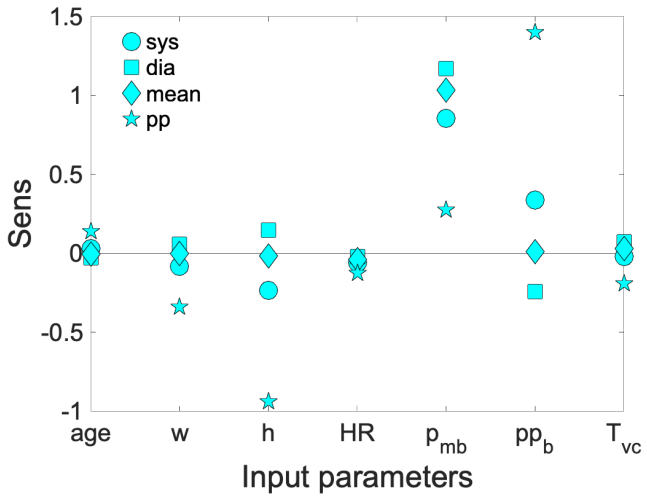

Figure 5.1: Sensitivities of central systolic (sys), diastolic (dia), mean (mean) and pulse (pp) BPs to the input model parameters (age, age, weight, w, height, h, heart rate, HR, mean left ventricular contraction time, T_{vc}, and mean and pulse brachial BPs, p_{mb} and pp_b) for a male subject. *Image extracted from* [94].

5.2 Testing of the patient-specific model

The proposed patient-specific model has been tested by comparing the computed central systolic, diastolic, mean and pulse BPs with the corresponding beat-averaged invasive BPs on 12 patients in sinus rhythm. Such a test aims at investigating the possibility to provide individual central BP via a patient-specific multiscale mathematical model of the cardiovascular system, that could be convenient from a clinical point of view. In fact, despite automatic brachial BP monitoring is routinely adopted in clinical practice, it is a poor indicator of central BP, mainly because of the pulse BP increase from central to distal arterial regions [207]. Thus, considering that target organs (such as heart, brain and kidneys) and peripheral vasculature are more sensible to central rather than brachial BP [377], the easy assessment of central BP is expected to be useful in diagnostics and decision-making. In behalf of this, it has been proved that central BP is a better predictor of cardiovascular risk factors like hypertension. In fact, more than 30% men and 10% women with normal brachial systolic BP suffer from stage 1 of hypertension considering their aortic systolic BP [208]. Moreover, antihypertensive drugs can have different effects on central BP but similar effects on brachial BP [368], making the idea to clinically use central BP instead of brachial BP attractive.

The best method to currently detect central BP is cardiac catheterisation, which is invasive, technically demanding and time consuming, thus not employable in routine screening of large population. Consequently, a number of noninvasive devices have been proposed to estimate central BP from peripheral pressure data, by exploiting a variety of calibration techniques [297]. Nevertheless, the explicit added value of noninvasive central BP compared to brachial BP in the prediction of serious cardiovascular events has not emerged yet, with different studies coming up to opposing interpretations. This seems to be due to the fact that current noninvasive methods are not always accurate enough to affirm the undisputed superiority of noinvasive central BP over brachial BP [170]. In this context, it emerges the need to identify the most accurate methods to noninvasively evaluate central BP, to definitely verify if brachial or aortic BP is the best prognostic parameter to be adopted in the future.

In this complex scenario, we present the characteristics of patients from which invasive BP signals are extracted in section 5.2.1, and the comparison between simulated and measured central BP signals/values in section 5.2.2

5.2.1 Patient recruitment and data collecting

Invasive BP signals come from a perspective clinical study by Olbers et al. [251] examining intra-arterial BP in patients undergoing routine coronary angiography. Olbers et al. acquired intra-arterial BP recordings from 12 patients with sinus rhythm, using pressure transducer-equipped manifolds (NAMIC, Navilyst Medical

Inc, Marlborough, MA, USA), connected with the RadiAnalyzer Xpress unit (St Jude Medical, St Paul, MN, USA) for digital storage. Right radial, right brachial and ascending aorta BP signals were sequentially recorded by advancing a diagnostic catheter from the right radial to the right brachial to the central site, and at least 15 cardiac cycles were saved at each location and for all the subjects.

Anthropometric and clinical data of patients in the trial are reported in Table 5.4, while the presence of comorbidities, like diabetes and ischaemic heart disease (IHD), and the smoking status are given in Table 5.5. In particular, Table 5.4 provides the following patient-specific information: s, age, w, h, mean HR, T_{vc}, p_{mb} and pp_b. HR and T_{vc} were extracted from the ECG, while pp_b and p_{mb} were calculated from systolic (p_{sb}) and diastolic (p_{db}) brachial BPs ($pp_b = p_{sb} - p_{db}$ and $p_{mb} = p_{db} + pp_b/3$), which were noninvasively measured from the upper left arm through automatic oscillometric recording, and simultaneously to the invasive BP at the level of the ascending aorta.

Table 5.4: Anthropometric and clinical data of patients in the trial. Averages and standard deviations of age, w, h, HR, T_{vc}, pp_b and p_{mb} are reported in bold in the last row. *Table extracted from* [94].

Patient number	s	age [years]	w [kg]	h [cm]	HR [bpm]	T_{vc} [s]	pp_b [mmHg]	p_{mb} [mmHg]
1	m	72	61	170	63	0.38	63	75
2	f	68	81	175	65	0.39	50	94
3	m	73	81	170	80	0.34	62	101
4	f	83	68	163	61	0.39	63	74
5	m	65	99	193	54	0.39	83	116
6	f	81	69	167	63	0.36	74	93
7	m	75	91	172	55	0.41	82	96
8	m	62	77	175	61	0.41	55	82
9	f	72	60	167	51	0.39	78	91
10	m	74	97	182	71	0.32	60	92
11	f	73	64	162	62	0.39	88	99
12	m	62	82	179	61	0.36	61	93
		71.67 ±6.61	**77.50 ±13.46**	**172.92 ±8.72**	**62.25 ±7.70**	**0.38 ±0.027**	**68.25 ±12.24**	**92.17 ±11.45**

Mean, μ_v, standard deviation, σ_v, and coefficient of variations ($cv = \sigma_v/\mu_v$) values of systolic and diastolic BPs recorded on all the patients at the three measurement sites are indicated in Table 5.6. Based on systolic BP transmission from central-to-peripheral sites, Picone et al. [267] individuated four BP phenotypes: (phenotype I) both central-to-brachial and brachial-to-radial systolic BP increase ($\geq$ 5 mmHg), (phenotype II) only aortic-to-brachial systolic BP increase, (phenotype III) only brachial-to-radial systolic BP increase, (phenotype IV) neither

Table 5.5: Presence of comorbidities, like diabetes and ischaemic heart disease (IHD), and the smoking status of patients in the trial. *Table extracted from* [94].

Patient Number	diabetes	IHD	smoking
1	x	x	
2		x	x
3			
4			
5			x
6	x	x	x
7	x	x	x
8			
9			x
10	x		
11			
12			

aortic-to-brachial nor brachial-to-radial systolic BP increase. Considering the invasive measurements of systolic BP at the ascending aorta, brachial and radial arteries on the 12 patients (all indicated in Table 5.6), we have recognized all the four BP phenotypes identified by Picone et al.. The phenotype associated to each patient is reported in Table 5.6.

5.2.2 Computed and invasive central pressure comparison

To test the reliability of the patient-specific multiscale model in estimating the individual central BP, the procedure schematised in Figure 5.2 has been implemented. For each patient, the average waveform, $\mu_{(p(t))}$, and standard deviation, $\sigma_{p(t)}$, of central BP per beat over the recorded cardiac cycles have been calculated. Then signals $\mu_{(p(t))} \pm \sigma_{p(t)}$ have been compared against the corresponding simulated waveform, $\mu_{(p(t))comp}$.

Figure 5.3 displays measured central BP signals ($\mu_{(p(t))}$, continuous thin line, and $\mu_{(p(t))} \pm \sigma_{p(t)}$, dotted thin line) and corresponding simulated signals ($\mu_{(p(t))comp}$, continuous thick line) for all the patients. All signals are reported as a function of the non-dimensional mean heartbeat period, RR. Simulated signals well match the average measured signals, as one can visually notice, despite some shape dissimilarities emerge. It can be observed that simulated systolic BPs almost entirely fall within the interval $\mu_{(p(t))} \pm \sigma_{p(t)}$ of the measured systolic BPs. On the contrary, simulated diastolic BPs do not often fall in the interval $\mu_{(p(t))} \pm \sigma_{p(t)}$ of the measured diastolic BPs. This implies that modelling errors of the estimated central systolic BP are comparable with the same BP variability during the measurements, which

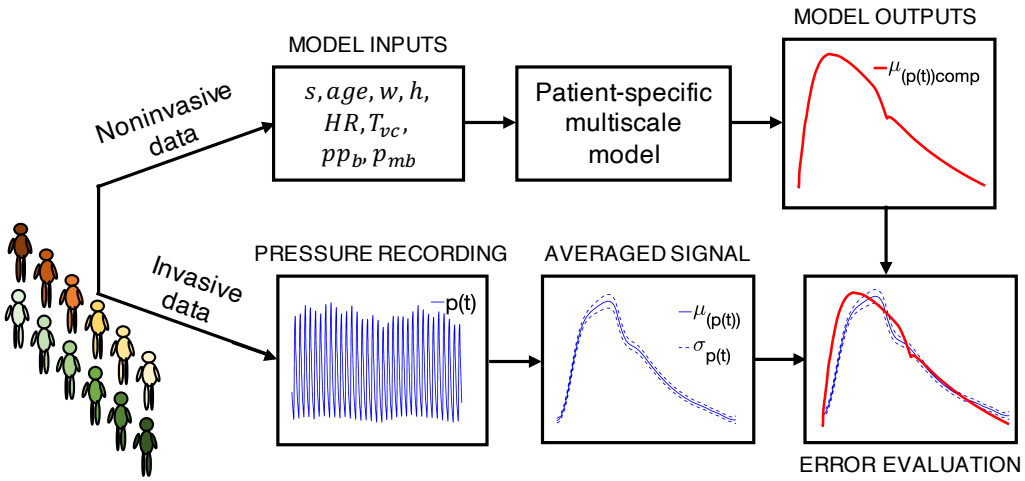

Figure 5.2: Schematic representation of the procedure implemented to prove the reliability of the patient-specific multiscale model.*Image extracted from* [94].

is due to both physiological BP fluctuations and measurement errors. By contrast, in the case of the central diastolic BP, modelling errors can be higher than diastolic BP variability detected during the measurements.

The accuracy of the model has been quantified, for each patient, by comparing the errors by both the reference model (the one without the patient-specific adjustments) and the patient-specific model in estimating central systolic, diastolic, mean and pulse BPs, with respect to the mean values of the related measured BPs indicated in Table 5.6. These results are reported in Table 5.7.

The reference model leads to higher mean errors in central systolic (26.12 mmHg), mean (10.43 mmHg) and pulse (28.46 mmHg) BPs with respect to the patient-specific model (4.2, 4.98 and 3.51 mmHg for systolic, mean and pulse BPs, respectively). Differently, slightly smaller mean errors occur in central diastolic BP (5 mmHg) with respect to the patient-specific model (5.86 mmHg). Based on these results, it is clear that the patient-specific adaptations we have proposed are effective in mimic the patient-specific BP responses. For diastolic BP, however, the mean error by the reference model is moderately littler than by the patient-specific model. One can observe that the reference model does not produce smaller errors in central diastolic BP for all the patients but for only five of the twelve patients, for who the error is significantly reduced. These five patients are associated to three over the four BP phenotypes indicated in Table 5.6, making it difficult to identify clear correlations between the error in central diastolic BP and one or more BP phenotypes. Therefore, only an extended number of patient data applied to this patient-specific model could tell us whether (i) central diastolic BP is actually smaller with the reference than with the patient-specific model, and (ii) the individual errors in central diastolic BP are correlated with one or more BP phenotypes.

Table 5.6: Mean values (μ_v) ± standard deviations (σ_v) of systolic (sys) and diastolic (dia) invasive BPs along the ascending aorta (AA), right brachial (RBA) and radial arteries (RRA). Coefficients of variation, $cv = \sigma_v/\mu_v$, are provided in percentage. The phenotype associated to each patient (I, II, III, or IV, see text), identified as indicated by Picone et al. [267], is reported in brackets below the Patient number. *Table extracted from* [94].

Patient number	AA		RBA		RRA	
	sys [mmHg]	dia [mmHg]	sys [mmHg]	dia [mmHg]	sys [mmHg]	dia [mmHg]
1	114.54	58.21	124.38	59.53	154.59	64.41
(I)	±3.21	±1.10	±4.07	±1.81	±2.33	±1.50
	2.80%	1.89%	3.27%	3.04%	1.51%	2.32%
2	131.66	78.95	113.25	82.07	127.44	72.79
(III)	±1.28	±1.01	±4.28	±2.49	±2.78	±1.49
	0.97%	1.28%	3.78%	3.03%	2.18%	2.05%
3	139.28	75.03	157.41	74.18	153.29	73.37
(II)	±3.02	±1.79	±2.34	1.54	±3.46	±2.04
	2.17%	2.39%	1.48%	2.07%	2.26%	2.79%
4	122.36	63.36	122.64	55.49	127.74	58.30
(III)	±1.89	±0.56	±2.41	1.09	±1.73	±0.84
	1.55%	0.89%	1.96%	1.97%	1.35%	1.45%
5	158.01	84.11	179.73	80.65	175.68	73.17
(II)	±5.19	±0.74	±4.32	3.46	±4.64	±2.78
	3.28%	0.88%	2.40%	4.29%	2.64%	3.80%
6	143.16	76.48	152.47	71.45	156.64	71.28
(II)	±2.34	±2.86	±2.95	1.91	±2.97	±2.34
	1.64%	3.74%	1.94%	2.68%	1.90%	3.28%
7	149.05	69.16	155.87	68.46	156.16	65.15
(II)	±5.29	±2.28	±4.78	1.67	±4.65	±2.63
	3.55%	3.30%	3.07%	2.45%	2.98%	4.04%
8	119.96	67.01	129.24	65.94	136.29	65.13
(I)	±3.51	±1.58	±2.75	1.95	±2.12	±1.11
	2.92%	2.36%	2.13%	2.96%	1.55%	1.70%
9	161.22	74.52	163.07	69.26	154.79	68.09
(IV)	±3.61	±2.12	±3.35	1.48	±10.63	±6.02
	2.24%	2.85%	2.05%	2.14%	6.87%	8.84%
10	135.91	73.69	140.07	70.72	157.84	72.85
(III)	±2.72	±0.95	±4.81	2.07	±2.22	±0.95
	2%	1.29%	3.43%	2.93%	1.41%	1.30%
11	177.26	74.32	177.21	72.86	183.60	73.26
(III)	±5.75	±2.82	±2.83	1.17	±3.28	±1.35
	3.24%	3.80%	1.60%	1.61%	1.79%	1.85%
12	137.46	71.90	152.44	69	145.57	65.81
(II)	±4.11	±2.03	±3.43	2.69	±3.01	±1.95
	3%	2.82%	2.25%	3.90%	2.07%	2.97%

By adopting the patient-specific model, differences between measured and modelled mean BPs appear quite acceptable. In fact, mean error is always ≤ 5 mmHg, apart from diastolic BP, and standard deviation is always ≤ 8 mmHg, which have been defined as the minimum acceptable errors in the central BP validation protocol [297].

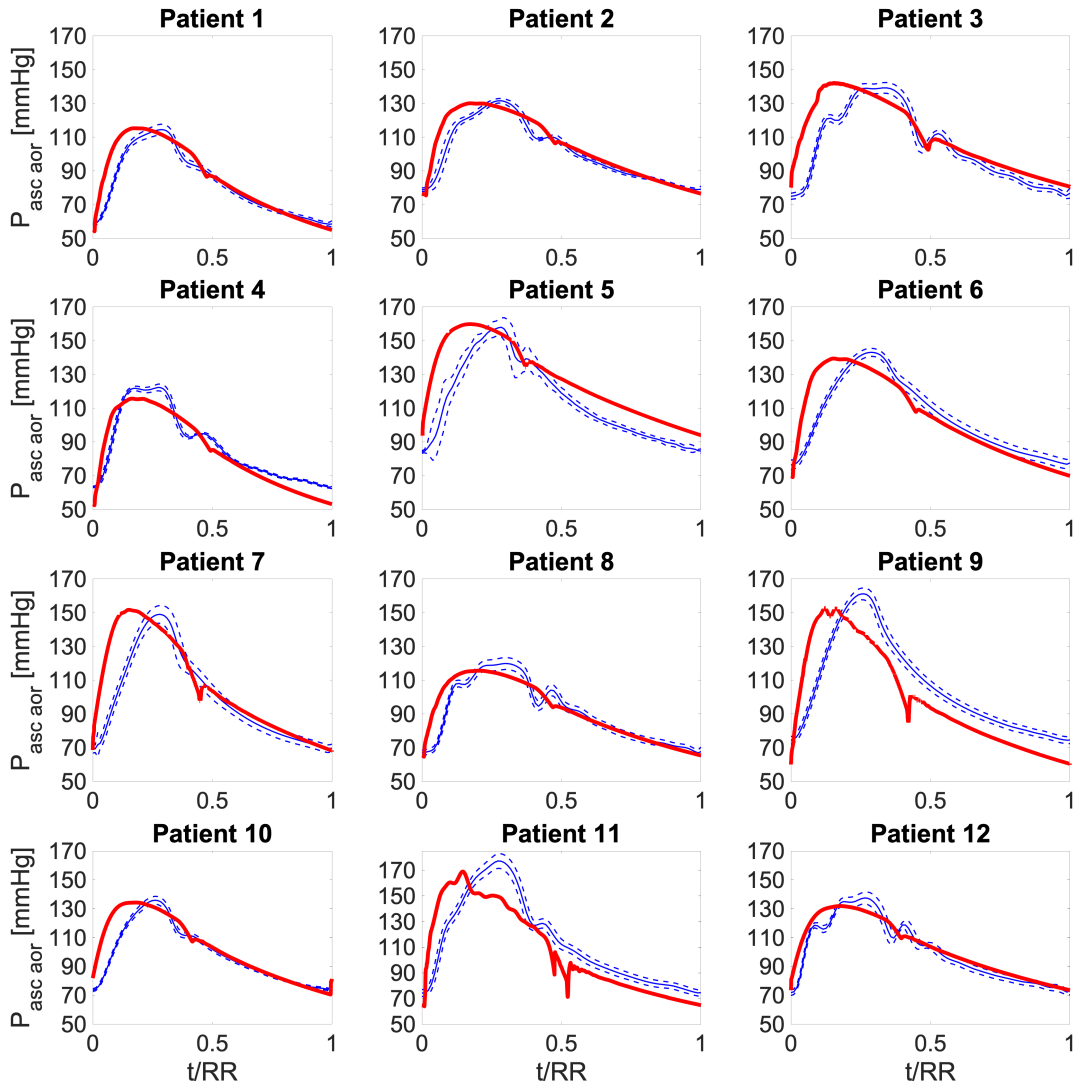

Figure 5.3: $\mu_{(p(t))}$ (continuous thin line) and $\mu_{(p(t))} \pm \sigma_{p(t)}$ (dotted thin line) of the measured central BP signals and corresponding simulated signals ($\mu_{(p(t))comp}$, continuous thick line). Time is made dimensionless by the heartbeat period, RR. *Image extracted from* [94].

Coherently with Figure 5.3, Table 5.7 confirms that diastolic BP errors are greater than systolic ones for the majority of patients. One can also notice that errors in mean BP are between errors in systolic and diastolic BPs, while large/small pulse BP errors do not necessarily correspond to large/small systolic and diastolic BP errors.

Scatter plots between simulated central systolic/diastolic BPs and catheter measurements are given in Figure 5.4, together with coefficients of determination (R^2).

Table 5.7: Errors ([mmHg]) in simulated central systolic (sys), diastolic (dia), mean (mean) and pulse (pp) BPs through both the general (superscript G) and patient-specific (superscript PS) models, evaluated with respect to the mean values of the same invasive BPs along the ascending aorta (AA). Moduli of mean errors ± standard deviation are reported in bold in the last row. *Table extracted from* [94].

Patient	General model				Patient-specific model			
	sys^G	dia^G	$mean^G$	pp^G	sys^{PS}	dia^{PS}	$mean^{PS}$	pp^{PS}
1	0.19	16.08	10.78	-15.89	0.14	-3.23	-2.10	3.37
2	-16.93	-4.66	-8.75	-15.89	-2.25	-2.71	-2.56	0.45
3	-24.55	-0.74	-8.68	-23.81	2.90	5.14	4.39	-2.23
4	-7.63	10.90	4.74	-18.56	-7.53	-10.16	-9.28	2.63
5	-43.28	-9.82	-20.97	-33.46	1.84	9.80	7.15	-7.96
6	-28.43	-2.19	-10.94	-26.24	-4.94	-6.55	-6.01	1.60
7	-34.32	5.13	-8.02	-39.45	2.62	-1.38	-0.045	3.99
8	-5.23	7.28	3.11	-12.51	-4.80	-1.62	-2.68	-3.18
9	-46.49	-0.23	-15.65	-46.26	-8.55	-14.56	-12.56	6.01
10	-21.18	0.60	-6.66	-21.78	-1.60	-3.07	-2.58	1.48
11	-62.53	-0.03	-20.86	-62.50	-8.34	-10.36	-9.69	2.02
12	-22.73	2.39	-5.98	-25.12	-5.56	1.69	-0.73	-7.25
	26.12 ±18.29	**5 ±5.10**	**10.43 ±5.87**	**28.46 ±14.68**	**4.26 ±2.81**	**5.86 ±4.38**	**4.98 ±3.95**	**3.51 ±2.38**

These latter are equal to 0.95 and 0.67 for systolic and diastolic BPs, respectively, thereby reflecting larger errors by the model for diastolic than for systolic BPs.

Bland-Altman plots of the central systolic and diastolic BP errors by the model are depicted in Figure 5.5. The coefficients of determination, R^2, for the relations between the central BP error and the mean central BP are 0.035 for systolic and 0.11 for diastolic BP. Thus, the present data suggest that the error magnitude does not depend on systolic BP, even if it is slightly correlated to diastolic BP.

To contextualise this patient-specific modelling approach within the current medical scenario, we have compared the errors produced by our method with the ones through one of the most common medical device to noninvasively estimate central BP, the SphygmoCor, and generalized/variable transfer functions. The SphygmoCor generates errors in central systolic, diastolic and pulse BPs of -8.2±10.3 mmHg, 7.6±8.7 mmHg, -12.2±10.4 mmHg, respectively, with the calibration performed through brachial cuff BP. These errors were extracted from a large meta-analysis including 857 subjects [51]. With respect to these results, our method seems promising, although it still needs to be verified in an extended cohort of individuals. In other works by Shih et al. [305, 304], where central BP was evaluated through an ensemble averaged generalised transfer function derived from 40 individual transfer functions, smaller mean errors (in modulus) in central systolic BP (-2.2±6.4 mmHg in [305] and -2.1±7.7 mmHg in [304]) were found,

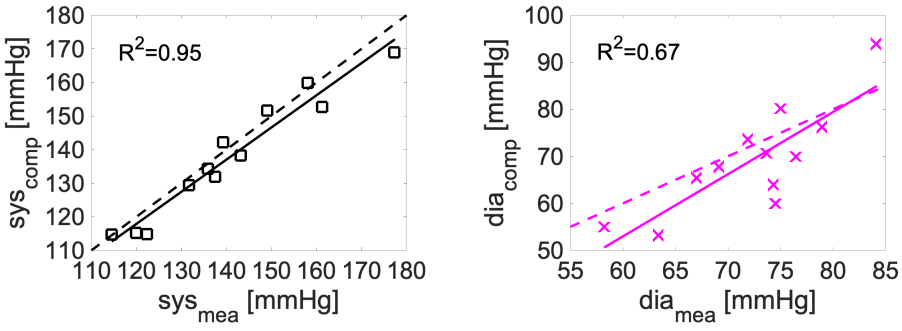

Figure 5.4: Scatter plots between computed (subscript comp) systolic (sys) and diastolic (dia) BPs and measured (subscript mea) values. R^2 is the coefficient of determination. *Image extracted from* [94].

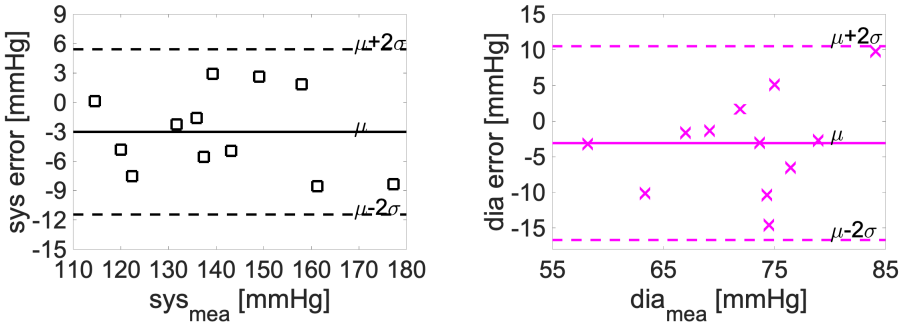

Figure 5.5: Bland-Altman plots of the central systolic (sys) and diastolic (dia) BPs errors by the model. *Image extracted from* [94].

albeit larger errors in central pulse BP (10.3±8 mmHg in [305]) were detected, compared to our patient-specific model. More recently, a new physiology-based technique was proposed by Natarajan et al. [230] to get central BP via a standard automatic arm cuff. In particular, they applied a variable transfer function method to the brachial BP-like waveform, which was in turn determined through an ensemble averaging/calibration procedure, with brachial systolic and diastolic BP for calibration obtained from the application of a patient-specific method to an oscillogram. The technique by Natarajan et al. yields errors in central systolic, diastolic and pulse BP between -0.6 and 2.6 mmHg and corresponding standard deviation in the range 6.8-9 mmHg. Thus, despite the proposal by [230] generates reduced mean errors with respect to our model, standard deviations double compared to ours.

It is clear that the errors by our modelling approach largely depend on the errors committed during the brachial oscillometric measurement, from which the brachial

mean and pulse BPs (p_{mb} and pp_b) adopted in the patient-specific calibration of the reference model were extracted. Indeed, the role of these two parameters in making the reference model patient-specific has been proved by the sensitivity analysis in section 5.1.8. Considering the latter, it is predictable that any error associated to the input data p_{mb} and pp_b is transmitted (with the same order of magnitude) to the output data, namely the central BP values. However, despite the automatic oscillometric device we adopted to assess brachial systolic and diastolic BP is widely used in clinical practice, no peer-reviewed clinical validation information is available on this technology. Therefore, a direct comparison between the input errors in the values of p_{mb} and pp_b and the output errors in the estimations of central BP for the 12 patients is not possible here.

5.3 Future developments for the present patient-specific model

The patient-specific modelling approach represents a promising instrument to noninvasively estimate central BP. However, successive efforts need to be addressed to test the reliability of this methodology over a larger cohort of individuals, and more deeply individuate correlations between BP errors and impacting factors. Moreover, a direct comparison between input and output errors by the model should be executed, and the possibility to further reduce the model errors should be investigated, for example, by adopting more accurate oscillometric BP measurement techniques, like the one proposed by Liu et al. [185] and employed by Natarajan et al. [230]. This because of the bias errors introduced by cuff on brachial BP. In any case, the outcomes provided by this patient-specific modelling approach may be regarded as an invitation to continuing working on similar *in-silico* techniques for their use in clinical trials. In fact, apart from providing central BP, they can offer the complete BP and flow rate map of the whole cardiovascular system, as well as the full list of the most common haemodynamic parameters adopted in medical treatments.

Chapter 6

Effects of atrial fibrillation on arterial haemodynamics

Some of the contents of this chapter have been previously published in [93, 291, 293].

This chapter offers some results about the direct effects of atrial fibrillation (AF) on arterial haemodynamics, based on a simplified version of the general multiscale mathematical model presented in chapter 3. An overview of AF is provided in section 6.1, the instrument to simulate atrial fibrillation is described in section 6.2, which precedes section 6.3, offering a brief description of the adopted modelling approach and detailing the model outcomes.

6.1 AF: definition, types, cures, epidemiology and associated risks

AF is one of the most common form of arrhythmia and belongs to the group of supraventricular tachycardias. It occurs when the electrical rhythm is not coordinated by the sinus node and many impulses fire at the same time in the atria with a frequency of 300-600 times/min [231]. Thus, atria experience fast and chaotic electrical signals and start quivering instead of contracting. In this condition, the atrioventricular node receives irregular impulses, resulting in an unsynchronized ventricular rhythm and a rapid ventricular rate (HR), which typically increases from 60-100 bpm to 100-175 bpm with respect to sinus rhythm (SR) [367].

AF can be simply detected through an ECG. Since standard atrial depolarisation is absent in AF, fibrillated ECGs lack of the classical P waves, which are replaced by the so called f waves. These latter appear as high frequency oscillations of the isoelectric line, as shown in Figure 6.1. In addition, irregular and high HRs

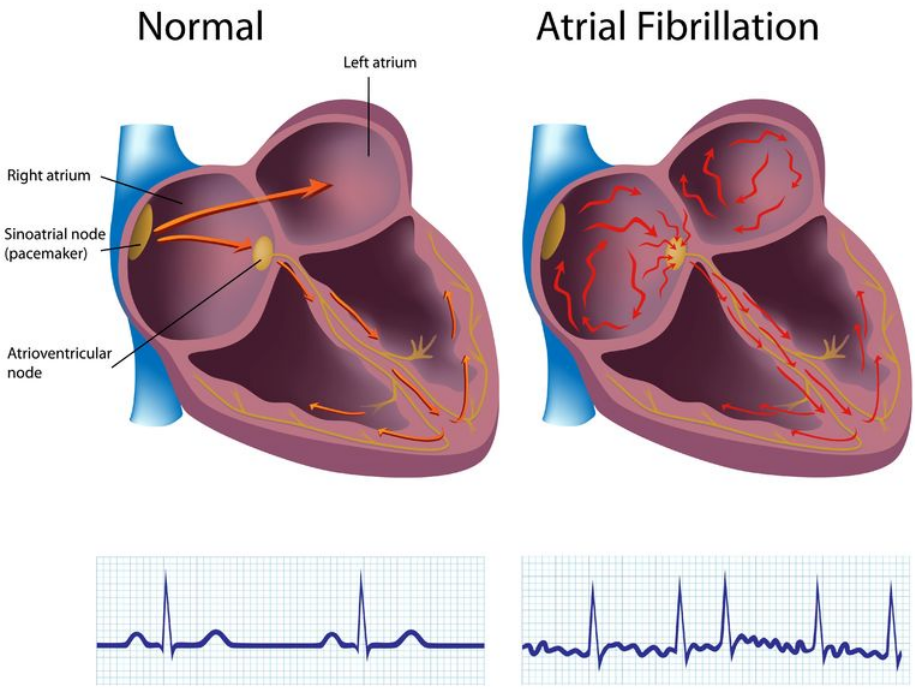

Figure 6.1: Comparison between the electrical signal propagation and the ECGs in SR, on the left, and AF, on the right. *Image extracted from* [45].

can be observed in AF ECGs, where the time intervals between the QRS complexes are more variable and smaller compared to SR, as visible in Figure 6.1.

Different classes of AF can be identified based on the duration of the episodes [133, 376]. Paroxysmal AF happens with variable frequency and terminates spontaneously or with intervention within 7 days. Persistent/long-standing AF consists in sustained anomalous heart rhythm for more than 7 days/12 months, even with treatment, and eventually resolves on its own or with help. Finally, permanent AF is characterized by the unresponsiveness to any therapy, and is so defined as patient and clinician decide to stop any attempt to come back to SR.

AF can be treated with different methods, going from pharmacological/electrical cardioversion, which aims at restoring SR through antiarrhythmic medications/electrical shocks, to catheter ablation, that is intended to destroy the areas of the myocardium where an abnormal and independent electrical signal production is discovered. Nevertheless, none of the methods implemented to date effectively leads to a definitive

resolution of AF, especially in persistent cases. To this purpose, a deeper understanding of AF determinants is unanimously believed necessary to design innovative and more effective treatment approaches [232]. In fact, despite it is well established that the two major causal factors of AF pathophysiology are the ectopic foci[1] activity and re-entry[2] [233], there are ongoing controversies about the fundamental mechanisms underlying AF and governing the initiation, maintenance and progression of this complex and evolutionary pathology [118].

Nowadays, AF represents a significant public health problem with a prevalence between 1% and 4% in Australia, Europe and the USA [386]. It has been verified that AF prevalence continues increasing over time, especially in industrialized countries, with about 14-17 millions of AF patients expected in 2030 in Europe alone [385]. The worrying and growing prevalence rate of AF, mainly due to both the rise of life expectancy and the improved capability to recognise and treat a great deal of disease conditions, results in huge economic burdens for the national heath services. One can just think that the current direct cost per patient and per year amounts to 10100-14200 $ in the USA and to 450-3000 € in Western Europe [371].

The probability to develop AF gets higher with age and among men then women of the same age [141]. Indeed, AF prevalence rate ranges between <0.5%-1.0%, 1%-4%, and 6%-15% at 50, 65 and 80 years, respectively. In addition, men have 1.5-fold risk to be affected by AF [10]. Apart from ageing and male sex, confirmed cardiovascular risk factors associated to AF are hypertension, valvular heart disease, congestive heart failure, coronary artery disease and diabetes mellitus, together with left ventricular hypertrophy, obesity and excessive alcohol use [168].

Despite 12-42.5% of patients affected by AF are asymptomatic, AF can often provoke disabling effects such as palpitations, chest pain, dyspnea, dizziness, shortness of breath and reduced exercise capacity, all contributing to a marked reduced quality of life [117]. In fact, even patients suffering from intermittent AF complain an impairment of their quality of life, based on measures of physical, social, mental and general heath, and evaluate these aspects similarly to people subjected to more severe cardiac diseases (e.g., heart failure and post infarction) [67].

AF is usually associated to a 3- to 5-fold enhanced risk of stroke, even if this association is not fully verified over the whole age range, as well as in case of sole AF, and seems to involve other comorbidities [138]. AF is also related to heart failure,

[1] Ectopic foci are automatic electrical impulse generators within the heart, which can trigger tachycardias depending on their locations and the electrical activity of the closest regions.

[2] Re-entry happens when an electrical impulse does not die after the expiration of its refractory period and continuously excites the same cardiac region [13].

with <10% and about 50% of AF cases among patients affected by mild and severe heart failure, respectively [196]. However, the cause-effect relationship between AF and heart failure has not been completely understood, with their frequent coexistence probably due to the presence of common risk factors favouring both the pathologies [11].

AF is though to independently increase the risk of death. At 10 years of follow-up during the Framingham Heart Study, amongst the subjects in the age range 55-74 years, died men with and without AF were 61.5% and 30%, and died women with and without AF were 57.6% and 20.9%, respectively [23]. Notwithstanding, the probability of individual survival in presence of AF is believed to be strongly dependant on age and a set of other disturbs. Good evidence of this can be found in the fact that AF patients above 75 years have 3 times the absolute risk of mortality than AF patients below 65 years, and the mortality rate among people with alone AF is comparable to that of AF-free subjects of similar age and same sex [288].

6.2 How to computationally reproduce atrial fibrillation?

AF and SR have been simulated in this Thesis by imposing artificially built RR interval time series, whose probability density functions, PDFs, and power spectra, $S(f)$ (f is the beat frequency), have the same characteristics of real fibrillated and healthy RR beatings, respectively. To this aim, we have exploited the results merging from the work by Hennig et al. [115, 122]. They found that the PDF of AF RR intervals shows a well visible exponential tail, which is absent in SR. Moreover, while the power spectrum of SR RR intervals exhibits a $1/f$ linear behaviour over the whole frequency range, the AF spectrum displays a characteristic angular shape. In particular, the long-term component (at low frequencies) of the AF spectrum is characterized by a $1/f$ linear pattern, instead, the short-term component (at high frequencies) appears flat, with the breakpoint frequency between the two components localised at 0.005 ± 0.002 Hz (see Figure 6.2). It was proved that the $1/f$ power spectrum is associated to the pink noise [150], which is negatively correlated, while the flat spectrum corresponds to the white noise, consisting in a series of uncorrelated values.

Based on the above findings, we have obtained the SR and AF RR interval time sequences used in the studies of the present chapter as follows. The generic SR RR sequence has been extracted from a pink noise-like Gaussian distribution, with mean value $\mu_v = 0.8$s and coefficient of variation $cv = \mu_v/\sigma_v = 0.07$ (μ_v=60/HR: mean of the RR distribution, σ_v: standard deviation), which is expected between 0.04-0.17 during SR [122, 268, 292, 315]. The generic RR sequence in AF, instead, has been constructed as combination of two statistically dependant times, as RR=$\tau_G + \tau_E$. τ_G has been drawn, as in SR, from a pink noise-like Gaussian distribution, with

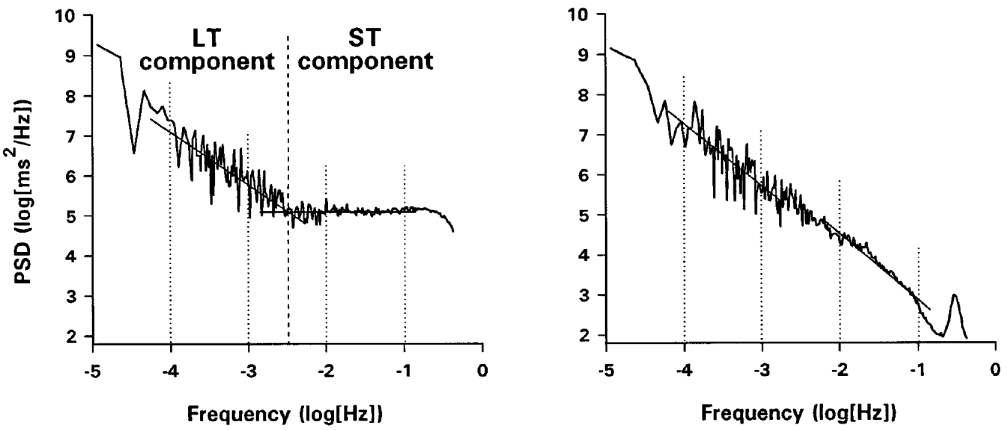

Figure 6.2: Power spectral densities of 24h RR fluctuations in AF, left, and SR, right. Vertical and horizontal axes are in logarithmic scales. *Image extracted from* [115].

mean value μ_G, standard deviation σ_G and coefficient of variation cv_G. τ_E has been taken from an uncorrelated white noise-like exponential distribution, characterized by the rate parameter γ_E [292]. To reproduce different mean HRs in AF, μ_G has been varied accordingly, while cv_G has been always maintained constant and equal to 0.24, as usual in AF [335]. The decay rate parameter γ_E has been estimated from 84 long-term RR recordings belonging to the MIT-BIH Long-Term AF Database [100, 266] as γ_E=-9.2RR+14.6. In this fashion, the generic AF RR sequence has been reproduced through an exponentially modified Gaussian distribution, with mean value $\mu_E = \mu_G + \gamma_E^{-1}$ and standard deviation $\sigma_E = \sqrt{\sigma_G^2 + \gamma_E^{-2}}$ [292].

Notice that this way to reconstruct the AF sequence of RR interbeat intervals can be applied to fibrillated unimodal distributions only, which represent the majority of the AF distributions (61%), together with the bimodal (32%), trimodal (5%) and multimodal (2%) [361]. Thus, we have modelled AF just considering the case of unimodal distributions, which are more typical among AF patients.

6.3 Two computational studies in atrial fibrillation

This section shows the results of two studies about the fallouts of AF on the arterial haemodynamics.

The first study (Arterial tree study) goal is to inquire into the impact of the sole heart rhythm variation from SR to AF at 75 bpm on the haemodynamics of the arterial tree, and is based on the work [291], which has been developed during

my PhD.

The second study (Coronary study) aims at inquiring into the effects of five different HRs in AF on coronary perfusion, and derives from the works [93, 293], which have been carried out as part of my research program.

In both studies AF (and SR) has been reproduced as explained in the above section, while the combination arterial tree-left coronary circulation has been simulated through a simplified version of the model presented in chapter 3. A summary of the main differences between the model in chapter 3 and the one used in the arterial tree and coronary studies is provided below.

6.3.1 A model of the left heart-arterial tree with the left coronary circulation

The simplified version of the model adopted in the arterial tree and coronary studies is made of the 1D model of the systemic arterial tree outlined in section 3.1, coupled with the multiscale (0D-1D) model of the left coronary circulation illustrated in section 3.4. The systemic arterial tree is then closed, at the ascending aorta, by a 0D model of the left heart and, at peripheral arteries, by 3-elements Windkessel models, which account for the total effect of distal circulation (from small arteries to capillaries) [107]. Thus, the most striking aspect of this simplified model, compared with the one in chapter 3, is that it is not closed-loop. This means that the pressure and flow rate signals at the ascending aorta are independent from the outlet signals, and are instead forced at each heartbeat period by the contracting activity of left ventricle. A sketch of this simplified model, with a representation of the 0D models applied to the extremities of the systemic arterial tree, is depicted in Figure 6.3.

As one can see from this last Figure, left-atrial pressure, p_{la}, is taken constant and equal to 8.5 mmHg, and mitral valve is simulated as a simple resistance, R_{MV}=3 mmHgs/l. Left-ventricular pressure, p_{lv}, continues to be reproduced through equation (3.96), while left-ventricular volume, V_{lv}, is obtained from the volume balance equation

$$V_{lv} = V_{0,lv} + \frac{p_{la} - p_{lv}}{R_{MV}} - Q_{aor}\Delta T/2. \tag{6.1}$$

In this last one, $V_{0,lv}$ is the unstressed left-ventricular volume, Q_{aor} is the aortic flow rate (provided by the resolution of the boundary condition at the ascending aorta as in the (B.2)), and ΔT is the constant time step imposed for the numerical resolution (it is divided by 2 since boundary conditions are solved at each half time step as explained in section 3.2.3). The aortic valve is represented through the

(3.100) and the relative coupling with the 1D aorta is done as in the (B.2).

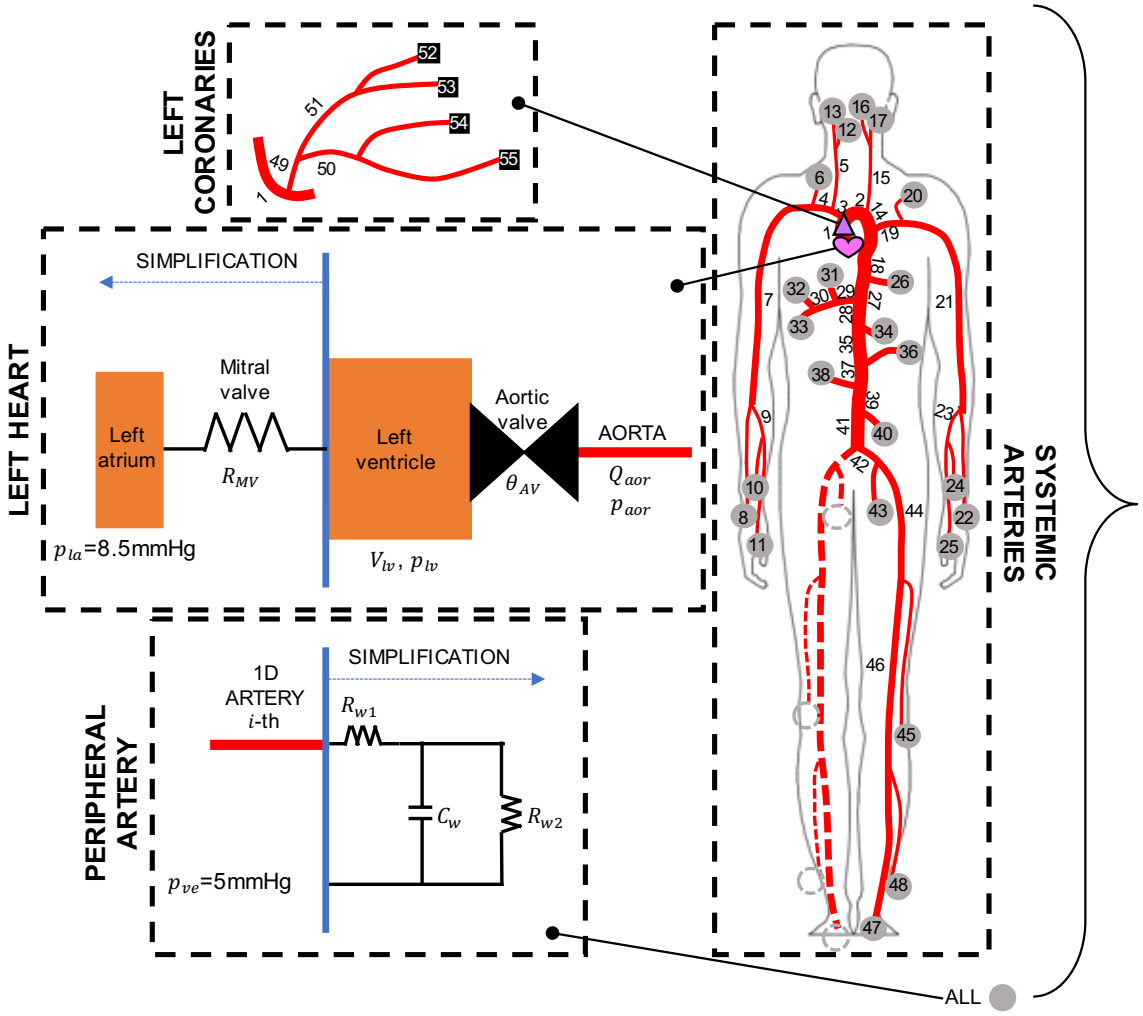

Figure 6.3: Representation of the simplified model adopted in this chapter. It includes the 1D representation of the systemic arterial tree and the multiscale (0D-1D) model of the left coronary circulation. It is closed by a 0D model of the left heart at the entrance to aorta and by a 3-elements Windkessel model at each peripheral artery. Differences with respect to the model in chapter 3 are marked with the term SIMPLIFICATION.

The 3-elements Windkessel model closing each peripheral 1D artery, also depicted in Figure 6.3, corresponds to equation

$$\frac{dQ_w}{dt} - \frac{1}{R_{w1}}\frac{dp_w}{dt} = \frac{p_w - p_{ve}}{R_{w1}R_{w2}C_w} - \left(1 + \frac{R_{w1}}{R_{w2}}\right)\frac{Q_w}{R_{w1}C_w}. \tag{6.2}$$

Q_w and p_w are the flow rate and pressure at the outlet of the terminal artery, R_{w1}, R_{w2} and C_w are the proximal resistance, distal resistance and compliance of the peripheral circulation beyond the terminal artery, and p_{ve}=5mmHg is a constant venular pressure. Q_w and p_w are calculated together with the other boundary conditions at each half time step, by combining equation (6.2) with the compatibility condition adopted for distal 1D arteries, similarly to what done in equation (B.3). The values of R_{w1}, R_{w2} and C_w are given in Table C.1.

Notice that this simplified model lack of the baroreflex model introduced in section 3.5, meaning that, in the arterial tree and coronary studies, we neglect to consider the internal mechanism of short-term automatic regulation of mean arterial pressure.

In simulating AF, we have not taken into account the cardiac force-frequency relationship due to the RR variability [156]. We recall that the left-ventricular elastance model (see equation (3.97)), here integrated in the left ventricular model, is defined through an activation function depending on RR (see equation (3.99)). However, a reduction in the maximum value of the left ventricular elastance, usually detected in chronic AF cases with concomitant cardiomyopathy, has been neglected [333]. This because of the contrasting trends merging in literature about the possibility that a similar dysfunction is present with AF alone [334].

6.3.2 Arterial tree study: effects of AF on arterial haemodynamics

Introduction of the arterial tree study.

The direct effect of AF on arterial haemodynamics is far from being well established, with literature results reporting contrasting information in terms of both cardiac and systemic arterial pressures [7, 55, 99, 137]. This is not surprising considering that AF rarely manifests alone but in concert with a variety of other cardiovascular disturbs, which make it difficult to isolate the net role of AF on our cardiovascular system. Moreover, the reliability of automated oscillometric instruments to assess blood pressure fluctuations in AF remains controversial [257, 322], and current clinical devices can fail in detailing the blood flow field throughout the vasculature. In fact, their resolving power can be insufficient to keep up with the continuous heart rate oscillations during AF [331].

In this context, we aim at exploring the variability of arterial haemodynamics triggered by the sole heart rhythm alterations in AF, which has been poorly analysed so far. In particular, it is not known how pressure and flow rate signals are affected by the AF rhythm, and whether the modifications induced by the AF

rhythm can have a negative impact on physiological tissue and organ perfusion. Olbers and co-authors [251] demonstrated that the beat-to-beat systolic and diastolic blood pressure variability in AF is 2-fold and 6-fold compared to SR, respectively, that is believed to alter the normal vascular structure and functioning. In fact, it seems that not only high blood pressure but also high blood pressure variability can lead to the development of atherosclerosis in the long term. This was proved in a numerical study by Xiong et al. [375], where the response of a two dimensional stenosed artery model to different blood pressure variations (during a single cardiac cycle and beat-to-beat) was simulated.

In this study, we have analysed the haemodynamic variability at arterial level by imposing two sequences of 2000 heartbeat periods, one in SR (RR_{SR}) and the other in AF (RR_{AF}), to the left heart-arterial tree model outlined in section 6.3.1. The RR sequences have been constructed as explained in section 6.2, and the number of simulated cardiac periods (that correspond to about half an hour of cardiac activity) has been chosen in order to guarantee the statistical reliability of the model outcomes. Since the scope of the present study is to focus on the role of the sole heart rhythm variations in AF compared to SR, we have simulated SR and AF at the same mean heart rate: HR=75bpm (mean RR value: 0.8 s). Thus, among the features of the RR beating, we have included the increased temporal variability and reduced temporal correlation but have neglected the accelerated heart rate.

Beating features of the arterial tree study.

The RR_{SR} and RR_{AF} series, and the relative PDFs are reported in Figure 6.4, while the main statistics of the same series are offered in Table 6.1.

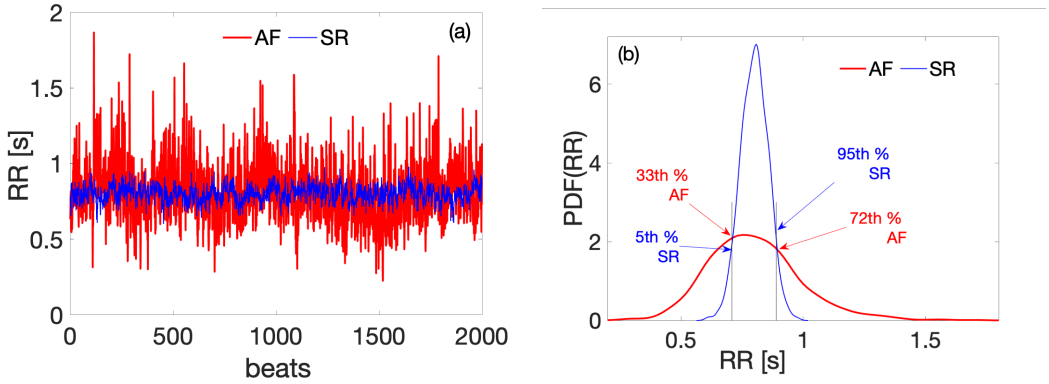

Figure 6.4: (a) Simulated sequences of 2000 RR interbeat intervals in SR (blue thin line) and AF (red thick line), and (b) relative PDFs, PDF(RR). The 5th and 95th percentiles of the PDF(RR) in SR correspond to the 33rd and 72nd percentiles in AF. *Image extracted from* [291].

Table 6.1: Statistics of the simulated sequences of 2000 RR interbeat intervals in SR (RR_{SR}) and AF (RR_{AF}). μ_v: mean value, σ_v: standard deviation, $cv = \sigma_v/\mu_v$: coefficient of variation. *Table extracted from* [291].

Case	μ_v [s]	σ_v [s]	cv
RR_{SR}	0.80	0.06	0.07
RR_{AF}	0.80	0.19	0.24

Results of the arterial tree study.

The multiscale modelling approach has allowed us to gain 2000 complete left-ventricular pressure and volume signals and 2000 complete pressure and flow rate signals at each arterial section of the modelled domain. Thus, we have identified some quantities of interest regarding the left ventricle and the following arteries, and have calculated their PDFs from the 2000 corresponding data. Each PDF has been characterized by its mean value, μ_v, standard deviation, σ_v, and coefficient of variation, $cv = \sigma_v/\mu_v$. The AF-induced changes for each haemodynamic parameter have been quantified through the changes in the μ_v and cv values from SR to AF, and/or by analysing the percentile variations between SR and AF. Regarding this last point, we have identified, for each variable, the 5th and 95th percentiles in the SR PDF as references. Then, we have evaluated to which percentile each of the SR reference corresponds to in the AF PDF. In this way, the probability to reach extreme haemodynamic values in AF compared to SR has been assessed, regardless of the specific PDF shape. This procedure is graphically represented in Figure 6.4b for the RR distribution. As one can see from this latter, the RR values associated to the 5th and 95th percentiles in SR correspond to the 33rd and 72nd percentiles in AF.

The main results of this study are presented in the following four paragraphs. In particular, the first one concerns (A1) the principal cardiac and haemodynamic parameters, the second one (A2) the pressure patterns from heart to periphery along large-to-medium arteries, the third one (A3) the mechanisms of wave propagation and reflection, and the fourth one (A4) the organ perfusion at the principal gastrointestinal bifurcations.

A1: Cardiac and haemodynamic parameters. The principal statistics of the most important cardiac and haemodynamic parameters got from the SR and AF simulations are reported in Table 6.2. In SR, one observes that the mean cardiac parameters (stroke volume: SV=66.57 ml, ejection fraction: EF=55.38%, cardiac output: CO=4.99 l/min, stroke work: SW=0.92 J) and aortic pressures (systolic aortic pressure: $p_{aor_{sys}}$=120.50 mmHg, diastolic aortic pressure: $p_{aor_{dia}}$=71 mmHg) are in good agreement with the expected physiological values [46, 110, 148, 365]. It

also emerges a satisfying qualitative correspondence between our results and those available in literature, concerning the mean AF variations with respect to SR (see the last two columns in Table 6.2).

Table 6.2: $\mu_v \pm \sigma_v$ of the indicated cardiac parameters (V_{edlv}: end-diastolic left-ventricular volume, V_{eslv}: end-systolic left-ventricular volume, p_{edlv}: end-diastolic left-ventricular pressure, p_{eslv}: end-systolic left-ventricular pressure, SV: stroke volume, CO: cardiac output, EF: ejection fraction, SW; stroke work, all defined in chapter 1.1) and aortic pressures ($p_{aor_{sys}}$, $p_{aor_{dia}}$ and pp_{aor}: systolic, diastolic and pulse pressures at the entrance to the aorta, respectively) in SR (Columns II) and AF (Columns III). Ratios of the cv values in AF and SR, cv_{AF}/cv_{SR}, (Column IV). Average variations during AF with respect to SR (Column V). Available literature variations (Column VI). "+" increase during AF, "-" decrease during AF, "=" no significant variations during AF, "/" no data available. *Table extracted from* [291].

Variable	$\mu_v \pm \sigma_v$		$\frac{cv_{AF}}{cv_{NSR}}$	Mean variations in AF with respect to NSR	
	NSR	AF		Present results	Literature results
V_{edlv} [ml]	120.21 ± 0.04	120.09 ± 1.17	31.41	-	= [255], + [11, 338]
V_{eslv} [ml]	53.64 ± 1.23	54.18 ± 3.70	2.97	+	= [255], + [11, 338]
p_{edlv} [mmHg]	8.35 ± 0.01	8.34 ± 0.09	31.42	-	- [7]
p_{eslv} [mmHg]	93.27 ± 2.29	92.26 ± 7.59	3.35	-	/
SV [ml]	66.57 ± 1.27	65.91 ± 4.19	3.34	-	- [7, 59, 99, 112, 287], = [144]
CO [l/min]	4.99 ± 0.09	4.94 ± 0.31	3.34	-	- [55, 59, 65, 112, 143] ... ...[220, 255, 287, 346], = [278, 296]
EF [%]	55.38 ± 1.04	54.87 ± 3.30	3.20	-	- [11, 52, 96, 338, 373]
SW [J]	0.92 ± 0.01	0.91 ± 0.04	3.10	-	- [143, 255]
$p_{aor_{sys}}$ [mmHg]	120.50 ± 3.17	120.73 ± 9.34	2.94	+	+ [99, 137], = [7, 55]
$p_{aor_{dia}}$ [mmHg]	71.00 ± 3.04	71.64 ± 9.69	3.16	+	+ [7, 99, 137], = [55]
pp_{aor} [mmHg]	49.51 ± 0.31	49.10 ± 1.40	4.51	-	- [137]

It is worth noting that a strict quantitative correspondence between our results and literature data in AF has not been possible here. In fact, literature results are often heterogeneous, with the analysed patients (i) having dissimilar age, sex, class of AF (paroxysmal, persistent, permanent), and concomitant pathologies, (ii) being subjected to different AF treatments (cardioversion, catheter ablation, anti-arrhythmic medications, etc.), and (iii) being observed for incomparable follow-up periods. Since this version of the model is not patient-specific and is intended to provide a global heart-arterial response to AF for a young man, the comparison between the present outcomes and the results available in literature can be just qualitative. Moreover, since the scope of the work is to investigate the sole heart

rhythm variations in AF on the arterial system, we have taken the same mean heart rate in both the SR and AF simulations. It follows that the percentage variations of the mean values from SR to AF are often negligible and underestimated. Nonetheless, it appears that an irregular and uncorrelated RR beating in AF, taken the same mean HR of the SR case, has the potential to trigger haemodynamic variations going in the same direction of the ones detected during fibrillated clinical measurements.

A representation of the P-V loops of the 2000 heartbeat periods in SR and AF is given in Figure 6.5. The limited variations in the end-diastolic volume and pressure during both SR and AF are of course due to the hypothesis of constant atrial pressure applied to the model adopted for this work (see section 6.3.1). However, despite this modelling limitation, the comparison between the P-V loop series in SR and AF well highlights the enhanced variability induced by AF at the level of the heart with respect to SR.

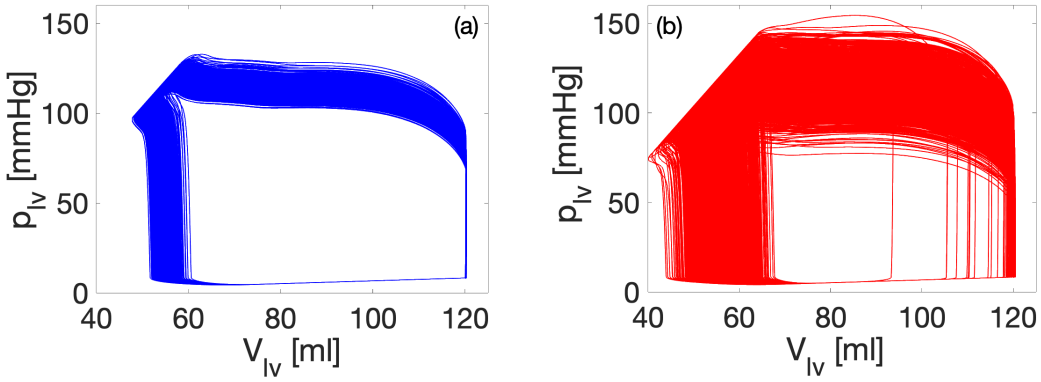

Figure 6.5: P-V loops of the 2000 heartbeat periods in SR (a) and AF (b). *Image extracted from* [291].

A2: Pressure patterns along large-to-medium arteries. The characteristic arterial pressure patterns in AF compared to SR have been evaluated in terms of systolic, diastolic and pulse pressure from the entrance to the aorta to the periphery. The distance from the heart has been identified through the the variable x [cm], which is just indicative of the arterial site and neglects to consider the different number of bifurcations between the heart and the considered site.

A representation of the PDFs of the systolic and diastolic pressures at some arterial locations, together with some portions of the complete pressure time series, are shown in Figure 6.6. One can observe from the latter that the tails of the PDFs in AF are much more extended than in SR, meaning that the probability of reaching extreme pressure values is much more higher in a fibrillated case than in

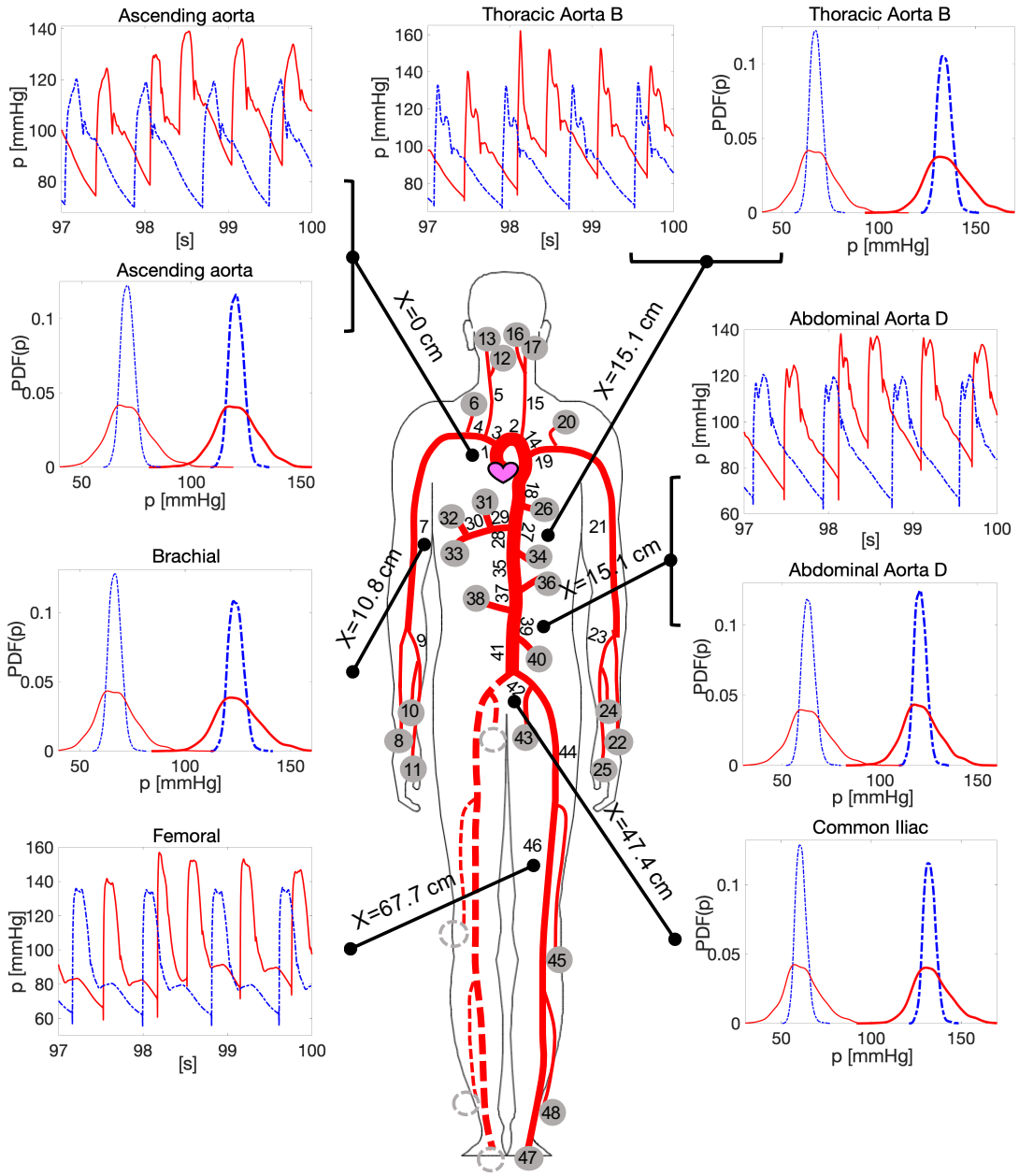

Figure 6.6: Representation of the pressure-time series and PDFs of systolic (thicker line) and diastolic (thinner line) pressures at the indicated arterial sites in SR (dotted blue line) and AF (continuous red line). x is the distance from the heart, starting from the entrance to the aorta (x=0 cm). *Image extracted from* [291] *with modifications.*

a healthy one. Moreover, it is apparent that the AF-induced pressure variability spreads over the whole arterial system up to the lower limbs.

The mean arterial pressure behaviour in SR, together with the typical arterial pressure oscillations during SR along x, is provided in Figure 6.7. Panel a shows that mean systolic pressures increase, while mean diastolic pressures decrease, with the distance from the heart, resulting in a growth in mean pulse pressures further away from the heart. This is in accordance with the physiological expectations [46, 110]. From Figure 6.7b, one sees that systolic, diastolic and pulse pressure oscillations around mean values are between 2-3%, 4-5% and 1-2%, respectively, and the *cv* values rise/reduce for diastolic/systolic pressures with x. This means that, already in SR, the arterial system non-monotonically amplifies diastolic fluctuations, while reducing systolic ones, thereby contributing to an extremely variable pattern for the *cv* pulse pressure values along the arterial tree.

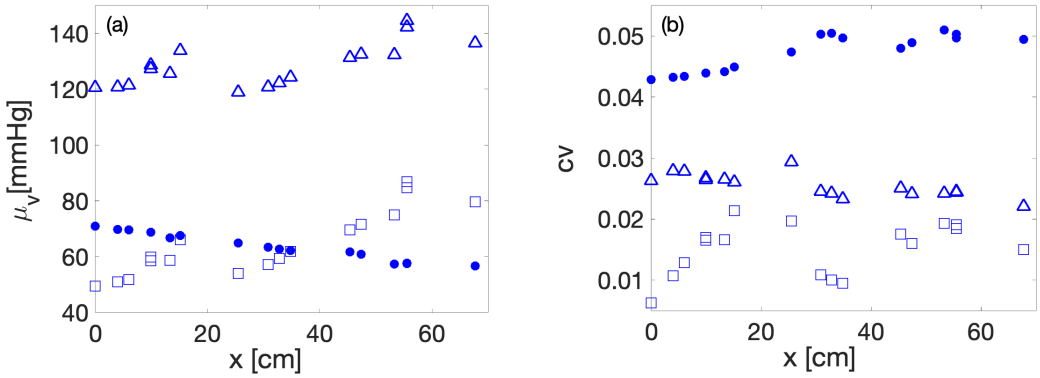

Figure 6.7: Mean (a) and *cv* (b) values of systolic (triangles), diastolic (bullets) and pulse (squares) pressures along the arterial tree (x) in SR. *Image extracted from* [291].

The mean values of systolic, diastolic and pulse pressures in AF vary minimally with respect to their counterparts in SR, mainly because of the common mean HR imposed in the SR and AF simulations. However, systolic, diastolic and pulse pressure fluctuations around mean values significantly rise in AF compared to SR, with corresponding *cv* values in the intervals 7-8%, 14-19% and 3-10%. These results, already predictable from Figure 6.6, are depicted in Figure 6.8a-b, displaying the *cv* ratios between AF and SR (cv_{AF}/cv_{SR}) for the systolic, diastolic and pulse pressures along the arterial tree. These figures, apart from showing a higher pressure variability in the fibrillated case (cv_{AF}/cv_{SR} is always higher than 1), individuate the ability of the arterial system to magnify or damp the pressure fluctuations introduced at the aortic root. These latter are identified by horizontal lines, which represent the aortic ratios cv_{AF}/cv_{SR} for the systolic (3.15), diastolic (2.95) and

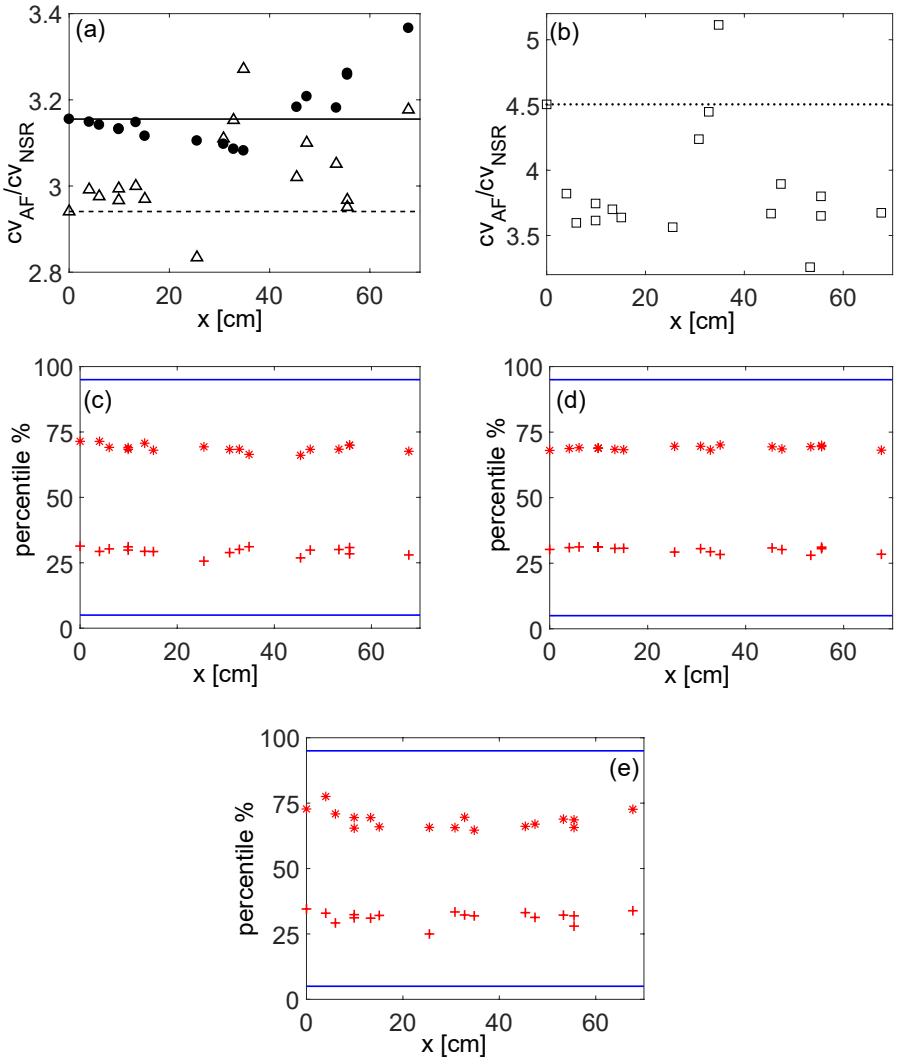

Figure 6.8: *cv* ratios between AF and SR along the arterial tree (x) for systolic (triangles) and diastolic (bullets) pressures in panel (a) and pulse (squares) pressures in panel (b). Horizontal lines stand for the *cv* ratios at the ascending aorta. AF percentiles corresponding to the 5th (+) and the 95th (*) percentiles in SR along the arterial tree (x) for systolic (c), diastolic (d) and pulse (e) pressures. Horizontal lines indicate the 5th and 95th percentiles in SR. *Image extracted from* [291].

pulse (4.5) pressures. Thus, *cv* ratios below the horizontal line imply a reduction of the pressure variability imposed at the beginning of the aortic root, and the opposite for *cv* ratios above the horizontal line. We have found that the *cv* ratios of systolic and diastolic pressures are amplified below the abdominal region (for x>30cm) with respect to the aortic root, while the *cv* ratios of pulse pressures

are dumped with respect to the starting aortic value, with an exception only at abdominal level.

The enlargement of the tails of the PDFs of systolic and diastolic pressures depicted in Figure 6.6 translates into strong modifications of the 5th and 95th percentiles from SR to AF, as shown in Figures 6.6c-e. We have obtained that the 5th and 95th percentiles of systolic, diastolic and pulse pressures in SR are associated to around the 30th and 70th percentiles during AF, respectively. There is not a strong dependence of the percentile behaviour from the location, with a stronger variability for pulse than for systolic and diastolic pressures.

A3: Wave propagation and reflection phenomena. The mechanisms of wave propagation and reflection, deriving from the complex interplay between forward and backward waves, are always responsible for the resultant shape and extreme values of pressure and flow rate signals. This section aims at exploring to what extend these mechanisms are altered in AF. To this purpose, we have focused on the variations from SR to AF on phase velocity, c_{FTF}, and reflection magnitude, RM, along the arterial tree. We recall that, at a given arterial section, c_{FTF} is an estimation of the pulse wave velocity through the foot-to-foot method (see section 1.2.5), while RM is the ratio between the amplitudes of the backward and forward pressure waves as explained by Westerhof et al. [365] (see section 1.2.3).

The behaviour of c_{FTF} from SR to AF is depicted in Figure 6.9. In particular, panels a and b show the mean and cv values of c_{FTF} in SR along the arterial tree. Mean values of c_{FTF} grow moving away from the heart as expected, while fluctuations around mean values reduce of 50% (from 3 to 1.5%) as the distance from the heart increases. Switching to AF, the mean values of c_{FTF} fairly change compared to SR, while fluctuations around mean values upsurge. As one can see from panel c, the ratio cv_{AF}/cv_{SR} of c_{FTF} values in AF and SR is among 2.5 at the beginning of the aorta, and continues growing further away from the heart, up to about 4 at femoral level. As for the other variables analysed so far, the tails of the AF PDFs for c_{FTF} dramatically extend with respect to SR, with the 5th percentiles in SR becoming the 30th percentiles in AF, and the 95th percentiles in SR translating into the 60-80th percentiles in AF, depending on the arterial site (see panel d of Figure 6.9). As a last remark, we recall that c_{FTF} is a function of blood density, here taken constant, and vessel distensibility. Since this latter depends on both pressure and frequency, which are both affected by the heart rhythm alterations induced by AF, it is reasonable that the phase velocity experiences a strong variability in a fibrillated case, as emerging from Figure 6.9c-d.

Regarding RM, its oscillations around mean values significantly grow in AF with respect to SR, as shown in Figure 6.10a, which depicts the ratio cv_{AF}/cv_{SR} for RM along the whole arterial tree. This ratio is in the range 2-6, with the highest values at femoral level (x>60 cm) and the minimum values between the thoracic and abdominal tracts (20<x<40 cm). Thus, the ratio cv_{AF}/cv_{SR} for RM

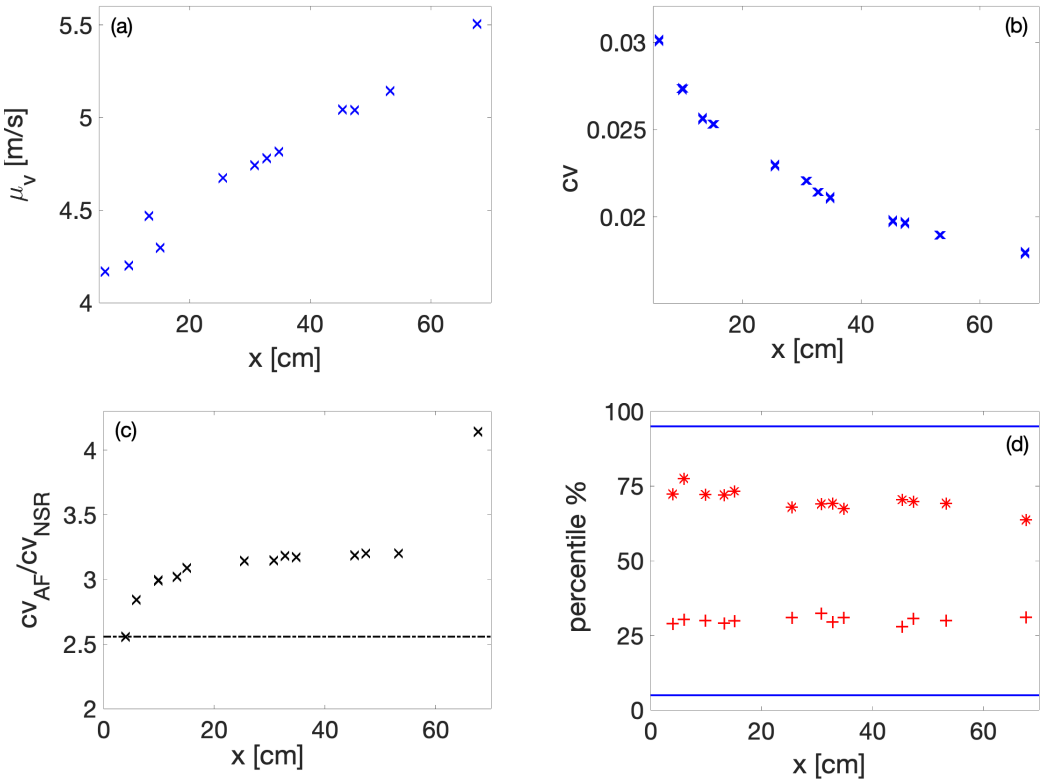

Figure 6.9: Mean (a) and *cv* (b) values of the phase velocity, c_{FTF}, along the arterial tree (x) in SR. *cv* ratio between AF and NSR for c_{FTF} (c) along the arterial tree (x), with the dotted line standing for the cv ratio at the beginning of the ascending aorta. (d) AF percentiles corresponding to the 5th (+) and the 95th (*) percentiles in SR along the arterial tree (x) for c_{FTF}. Horizontal lines indicate the 5th and 95th percentiles in SR. *Image extracted from* [291].

is quite variable along the arterial tree, both rising and reducing with respect to the ascending aorta, where it is around 4. The AF percentiles for RM corresponding to the 5th and 95th percentiles in SR throughout the arterial tree are illustrated in Figure 6.10b. We have found that the 5th percentiles in SR reach the range 20th-40th in AF, and the 95th percentiles in SR become in the interval 60th-85th during AF, respectively, with the widest extreme PDF areas along the abdominal aorta.

A4: Organ perfusion at the principal gastrointestinal tracts. To inquire into the effect of AF on organ perfusion, we have also investigated the variations in the mean flow rates per beat, q [ml/beat], at the principal gastrointestinal bifurcations of the model domain from SR to AF. As for the pressures, mean values of

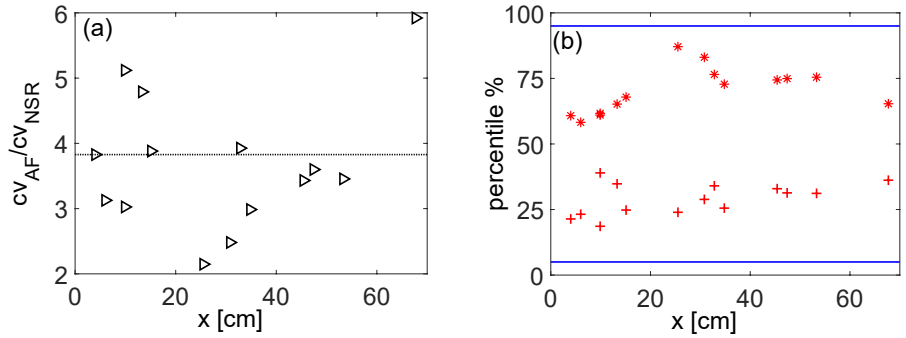

Figure 6.10: *cv* ratio between AF and SR for RM (a) along the arterial tree (x), with the dotted line standing for the *cv* ratio at the beginning of the ascending aorta. (b) AF percentiles corresponding to the 5th (+) and the 95th (*) percentiles in SR along the arterial tree (x) for RM. Horizontal lines indicate the 5th and 95th percentiles in SR. *Image extracted from* [291].

q are not seriously affected by AF with respect to SR. By contrast, q fluctuations around mean values and q variability upsurge in AF with respect to SR as documented by Table 6.3. This Table indicates that the ratios cv_{AF}/cv_{SR} are always higher than 1 at each gastrointestinal site, although they reduce compared to the ascending aorta. In addition, as for all the other variables analysed so far, there is an enlargement of the PDF tails for q, with the 5th and 95th percentiles in SR becoming the 25–30th and 65–70th percentiles in AF, respectively.

Table 6.3: *cv* ratios between AF and SR for the mean flow rate per beat, q [ml/beat], (Column II), AF percentiles of q corresponding to the 5th (Column III) and 95th (Column IV) percentiles in SR at the indicated vessels (numbers follow the numeration in Figure 3.1). *Table extracted from* [291].

Vessel	$\frac{cv_{AF}}{cv_{NSR}}$	AF percentile corresponding to the $5th$ percentile in SR	AF percentile corresponding to the $95th$ percentile in SR
Ascending aorta (1)	3.70	30.1	65.5
Intercostal (26)	2.26	30.6	69.3
Celiac (29)	1.75	28.2	68.1
Superior mesenteric (34)	1.79	28.1	70.7
Left Renal (36)	1.65	29.6	67.7
Right Renal (38)	1.67	28.2	66.9
Inferior mesenteric (40)	1.95	28.8	63.9

Conclusions of the arterial tree study.

Based on the above results, the following conclusions emerge.

- Both in SR and AF, coefficients of variation are higher for diastolic than for systolic pressures, and increase/decrease for diastolic/systolic pressures moving away from the heart. This behaviour is magnified in AF, with the *cv* ratios between AF and SR always larger than one, greater for diastolic than for systolic pressures (apart from a few exceptions at abdominal level), and growing towards distal locations. It can also be observed how (i) diastolic pressures need more or the same time than systolic pressures to come back to their initial values as a single RR perturbation comes into play, and (ii) peripheral locations have a more powerful inertia than central ones in recovering from a RR disturbance towards their initial equilibrium condition. Thus, it is clear that the arterial system is not able to annihilate the AF-related variability, which instead takes over at peripheral level, where the strongest variations with respect to SR are detected.

- The probability of reaching extreme and uncommon pressures, flow rates, phase velocities and reflection indexes dramatically grow during AF, with the tails of the PDFs seriously expanding from SR to AF. As a matter of fact, the 5th and 95th percentiles in SR transform into the 30th and 70th percentiles in AF, respectively, with limited variations along the arterial tree, apart from RM, which is more variable along the path heart-periphery.

- AF triggers not negligible fluctuations in pressures, whose magnitude vary site by site. This feature is easily explained taking into account the fact that pressure, as well as flow rate signals, are nothing but waves. These latter are generated by the contracting activity of left ventricle, travel at a finite and locally variable speed (estimated through c_{FTF}), and reflect most of all at arterial bifurcations (whose reflection magnitude is given by RM). Based on this consideration, it is clear that the pressure and flow rate signals at a generic site depend on four different factors: the pressure signal at the aortic root, the local phase velocity, how waves are reflected close to the chosen site, and the distance between the nearest bifurcations and the site of interest [365]. We have demonstrated here that the first three factors are affected by AF, with the signal at the entrance to the aorta depending on the RR variations, and the mechanisms of wave propagation and reflection, evaluated in terms of c_{FTF} and RM, varying site by site from SR to AF. Therefore, the interplay among these three sources of variations can be judged responsible for the complex haemodynamic scenario resulting from this study.

The arterial tree study represents a first attempt to quantify the effects of the sole heart rhythm variations in AF on the arterial haemodynamics. It appears that,

at a normal HR, rhythm alterations alone during AF are perfectly able to induce serious modifications in terms of pressure and peripheral perfusion with respect to SR. This suggests that prolonged rhythm disorders in AF could cause additional and more severe dysfunctions, due to the long-term exposure to abnormal pressure/flow rate values and oscillations. It seems to us that these conclusions deserve to be further explored in the future, through both clinical and computational studies. In fact, they could explain the higher probability of morbidity and mortality among AF patients, even in absence of other concomitant pathologies.

Limitations of this study are the lack of a short-term baroreceptor mechanism, as anticipated in section 6.3.1, the absence of any AF-induced remodelling caused by a prolonged exposure to a fibrillated state, and the hypothesis of constant atrial pressure, which underestimates the end-diastolic left-ventricular pressure and volume fluctuations. As a last remark, one can also notice that, despite the model adopted in this study represents a simplification of the complete model provided in chapter 3, the missing cardiovascular regions are reasonably replaced by adequate central and distal boundary conditions.

6.3.3 Coronary study: effects of different HRs on coronary perfusion in AF

Introduction of the coronary study.

It is well established that AF is associated with impaired coronary blood flow and reduced myocardial perfusion, even in absence of coronary heart disease (CAD) [191, 192]. In fact, the prevalence of CAD among AF patients is between 17-46.5%, while the prevalence of AF among patients with CAD is in the smaller range 0.2-5% [210]. Although different studies have examined the effects of AF on animal coronary flow, there are not so many data on humans [152]. Recent investigations, however, suggest that in case of AF there could be a mismatch between coronary blood flow and myocardial metabolic demand, concomitantly to a reduction in the coronary flow reserve [151]. It would be this mismatch to cause/worse new/pre-existent myocardial ischaemias as a consequence of accelerated and irregular heart rates during AF. However, the mechanisms through which an irregular rhythm could have deleterious consequences on the coronary function is not absolutely clear and still remains object of discussion with different solutions on the table: decreased aortic pressure because of smaller RR intervals, coronary vasoconstriction and limited coronary blood flow. To further shed light into the fallouts of AF without CAD on the coronary behaviour and performance, more investigations are needed. However, since AF and CAD often coexist [158, 366], it is difficult to evaluate the role of AF alone on coronary haemodynamics from clinical studies, despite an attentive evaluation of the reciprocal interaction AF-CAD continues to be required for clinical purposes [203]. Moreover, together with the role of the

fibrillated ventricular rhythm, the impact of the HR in AF on the coronary function has remained largely unexplored. Indeed, although different rate control strategies resulted on similar midterm cardiovascular outcomes [95], ultimate evidence is still lacking [374] and data on coronary flow impairment remain sparse.

In this context, we aim at exploring the influence of ventricular rate during AF on coronary flow impairment. To this purpose, we have imposed five sequences of 2000 heartbeat periods in AF, each of which with its own mean heart rate (50, 70, 90, 110, 130 bpm), to the mathematical model of the left heart-arterial tree and left coronary circulation outlined in section 6.3.1. As in the arterial tree study, the fibrillated RR sequences have been extracted as discussed in section 6.2, and the number of simulated cardiac periods has been imposed to assure the statistical reliability of the model results. Among the model outputs, we have focused on the flow rate signals along the Left Anterior Descending (LAD) artery, Q_{LAD}, from which some analyses on the waveform amplitudes and coronary blood flows at the five mean HRs have been conducted. A flow chart of the procedure followed in this study is offered in Figure 6.11.

Definition of the haemodynamic parameters to analyse the coronary perfusion.

To quantify coronary blood flow variations at each mean HR in AF, we have used some haemodynamic parameters, all derived from the flow rate signals along the LAD artery, Q_{LAD}, which is one of the most characteristic vessel to study myocardial blood supply. Considering the complete LAD flow rate signal for a single heartbeat period RR, as the one represented in Figure 6.12, we have identified the ventricular systolic, $\mathrm{RR_{sys}}$, and diastolic, $\mathrm{RR_{dia}}$, periods. The mean values±standard deviations of $\mathrm{RR_{sys}}$ and $\mathrm{RR_{dia}}$ associated to each of the simulated HR, together with the corresponding ratios $\mathrm{RR_{dia}/RR_{sys}}$, are provided in Table 6.4.

We have defined

$$V_{sys}[\mathrm{ml/beat}] = \int_{RR_{\mathrm{sys}}} Q_{LAD}, \tag{6.3}$$

and

$$V_{dia}[\mathrm{ml/beat}] = \int_{RR_{\mathrm{dia}}} Q_{LAD}, \tag{6.4}$$

as the blood volumes through the LAD artery during systole and diastole, respectively. The sum of these two volumes has been identified as the LAD stroke volume, $SV_{LAD} = V_{sys} + V_{dia}$ [ml/beat]. From this latter, we have expressed the coronary blood flow, CBF, as $CBF = SV_{LAD}$xHR [ml/min], representative of both myocardial perfusion and oxygen supply. As other variables, we have chosen $Q_{max,sys}$ and

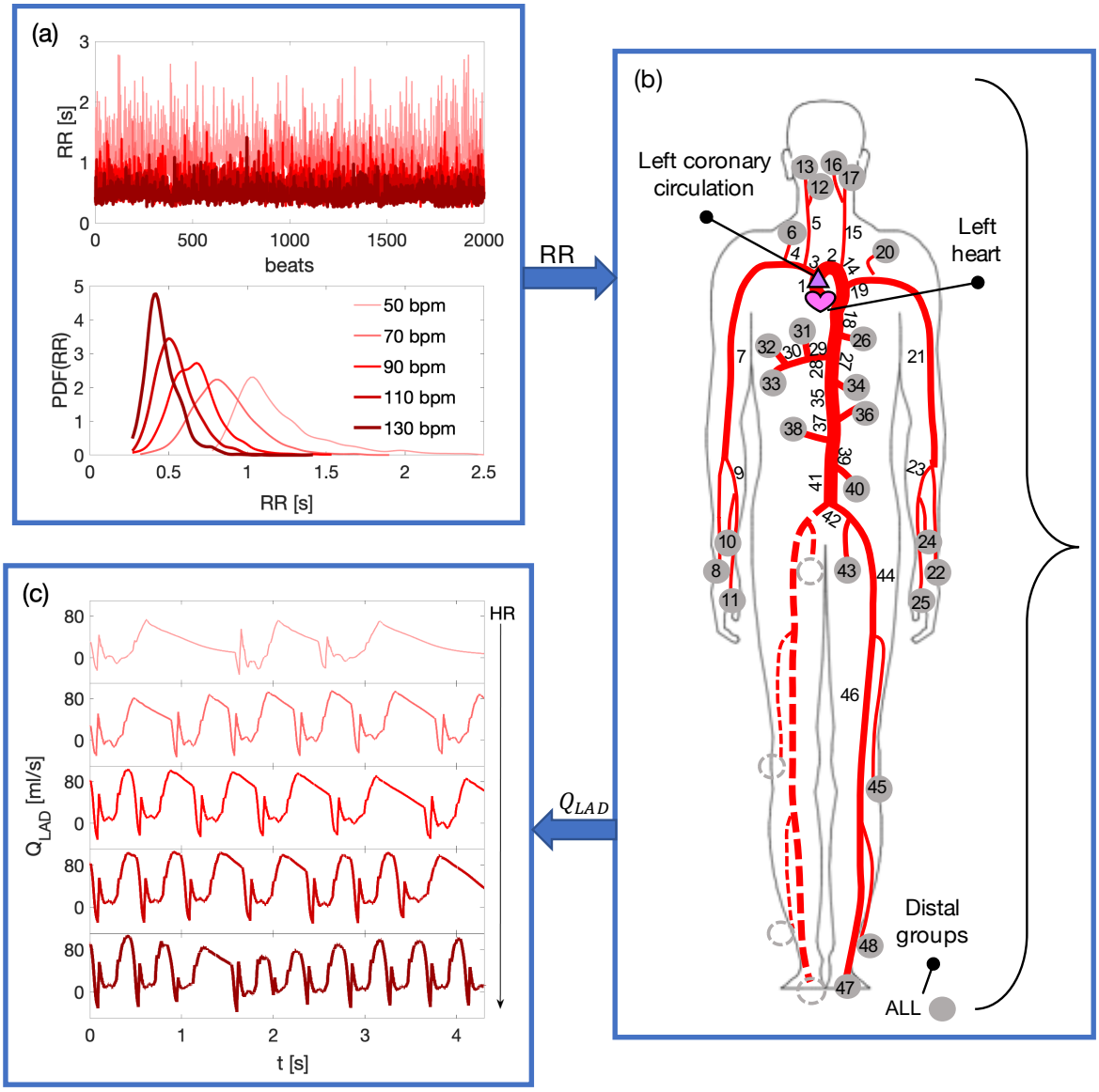

Figure 6.11: Flow chart of the procedure implemented in study B. (a) Extraction of 2000 RR interbeat intervals in AF at five different mean HRs (50, 70, 90, 110, 130 bpm). (b) Resolution, for each RR sequence, of the 0D–1D cardiovascular model. (c) Analysis of the Q_{LAD} (Left Anterior Descending Artery flow rate) time series provided by the mathematical model at each mean HR. *Image extracted from* [293] *with modifications.*

$Q_{max,dia}$ as the maximum flow rates during RR_{sys} and RR_{dia}, respectively, and Q_{min} as the minimum flow rate throughout RR. An indication of all these parameters for a single Q_{LAD} signal is also given in Figure 6.12.

Table 6.4: Mean values, μ_v, $\pm$ standard deviations, σ_v, and coefficients of variation, $cv = \mu_v/\sigma_v$, (in brackets) of RR_{sys} and RR_{dia} for each simulated mean HR (50, 70, 90, 110, 130 bpm). Ratio between mean values of RR_{dia} and RR_{sys}. *Table extracted from* [93].

HR [bpm]	RR_{sys} [s]	RR_{dia} [s]	RR_{dia}/RR_{sys}
50	0.41±0.049 (0.12)	0.79±0.26 (0.33)	1.93
70	0.35±0.034 (0.097)	0.50±0.17 (0.34)	1.43
90	0.32±0.026 (0.081)	0.35±0.14 (0.35)	1.09
110	0.31±0.019 (0.061)	0.24±0.11 (0.32)	0.77
130	0.30±0.019 (0.063)	0.17±0.096 (0.56)	0.57

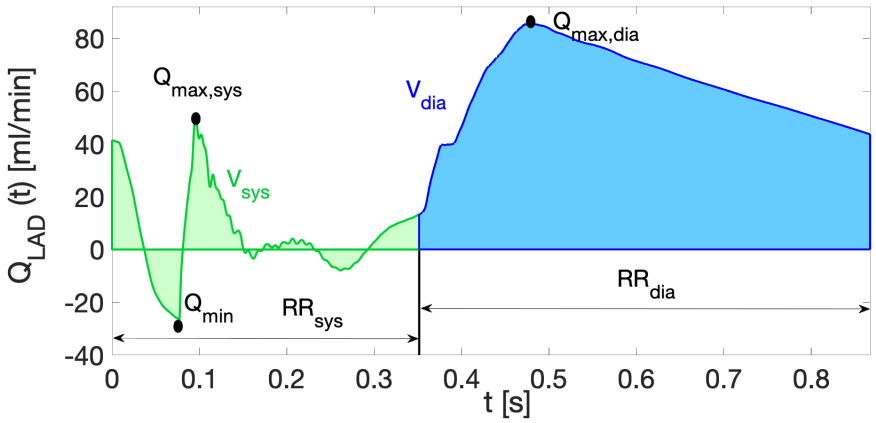

Figure 6.12: An example of LAD flow rate signal, Q_{LAD}, in AF for a single heartbeat period RR=0.87 s. Q_{min} is the minimum flow rate, $Q_{max,sys}$ and $Q_{max,dia}$ are the maximum flow rates during the systolic RR_{sys} and diastolic RR_{dia} periods, respectively. V_{sys} (green area) and V_{dia} (blue area) are the blood volumes per beat during RR_{sys} and RR_{dia}, respectively. *Image extracted from* [293].

Notice that all the haemodynamic parameters associated to the LAD artery here introduced are beat-to-beat measures. It means that, for each variable, one value per RR, is obtained. Thus, in this study, we have got 2000 values for each of the

haemodynamic parameters analysed at a given mean HR. To better compare the waveforms of the LAD flow rate at all the simulated mean HRs, we have calculated the average behaviour of the LAD flow rate per beat for each mean HR. Namely,

$$< Q_{LAD} >= \frac{1}{N}\sum_{i=1}^{N} Q_{LAD_i}(\tau), \tag{6.5}$$

where $N = 2000$ is the number of simulated heartbeat periods for each mean HR, Q_{LAD_i} is the LAD flow rate signal at the i-th heartbeat period, and τ is the nondimensional heartbeat period (t/RR_i). Beside $< Q_{LAD} >$, we have also determined the standard deviation of all the Q_{LAD_i} signals, that is σQ_{LAD}. It follows that, for each HR configuration, $< Q_{LAD} >$ and σQ_{LAD} represent the average LAD flow rate waveform and the standard deviation of the LAD flow rate waveform per beat over the 2000 cardiac cycles. Notice that, since both $< Q_{LAD} >$ and σQ_{LAD} are expressed in terms of the non-dimensional beating period, $\tau = [0,1]$, they are fully comparable at any mean HR.

Finally, we have considered two additional variables, the coronary perfusion pressure, CPP, and the rate pressure product, RPP. CPP is normally taken as an estimate of myocardial perfusion and has been calculated as $CPP = p_{aor_{dia}} - p_{edlv}$, with $p_{aor_{dia}}$ the aortic diastolic pressure and p_{edlv} the end-diastolic left-ventricular pressure. To this purpose, we recall that the mathematical model adopted for this study (6.3.1) assumes constant the left atrial pressure. This means that fluctuations of p_{edlv} are underestimated at any mean HR. RPP is usually considered as a measure of oxygen consumption and is defined in section 1.2.3.

Results of the coronary study.

The main results of this study are presented in the following four paragraphs. In particular, the first one regards (B1) the changes experienced by the Q_{LAD} signals, the second one (B2) the HR-induced variations in CBF and associated variables, the third one (B3) the possibility to consider CPP as surrogate measure of CBF, and the fourth one (B4) the beat-to beat variability in CBF.

B1: Waveforms and amplitudes of the Q_{LAD} signals at different HRs in AF. The changes experienced by the Q_{LAD} signals at different HRs in AF have been investigated in terms of both waveform and amplitude variations.

Waveform variations have been analysed by comparing signals $< Q_{LAD} >$ and σQ_{LAD} at each simulated HR. From Figure 6.13a it is immediately visible how $< Q_{LAD} >$ signals significantly modify as HR increases. In particular, one notices that, at higher HRs, $< Q_{LAD} >$ waveforms are stretched forward in time both in systole and diastole, compared to smaller HRs. In addition, the typical behaviour of Q_{LAD} signals during diastole (see Figure 6.12) is lost at high cardiac frequencies.

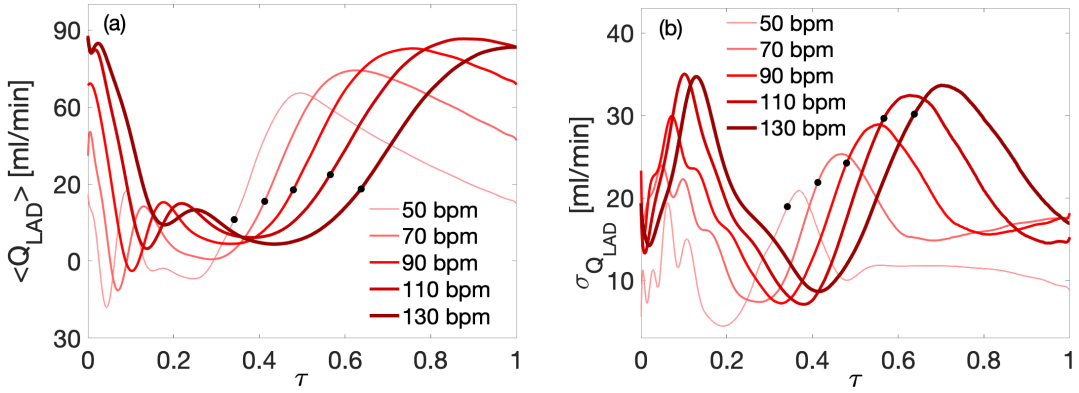

Figure 6.13: (a) Average ($< Q_{LAD} >$) and (b) standard deviation (σQ_{LAD}) of the LAD flow rate signals at different HRs (50, 70, 90, 110, 130 bpm) as functions of the non-dimensional time, τ. Black dots mark the beginning of diastole. *Image extracted from* [293].

In fact, while at lower HRs $< Q_{LAD} >$ signals reach a peak in diastole and then start slowly decreasing up to the end of the heartbeat duration, at higher HRs the diastolic decreasing phase tends to disappear. This is due to the fact that when HR grows, diastole shortens more than systole, with the ratio $\mathrm{RR}_{dia}/\mathrm{RR}_{sys}$ going from 1.97 to 0.57 in the HR range 50-130 bpm (see Table 6.4). Thus, one can observe that, for HR>90 bpm, the maximum diastolic peak within RR_{dia} is detected towards the end of the beat and systole starts with much higher $< Q_{LAD} >$ values. The curves σQ_{LAD} for mean HRs between 50 and 130 bpm are shown in Figure 6.13b. As one can see from this latter, σQ_{LAD} in general enhances with HR and its waveform moves forward in time for higher HRs. One can recognize two maxima in each σQ_{LAD} signal, one within $\mathrm{RR}_{\mathrm{sys}}$ and the other within $\mathrm{RR}_{\mathrm{dia}}$. The first one is due to the rapid decrease of $< Q_{LAD} >$ from $Q_{max,sys}$ to Q_{min}, while the second one seems to be related to the rapid growth of $< Q_{LAD} >$ from Q_{min} to $Q_{max,dia}$.

The amplitude variations of the Q_{LAD} signals with HR in AF have been quantified through the main statistics (mean value, standard deviation and coefficient of variation) of $Q_{max,sys}$, $Q_{max,dia}$ and Q_{min} over the 2000 simulated cardiac periods for each mean HR taken into account. Mean values of the maxima, $Q_{max,sys}$ and $Q_{max,dia}$, both rise towards the high frequency range, with an exception only for $Q_{max,dia}$ at 130 bpm. In particular, mean $Q_{max,sys}$ values monotonically grow of 78% from 50 to 130 bpm. Mean $Q_{max,dia}$ values, instead, not-monotonically increase of 21% between 50 and 130 bpm, with the maximum at 110 bpm. Looking at the coefficients of variation of $Q_{max,sys}$ and $Q_{max,dia}$, it appears that the system tends to amplify and damp diastolic and systolic fluctuations with respect to mean values, respectively, at higher HRs. This means that the LAD flow rate variability is

Table 6.5: Mean values, μ_v, ± standard deviations, σ_v, and coefficients of variation, $cv = \mu_v/\sigma_v$, (in brackets) of $Q_{max,sys}$, $Q_{max,dia}$ and Q_{min} for each simulated HR (50, 70, 90, 110, 130 bpm). *Table extracted from* [93].

HR [bpm]	$Q_{max,sys}$ [ml/s]	$Q_{max,dia}$ [ml/s]	Q_{min} [ml/s]
50	49.97±5.36 (0.11)	73.92±7.07 (0.096)	-27.65±3.54 (-0.13)
70	56.36±10.65 (0.19)	86.75±8.60 (0.099)	-28.06±3.03 (-0.11)
90	71.11±15.07 (0.21)	94.30±9.70 (0.10)	-27.86±3.92 (-0.14)
110	84.68±15.08 (0.18)	96.61±11.15 (0.12)	-27.49±3.81 (-0.14)
130	87.41±14.85 (0.17)	89.52±17.24 (0.19)	-25.93±5.38 (-0.21)

particularly sensitive to the HR variability, considering that the coefficient of variations of the RR sequences for all the simulated HRs is taken constant and equal to 0.24. Regarding Q_{min}, one can notice that its mean values, standard deviations and coefficients of variation fairly change throughout the observed frequency range, suggesting that it is less sensitive than $Q_{max,sys}$ and $Q_{max,dia}$ to the HR variations in AF.

B2: HR-induced variations in CBF and related variables in AF. Coronary blood flow at different HRs in AF has been investigated through the mean values, standard deviations and coefficients of variations of V_{sys}, V_{dia}, SV_{LAD}, CBF and RPP for each simulated HR. All these variables are represented in Figure 6.14.

Panel a shows how V_{sys} slightly increases and V_{dia} dramatically decreases with HR, resulting in a not negligible reduction of SV_{LAD} over the whole frequency range. This reduction surely depends on the fact that RR_{dia} lowers more than RR_{sys} when HR rises (see Table 6.4). In fact, considering the LAD flow rate signal shape (see Figure 6.12), it is noticeable that the major contribution to SV_{LAD} is given by V_{dia} rather than V_{sys}. The not linear decrease in SV_{LAD} with HR leads to a not trivial behaviour of CBF in Figure 6.14b. It grows between 50 and 90 bpm, remains almost constant from 90 to 110 bpm, finally reducing for higher HRs. The oxygen demand, expressed through RPP and shown in Figure 6.14b, monotonically increases with HR.

Notice that the cv values of all these parameters rise with HR, apart from V_{sys} and RPP. It implies that the AF-induced variability associated to SV_{LAD} and

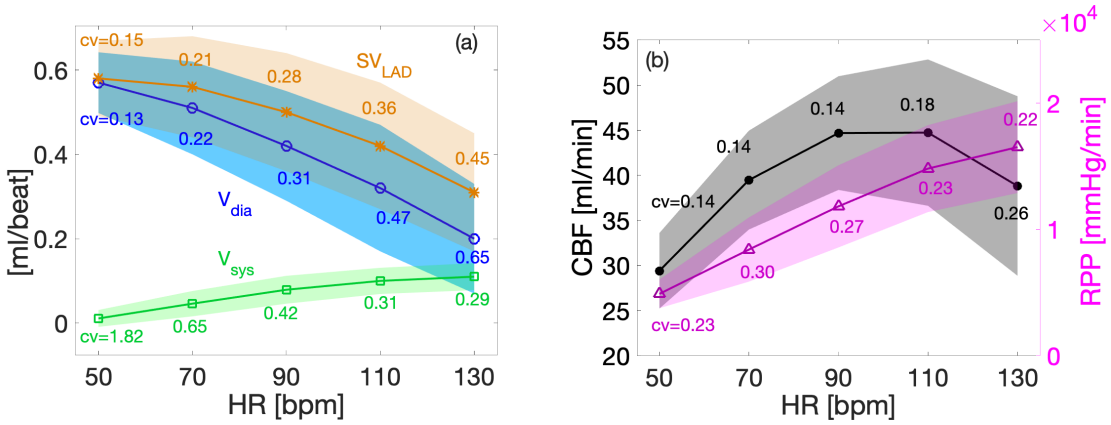

Figure 6.14: Mean values (μ_v, solid curves) and standard deviation values (in terms of $\mu_v \pm \sigma_v$, shaded areas) of V_{sys}, V_{dia} and SV_{LAD}, in panel (a), and CBF (left y-axis) and RPP (right y-axis), in panel (b), computed over 2000 heartbeat periods at each simulated HR. $cv = \mu_v/\sigma_v$ values are also reported for each variable and HR. *Image extracted from* [293].

CBF becomes stronger in the high frequency range, despite the cv value of the RR sequences remains constant among all the simulated HRs.

B3: CPP as a surrogate measure of CBF in AF?. In SR, CPP is often adopted as a surrogate measure of CBF, by exploiting the positive correlation among these two variables due to the coronary autoregulation. Thus, we have verified the possibility to extract CBF from CPP also in case of AF. To this end, we have focused on the distributions $CBF(CPP)$ at all the simulated HRs, that are shown in Figure 6.15. It is apparent from this latter that a strong linear correlation $CBF(CPP)$ is still present in AF up to 70 bpm (panels a and b), but data become sparse and uncorrelated for higher HRs (panels c-e). Indeed, as depicted in Figure 6.15f, the R-square (R^2) values non-monotonically drop from high to low HRs, implying that CPP stops to be a good estimate of CBP in AF for HR higher than 90 bpm. It is worth noting that at 90 bpm, a CPP of 70 mmHg can correspond to a CBP between 10 and 55 mm/min. Therefore, based on presented results, one can conclude that CBF and CPP can be also correlated in case of AF but HR values have to remain small enough. If this condition is not verified, responses will be irregular and not linear and the range of possible haemodynamic values will enlarge.

B4: Beat-to-beat variability of CBF during AF. In order to estimate the beat-to-beat variability of CBF in AF, we have considered the correlations between CBF and the current (RR), the preceding (RR_{-1}) and the pre-preceding (RR_{-2})

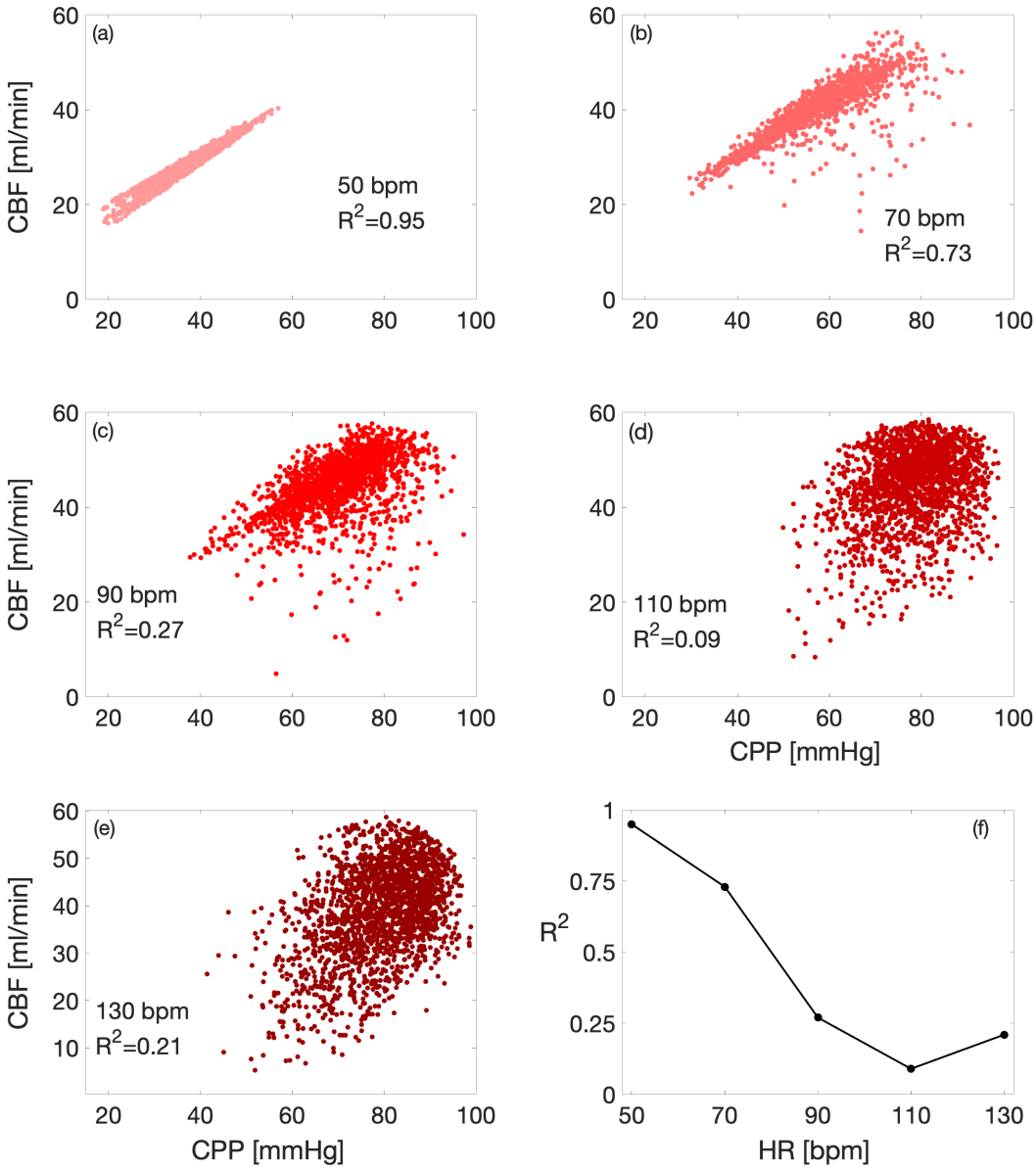

Figure 6.15: $CBF(CPP)$ relation over 2000 cardiac cycles at each simulated HR (panels (a)-(e)). Coefficient of determination, R^2, for the relation $CBF(CPP)$ as function of HR (f). *Image extracted from* [293].

heartbeats at each simulated HR.

The Pearson correlation coefficients, P_r, for the relations $CBF(\mathrm{RR})$, $CBF(\mathrm{RR}_{-1})$ and $CBF(\mathrm{RR}_{-2})$ are indicated in Table 6.6 for HR=50-130 bpm. One can see that, for all three relations, correlations switch from negative to positive as HR increases.

Table 6.6: Pearson correlation coefficients, P_r, for the relations CBF(RR), CBF(RR$_{-1}$) and CBF(RR$_{-2}$) at each simulated HR (50, 70, 90, 110, 130 bpm). *Table extracted from* [293].

HR [bpm]	CBF(RR)	CBF(RR$_{-1}$)	CBF(RR$_{-2}$)
50	-0.70	-0.66	-0.29
70	-0.35	-0.81	-0.48
90	0.24	-0.57	-0.24
110	0.67	-0.17	0.15
130	0.73	0.05	0.28

Moreover, choosing as significant correlation $|P_r| \geq 0.3$, a stronger correlation with RR than with RR$_{-1}$ and RR$_{-2}$ is detected. Indeed, while $CBF(RR)$ shows significant correlation at all HRs apart from 90 bpm, CBF(RR$_{-2}$) presents significant correlation at 70 bpm only. Similar results are reported in the work by Kochiadakis et al. [151], who indicated not negligible/negligible correlation between the coronary flow and RR/RR$_{-1}$,RR$_{-2}$ in all the fibrillated patients considered.

Conclusions of the coronary study.

Based on the above findings, the following conclusions emerge

- A rise in mean HR during AF causes serious changes in both the waveform and amplitude of the LAD flow rate signals, with a considerable delay of the diastolic peak and a marked decline of the total flow rate per beat. The systolic and diastolic flow rate maxima, $Q_{max,sys}$ and $Q_{max,dia}$, as well as their variability, increase with HR, while negligible changes are associated to Q_{min} as HR varies.
- CBF exhibits an ideal value at about 90 bpm, while RPP regularly increases with HR, thereby causing an impairment of the coronary circulation between 90-110 bpm in AF.
- The correlation between CBF and CPP in AF is lost above 90 bpm, when data become sparse. This means that CPP is not a good estimate of CBF during AF when HR$\geq$90 bpm.
- CBF is mainly correlated to RR and RR$_{-1}$, but it is largely independent from the previous heartbeats.

Thus, this work sustains a coronary impairment at high cardiac frequencies in AF, which seems to be due to the changes in both HR and RR variability.

HR variations have a big impact on the shape of the average LAD flow rate per beat, $< Q_{LAD} >$. In fact, as HR grows, there is a shortening of the corresponding cardiac cycle, with a greater reduction of $\mathrm{RR_{dia}}$, with respect to $\mathrm{RR_{sys}}$, per cardiac cycle. It follows the disappearance of the traditional diastolic decay and the growth of the maximum value during systole in $< Q_{LAD} >$ signals for increasing HR, as displayed in Figure 6.13. Such changes in $< Q_{LAD} >$ waveforms are responsible for the observed variations in mean coronary perfusion towards the high frequency range. Indeed, since SV_{LAD} receives its highest contribution during diastole, it is clear that a reduction in $\mathrm{RR_{dia}}$ is responsible for a decline in V_{dia} and, thus, in SV_{LAD}. This SV_{LAD} reduction, however, is not monotonic, being rapid at hight HRs and slow at low HRs. As a consequence, there is an increase in CBF up to 90 bpm, due to the slow decline in SV_{LAD}, and a decrease in CBF above 110 bpm, due to the rapid diminution in SV_{LAD}. Going from 90 to 110, the SV_{LAD} reduction is compensated by the accelerated HR and CBF levels off. Contrary to CBF, the oxygen demand, here represented through RPP, always grows with HR. This implies that, while below 90 bpm the coronary perfusion is sufficient to keep up with the enhanced myocardial oxygen demand, above 90-110 bpm there is a disproportion between myocardial oxygen supply and demand. In other words, beyond 90-110 bpm there is an impairment of the coronary perfusion.

The variability introduced by AF is not assimilated by the coronary circulation at different HRs, despite the *cv* value of all the RR sequences we have simulated is taken constant. Among the haemodynamic parameters used to quantify the variations in the amplitudes of the LAD flow rate signals, $Q_{max,dia}$ and $Q_{max,sys}$ are the most prone to the AF-variability, reporting the highest *cv* increases within the observed frequency range (of 78% and 21% between 50 and 130 bpm, with the maxima at 130 and 110 bpm, respectively). Also the coronary perfusion parameters, SV_{LAD} and CBF, exhibit continuous increases in their *cv* values moving toward the high frequency range. The fact that there is an enhanced coronary haemodynamic variability as HR grows has been highlighted in the scatter plots $CBF(CPP)$ for HR=50-130 bpm (Figure 6.15), which turn out to be extremely sparse for HR higher than 90 bpm.

Therefore, the main conclusion suggested by the present model is that during AF high ventricular rates, together with the irregularity of the ventricular rhythm, are responsible for the impairing of the coronary circulation; there is a reduction of the myocardial oxygen demand-supply ratio and an enhanced coronary perfusion variability. It is important to note that this conclusion has been obtained from an *in-silico* framework, which neglects to model the typical cardiovascular co-morbidities associated to AF patients. This implies that even in absence of relevant cardiovascular disorders, normally present together with AF, high HRs in AF can represent a serious risk in terms of coronary blood supply. In this sense,

the present study offers relevant clinical information, not easily obtainable from standard medical examinations.

The main limitations of this study are the absence of a baroreflex model and a mechanism of metabolic regulation for the coronary circulation, together with the model incapability to consider some mechanical properties of both cardiac vessels (viscoelasticity of extracellular matrix) and muscle (strain rate). However, the global framework results to be adequate to the purpose of the study, that is investigating the standalone effect of the irregular and faster AF beating on the coronary circle.

Chapter 7

Effects of long-term microgravity exposure on the cardiovascular system

Some of the contents of this chapter have been previously published in [92].

Microgravity is that special condition where objects are subjected to net accelerations smaller than the ones measured on Earth surface, from 1% of Earth gravitational acceleration (during parabolic flights) to less than one part in a million (aboard Earth-orbiting free flyers, e.g., the International Space Station - ISS) [285]. Astronauts are normally exposed to such an environment, which alters the physiological functioning of human body [109]. In fact, any part of us is accustomed to work because of gravity or in spite of gravity [12], and starts looking for another equilibrium point upon entering microgravity, in order to optimize its performance for the new state.

The set of all the body changes experienced during a period in space is called *space deconditioning*, which is currently studied by numerous institutions all around the world working in the field of Space Medicine. By definition, the term *deconditioning* is used when there is an adaptation to a less demanding environment [209]. Indeed, living in microgravity is genuinely less stressful than living on Earth, considering the abolishment of the head-to-foot gravity vector ($g_z = 9.81$ m/s^2) and the consequent unloading of human body. However, even if space deconditioning is not a problem during spaceflight, it can be an handicap after returning on Earth, or after landing on the Moon ($g_z = 1.62$m/s^2) or Mars ($g_z = 3.73$m/s^2), where a partial gravity restoration takes place.

International space agencies and private organizations are working to expand the human presence into the solar System, putting several efforts into the preparation

of space missions beyond the Low Earth Orbit (LEO), towards the lunar surface and on the path to Mars [1, 129]. In this context, a though understanding of the 0G adaptation point after long-term microgravity exposure turns out to be of great scientific interest, in order to (i) assure the well-being of astronauts throughout the mission, (ii) individuate target countermeasures to avoid or limit microgravity-related disabling effects, and (iii) guarantee the mission success.

In this chapter, we focus on cardiovascular deconditioning, and present some computational-obtained results about the direct effects of microgravity on the cardiovascular system behaviour after 5-6 months in space. To this aim, a slight different version of the general model presented in chapter 3 has been adopted, and a comprehensive bibliographic investigation of more than fifty studies has been exploited to model the main cardiovascular alterations induced by microgravity in the long period.

An overview of space deconditioning, with particular attention on cardiovascular deconditioning, is given in section 7.1, while the computational study we have developed is presented in section 7.2. This latter includes a brief description of the main differences between the model in chapter 3 and the one used in this chapter (section 7.2.1), the setting of the model parameters to simulate the effects of microgravity on the circulation in the long-term (section 7.2.2), and the results of the *in-silico* investigation (section 7.2.3).

7.1 Space deconditioning

Space deconditioning involves different body functions, related to the skeletal, muscular, neurovestibular and cardiovascular systems, all subjected to an accelerated ageing-like process, further complicated by the high radiation environment. These phenomena will be summarized in the following sections, with a focus on cardiovascular deconditioning, which is more relevant to the purpose of this chapter.

7.1.1 Skeletal deconditioning

One of the most serious problem associated to microgravity is osteoporosis [336], consisting in a gradual loss of bone density. It's quite accepted that bones are the result of a continuous remodelling process, regulated by the applied mechanical stimuli [87], which derive from the daily physical activity and gravity load. In fact, an increase in physical activity has been demonstrated to be beneficial in terms of bone density [132, 308], and a decline in bone density has been found in case of prolonged sedentary lifestyle [24, 165]. It has been quantified that astronauts experience a reduction in the bone mass per month of 1-1.6% in the spine, femoral neck, trochanter and pelvis [173], while their upper extremities and skull remain

almost unaffected or even gain bone mass [105]. Thus, the highest percentage of bone loss is localised at lower extremities, which feel the most important variations in terms of gravity load while in space. Indeed, one of the prime determinant of bone loss during spaceflight is the abolishment of the gravity vector, which is continually present on Earth [42].

The fact that bone loss is currently judged as one of the most risky threats astronauts encounter during space missions is due to three different reasons.

- Bone loss is difficult to be recovered after re-entry on Earth. Data from one individual involved in the Mir programme indicate that a loss in bone mass of 12% within 4.5 months in space was followed by a recuperation of 6% only after 1 year from re-entry on Earth [42, 184]. Other studies done on Skylab crew members, instead, report that 5 years on Earth were not sufficient to recover from the bone loss detected after 1-3 months in space [42, 342]. Nevertheless, the latest countermeasure protocols aboard the ISS, combining resistive exercise and a more attentive dietary intake, are proving to largely attenuate the dramatic bone mass losses recorded during older space missions [311].

- The risk of bone fractures is a real possibility, especially in view of future missions on the Moon or Mars, where astronauts are required to be physically active after having spent a period in microgravity [179]. Thus, procedures to avoid or at least limit this risk appear crucial to the mission success and to the health of astronauts throughout the mission.

- The formation of kidney stones during microgravity is absolutely realistic, with more than 30 cases reported postflight and one probable case aboard the Salyut 7 space station [172]. The typical explanation of this phenomenon is that the unloading of the skeleton, which leads to the release of calcium in the bloodstream, kidneys and urine, increases the probability of stone production. Renal stones are very painful when break and travel into the ureter, therefore, a successful kidney stone prevention programme is necessary to avoid medical emergencies in space [42].

Microgravity also leads to the elongation of the vertebral column, with a consequent increase in the total body height of about 3% with respect to Earth. Because of this, 52% of astronauts suffer from back pain, with 86%, 11% and 3% of them referring mild, moderate and severe pain [142]. This pain seems to be due to an excessive swelling of the lumbar intervertebral discs, which explains the high incidence of hernias, especially in cervical discs, postflight [289].

7.1.2 Muscle deconditioning

Another problem caused by microgravity is muscle deconditioning or muscle atrophy. On Earth, even in sedentary conditions, we use specific muscles to sustain our body in spite of gravity. These muscles, called antigravity muscles, are the ones of the back and in the back of the legs (e.g., the quadriceps femoris, the hamstrings and the solei), and have several functions, from maintaining the standing position, to changing posture, to allowing one walking and running. All these functions stop to be performed in space, where the body is more guided by arms and hands in the movements than by legs. Thus, antigravity muscles start loosing their structure and function in microgravity, leading to smaller muscle masses. In this process, the cross-sectional areas of the muscle fibres shrink and remain equal in number, which is typical of muscular atrophy. The loss of muscle mass determines the reduction in muscle strength, that justifies the sensation of fatigue felt by astronauts immediately after re-entry on Earth. Antigravity muscles have a high concentration of type I muscle fibres, which are particularly sensitive to the inactivity associated to microgravity. The other muscles, which are used on Earth to provide rapid but not sustained power, contain larger percentages of other types of muscle fibres (e.g., type II muscle fibres). These latter are less exposed to muscle atrophy, which often provokes the transformation of type I into type II muscle fibres [42]. Although current astronauts on the ISS spend about 2 hours per day on a rigorous programme of exercise, after six months in microgravity most performance measures still require an attentive reconditioning plan to come back to the preflight levels. In particular, the majority of physical abilities result recovered after about 21 days of reconditioning, while more powerful dynamic tasks, like jumps, need more time to restore their preflight status [265].

7.1.3 Neurovestibular deconditioning

To maintain the sense of balance and spatial orientation and, thus, to perform normal activities on Earth, central nervous system combines different inputs. These latter derive from the vestibular organs of the inner ear (i.e., semicircular canals and otolith organs), the eyes, the tactile and proprioceptive sensors (in the skin, joints, muscle and viscera), whose performance can be affected by microgravity. Indeed, the otolith organs, which are normally involved on Earth in detecting linear accelerations and the static tilt of the body, send strange inputs to the brain in microgravity due to their unloading. Thus, astronauts loose the sensation of up and down with their eyes closed during spaceflights. Together with the otoliths, also other senses stop working as on Earth in space. For instance, astronauts have difficulty in perceiving the position of their limbs, targeting specific objects with one finger, and quantifying changes of mass, due to alterations of the proprioceptive system. Alterations in the body's sensory and response systems in microgravity

typically cause the well known space motion sickness, which affects 60-80% of space travellers within the first hours/days of microgravity exposure [116]. Among the symptoms, there are depressed appetite, headache, lethargy, dizziness, gastrointestinal discomfort nausea and vomiting, all contributing to an impairment of the affected astronauts' performance within the first 12-72 hours of flight. Normally, the neurovestibular system re-adapts again to gravity in a few days after landing [42, 56].

7.1.4 Radiations

Astronauts are continuously exposed to space radiation, which consists mainly of ionizing radiation. This latter, contrary to non-ionizing radiation, has sufficient energy to remove electrons from the orbits, thus resulting in high-energy charged particles. Space radiation has three different sources: particles trapped in the Earth magnetic field, solar energetic particle (SEP) events and galactic cosmic radiation (GCR). Exposure to space radiation can be responsible for serious health risks, among which cancer, degenerative diseases and central nervous system damages. Current space missions in LEO represent relatively low risk occasions, considering that the shielding provided by the Earth magnetic field mitigates the most dangerous fallouts from space radiation exposure [47]. However, the effects of space radiations are expected to be decisively more conspicuous beyond LEO, where the quality and quantity of radiation are definitely different [323]. It has been, in fact, estimated that the dose rate in a generic shielded ship in deep space could be three times that measured on the ISS [324]. Moreover, based on experiments conducted at ground-based accelerator facilities, deep space radiation is believed to be more effective in producing biological damages than LEO radiation [70]. Indeed, based on NASA's models of risks and uncertainties, it seems that a mission to Mars could dramatically increase the risk of radiation-induced morbidity and mortality with respect to the actual NASA limits [63], posing new challenges for the future.

7.1.5 Cardiovascular deconditioning

On Earth we live under the constant presence of gravity and spend about 2/3 of our day in an upright position. This means that our cardiovascular system, which is vertically organised, is usually subjected to an hydrostatic pressure gradient of about 100 mmHg between the head and the feet. The presence of this pressure gradient constantly conditions the functioning of the whole cardiovascular system, which has evolved in order to guarantee the necessary blood supply to all the body organs in spite of gravity [109]. In fact, the higher is the total body height, the greater is the heart to brain distance (and thus the heart-brain hydrostatic pressure gradient), and the larger is the pressure difference heart has to generate in order to efficiently pump blood to the brain. If we were as high as giraffes, our heart to brain

distance would amount to about 2.4 m, and our heart should create a pressure difference of around 400 mmHg to assure an adequate brain oxygenation. Fortunately, we are as high as humans, with an average heart to brain distance of 30-35 cm. Thus, it is sufficient for our heart to produce a less demanding pressure difference of around 120 mmHg to allow cerebral blood flow [4]. In addition, because of the gravity vector, our cardiovascular system has developed a number of mechanisms to aid the venous return from the legs to the heart, which has to work against gravity. Among these, the venous valves to avoid backward blood movements, the constrictive muscles surrounding leg veins, and the variable arterial/venous tone of lower extremities preventing local accumulations of blood [109].

When we go to space, the hydrostatic pressure gradient we are everyday exposed to disappears and our cardiovascular system behaviour modifies, experiencing the so called *cardiovascular deconditioning*. The latter is initially triggered by the abolishment of the gravity vector, which in turn activates a series of other reactions, leading to the optimal cardiovascular functioning in microgravity. In other words, different essential mechanisms for the cardiovascular system to properly work on Earth become useless in space and a new equilibrium is gradually reached. Therefore, to describe the cardiovascular deconditioning, one can differentiate between acute adaptations, which include the set of changes produced by the immediate abolishment of the gravity vector, and long-term adaptations, which are consequence of the acute adaptations and require more time to come into play [109]. Both these changes will be discussed below, paying greater attention to the long term adaptations in light of this chapter purpose: exploring the behaviour of the cardiovascular system after 5-6 months in space.

Acute adaptations

The abolishment of the gravity vector upon entering microgravity determines a shift of blood and other fluids from lower to upper body. This shift was first quantified by Thornton et al. [340, 339] and Moore et al. [219], who measured the changes in the leg volumes of some astronauts during Skylab and Space Shuttle missions, respectively. They found that about two litres of fluid (one per leg) leave lower extremities and move upwards within the first 6-10 hours of spaceflight, while, postflight, the return of fluid to the legs is almost complete after a couple of hours from landing. A fluid shift of 2 l early in spaceflight was also confirmed by the measurement of tissue thickness, which was proved to decrease of 15% in the tibia and increase of 7% in the forehead [53]. Fluid shift in microgravity has also visible consequences: face becomes red, more rounded and with the superficial neck veins engorged (see Figure 7.1), while legs appear thinner. For this reason, it is common to say that astronauts exhibit puffy faces and bird legs.

Fluid shift naturally reflects on changes in cardiovascular measures during the

Figure 7.1: Crew of the Odissea Mission before launch in the upper panel, same crew during the first day of spaceflight in the lower panel. *Image extracted from* [19].

first hours/days in microgravity.

Contrasting results have been reported in terms of mean arterial pressure, despite there is good evidence that diastolic brachial pressure decreases with respect to the sitting position on the ground [86, 140, 242, 307]. No variations or even temporary increases in blood pressure [281, 71] have been detected at more peripheral locations during short periods in space, for example at the level of the finger, suggesting that conflicting pressure behaviours can emerge from more or less distal pressure measurements [351].

Different studies have been conducted to measure central venous pressure (CVP) early in spaceflight. It was initially found that CVP decreases immediately after entering microgravity [146], which seemed in contradiction with the increase in the

cardiac preload because of the fluid shift, and with the increase in CVP detected during bed rest with head-down tilt [89]. Thus, other measurements were performed both during spaceflights [43, 77] and parabolic flights [77, 171, 353], trying to further verify and explain the reduction in CVP during the initial phases of microgravity exposure. Data collected during parabolic flights by Videbaek et al. [353] resolved this issue. They measured, apart from CVP, the oesophageal pressure (which is an index of inter-pleural pressure - IPP) and the left atrial diameter on 7 subjects in supine position before and during a sequence of parabolic flights. It was found that left atrial diameter rises of 13.43%, CVP reduces of 22.41% and IPP decreases of 373.33%. Since IPP falls faster than CVP, transmural CVP (TCVP=CVP-IPP) increases, leading to a rise in the left atrial size, which is in accordance with the expected growth in the cardiac preload. Therefore, in microgravity, chest relaxes and stops to be compressed as on Earth, thereby justifying the reduction in CVP, in spite of the rise in the cardiac filling [240].

The enhanced cardiac filling early in spaceflight was proved by echocardiographic measurements of the left ventricular volume within the first 48 hours in microgravity [32]. Also CO was verified to rise, with Prisk et al. [270] reporting an increase of 18% within 2 days of flight with respect to the standing position on Earth, and Norsk et al. [243] indicating an increment of 22% with respect to the preflight upright seated position after a week in microgravity.

Concerning the early behaviour of HR in microgravity, some authors observed a reduction with respect to the 24-h ambulatory ground condition [86], while others measured no changes with respect to the sitting position on Earth [243]. These results seem to be due to the capability of the circulation to work at lower HRs after entering microgravity because of the higher cardiac preload [109].

Long-term adaptations

As written before, fluid shift causes an increase in central blood volume, sensed by the cardiopulmonary reflexes, which come into action to reduce total blood volume. This phenomenon is witnessed by a marked decrease in the Atrial Natriuretic Peptide (ANP) levels, corresponding to a reduction of 17% in plasma volume and of 10-15% in total blood volume [18]. Moreover, the initial increase in cardiac chambers size, with a total cardiac volume 20% higher than the preflight supine value, disappears after the first day of flight. Indeed, 6 days in microgravity make total cardiac volume smaller than the supine value on Earth of about 10-15% [56]. Apart from this, while staying in microgravity, a reduction in cardiac mass of 8-10% [328, 327], an increase in leg venous compliance [382], and a decrease in lower body arterial resistances [104] were detected.

The drop in total blood volume and cardiac dimensions has a direct impact on cardiac parameters such as the left-ventricular end-diastolic volume, V_{edlv}, stroke volume, SV, cardiac output, CO, and ejection fraction, EF. Mean variations of each

of these parameters according to literature data collected during spaceflights are given in Tables 7.1, for V_{edlv}, 7.2, for SV, 7.3, for CO, and 7.4, for EF.

Table 7.1: Changes in V_{edlv} due to microgravity exposure during spaceflight (column III) according to literature data ordered by year (column IV). $<$ decrease, $>$ increase, $=$ no variation, $\leq$ limited decrease, $\geq$ limited increase, with respect to preflight measures. x d/m means x days/months of exposure to microgravity. Reference body position and applied countermeasures (LBNP: lower body negative pressure) are indicated in column I when available, while the number of subjects involved (n) is indicated in column II. supine*: probably supine considering the observed percent variations.

Baseline Position, Countermeasures aboard	n	Variation (time frame)	Reference (year)
supine, /	2	<, -15% (84d)	Henry et al. [123] (1977)
supine, /	32	<, -11.44% (4/5d)	Charles et al. [48] (1999)
recumbent, irregular exercise	4	<, -5.44% (129/144d)	Martin et al. [201, 200] (2000/02)
supine, cuffs	6	<, -8% (5m)	Herault et al. [124] (2001)
supine, various	5-19	<, -8/13% (5m)	Arbeille et al. [14] (2001)
supine*, LBNP	17	<, -8/10% (5m)	Grigoriev et al.[104] (2011)

From these latter, it emerges that SV and CO exhibit quite contrasting behaviours depending, first, on the reference position on the ground and, second, on the amount and efficacy of countermeasures implemented aboard. It results that SV decreases/increases with respect to the supine/seated position on Earth. CO, instead, decreases or slightly increases with respect to the supine position, and increases with respect to the seated position on the ground. The fact that SV and CO spaceflight variations are conditioned by the preflight position is not surprisingly, if one takes into account the changes experienced by the same variables when just moving from a standing to a supine posture on Earth: a blood shift of 500-1000 ml from lower to upper body occurs, leading to a rise in SV of 18/20% and CO of 13/15% [260]. Thus, based on this, the huge gap between some of the spaceflight variations in SV and CO indicated in literature appears less dramatic. The magnitude of the variations in these cardiovascular parameters from preflight to in-flight, with the same baseline position on Earth, is then strongly associated to the effectiveness of the protocol of exercise or other countermeasures adopted during

Table 7.2: Changes in SV due to microgravity exposure during spaceflight (column III) according to literature data ordered by year (column IV). < decrease, > increase, = no variation, ≤ limited decrease, ≥ limited increase, with respect to preflight measures. x d/m means x days/months of exposure to microgravity. Reference body position and applied countermeasures are indicated in column I when available, while the number of subjects involved (n) is indicated in column II.

Baseline Position, Countermeasures aboard	n	Variation (time frame)	Reference (year)
supine, /	2	<, -14% (84d)	Henry et al. [123] (1977)
recumbent, irregular exercise	4	<, -22.72% (129/144d)	Martin et al. [201, 200] (2000/02)
supine, cuffs	6	<, -15% (5m)	Herault et al. [124] (2001)
supine various	5-19	<, -13.54% (5m)	Arbeille et al. [14] (2001)
/, regular exercise	3	<, -8.22/-19.47% (149d)	Hamilton et al. [113] (2011)
seated, regular exercise	8	>, +35% (85-192d)	Norsk et al. [242] (2015)
supine, regular exercise	11	<, -4.5% (150d)	Marshall-Goebel et al. [199] (2019)
seated, regular exercise	11	>, +23.19% (150d)	Marshall-Goebel et al. [199] (2019)

the mission. A demonstration of this can be given by comparing the spaceflight variations in SV and CO (in Tables 7.2 and 7.3, respectively) by Martin et al. [201, 200] and Marshall-Goebel et al. [199] for reference supine subjects, both obtained during long-term spaceflights. Results by Martin et al. were obtained in case of irregular exercise, while Marshall-Goebel et al. referred to astronauts involved in a regular and effective exercise programme. One observes that there is a significant fall in SV (-22.72%) according to Martin et al., while a negligible decrease in SV (-4.5%) is reported in the study by Marshall-Goebel et al.. Thus, it seems that an effective programme of exercise implemented throughout the mission maintains the supine SV values, while the lack of countermeasures aboard can lead to SV values smaller than in the preflight seated posture. Then, HR increases with respect to the supine state on Earth in both the studies (+9.26% in Marshall-Goebel et al. and +6.77% in Martin et al.). However, the small reduction in SV according to Marshall-Goebel et al. leads to an increase in the supine CO preflight, while the huge reduction in SV according to Martin et al. causes a decrease in CO with respect to the supine value on the ground.

Table 7.3: Changes in CO due to microgravity exposure during spaceflight (column III) according to literature data ordered by year (column IV). < decrease, > increase, = no variation, ≤ limited decrease, ≥ limited increase, with respect to preflight measures. x d/m means x days/months of exposure to microgravity. Reference body position and applied countermeasures are indicated in column I when available, while the number of subjects involved (n) is indicated in column II.

Baseline Position, Countermeasures aboard	n	Variation (time frame)	Reference (year)
recumbent, irregular exercise	4	<, -12.50% (129/144d)	Martin et al. [201, 200] (2000/02)
supine, cuffs	6	<, -18% (5m)	Herault et al. [124] (2001)
supine various	5-19	<, -11.37% (5m)	Arbeille et al. [14] (2001)
/, regular exercise	3	= (149d)	Hamilton et al. [113] (2011)
seated, regular exercise	8	>, +41% (85-192d)	Norsk et al. [242] (2015)
seated, regular exercise	9	>, +46.6% (119-166d)	Hughson et al. [130] (2017)
supine, regular exercise	11	>, +6.25% (150d)	Marshall-Goebel et al. [199] (2019)
seated, regular exercise	11	>, +21.43% (150d)	Marshall-Goebel et al. [199] (2019)

Concerning V_{edlv} and EF, reported in Tables 7.1 and 7.4, respectively, all spaceflight variations are given with respect to the supine position on the ground. It appears that both parameters reduce in microgravity compared to the supine preflight position. It is worth notice that the more EF reduces, the more cardiac contractility risks to be impaired. However, it is accepted that the conclusion about decreased myocardial contractility holds as EF reduces by 20% or more, that has never happened in any spaceflight [79]. Thus, it results that cardiac contractility is not at risk after long permanences in space (less than 1 year), even without the application of a regular plan of exercise aboard.

Therefore, considering the supine posture as ground reference and an irregular countermeasure programme throughout the mission, V_{edlv}, SV, CO and EF are all expected to reduce of 5-15%, 13-23%, 11-18%, 4-11%, respectively.

Some controversies emerge about the changes in HR and mean arterial pressure, MAP, during spaceflight (see Tables 7.5 and 7.6). However, it seems that HR remains constant or increases with respect to the supine value on Earth, while MAP is lower than the supine value or between the seated and supine values on Earth.

Table 7.4: Changes in EF due to microgravity exposure during spaceflight (column III) according to literature data ordered by year (column IV). < decrease, > increase, = no variation, ≤ limited decrease, ≥ limited increase, with respect to preflight measures. x d/m means x days/months of exposure to microgravity. Reference body position and applied countermeasures (LBNP: lower body negative pressure) are indicated in column I when available, while the number of subjects involved (n) is indicated in column II. supine*: probably supine considering the observed percent variations.

Baseline Position, Countermeasures aboard	n	Variation (time frame)	Reference (year)
supine, /	32	<, -4.62% (4/5d)	Charles et al. [48] (1999)
recumbent, irregular exercise	4	<, -10.96% (129/144d)	Martin et al. [201, 200] (2000/02)
supine, cuffs	6	<, -5% (5m)	Herault et al. [124] (2001)
supine, various	5-19	<, -5.80% (5m)	Arbeille et al. [14] (2001)
supine*, LBNP	17	<, -7.20% (5m)	Grigoriev et al. [104] (2011)

These results are strongly dependent on the protocol of countermeasures performed aboard. In older mission, when a regular programme of exercise was absent, it is typical to find HR higher and MAP smaller than the supine preflight levels. During more recent missions, instead, when countermeasures are demonstrating to be effective, HRs similar to the supine values on the ground result sufficient in maintaining a MAP between the supine and seated levels on Earth. In light of this, when considering the supine posture as reference on the ground and an irregular programme of countermeasures implemented during the mission, HR is expected to be up to 15% higher than on the ground and MAP is supposed to be about -10% than on Earth.

At the moment, there are no CVP measurements in long-duration spaceflights [194, 202], making it difficult to quantifying the time evolution of this variable while in space.

The combination of all the changes experienced by the cardiovascular system after months in microgravity do not appear extremely hazardous while in space, although it is not clear what could happen for more extended periods of exposure. What is sure is that the longer is the stay in space, the more difficult is the re-adaptation to the gravitational environment. In fact, one of the most arduous challenge astronauts have to face is orthostatic intolerance, which manifests upon

Table 7.5: Changes in HR due to microgravity exposure during spaceflight (column III) according to literature data ordered by year (column IV). < decrease, > increase, = no variation, ≤ limited decrease, ≥ limited increase, with respect to preflight measures. x d/m means x days/months of exposure to microgravity. Reference body position and applied countermeasures are indicated in column I when available, while the number of subjects involved (n) is indicated in column II.

Baseline Position, Countermeasures aboard	n	Variation (time frame)	Reference (year)
supine, various	3-19	>, +5/+15% (5/7m)	Arbeille *et al.* [15, 14] (1987/2001)
recumbent, irregular exercise	4	>, +6.78% (129/144d)	Martin *et al.* [201, 200] (2000/02)
supine, cuffs	6	= (5m)	Herault *et al.* [124] (2001)
supine, regular exercise	11	= (160/173d)	Verheyden *et al.* [351, 352] (2010)
/, regular exercise	3	≥, 0/+19.56% (149d)	Hamilton *et al.* [113] (2011)
seated, regular exercise	6	>, +4.88% (more than 31d)	Hughson *et al.* [131] (2012)
supine, regular exercise	11	>, +9.26% (150d)	Marshall-Goebel et al. [199] (2019)
seated, regular exercise	11	<, -3.28% (150d)	Marshall-Goebel et al. [199] (2019)

return in the form of dizziness, sweating and pre-syncope. It is mainly due to the reduced total blood volume, the smaller cardiac dimensions and mass, the increased leg vein capacity, and the decreased leg arterial resistances, compared to preflight. These factors significantly contribute to venous pooling, limiting the movement of blood to the heart and brain, with the consequent risk of fainting. The severity of orthostatic intolerance was proved to increase with the mission duration, with the proportion of astronauts able to complete the orthostatic tilt test[1] on landing day higher after Space Shuttle (80%) than ISS (33%) missions [174]. However, the use of more recent exercise devices aboard the ISS, such as the advance resistive exercise devise and the second generation treadmill, is not considered in this latter result. Indeed, more recent investigations report that no ISS astronaut suffers from orthostatic hypotension or intolerance during routine activity in the first 24 hours

[1]Orthostatic tilt test is used to assess the response of an individual to orthostatic tolerance. It consists in monitoring blood pressure and symptoms of a subject strapped to a table, which is progressively tilted from the horizontal, to different degrees, to the vertical position.

Table 7.6: Changes in MAP due to microgravity exposure during spaceflight (column III) according to literature data ordered by year (column IV). < decrease, > increase, = no variation, ≤ limited decrease, ≥ limited increase, with respect to preflight measures. x d/m means x days/months of exposure to microgravity. Reference body position and applied countermeasures are indicated in column I when available, while the number of subjects involved (n) is indicated in column II.

Baseline Position, Countermeasures aboard	n	Variation (time frame)	Reference (year)
supine, various	3-19	<, -2/-10% (5/7m)	Arbeille *et al.* [14] (2001)
supine, cuffs	6	= (5m)	Herault *et al.* [124] (2001)
supine, regular exercise	11	≥, +1.15% (160/173d)	Verheyden *et al.* [351, 352] (2010)
seated, regular exercise	6	<, -6.32% (more than 31d)	Hughson *et al.* [131] (2012)
supine, regular exercise	11	>, +3.45% (150d)	Marshall-Goebel et al. [199] (2019)
seated, regular exercise	11	= (150d)	Marshall-Goebel et al. [199] (2019)

from landing after 6 months in space [88].

7.2 A computational study about the long-term microgravity effects on the cardiovascular system

Although the overall scenario of cardiovascular deconditioning is widely accepted, numerous details about the haemodynamic response to microgravity, especially in the long period, remain unexplored. To the best of our knowledge, the oxygen consumption and exercise tolerance have not still quantified, and almost no information is available along the vasculature in terms of blood supply to the tissues and wave propagation/reflection phenomena. These gaps in our understanding of the cardiovascular system behaviour in microgravity are difficult to be filled through direct measurements in space. In fact, the number of available subjects per mission is small, the time astronauts can dedicate to physiological measurements is short, and the methodological possibilities of the measurement instruments to use on orbit are quite limiting [109]. In addition, there is no way to perfectly reproduce the effects of microgravity on Earth. Ground-based analogs, such as bed rest

and water immersion, cannot fully reproduce all the changes observed in space, as they introduce hydrostatic pressures which are absent in microgravity. Indeed, microgravity and ground-based analogs can have opposite effects on some measures, like CVP, which is found to reduce upon entering microgravity [43, 77, 146] but to increase during both bed rest [89] and water immersion [78]. Parabolic flights are able to reproduce microgravity, but for short time intervals (20-25 seconds) and between hypergravity sessions, thus are not useful to investigate the impact of microgravity during long-duration spaceflights. In this context, the computational approach has become more and more used [17, 98, 145, 163, 298] to inquire into hardly measurable haemodynamic processes, and analyse the benefits of specific countermeasure protocols on a deconditioned cardiovascular system after a period in space.

In this study, we aim at exploring the behaviour of the cardiovascular system after about 5-6 months in microgravity without the application of a regular programme of exercise. In particular, we compare the supine haemodynamics of a generic healthy and young man on Earth (1G) and in microgravity (0G), to better describe the mechanisms leading to cardiovascular deconditioning, and detail the haemodynamics of areas where clinical data are not available or contrasting. The choice of the supine position as reference on the ground has a twofold justification: supine is the reference position in clinical practice, and cardiovascular modelling has been developed to simulate the supine posture, for which a more solid data-based parameter setting is available. Thus, all the haemodynamic changes presented in the following are calculated with respect to the supine position at 1G. The fact that no countermeasure is introduced in the model derives from the need to establish a baseline framework, able to well reproduce the direct long-term effects of microgravity exposure on the cardiovascular system. The introduction of any countermeasure, in fact, would confound the pure haemodynamic response to microgravity.

The model adopted in this study is slightly different from the one presented in chapter 3. Thus the main differences between the two models are shown is section 7.2.1. To reproduce the long-term microgravity effects on the cardiovascular system, we have modelled the blood shift and blood volume reduction, together with the changes in the cardiac function, leg venous compliance, arterial resistances and baroreflex mechanisms, which are the most important effects induced by microgravity during long-term spaceflights. Therefore, the model parameters have been modified with respect to the baseline configuration at 1G, to include all these deconditioning factors into the *in-silico* framework (see section 7.2.2). The spaceflight model setting is based on an extensive bibliographic investigation of more than fifty studies on cardiovascular deconditioning. Among the haemodynamic data available in literature, we have favoured those collected during spaceflights rather than ground-based experiments. However, some pieces of information have

been extracted from these latter, in absence of useful direct measurements on astronauts in space, as it has been the case of blood shift. Within the subset of spaceflight data, we have prioritized those obtained from long-duration missions, where regular programmes of exercise and attentive countermeasures were lacking. Studies adopting particular *ad hoc* countermeasures have not been used for the model setting, but just to qualitatively compare our results. Despite we have paid great attention to the spaceflight setting, three aspects deserve to be highlighted: (i) some spaceflight data are given with respect to the standing or sitting 1G configuration, while we have used the supine posture as baseline state at 1G. Thus, in these situations, we have done some estimates in order to make the information available in literature applicable to our case; (ii) since more recent missions adopt a great deal of countermeasures with respect to older missions, we have often taken advantage of older measurements to get rid of the effects of countermeasures on the cardiovascular system response to microgravity; (iii) literature data are sometimes controversial, making the spaceflight setting even more challenging.

7.2.1 A model to simulate the effects of microgravity on the cardiovascular system

The model adopted for this study is represented in Figure 7.2. It is equal to the general model in chapter 3, but it lacks of the coronary circulation and contains a more detailed subdivision of the arteriolar groups among the different body regions. Indeed, the arteriolar groups are divided into four compartments: head and arms, upper abdomen, lower abdomen, and legs, instead of two compartments as in chapter 3. The subdivision between upper and lower abdomen has been done based on the position of the volume indifference point (VIP), which serves to model blood shift as explained below. Then the number (4) and type (one capillary, one venula and one vein) of components making up each of the four compartments, as well as the model equations, do not change with respect to the ones in chapter 3. The 0D model parameters reproducing the haemodynamics of a healthy and supine subject on Earth are somewhere different from those adopted in the general model and are provided in Table C.2.

7.2.2 Spaceflight setting

Blood shift

Blood shift is caused by alterations in the hydrostatic pressure gradient, which becomes null immediately after entering microgravity. Blood shift leads to a redistribution of blood from lower to upper body, where regional blood volumes are expected to grow, if compared to the reference values on the ground. To characterize blood shift, one has to define 1. the point with respect to which blood moves

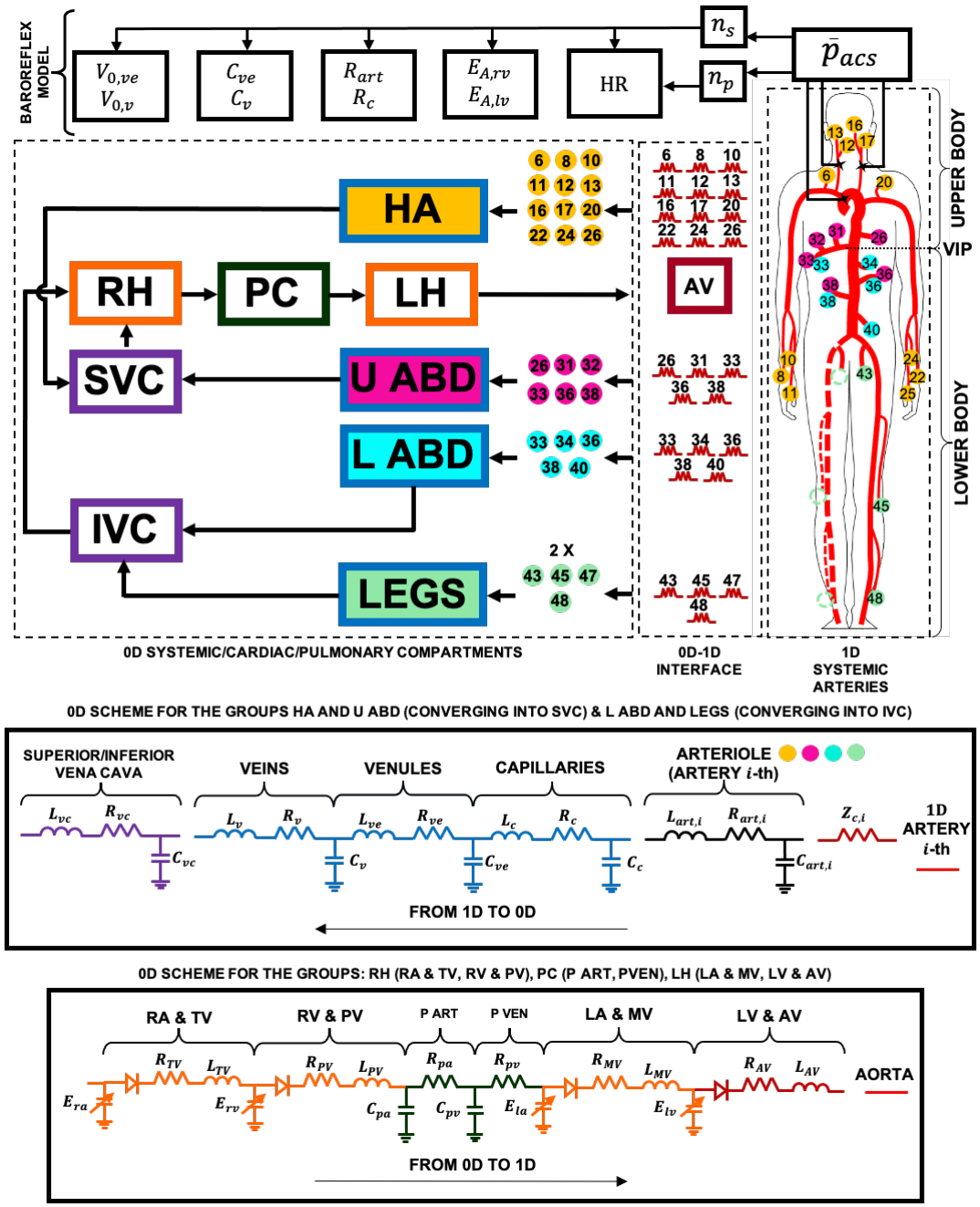

Figure 7.2: Representation of the model adopted in this chapter. It is equal to the general model in chapter 3, apart from the absence of the coronary circulation and the subdivision of the arteriolar groups among the different body regions. The complete legend is provided in Table 3.2.

and 2. the amount of blood shifting from lower to upper body.

1. The reference point for blood shift has been taken equal to the volume indifference point (VIP), which is defined as the body region where blood volume does not change while posture varies. It can be located between the xiphoid process and iliac crest, with the majority of subjects having their VIP at abdominal level (between the epigastric and mesogastric planes), at about 65% of the total body height from the feet [134, 135]. Thus, we have positioned the VIP in the model within the abdomen, in compliance with these instructions.

It is important to note that VIP position is strictly related to orthostatic tolerance: the more VIP is close to the heart, the less cardiac parameters are affected when standing. In other words, orthostatic intolerance is expected to be less impacting on astronauts with a VIP at the level of the xiphoid process rather than of the pelvic region. In this study, however, we have considered the average VIP position, neglecting to evaluate the role of the distance VIP-heart on the cardiovascular response to microgravity.

2. The volume of blood to move from lower to upper body depends on the reference body position on the ground. However, to the best of our knowledge, there are no data from spaceflights about the amount of blood shift with respect to the supine 1G condition, which is our reference position on Earth.

Numerous experiments in simulated weightlessness [186, 216, 217, 244] could give an estimation of the variations in the blood volumes of the main body segments with respect to the supine state. Nevertheless, data extrapolated from ground-based experiments cannot be fully representative of the cardiovascular response to spaceflight. In fact, they introduce side effects, such as interstitial to intravascular fluid movements and, in case of bed-rest, mechanoreceptor stimulation due to the contact with bed.

Measures of the changes in total leg volume have been done during Skylab and Space Shuttle missions [219, 339, 340, 341]. It has been demonstrated that, with respect to the 1G standing posture, each leg looses 600-700 ml within the first day in microgravity and 1 l after 4/5 days from launch. Using the supine position as reference, instead, each leg looses about 900 ml after 4/5 days from launch. However, these data rather than to blood shift refer to fluid shift, which is ruled by other midterm transient mechanisms, such as interstitial fluid shift, blood volume reduction and muscle atrophy [340, 21].

Therefore, in absence of reliable indications on pure blood shift, we have started evaluating leg blood shift based on measures during parabolic flights. We have reasonably assumed that 20-30 s of microgravity are sufficient to induce blood shift only, and not fluid shift, which acts on larger temporal scales. Blood shift from the remaining lower body, as well as the redistribution of blood volume from lower to upper body, has been done by combining considerations based on vessel distensibility and distance from VIP with data on leg blood shift. A more detailed description of the implemented procedure is provided below.

Lower Body Based on parabolic flight measures, we know that during microgravity both legs lose about 330 ml of blood with respect to the standing posture on Earth [21, 263]. We have considered that blood shift is directly proportional to total leg blood volume on Earth (either supine or upright), which amounts to about 900 ml in supine position and 1265 ml in upright position. Thus, by exploiting this proportionality criterium, we have obtained a blood shift of 235 ml (330x900/1265 ml) from both legs, in reference to the supine condition on the ground.

Concerning lower abdomen blood shift, it has been calculated proportionally to leg blood shift. We have plausibly considered two different proportionality criteria: a) the distance of the centres of mass for legs and lower abdomen with respect to VIP, and b) the compliances of legs and lower abdomen. Lower abdomen is more compliant than lower limbs (17.28 vs 10.42 ml/mmHg - estimated by [181]), but closer to VIP than legs (14.70 vs 44.10 cm, center of mass distance - estimated by [229]). Referring to a supine subject on Earth, blood shift for lower abdomen is about 78 ml (235x14.70/44.10 ml) following criterium a), and 390 ml (235x17.28/10.42 ml) according to criterium b). By averaging the blood shifts obtained through the two criteria, we have got a lower abdomen blood shift of 234 ml.

Thus, total blood shift with respect to a supine position on the ground, calculated as the sum of leg (235 ml) and lower abdomen (234 ml) blood shifts, amounts to 469 ml. It is interesting to note that, if one referred to the upright 1G condition, blood shift would be 330 ml from legs [21, 263] and 329 ml from lower abdomen (applying the above criteria). Thus, total blood shift would amount to 659 ml. This latter is close to 700 ml, which is reported in literature as the most reliable estimate of lower body blood shift upon entering weightlessness with respect to the upright 1G condition [339]. This good agreement is an a posteriori validation of the realistic blood shift here proposed for a reference supine subject on Earth.

Upper Body Volume of blood leaving lower body has been distributed to upper body regions following the above criteria, which equally weight vessel compliance (C) and distance from VIP (d). Therefore, considering the three upper body regions (head-arms: C=15.63 ml/mmHg, d=24.20 cm; cardiac-thoracic: C=50.12 ml/mmHg, d=24.20 cm; upper abdomen: C=50ml/mmHg, d=7.85 cm [181, 229]), we have attributed 28% (133 ml), 43% (202 ml) and 29% (134 ml) of total blood shift to head-arms, cardiac-thoracic and upper abdomen, respectively.

We recall that each of the regions named above (legs, lower abdomen, upper abdomen, cardiac-thoracic and head-arms) contains three different compartments (capillary, venular and venous). Thus, the variation in the total blood volume of each region has been applied to the total blood volumes of the compartments within each region. In particular, total, V, and unstressed blood volumes, V_0, of each compartment within a generic region have been modified proportionally to the supine 1G condition, and to maintain the local ratio V_0/V as in the supine 1G

condition, respectively.

Total blood volume reduction

During long periods of exposure to microgravity, total blood volume reduces compared to the supine body position on the ground [8, 241]. This reduction starts 48h after launch [369] and can be considered concluded 6 weeks later [42, 109]. It is found in literature that total blood volume reduces of 9 to 15% compared to preflight [18, 42, 201, 200, 369]. Thus, we have diminished total blood volume of a percentage in the middle of the above interval (-11.5%). To this aim, total blood volumes, V, have been decreased proportionally to the volume distribution after the application of blood shift, while unstressed volumes, V_0, have been chosen in order to preserve local ratios V_0/V after blood shift.

Arterial resistances

The general trend seems that, after a long period of exposure to microgravity, resistances of lower limbs tend to reduce, while cerebral resistances can oscillate during the mission, usually increasing after some months in space. In particular, after 4/6 months in space, it has been observed that renal and femoral resistances decrease of 15% [79, 124] and between 5 and 12% [14, 104, 124], respectively, while cerebral resistances increase in the range 5-15% [79, 124]. Moreover, Grigoriev et al. [104] suggested that all arterial resistances below the heart level reduce because of the lack of the gravitational stimulus. In accordance with these findings, we have applied a decrease of 10% to all lower body resistances and an increase of 10% to carotid and vertebral resistances, with respect to the corresponding supine values at 1G.

Leg venous compliance

Despite the fact that literature results are not always in accordance [69, 360], the increase in leg venous compliance after a long period of exposure to weightlessness is widely accepted [381]. Different authors have found a rise in leg venous compliance of 25 to 30% with respect to the preflight values [57, 58, 83, 104, 157]. We have thus imposed an increase in leg venous compliance, C_{v_LEGS}, of 27% with respect to the supine 1G condition.

Cardiac function

There are contrasting data in literature about the effects of microgravity in cardiac function. It all depends on the effectiveness and regularity of the applied countermeasures aboard. As observed by Arbeille et al. [14], if a good programme of

exercise is regularly followed by long-term crews, cardiac adaptation to microgravity remains stable for several months of missions and does not lead to problematic cardiac dysfunctions (no significant alterations in EF and myocardial thickness are observed). On the other hand, when physical activity is absent (as happens in bed rest studies) or the recommended programme of exercise is not accurately implemented, cardiac function starts to be compromised [201, 200, 178, 262]. It has been demonstrated that endurance and strength training countermeasures implemented during prolonged missions on the ISS are adequate to avoid cardiac atrophy [129], which is defined as a reduction in the size and mass of the heart [121]. In fact, Abdullah et al. [2] verified that left and right ventricular end-diastolic and end-systolic volumes, as well as right/left ventricular masses and supine stroke volume, do not change significantly or are maintained as staying on the ISS up to 6 months. In addition, considering the rapid postflight cardiac recovery, it seems that even the largest variations in cardiac parameters are not due to significant structural cardiac changes [328, 327], but to a cardiac remodelling caused by an intrathoracic overpressure, which in turn leads to cardiac volume and compliance variations.

In case of long duration spaceflight without the application of a regular/effective countermeasure programme, the reduction of cardiac contractility and function has been quantified through decreases in V_{edlv} (-5/13%) [14, 48, 104, 123, 124, 201, 200], SV (-14/23%) [14, 123, 124, 201, 200], and EF (-5/11%) [14, 48, 104, 124, 201, 200].

To take into account these changes, we have modified the maximum and minimum values of ventricular elastances and cardiac dimensions as follows. Amplitudes of left ($E_{A,lv}$) and right ventricular ($E_{A,rv}$) elastances have been decreased of 27% with respect to the supine 1G condition, as leg venous compliance. Minimum left and right ventricular elastance values ($E_{B,lv}$ and $E_{B,rv}$, respectively) have been instead incremented to accommodate contractile reduction. We have applied a percent increment of 2.7% (about ten-fold lower) only, considering that the minimum elastance values are mildly involved in defining the contractile capability. We have treated left and right ventricles equally in absence of definitive data in literature.

It is worth noting that unbalances in compliance variations between upper and lower body would induce modifications in VIP position. To avoid this mechanism, we have increased pulmonary arterial and venous compliances of 4% and 5%, respectively.

Regarding cardiac volume, it is usually expected to decrease of 8 to 14% [56] with respect to preflight values. Thus, we have considered an intermediate reduction of about 10% with respect to the supine 1G condition. This variation has been applied by decreasing the unstressed volumes of all cardiac chambers of 90% compared to the supine 1G reference.

Baroreflex function

Concerning the baroreflex function, we have just considered the variations in the reference values of the aortic-carotid sinus pressure, $p_{acs,ref}$, sensed by the baroreceptors and HR.

During long-duration spaceflights, mean arterial pressure is reported to reduce between 2 to 10% [14, 131, 351, 352], with the smallest reductions occurring as specific countermeasures are applied. Recalling that we aim at studying the situation in which *ad hoc* countermeasures are absent, we have imposed a reduction in $p_{acs,ref}$ of 10% with respect to the supine 1G values (83.7 mmHg in microgravity against 93 mmHg on the ground).

Regarding the behaviour of HR after long periods in space, it has been found that it remains constant or increases. The great variability of results is mainly due to the choice of the reference body position on the ground. In fact, already on Earth, HR grows of about 24% when moving from supine to standing [351]. Considering the supine position at 1G, variations in HR in microgravity are indicated in the range 5/15% [14, 131, 351, 352, 201, 200]. Accordingly, we have set a reference HR 13% higher than the supine 1G value (84.75 bpm in microgravity against 75 bpm on the ground).

A summary of the main mechanisms considered to simulate the long-term effects of microgravity on the cardiovascular system functioning, without *ad hoc* countermeasures and with respect to the supine 1G position, is provided in Table 7.7.

7.2.3 Global haemodynamic response after 5/6 months of spaceflight

Results are organised first showing the mean variations in the main cardiac parameters from preflight supine to spaceflight values. These mean variations are compared, when possible, with the ones obtained from literature, which are referred to long-duration spaceflights without the application of a regular plan of countermeasures. Thus a validation of our modelling response has been performed. After that, time-series, characteristic levels (i.e., mean, maximum, excursion) and waveform changes of pressures, flow rates and volumes have been analysed at some sites within four different macro areas: cerebral, cardio-thoracic, abdominal and lower limbs.

Cardiac parameters

The values of the most important cardiac parameters preflight in the supine position and after months in space are indicated in Table 7.8, together with the corresponding percent variations from the configurations supine 1G and spaceflight

Table 7.7: Summary of the mechanisms considered (column i) to simulate the long-term effects of microgravity on the cardiovascular system without the application of *ad hoc* countermeasures. The adopted cardiovascular changes with respect to the 1G supine condition and the details of the corresponding model implementation are reported in columns ii and iii. Legend is provided in Appendix D. *Table extracted from* [92].

Mechanism	**Changes**	**Implementation**
Blood shift	Legs volume: -235 ml Lower abdomen volume: -234 ml Head-arms volume: +133 ml Cardiac-thoracic volume: +202 ml Upper abdomen volume: +134 ml	Total, V, and unstressed volumes, V_0, of the compartments within each region are varied proportionally to the 1G condition and to preserve the ratio V_0/V as in 1G, respectively.
Blood volume reduction	-11.5%	Total, V, and unstressed volumes, V_0, of the compartments within each region are varied proportionally to the blood shift condition and to preserve the ratio V_0/V as after blood shift, respectively.
Cardiac function	$E_{A,lv}$, $E_{A,rv}$: -27% $E_{B,lv}$, $E_{B,rv}$: +3% C_{pa}: +4% C_{pv}: +5% Cardiac volume: -10%	Cardiac volume reduction is implemented by reducing the unstressed volumes, V_0, of all cardiac chambers of -90%.
Legs venous compliance	C_{v_LEGS} : +27%	Model parameters are changed of the same percentage.
Arterial resistances	Vertebral and carotid R_{art}: +10% Lower body R_{art}: -10%	Model parameters are changed of the same percentage.
Baroreflex response	Reference HR: +13% $p_{acs,ref}$: -10%	Model parameters are changed of the same percentage.

0G. These outcomes are compared with literature data when available. As already observed in section 7.1.5, the number of cardiac parameters actually measured during long-term microgravity is quite limited, and they are sometimes discordant, mainly because of the different postures adopted during the preflight measurements and the different levels of countermeasures applied aboard [240]. Thus, a comparison between our results and those in literature has been possible for some metrics only: V_{edlv}, SV, EF, CO and $p_{aor_{mean}}$. Among literature data, we have selected those collected during long-duration spaceflights without the application of *ad hoc* countermeasures, which are the most reliable results to be used as references in our investigation.

One observes that, in accordance with literature [14, 48, 123, 124, 199, 201, 200], left ventricular parameters, such as V_{edlv} (-9.30%), SV (-18.32%) and EF (-9.93%), decrease. CO (-7.58%) falls less than SV, due to the increase in HR (+13%, as explained in section 7.2.2), in agreement with the spaceflight data using the supine 1G position as reference [14, 124, 201, 200]. In fact, as shown in Table 7.3, the sign of the variation in CO strongly depends on the 1G position. CO typically increases [130, 199, 242] with respect to the 1G standing/sitting posture, while decreases

Table 7.8: Modelled cardiac parameters for the supine 1G configuration and during long-term 0G spaceflight: end-systolic left ventricular volume, V_{eslv}; end-diastolic left ventricular volume, V_{edlv}; stroke volume, SV; ejection fraction, EF; cardiac output, CO; stroke work per minute, SW; central venous pressure, CVP; systolic and diastolic ascending aortic pressures, $p_{aor_{sys}}$ and $p_{aor_{dia}}$; mean arterial pressure, $p_{aor_{mean}}$; tension time index per minute, TTI; rate pressure product, RPP; augmentation index and pulse pressure for the ascending aortic district, AI_{AA} and pp_{aor}. *Table extracted from* [92].

Variable	Supine 1G	Spaceflight 0G	% Variation	Literature data
V_{eslv} [ml]	48.43	50.73	+4.75%	/
V_{edlv} [ml]	123.96	112.43	- 9.30%	[-5%,-15%] [14, 48, 104, 123, 124, 201, 200]
SV [ml]	75.54	61.70	- 18.32%	[-14%,-23%] [14, 123, 124, 199, 201, 200]
EF [%]	60.93	54.88	- 9.93%	[-5%,-11%] [14, 48, 104, 124, 201, 200]
CO [l/min]	5.67	5.24	- 7.58%	[-11%,-18%] [14, 124, 201, 200]
SW [J/min]	80.01	64.58	- 19.29%	/
CVP [mmHg]	6.49	6.16	-5.08%	/
$p_{aor_{sys}}$ [mmHg]	121.03	104.82	- 13.39%	/
$p_{aor_{dia}}$ [mmHg]	69.99	65.16	-6.90%	/
$p_{aor_{mean}}$ [mmHg]	87.01	78.38	-9.92%	[-2%,-10%] [14, 131, 351, 352]
TTI [mmHg s/min]	2590	2373	- 8.38%	/
RPP [mmHg/min]	9078	8905	-1.91%	/
AI_{AA}	0.17	0.10	- 41.18%	/
pp_{aor} [mmHg]	51.04	39.66	- 22.30%	/

[14, 124, 201, 200] or slightly grows [199] with respect to the 1G supine posture. $p_{aor_{mean}}$ (as well as mean brachial pressure) declines of 9.92% in our model, being thus in accordance with spaceflight data referred to both the supine [14, 131, 351, 352] and seated [242, 240] postures on the ground.

Based on the above, it emerges a satisfactory comparison between model and literature results, that is a proof of the accuracy of both the spaceflight setting and model outcomes. Notice that this comparison has not been exploited to tune the model parameters but to *a posteriori* assess the reliability of the model response to long-term microgravity, after the completion of the parameter setting. Despite the limited number of spaceflight measurements does not allow us an extensive validation of the model, it justifies the need to rely on computational approaches to inquire into the microgravity-induced variations of cardiac and cardiovascular parameters not still measured in space.

We have also evaluated the changes experienced in space by other cardiac parameters not typically detected during spaceflights: the stroke work, SW, the tension time index per minute, TTI, the rate pressure product, RPP, and the augmentation

index, AI_{AA}. SW, TTI and RPP have been calculated through the equations (1.3), (1.6) and (1.7), respectively, while AI_{AA} has been defined in section 1.2.5.

We have found that the work done by the heart and the oxygen consumption reduce in microgravity (-19.29% for SW, -1.91% and -8.38% for RPP and TTI, respectively). pp_{aor} also falls (-22.30%), since $p_{aor_{sys}}$ decreases more than $p_{aor_{dia}}$ (-13.39% and -6.90%, respectively). As a consequence of the pulse pressure behaviour, there is a decline in AI_{AA} (-41.18%) too.

CVP has been taken equal to the mean value of the average pressures in the two venae cavae and has been found to decrease of 5.08%, that is in qualitative agreement with the CVP reduction observed during both parabolic flights [77, 171, 353] and early in microgravity. [43, 77, 146]. However, these latter variations are not fully comparable with our results, since they are associated to different time frames. At the moment there are no CVP measurements after long-periods in space, considering the impossibility to accurately evaluate this pressure through noninvasive instruments [194, 202].

These results reflect the general cardiovascular deconditioning astronauts are subjected to during long microgravity exposure without an effective countermeasure programme. In this situation, cardiac parameters are affected as in sedentary lifestyle.

Pressure, flow rates and volumes

Pressure, $p(t)$, and flow rate, $Q(t)$, steady-state signals in the supine 1G and 0G configurations have been analysed together with the spaceflight variations in the corresponding beat-averaged values ($\bar{p}$, $\bar{Q}$, and $\bar{V}$). In order to evaluate the vertical stretching of pressure signals, the spaceflight variations in pulse, pp, and maximum, p_{max}, pressures have been also assessed. These results are shown in Figure 7.3 at four different sites, while the values of the couples $\bar{p}$-$\bar{Q}$ and pp-p_{max} everywhere in the model domain are indicated in Tables 7.9 and 7.10, respectively. From Table 7.9, one observes that $\bar{p}$ and $\bar{Q}$ reduce in space, with a more homogeneous behaviour throughout the whole cardiovascular system for $\bar{p}$ than for $\bar{Q}$. In fact, $\bar{p}$ values are in the range -8 to -12% (except at cardiac level and along the venous return where variations are between -2 and -6%), while $\bar{Q}$ values range between -16 to -18% at cerebral level and -2 to -6% along the lower limbs (excluding the anterior tibial artery where a variation of -11.94% is detected). p_{max} exhibits a greater variability than $\bar{p}$, oscillating between -5 and -15%. pp variations are in the interval +4.82% and -56.00%, without a clear correlation with location, type (venous/arterial), and size region. As an example, one can notice that the superior and inferior venae cavae show absolutely different pp variations (+4.82% and -32.97%, respectively), although they have similar sizes and are both connected to the right atrium.

Volume, $V(t)$, signals in the supine 1G and 0G states have been evaluated together with the spaceflight variations of the beat-averaged values, $\bar{V}$. Results are

reported in Figure 7.4 for the 0D compartments. $\bar{V}$ values are decisively negative (up to -42%) below VIP, while are positive or up to -13% negative above VIP. These differences between lower and upper body are mainly due to blood shift, which mitigates volume reductions at cardiovascular regions above VIP. However, the decrease in cardiac contractility and volume, manly caused by the rise in the amplitude of the ventricular elastances and the reduction in the cardiac unstressed volumes, works against central blood shift. It follows that cardiac $\bar{V}$ variations are more negative than in the surrounding thoracic regions.

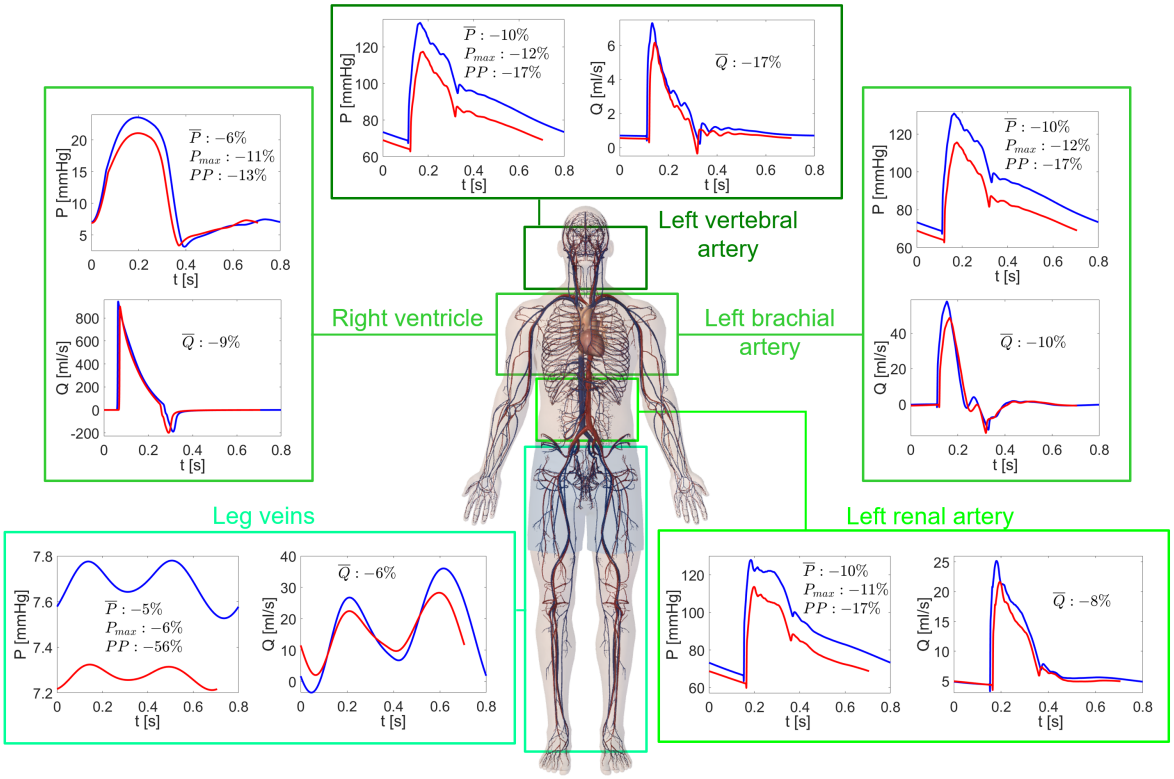

Figure 7.3: Steady-state pressure, $p(t)$, and flow rate, $Q(t)$, signals at different sites for the supine 1G (blue) and 0G (red) configurations. Variations between 1G and 0G states of the beat-averaged pressure ($\bar{p}$) and flow rate ($\bar{Q}$), together with the maximum pressure (p_{max}) and pulse pressure (pp), are also indicated in each panel. *Image extracted from* [92].

Waveform alterations of the haemodynamic signals

To quantify the waveform alterations in pressure and flow rate signals throughout the whole cardiovascular system, we have used the normalised signal difference,

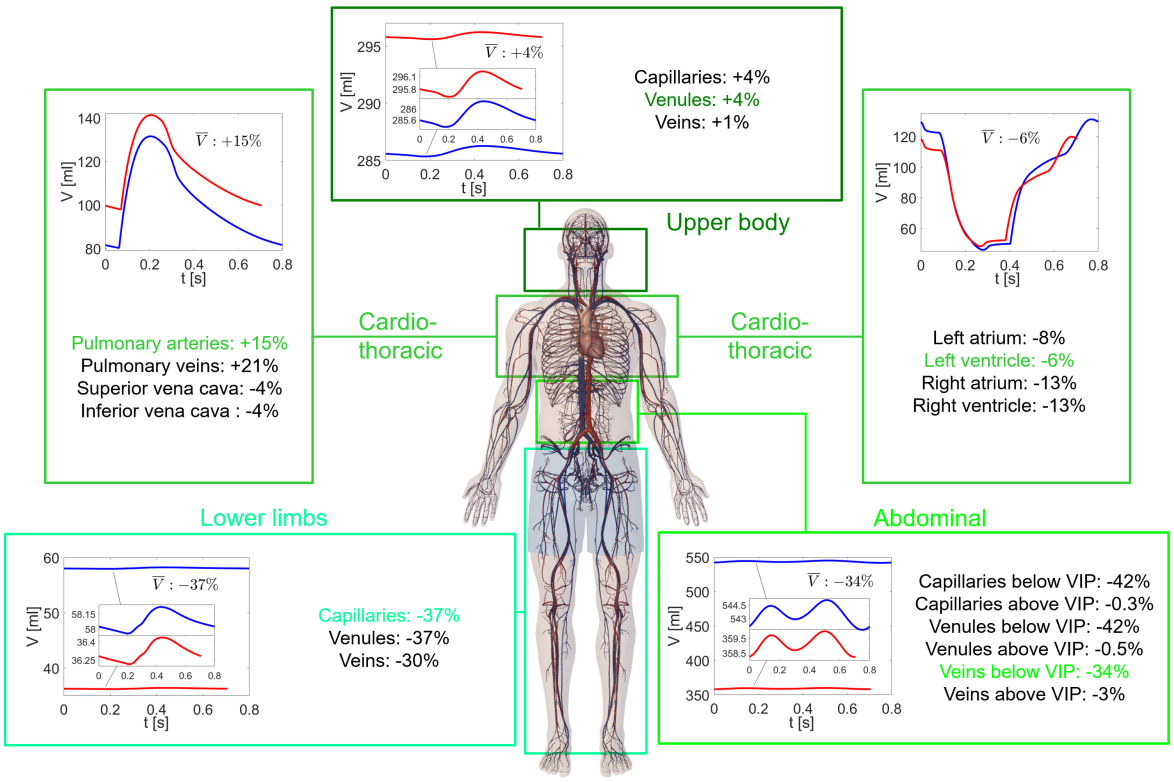

Figure 7.4: Steady-state volume, $V(t)$, signals at different sites for the supine 1G (blue) and 0G (red) configurations. Variations between 1G and 0G states of the beat-averaged volume ($\bar{V}$) are also indicated in each panel. *Image extracted from* [92].

NSD. It is a not-dimensional parameter ranging between 0 and 2, representative of the similarity between two signals in the 1G supine and 0G states, respectively.

Given the generic p or Q signal, $y(t)$, we have normalised it both in time and amplitude as $y'(t') = (y(t') - \mu_y)/\sigma_y$, where $y(t')$ is the signal over the dimensionless cardiac period (time is normalised as $t' = t/\mathrm{RR}$), while μ_y and σ_y are the mean value and standard deviation of $y(t')$, respectively. Thus, NSD is defined as

$$NSD = \int_0^1 |y'(t')_{1\mathrm{G}} - y'(t')_{0\mathrm{G}}| dt', \quad NSD = [0,2], \tag{7.1}$$

where the subscripts 1G and 0G refer to the preflight supine and spaceflight configurations, respectively. Notice that since $y'(t')$ signals (p' and Q') are normalised in both time and amplitude, they are perfectly comparable, even referring to different configurations (1G and 0G). In particular, for NSD=0, no waveform variation is detected between $y'(t')_{1\mathrm{G}}$ and $y'(t')_{0\mathrm{G}}$, while, for NSD=2, the two signals are complementary to each other.

p' and Q' signals at 1G and 0G, together with the corresponding NSD values, are provided at different locations in Figure 7.5. NSD values throughout the whole domain are given in Table 7.11.

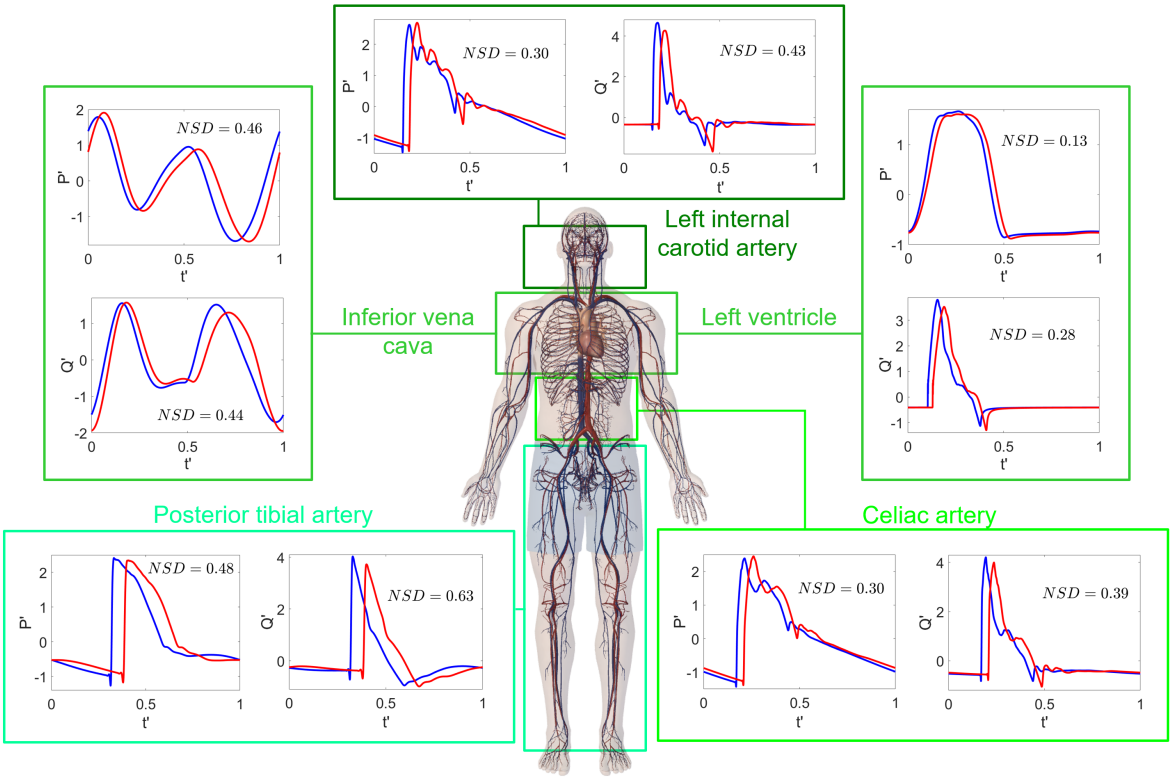

Figure 7.5: Normalised pressure, p', and flow rate, Q', signals in both time and amplitude at different sites for the supine 1G (blue) and 0G (red) configurations. NSD values for p' and Q' are also indicated in each panel. *Image extracted from* [92].

Normalised signals p' and Q' in 0G are always delayed with respect to 1G signals, mainly because of the higher HR in 0G. However, it seems that this is not the only reason. In fact, the magnitude of this delay changes region by region, without a clear trend. NSD values are often not negligible and beyond 0.5. Moreover, as apparent from the NSD values in Table 7.11, flow rates are more affected than pressures, and proximal regions are more affected than distal regions.

Discussion about this investigation

The combination of blood shift and volume reduction, together with the alterations in arterial resistances, leg venous compliance and cardiac/baroreflex functions, leads to not negligible variations in the cardiovascular behaviour with respect

to the preflight configuration. One can observe that, while the volume reduction and altered baroreflex function have equal effects on the whole circulation, the blood shift and altered arterial resistances, leg venous compliance and cardiac function create heterogeneous responses site by site.

Volume variations are mainly due to blood shift and volume reduction, which cause important volume decreases in the lower body, where the two contributions sum up. Smaller volume decreases are instead found in the upper body, where blood shift partially compensates for volume diminution. Nonetheless, smaller volume decreases in the upper body do not cause smaller pressure decreases with respect to the other body regions, due to the local alterations in arterial resistances and compliances. The increase in cardiac compliance limits central pressure variations (-1 to -8%), while the increase in leg venous compliance contributes to pressure variations along the lower limbs (-8 to -12%) similar to the ones detected in the upper body. In spite of the homogenous pressure variations in upper and lower body, flow rate variations are higher in the upper body (-17 to 19%), smaller in the lower body (-2 to -5%), and in the middle in the cardio-thoracic region (-8 to -10%). The difference in the flow rate variations between upper and lower body is due to the fact that while lower body arterial resistances decrease, cerebral arterial resistances increase.

Maximum and mean pressure variations are smaller at venous than arterial level, because of the bigger venous compliance, which even increases during spaceflight in the legs. This means that venous vessels can more easily absorb the received pressure changes than their arterial counterparts. In general, pulse pressure variations are more important than mean and maximum pressure variations. Signals become less pulsatile in space than on Earth (from -10 to -30%), especially at the periphery, where pulsatility of pressure signals is already small at 1G.

During spaceflight, flow rate variations get lower along the arterial tree, from the aortic root to the abdominal aorta, as a consequence of the changes in the arterial resistance and the reduction in both cardiac volume and contractility. Flow rate variations then start increasing again from the inner iliac to the posterior tibial, probably because of (i) the smaller influence of resistance variations on conduction arteries (femoral and external iliac arteries) than on their bifurcating branches (deep femoral and inner iliac arteries), and (ii) the higher absolute value of posterior tibial artery resistance on Earth compared to anterior tibial.

Globally, both cardiac and cardiovascular parameters reflect a status of relaxed and sedentary lifestyle. Cardiac work, oxygen consumption and contractility indexes all decrease, together with central mean and pulse pressures. These variations create the well known cardiovascular deconditioning, which is manly triggered by the blood volume reduction and the decrease in cardiac volume and contractility.

Variations in pulse pressure and NSD are quite variable throughout the body, being affected differently site by site. Along the arterial tree, pp and NSD variations are inverted, with high and low pp and NSD variations, respectively, at aortic

root, and the opposite at tibial level. The fact that the highest NSD variations are localised distally is not surprising, if one considers that, already in 1G, peripheral regions are the sites where the most important waveform variations occur. Moreover, variations in arterial resistances are expected to lead to more profound alterations in peripheral than central pressure/flow rate signals. Thus, centrally, where pressure and flow rate waveforms are mainly influenced by the forward contribution, NSD variations are limited (NSD<0.2). By contrast, close to reflection sources (like bifurcations, geometrical discontinuities and arteriolar interfaces), where forward and backward waves are comparable, NSD variations upsurge ($NSD \geq$0.5). It appears that there are greater NSD variations for Q than p. In fact, while the backward pressure waves are reflected upright, the backward flow rate waves are reflected upside down, with respect to the corresponding forward waves. It follows that the same variation in the backward wave impacts more on total flow rate than on total pressure wave. Waveform variations at central level are not absorbed at the arteriolar-capillary districts (NSD=0.4-0.5). It follows that phenomena like regular perfusion and nutrient supply at cellular level can be affected at 0G.

Although the 0G exposure impacts the majority of cardiac and cardiovascular parameters, it does not induce dramatic consequences in terms of cardiac contractility. In fact, despite EF is here found to decrease of 10%, reductions in EF are judged critical when below 20%, that has never happened during any spaceflight [79]. The 0G adaptation point, however, can be seriously challenging for astronauts, upon re-entry on Earth or in case of partial gravity restoration. In these situations, indeed, a portion of blood moves again below VIP, posing the risk of irregular cerebral perfusion, especially considering the state of general hypovolaemia (blood volume is 11.5% smaller) and hypotension (mean pressure is 10% lower) affecting the whole circulation after months in space. Apart from this, the increase in leg venous compliance and the decrease in lower body arterial resistances contribute to aggravate the venous pooling provoked by the re-introduction of the gravity vector after landing. In addition, a reduced effectiveness of the baroreflexes in guaranteeing the preflight chronotropic and inotropic effects can make the maintenance of a normotensive state even more difficult [56]. This condition, the orthostatic intolerance, is pretty common among astronauts after re-entry on Earth, with important mitigations sources coming from the execution of regular programmes of exercise throughout the mission.

We have found that central pulse pressure reduces of about 22.30% during spaceflight. Since central pulse pressure is typically lower in sedentary than resistive-trained people on Earth [26, 60, 153, 213], it can be considered as a marker of training and physical activity, both lower after months in space. In other words, in absence of effective countermeasures, the exercise tolerance of astronauts becomes similar to the one of a sedentary person at 1G.

Therefore, all in all, this investigation provides a lot of data about the changes

experienced by the cardiovascular system after months in space, without the application of a regular and effective plan of countermeasures. The majority of these data could not be obtained from direct space measurements, thereby proving the utility of the computational approach to inquire into the cardiovascular behaviour in extreme environments like space. As future steps, subject-specific responses to microgravity could be provided by the present model, also exploring the role of factors such as age on the cardiovascular response to long-term spaceflights. Moreover, starting from the deconditioned configuration here presented, the inclusion of one or more countermeasures to the present model is expected in future works. This would allow us to quantify the effects of specific countermeasure protocols on the deconditioned circulation.

Among the limits of the model here adopted, the fact that it does not specifically include the interstitial fluid shift. Nevertheless, this mechanism is intrinsically included in the model setting, through the variations in the total and unstressed volumes of all the cardiovascular compartments. In addition, the gravity term is not introduced in the model, even if it could be inserted in the model equations, to replicate the action of martial or lunar gravity in view of future interplanetary space missions.

Table 7.9: Beat-averaged values of pressure, $\overline{p}$ [mmHg] and flow rate $\overline{Q}$ [ml/s] at different sites in supine 1G and 0G conditions, with relative variations [%]. *Table extracted from* [92].

Cardiovascular area	$\overline{p}$ **[mmHg]**			$\overline{Q}$ **[ml/s]**		
	1G	**0G**	**Variation [%]**	**1G**	**0G**	**Variation [%]**
Arterial tree pathway (1D)						
Ascending aorta	92.61	83.19	-10.17%	87.85	80.01	-8.92%
Thoracic aorta	92.38	82.99	-10.16%	67.07	62.20	-7.26%
Abdominal aorta A	90.29	81.12	-10.16%	46.95	44.04	-6.20%
Abdominal aorta E	90.76	81.45	-10.26%	17.01	16.02	-5.82%
External iliac	90.48	80.93	-10.55%	6.31	5.86	-7.13%
Femoral	89.47	80.20	-10.36%	3.24	2.94	-9.26%
Cerebral region (0D-1D)						
HA veins	6.94	6.54	-5.76%	20.82	17.86	-14.22%
Left vertebral	92.47	83.13	-10.10%	1.60	1.33	-16.88%
Left vertebral arterioles	70.60	64.86	-8.13%	1.61	1.34	-16.77%
Left internal carotid	92.27	83.03	-10.01%	2.16	1.76	-18.52%
Left internal carotid arterioles	80.40	73.32	-8.81%	2.18	1.78	-18.35%
Left external carotid	92.28	83.05	-10.00%	2.34	1.90	-18.80%
Left external carotid arterioles	80.37	73.32	-8.77%	2.35	1.93	-17.87%
Cardio-thoracic region (0D-1D)						
LA and MV	7.51	7.39	-1.60%	87.91	80.11	-8.87%
LV and AV	43.20	39.59	-8.36%	87.85	80.01	-8.92%
RA and TV	6.47	6.14	-5.10%	87.90	80.15	-8.82%
RV and PV	11.64	10.95	-5.93%	87.84	80.04	-8.88%
Pulmonary arteries	15.42	14.59	-5.38%	87.83	80.02	-8.89%
Pulmonary veins	8.39	8.19	-2.38%	87.86	80.05	-8.89%
SVC	6.48	6.15	-5.09%	20.80	17.85	-14.18%
IVC	6.50	6.17	-5.08%	67.16	62.35	-7.16%
Intercostals	92.64	83.22	-10.17%	9.93	8.85	-10.88%
Intercostals arterioles	85.39	76.74	-10.13%	9.89	8.85	-10.52%
Left brachial	92.33	82.97	-10.14%	4.29	3.85	-10.27%
Abdominal region and organs (0D-1D)						
Gastric	89.36	80.44	-9.98%	4.92	4.41	-10.37%
Gastric arterioles	48.88	44.05	-9.88%	4.92	4.42	-10.16%
Coeliac A	91.57	82.26	-10.17%	10.17	9.19	-9.63%
Left renal	90.43	81.23	-10.17%	8.50	7.81	-8.12%
U left renal arterioles	66.18	58.90	-11.00%	4.19	3.68	-12.17%
L left renal arterioles	66.18	58.90	-11.00%	4.30	4.13	-3.95%
U ABD venules	12.94	11.90	-8.04%	26.35	23.44	-11.04%
L ABD venules	12.98	12.38	-4.62%	23.64	22.68	-4.06%
Lower limbs region (0D-1D)						
Inner iliac	90.47	81.17	-10.28%	2.20	2.15	-2.27%
Inner iliac arterioles	78.65	69.59	-11.52%	2.20	2.15	-2.27%
Deep femoral	89.44	80.17	-10.36%	3.08	2.93	-4.87%
Deep femoral arterioles	68.12	59.74	-12.30%	3.07	2.93	-4.56%
Anterior tibial	84.44	75.61	-10.46%	2.01	1.77	-11.94%
Anterior tibial arterioles	38.20	34.16	-10.58%	2.01	1.78	-11.44%
Posterior tibial	84.90	76.00	-10.48%	1.22	1.15	-5.74%
Posterior tibial arterioles	64.36	56.33	-12.48%	1.23	1.16	-5.69%
Legs capillaries	27.13	25.63	-5.53%	17.02	16.04	-5.76%
Legs veins	7.68	7.28	-5.21%	17.03	16.04	-5.81%

Table 7.10: Maximum pressure, p_{max}, and pulse pressure, pp, values [mmHg] at different sites in supine 1G and 0G conditions, with relative variations [%]. *Table extracted from* [92].

Cardiovascular area	p_{max} **[mmHg]**			pp **[mmHg]**		
	1G	**0G**	**Variation [%]**	**1G**	**0G**	**Variation [%]**
Arterial tree pathway (1D)						
Ascending aorta	121.03	104.82	-13.39%	51.04	39.66	-22.30%
Thoracic aorta	129.83	114.49	-11.82%	61.77	51.04	-17.37%
Abdominal aorta A	123.92	109.98	-11.25%	58.75	48.83	-16.89%
Abdominal aorta E	135.38	119.27	-11.90%	72.78	60.26	-17.20%
External iliac	135.07	119.46	-11.56%	74.55	62.15	-16.63%
Femoral	135.63	119.75	-11.71%	76.97	63.71	-17.23%
Cerebral region (0D-1D)						
HA veins	7.33	6.84	-6.68%	0.72	0.64	-11.11%
Left vertebral	133.17	117.39	-11.85%	65.80	54.55	-17.10%
Left vertebral arterioles	82.67	74.08	-10.39%	25.66	19.77	-22.95%
Left internal carotid	140.36	124.19	-11.52%	74.99	62.99	-16.00%
Left internal carotid arterioles	101.30	90.77	-10.40%	39.52	32.47	-17.84%
Left external carotid	141.51	125.13	-11.58%	76.19	63.99	-16.01%
Left external carotid arterioles	100.25	89.30	-10.92%	38.03	30.53	-19.72%
Cardio-thoracic region (0D-1D)						
LA and MV	8.67	8.54	-1.50%	2.49	2.27	-8.84%
LV and AV	121.27	105.10	-13.33%	118.26	101.38	-14.27%
RA and TV	7.93	7.42	-6.43%	3.12	3.12	/
RV and PV	23.56	21.08	-10.53%	20.40	17.73	-13.09%
Pulmonary arteries	23.35	20.92	-10.41%	13.49	10.93	-18.98%
Pulmonary veins	9.10	8.68	-4.62%	1.21	0.83	-31.40%
SVC	9.09	8.59	-5.50%	4.77	5.00	+4.82%
IVC	7.91	7.14	-9.73%	2.73	1.83	-32.97%
Intercostals	141.78	124.59	-12.12%	74.57	61.88	-17.02%
Intercostals arterioles	115.90	103.48	-10.72%	51.63	43.67	-15.42%
Left brachial	130.85	115.57	-11.68%	63.59	52.85	-16.89%
Abdominal region and organs (0D-1D)						
Gastric	130.97	116.02	-11.41%	67.09	56.02	-16.50%
Gastric arterioles	56.93	50.23	-11.77%	16.94	13.02	-23.14%
Coeliac A	135.66	119.61	-11.83%	70.55	58.49	-17.09%
Left renal	127.89	113.58	-11.19%	64.44	53.80	-16.51%
Left renal arterioles (U and L)	78.37	68.11	-13.09%	24.92	18.91	-24.12%
U ABD venules	13.64	12.39	-9.16%	1.60	1.15	-28.12%
L ABD venules	13.81	13.03	-5.65%	1.74	1.38	-20.69%
Lower limbs region (0D-1D)						
Inner iliac	137.60	121.48	-11.72%	76.79	63.97	-16.69%
Inner iliac arterioles	105.54	90.17	-14.56%	46.21	35.46	-23.26%
Deep femoral	136.30	120.03	-11.94%	77.21	63.70	-17.50%
Deep femoral arterioles	86.66	73.92	-14.70%	33.69	25.66	-23.83%
Anterior tibial	144.32	124.92	-13.44%	91.07	73.91	-18.84%
Anterior tibial arterioles	45.93	40.33	-12.19%	14.13	10.91	-22.79%
Posterior tibial	144.91	125.36	-13.49%	91.46	74.11	-18.97%
Posterior tibial arterioles	85.48	72.87	-14.75%	35.96	27.65	-23.11%
Legs capillaries	31.59	29.23	-7.47%	8.30	6.71	-19.16%
Legs veins	7.78	7.32	-5.91%	0.25	0.11	-56.00%

Table 7.11: NSD values at different sites for pressure, p', and flow rate, Q', signals. *Table extracted from* [92].

Cardiovascular region	**NSD** p'	**NSD** Q'
Arterial tree pathway (1D)		
Ascending aorta	0.19	0.28
Thoracic aorta	0.24	0.37
Abdominal aorta A	0.31	0.37
Abdominal aorta E	0.33	0.47
External iliac	0.34	0.49
Femoral	0.37	0.56
Cerebral region (0D-1D)		
HA veins	0.56	0.56
Left vertebral	0.25	0.32
Left vertebral arterioles	0.25	0.23
Left internal carotid	0.30	0.43
Left internal carotid arterioles	0.26	0.27
Left external carotid	0.30	0.41
Left external carotid arterioles	0.23	0.25
Cardio-thoracic region (0D-1D)		
LA and MV	0.26	0.34
LV and AV	0.13	0.28
RA and TV	0.41	0.44
RV and PV	0.15	0.23
Pulmonary arteries	0.16	0.17
Pulmonary veins	0.31	0.23
SVC	0.51	0.49
IVC	0.46	0.44
Intercostals	0.29	0.49
Intercostals arterioles	0.26	0.28
Left brachial	0.25	0.42
Abdominal region and organs (0D-1D)		
Gastric	0.31	0.32
Gastric arterioles	0.28	0.31
Coeliac A	0.30	0.39
Left renal	0.27	0.32
U left renal arterioles	0.30	0.33
L left renal arterioles	0.30	0.30
U ABD venules	0.30	0.30
L ABD venules	0.33	0.33
Lower limbs region (0D-1D)		
Inner iliac	0.34	0.48
Inner iliac arterioles	0.34	0.35
Deep femoral	0.37	0.48
Deep femoral arterioles	0.38	0.37
Anterior tibial	0.48	0.54
Anterior tibial arterioles	0.45	0.60
Posterior tibial	0.48	0.63
Posterior tibial arterioles	0.48	0.52
Legs capillaries	0.40	0.40
Legs veins	0.50	0.50

Chapter 8

Conclusions

Cardiovascular modelling has been adopted in the last two decades to provide additional answers to a number of different clinical and aerospace questions. In this Thesis, we have developed a closed-loop multiscale model of human circulation, which can be applied to both the clinical and aerospace worlds, and has been exploited to investigate the cardiovascular system functioning during atrial fibrillation and microgravity exposure. The results of the present work confirm the enormous potentiality of the computational approach in exploring cardiovascular-related topics, and demonstrate the possibility to use cardiovascular models to noninvasively estimate haemodynamic measurements on either general and specific subjects.

The development of the global cardiovascular model has relied on former studies, which have however been modified and arranged together, in order to create a comprehensive and versatile framework reproducing the most important aspects of the cardiovascular apparatus. This model combines a 1D representation of the systemic arterial tree, with a multiscale (0D-1D) model of the coronary circulation, a 0D model of the microcirculation, venous return, heart-pulmonary circulation, and a short-term baroreflex mechanism assuring the mean arterial pressure control and regulation beat by beat.

The reliability of the proposed modelling approach has been tested through the generic model, whose geometrical and mechanical properties refer to a healthy and young man, and on 12 individuals through a patient-specific version of the same modelling solution. The validity of the generic model has been proved by qualitatively/quantitatively comparing the pressure, flow rate and volume waveforms/mean values provided by the model (for a normal heart rhythm of 75 bpm) with the same variables available in literature along the systemic arterial tree, venous return, heart-pulmonary and coronary circulation. Key haemodynamic parameters at heart level obtained by the model have also been compared with the corresponding mean values indicated in literature. For all these data, we have found a good correspondence between measurements/behaviours reported in literature and model outcomes. In the patient-specific case, instead, the beat-averaged

values of systolic, diastolic, mean and pulse aortic pressures invasively detected on 12 supine elderly subjects have been likened with the relative steady-state pressure values got from the model tailored on each patient. The strong point of the patient-specific model is that it requires as input data just noninvasive information from each individual to simulate. Since the errors committed by the patient-specific model are smaller or slightly higher than the ones produced by common noninvasive techniques to evaluate central blood pressure, the model exhibits a good patient-specific response, although it deserves to be further analysed in a larger cohort of individuals.

A simplified version of the model, describing the systemic arterial tree and left heart-coronary circulation, has been applied to inquire into two different topics in case of atrial fibrillation (AF): the effects of the sole heart rhythm variations on the systemic arterial tree at a normal mean heart rate of 75 bpm (Arterial tree study), and the consequences of five different mean heart rates (HRs), from 50 to 130 bpm, on the coronary function (Coronary study).

- The arterial tree study demonstrates that rhythm alterations alone during AF are perfectly able to induce serious modifications in terms of pressure and peripheral perfusion, if compared to sinus rhythm (SR). In fact, systolic and diastolic pressure fluctuations significantly grow from SR to AF, especially at peripheral districts, and the probability of reaching extreme pressure values is much more higher in AF than in SR. Therefore, pressures which are uncommon in SR become likely in AF. It follows that AF could be responsible for important dysfunctions, especially in persistent cases, when the whole circulation is continuously exposed to abnormal pressure values and oscillations.

- The coronary study highlights that higher mean HRs in case of AF cause significant changes in the waveform and amplitude of the LAD (along the Left Anterior Descending Coronary artery) flow rate signals, and also lead to a not negligible decline in the total coronary flow rate (CBF) per heartbeat period. In other words, CBF shows a maximum value at about 90 bpm, decreasing for higher mean HRs. However, since the amount of oxygen required by the coronary circulation to properly work always rises with the mean HR, it results an impairment of the coronary circulation between 90 and 110 bpm. In addition, it has been verified that the typical correlation in SR between CBF and CPP (i.e., the coronary perfusion pressure) is basically lost in AF for mean HRs higher than 90 bpm, when CPP cannot longer be used as a surrogate measure of CBF.

A slight different version of the global model has been employed to analyse the functioning of the whole cardiovascular apparatus after about 5/6 months in space, without countermeasures and with respect to the supine configuration on Earth.

The model outcomes have been compared with the small set of haemodynamic parameters directly measured on astronauts in space after long-duration spaceflights and available in literature, obtaining a satisfying feedback. A more precise description of human circulation after long-term microgravity exposure has been also provided in terms of beat-averaged pressure/flow rate/volume values, maximum and pulse pressure values, and pressure/flow rate waveform variations. It emerges that the 0G adaptation point after months in space resembles a relaxed and sedentary cardiovascular configuration, with important and varied haemodynamic changes. Moreover, not negligible waveform modifications at capillary-venous level can alter the regular perfusion and nutrient supply to all the body tissues with respect to the 1G state.

One of the main limitation of the modelling approach is the presence of many free parameters. The latter are often difficult to set, especially on specific subjects, and introduce a degree of uncertainty, which slows down the spread of the computational approach to clinical uses. In fact, despite the uncertainty associated to parameters like the vessel lumen areas and lengths could be reduced by adopting real geometries derived from scans, a great deal of other parameters should be still imposed. This problem is surely intrinsic to the modelling approach and is thus arduous to eliminate. However, an extensive uncertainty quantification should be performed as future step before further progressing along this line of research. Such a study would be useful to better identify the major sources of errors in the model, which could maybe be mitigated, by better adjusting the parameter setting or introducing additional improvements to the modelling of specific physiological phenomena and cardiovascular regions.

All in all, this work represents an invitation to continue exploring the universe of the multiscale cardiovascular modelling, which is nowadays proposed as innovative instrument in a variety of fields and for multiple applications. It starts to be used as support to clinicians in diagnostics and decision-making, and to reproduce the haemodynamics of more or less extended patient-specific cardiovascular regions in presence of identified diseases. Specific cardiovascular domains, in fact, can be recreated from the scans of real patients through advanced imaging techniques, thus making detailed multiscale models patient-specific through the exact cardiovascular geometry of the subject to treat. Multiscale modelling is also employed to identify effects and determinants of specific pathologies, which can be simulated by actively modify the geometrical and mechanical properties of reference models, which are representative of healthy cases. This can be done on both generic and patient-specific frameworks. In the first case, to investigate punctual clinical questions associated to one or more cardiovascular diseases, thus neglecting all the other confounding factors derived from concomitant disorders. In the second case, to forecast the progression of recognised cardiovascular pathologies,

such as aneurysms, on the affected patients. Multiscale modelling is then exploited to answer space medicine questions, which are becoming numerous in view of new and more challenging space journeys. Indeed, different researchers are proposing cardiovascular models to more deeply understand the consequences of long-term microgravity and hypogravity exposure on the cardiovascular physiology, and propose optimal programmes of countermeasures to partially or totally compensate for the drawbacks of demanding environments like the outer space. In this complex and variegated scenario and on the wake of the results shown in the above, two possible future projects seem particularly interesting

- The first one could consist in a more extended validation of the patient-specific model presented in this work. In fact, as written before, it should be tested over a larger cohort. The latter should include about 50 young and old individuals, equally distributed among men and women. Moreover, contemporary pressure measurements at different arterial locations would be useful to verify the reliability of the model, not only at central but also at peripheral locations. This study would allow us to definitely prove the effectiveness of the proposed framework as patient-specific model and more precisely identify possible correlations between model errors and patient-specific input data.

- The second one could instead consist in verifying the role of specific countermeasures, such as resistive exercise, lower body negative pressure and hypergravity exposure through centrifugation, on the cardiovascular deconditioning experienced by astronauts while in space. Such a study would be helpful to identify the best countermeasure protocols to apply to different mission configurations and acceleration conditions. This would be extremely useful in a near future, as human presence in space is though to increase. In fact, a Moon base is going to be constructed and a trip to Mars is being planned.

Appendix A

1D model details

This appendix contains additional information on the 1D model of the systemic arterial tree presented in section 3.1. Details about the resolution of the boundary condition at arterial bifurcations and the numerical method are also provided.

A.1 Geometry and properties of 1D arteries

For each artery, Table A.1 indicates the length (l_{v_0}), the number of segments discretising l_{v_0} (N_v), the proximal (D_{in_0}) and distal (D_{out_0}) diameters, the wall thickness (h_{w_0}) - assumed constant over the vessel length -, and the viscoelasticity coefficient (K_{visc}). For distal arteries, the relative characteristic impedance (Z_c) is also reported. Diameters and lengths are the ones by Reymond et al. [279], while wall thickness values and viscoelasticity coefficients are the ones by Blanco et al. [30], with modifications at some sites. Characteristic impedances are obtained as

$$Z_c = \rho c / A_{out_0}, \tag{A.1}$$

with $\rho = 1050$ kg/m^3 the blood density, c the pulse wave velocity in resting blood - calculated according to the (3.73) -, and $A_{out_0} = \pi \left(D_{out_0}^2 / 4 \right)$ the distal area. All these data refer to the reference pressure: $p_0 = 100$ mmHg.

A.2 Initial conditions of 1D arteries

At the initial state, area and flow rate at the extremes (nodes) of the segments of all the 1D arteries are imposed. Flow rates are set null everywhere, while areas are obtained from data in Table. A.1. Knowing the areas at the inlet and outlet of the generic artery and its length (A_{in_0}, A_{out_0} and l_{v_0}, respectively), one calculates the angle between the apothem and the vessel axis, α_v, and determines the area at the j-th node as

Table A.1: Data of the systemic arterial tree adopted for the relative 1D model. For each artery the following information are provided: reference number according to Figure 3.1 (column i), name (column ii), length (l_{v_0}), number of segments discretising l_{v_0} (N_v), proximal diameter (D_{in_0}), distal diameter (D_{out_0}), wall thickness (h_{w_0}), viscoelasticity coefficient (K_{visc}). Characteristic impedances (Z_c) - calculated through the (A.1) - are provided for all distal arteries. All these data refer to the reference pressure $p_0 = 100$ mmHg.

N right/left	**Arterial tract**	l_{v_0} (N_v) [mm]	D_{in_0} [mm]	D_{out_0} [mm]	h_{w_0} [mm]	K_{visc} [mmHg s]	Z_c [$\frac{\text{mmHg*s}}{\text{ml}}$]
1	Ascending Aorta	40 (8)	29.40	29.30	1.63	33	
2	Aortic Arch A	20 (4)	24.10	24	1.32	33	
3	Brachiocephalic	34 (6)	19.40	18	0.86	33	
4/19	Subclavian A	34 (6)	12.90/11	9/8.5	0.67	33	
5/15	Common Carotid	94/139 (10)	15.10/12.40	7/6	0.63	33	
6/20	Vertebral	149/148 (10)	4.10/3.80	2.80/2.80	0.45	67	11.72
7/21	Subclavian B, Axillary, Brachial	422 (10)	8.90/8.40	4.70	0.66	33	
8/22	Radial	235 (10)	3.70/3.30	3.10/2.80	0.43	67	9.27/11.72
9/23	Ulnar A	67 (10)	3.70/4	3.40/4	0.49	67	
10/24	Interosseous	79 (10)	2.10/1.80	1.80/1.80	0.28	134	32.37
11/25	Ulnar B	171 (10)	3.20/4.10	2.80/3.70	0.49	67	11.72/6.17
12/16	Internal Carotid	178 (10)	5.70/5	4.30/4.10	0.39	67	4.37/4.87
13/17	External Carotid	41 (6)	5/4.50	4.50/4.10	0.42	67	3.93/4.87
14	Aortic Arch B	39 (8)	22	20.80	1.27	33	
18	Thoracic Aorta	52 (10)	20	18.90	1.20	33	
26	Intercostals	80 (10)	12.60	9.50	1.20	67	0.71
27	Thoracic Aorta B	104 (10)	16.50	12.90	1.16	33	
28	Abdominal Aorta A	53 (10)	12.20	12.20	1.08	33	
29	Coeliac A	20 (4)	7.80	6.90	0.64	33	
30	Coeliac B	25 (4)	5.20	4.90	0.64	33	
31	Hepatic	66 (10)	5.40	4.40	0.49	33	4.14
32	Gastric	71 (10)	3.20	3	0.45	33	7.10
33	Splenic	63 (10)	4.20	3.90	0.54	33	5.47
34	Superior Mesenteric	59 (10)	7.90	7.10	0.69	33	1.38
35	Abdominal Aorta B	20 (4)	11.50	11.30	0.8	33	
36/38	Renal	32 (6)	4.90	4.90/5.2	0.53	33	3.17/2.82
37	Abdominal Aorta C	20 (4)	11.20	11.20	0.8	33	
39	Abdominal Aorta D	106 (10)	11	11	0.8	33	
40	Inferior Mesenteric	50 (8)	4.70	3.20	0.43	33	8.62
41	Abdominal Aorta E	20 (4)	10.80	10.40	0.8	33	
42	Common Iliac	59 (10)	7.90	7	0.76	33	
43	Inner Iliac	50 (8)	4	4	0.4	134	5.16
44	External Iliac	144 (10)	6.40	6.10	0.55	33	
45	Deep Femoral	126 (10)	4	3.70	0.49	134	6.17
46	Femoral	443 (10)	5.20	3.80	0.5	67	
47	Anterior Tibial	343 (10)	2.60	2.30	0.39	134	10.22
48	Posterior Tibial	321 (10)	3.10	2.80	0.45	134	11.72

$$A_{j_0} = A_{in_0} + \alpha_v j L_{spezz}, \quad \text{for} \quad j = 1 : N_v + 1,$$

Table A.2: Data of the systemic left and right coronary arteries for the relative 1D model (geometry by Mynard et al. [227]). For each artery the following information are provided: reference number according to Figure 3.13 (column i), name (column ii), length (l_{v_0}), number of segments discretising l_{v_0} (N_v), proximal diameter (D_{in_0}), distal diameter (D_{out_0}), wall thickness (h_{w_0}), viscoelasticity coefficient (K_{visc}). Characteristic impedances (Z_{ca}) - calculated through the (A.1) - are provided for all distal arteries. All these data refer to the reference pressure $p_0 = 100$ mmHg.

N right/left	**Arterial tract**	l_{v_0} (N_v) [mm]	D_{in_0} [mm]	D_{out_0} [mm]	h_{w_0} [mm]	K_{visc} [mmHg s]	Z_{ca} [$\frac{\text{mmHg*s}}{\text{ml}}$]
49	Left Main Coronary Artery	12 (4)	4.50	4.50	0.4	134	
50	Left Anterior Descending Artery I	18 (4)	3.70	3.70	0.4	134	
51	Circumflex Artery I	32 (4)	3.60	3.60	0.4	134	
52	Marginal Artery	73 (6)	2.50	2.50	0.3	134	15.21
53	Circumflex Artery II	43 (6)	3	3	0.3	134	10
54	Diagonal Artery	65 (6)	2.40	2.40	0.2	134	16.71
55	Left Anterior Descending Artery II	22 (6)	3.30	3.30	0.3	134	
56	Septal Artery	45 (6)	2.40	2.40	0.2	134	16.71
57	Left Anterior Descending Artery III	100 (8)	2.70	2.70	0.3	134	12.74
58	Right Coronary Artery I	50 (6)	4.10	4.10	0.4	134	
59	Acute Marginal Artery I	34 (6)	2.50	2.50	0.3	134	15.21
60	Right Coronary Artery II	48 (6)	3.60	3.60	0.4	134	
61	Acute Marginal Artery II	23 (6)	2.10	2.10	0.2	134	22.71
62	Right Coronary Artery III	89 (8)	3.20	3.20	0.3	134	8.62

with $L_{spezz} = l_{v_0}/N_v$ the length of the N_v segments making up the generic artery.

A.3 Details on the numerical method

The strong form of a given physical problem is represented by its governing equations (which are typically partial differential equations) and boundary conditions. The weak form is an integral representation of the strong form and is necessary for the application of the so called variationally-based methods, such as the Finite Element Method (FEM). In fact, while techniques like the Finite Difference Method (FDM) lead to a direct discretisation of partial differential equations, variationally-based methods require the weak form as basis of discretisation [75]. This feature of variationally-based methods is in common with the Discountinuous Galerkin Method (DGM), which we here use.

In order to obtain the weak form of system (3.40) over the generic elemental region Ω_e, we multiply it for a set of arbitrary functions, ψ, and integrate it over

Table A.3: Arterial diameters and lengths by Liang et al. [180]. For each artery the following information are provided: reference number according to Figure 3.1 (column i), name (column ii), length (l_{v_0}), proximal diameter (D_{in_0}), distal diameter (D_{out_0}).

N right/left	**Arterial tract**	l_{v_0} [mm]	D_{in_0} [mm]	D_{out_0} [mm]
1	Ascending Aorta	40	30.50	28.40
2	Aortic Arch A	30	28.40	26.84
3	Brachiocephalic	35	13	12.40
4/19	Subclavian A	35	8.50	8.14
5/15	Common Carotid	117/208	8	7.7/7.4
6/20	Vertebral	135	4	4
7/21	Subclavian B, Axillary, Brachial	398	8.14	4.60
8/22	Radial	220	3.50	2.80
9/23	Ulnar A	67	4.30	4.30
10/24	Interosseous	70	2	2
11/25	Ulnar B	170	4.06	3.60
12/16	Internal Carotid	176	6	5.5
13/17	External Carotid	145/177	7.40/4	6.28/4
14	Aortic Arch B	40	26.84	24.92
18	Thoracic Aorta	55	24.92	22.48
26	Intercostals	73	6	6
27	Thoracic Aorta B	105	22.48	18.48
28	Abdominal Aorta A	53	18.48	16.76
29	Coeliac A	20	7	6
30	Coeliac B	20	6	5
31	Hepatic	65	5.50	5
32	Gastric	55	4	4
33	Splenic	58	3.5	3
34	Superior Mesenteric	50	8	7
35	Abdominal Aorta B	15	16.76	16.28
36/38	Renal	30	5.50	5.50
37	Abdominal Aorta C	15	16.28	15.84
39	Abdominal Aorta D	125	15.84	12.54
40	Inferior Mesenteric	38	4	3.50
41	Abdominal Aorta E	80	12.54	11
42	Common Iliac	58	8	7.4
43	Inner Iliac	45	4	4
44	External Iliac	145	7.40	6.28
45	Deep Femoral	113	4	4
46	Femoral	443 (10)	6.28	5.5
47	Anterior Tibial	322	5	5
48	Posterior Tibial	344	3.5	3.5

Ω_e. Namely,

$$\int_{\Omega_e} \frac{\partial \mathbf{U}}{\partial t}\psi dz + \int_{\Omega_e} \frac{\partial \mathbf{F}}{\partial z}\psi dz + \int_{\Omega_e} \mathbf{S}\psi dz = 0,$$

which one can more synthetically write as

$$\left(\frac{\partial \mathbf{U}}{\partial t}, \psi\right)_{\Omega_e} + \left(\frac{\partial \mathbf{F}}{\partial z}, \psi\right)_{\Omega_e} + (\mathbf{S}, \psi)_{\Omega_e} = 0.$$

ψ are usually called weight functions or test functions. They are required to be arbitrary, in order to guarantee the equivalence between strong and weak forms, and continuously differentiable over the integration domain (in this case Ω_e).

The last equation above is usually simplified by integrating the second term by part:

$$\left(\frac{\partial \mathbf{F}}{\partial z}, \psi\right)_{\Omega_e} = [\mathbf{F}\psi]_{\delta\Omega_e} - \left(\mathbf{F}, \frac{\mathrm{d}\psi}{\mathrm{d}z}\right)_{\Omega_e}.$$

Thus, the complete equation becomes

$$\left(\frac{\partial \mathbf{U}}{\partial t}, \psi\right)_{\Omega_e} + [\mathbf{F}\psi]_{\delta\Omega_e} - \left(\mathbf{F}, \frac{\mathrm{d}\psi}{\mathrm{d}z}\right)_{\Omega_e} + (\mathbf{S}, \psi)_{\Omega_e} = 0,$$

which is the weak form of system (3.40) over Ω_e. This form is said weak because, contrary to system (3.40), it has to hold in integral sense and is thus subjected to weaker continuity requirements. Nonetheless, it is worth to say that strong and weak forms imply each other, meaning that the resolution of the weak form includes the resolution of the strong form, as demonstrated in simpler cases elsewhere [75].

Since the problem has to be solved in descrete form, both the solution $\mathbf{U}$ and test functions ψ have to be discretised. We define the descrete solution as $\mathbf{U_h}$ and the descrete test functions as $\psi_\mathbf{h}$. The latter equation is thus rewritten as

$$\left(\frac{\partial \mathbf{U_h}}{\partial t}, \psi_\mathbf{h}\right)_{\Omega_e} + [\mathbf{F}(\mathbf{U_h})\psi_\mathbf{h}]_{\delta\Omega_e} - \left(\mathbf{F}(\mathbf{U_h}), \frac{\mathrm{d}\psi_\mathbf{h}}{\mathrm{d}z}\right)_{\Omega_e} + (\mathbf{S}(\mathbf{U_h}), \psi_\mathbf{h})_{\Omega_e} = 0.$$

When adopting a variationally-based method, $\mathbf{U_h}$ can be taken to belong to any class of functions (from Legendre polynomials to exponential functions). We here suppose that $\mathbf{U_h}$ belongs to the finite dimensional space of the Langrange polynomials of degree 1. Thus, one can write $\mathbf{U_h}$ over the linear element Ω_e as

$$\mathbf{U_h} = \sum_{i=1}^{2} \alpha_\mathbf{i} \phi_i,$$

where $\alpha_\mathbf{i}$ are the (time dependent) unknown weights at the nodes (1 and 2) of the element Ω_e, and ϕ_i are the trial functions over the element Ω_e, which are represented in Figure A.1. In particular, $\phi_1 = \frac{1-\xi}{2}$ and $\phi_2 = \frac{1+\xi}{2}$, with ξ a non dimensional coordinate of z (see equation (3.46)). ϕ_1 and ϕ_2 are equal to 1 at one node (at node 1 for ϕ_1 and at node 2 for ϕ_2), 0 at the other node, and 1/2 at the middle of the element. Thus, the descrete solution $\mathbf{U_h}$ coincides with the local weight at each elemental node ($\alpha_\mathbf{1}$ at node 1 and $\alpha_\mathbf{2}$ at node 2). Notice that, since the solution $\mathbf{U}$ is a column vector ($\mathbf{U} = [A, Q]^T$), $\alpha_\mathbf{1}$ and $\alpha_\mathbf{2}$ are column vectors too. Namely, $\alpha_\mathbf{1} = [\alpha_{1A}, \alpha_{1Q}]^T$ and $\alpha_\mathbf{2} = [\alpha_{2A}, \alpha_{2Q}]^T$, where each subscript ($1A$, $1Q$, $2A$ and $2Q$) identifies the node (1 or 2) and the unknown (A or Q) each weight is associated to. It follows that $\mathbf{U_h}$ can be written in matrix form as in equation (3.45). As usually done with the DGM, descrete test functions $\psi_\mathbf{h}$ are chosen in the same descrete space as $\mathbf{U_h}$. Therefore, $\psi_1 = \phi_1 = \frac{1-\xi}{2}$ and $\psi_2 = \phi_2 = \frac{1+\xi}{2}$.

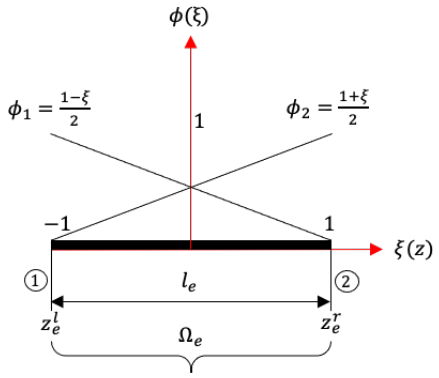

Figure A.1: Representation of the trial functions ϕ_1 and ϕ_2 over the generic element Ω_e.

To summarize, the resolution of equation (3.40) over the elemental region Ω_e through the DGM is based on the weak form of the same equation, which can then be discretised. The resolution of the discretised equation on the generic element Ω_e is described in section 3.1.5.

A.4 Equation (3.70)

$$
\begin{aligned}
&\det\left(\bar{\mathbf{H}}-\mathbf{\Lambda}\bar{\mathbf{I}}\right)=0,\\
&\det\begin{bmatrix}-\lambda, & 1\\ \sum_{j=1}^{3}\frac{jA^jB_{j+1}}{\rho}-\frac{\beta Q^2}{A^2}, & \frac{2\beta Q}{A}-\lambda\end{bmatrix}=0,\\
&-\lambda\left(\frac{2\beta Q}{A}-\lambda\right)+\frac{\beta Q^2}{A^2}-\frac{A}{\rho}\left(B_2+2AB_3+3A^2B_4\right)=0,\\
&\lambda^2-\frac{2\beta Q}{A}\lambda+\frac{\beta Q^2}{A^2}-\frac{A}{\rho}\left(B_2+2AB_3+3A^2B_4\right)=0,\\
&\lambda=\frac{\beta Q}{A}\pm\sqrt{\frac{A}{\rho}\left(B_2+2B_3A+3B_4A^2\right)+\frac{Q^2}{A^2}\beta(\beta-1)},\\
&\lambda=\frac{\beta Q}{A}\pm c;\lambda_1=\frac{\beta Q}{A}-c;\lambda_2=\frac{\beta Q}{A}+c.
\end{aligned}
$$

A.5 Equation (3.74)

$$
\begin{aligned}
&[k1_{\lambda_1},k2_{\lambda_1}]\det\left(\bar{\mathbf{H}}-\lambda_1\bar{\mathbf{I}}\right)=[0,0]\,,\\
&[k1_{\lambda_1},k2_{\lambda_1}]\begin{bmatrix}-\lambda_1, & 1\\ \sum_{j=1}^{3}\frac{jA^jB_{j+1}}{\rho}-\frac{\beta Q^2}{A^2}, & \frac{2\beta Q}{A}-\lambda_1\end{bmatrix}=[0,0]\,,\\
&[k1_{\lambda_1},k2_{\lambda_1}]\begin{bmatrix}-\lambda_1, & 1\\ (), & \frac{2\beta Q}{A}-\lambda_1\end{bmatrix}=[0,0]\,,\\
&\left[-k1_{\lambda_1}\lambda_1+k2_{\lambda_1}(),k1_{\lambda_1}+\left(\frac{2\beta Q}{A}-\lambda_1\right)k2_{\lambda_1}\right]=[0,0]\,,\\
&\begin{cases}-k1_{\lambda_1}\lambda_1+k2_{\lambda_1}()=0,\\ k1_{\lambda_1}\lambda_1+\left(\frac{2\beta Q}{A}-\lambda_1\right)k2_{\lambda_1}=0,\end{cases}\\
&\begin{cases}k1_{\lambda_1}=\frac{k2_{\lambda_1}()}{\lambda_1}=0,\\ \cancel{k2_{\lambda_1}}()+\left(\frac{2\beta Q}{A}-\lambda_1\right)\cancel{k2_{\lambda_1}}\lambda_1=0.\end{cases}
\end{aligned}
$$

The second equation of the system above is verified for any value of $k2_{\lambda_1}$. Thus, one can choose $k2_{\lambda_1}=1$. Substituting this expression into either the first or second equation, one finds the value of $k1_{\lambda_1}$ satisfying the above system. Working on the first equation, one gets

$$
\begin{aligned}
k1_{\lambda_1} &= \frac{()}{\lambda_1}, \\
&= \frac{\frac{A}{\rho}\left(B_2 + 2B_3 A + 3B_4 A^2\right) - \frac{\beta Q^2}{A^2}}{\frac{\beta Q}{A} - c}, \\
&= \frac{c^2 - \frac{\beta^2 Q^2}{A^2}}{\frac{\beta Q}{A} - c}, \\
&= \frac{\cancel{\left(c - \frac{\beta Q}{A}\right)}\left(c + \frac{\beta Q}{A}\right)}{-\cancel{\left(c - \frac{\beta Q}{A}\right)}}, \\
&= -\lambda_2.
\end{aligned}
$$

Therefore, the row eigenvector corresponding to λ_1 is $\mathbf{l_1} = [-\lambda_2, 1]$.

A.6 Equation (3.75)

$$
\begin{aligned}
&[k1_{\lambda_2}, k2_{\lambda_2}] \det\left(\bar{\mathbf{H}} - \lambda_2 \bar{\mathbf{I}}\right) = [0,0]\,, \\
&[k1_{\lambda_2}, k2_{\lambda_2}] \begin{bmatrix} -\lambda_2, & 1 \\ \sum_{j=1}^{3} \frac{j A^j B_{j+1}}{\rho} - \frac{\beta Q^2}{A^2}, & \frac{2\beta Q}{A} - \lambda_2 \end{bmatrix} = [0,0]\,, \\
&[k1_{\lambda_2}, k2_{\lambda_2}] \begin{bmatrix} -\lambda_2, & 1 \\ (), & \frac{2\beta Q}{A} - \lambda_2 \end{bmatrix} = [0,0]\,, \\
&\left[-k1_{\lambda_2}\lambda_2 + k2_{\lambda_2}(), k1_{\lambda_2} + \left(\frac{2\beta Q}{A} - \lambda_2\right) k2_{\lambda_2}\right] = [0,0]\,, \\
&\begin{cases} -k1_{\lambda_2}\lambda_2 + k2_{\lambda_2}() = 0, \\ k1_{\lambda_2}\lambda_2 + \left(\frac{2\beta Q}{A} - \lambda_2\right) k2_{\lambda_2} = 0, \end{cases} \\
&\begin{cases} k1_{\lambda_2} = \frac{k2_{\lambda_2}()}{\lambda_2} = 0, \\ \cancel{k2_{\lambda_2}}() + \left(\frac{2\beta Q}{A} - \lambda_2\right) \cancel{k2_{\lambda_2}} \lambda_2 = 0. \end{cases}
\end{aligned}
$$

The second equation of the system above is verified for any value of $k2_{\lambda_2}$. Thus, one can choose $k2_{\lambda_2} = 1$. Substituting this expression into either the first or second equation, one finds the value of $k1_{\lambda_2}$ satisfying the above system. Working on the first equation, one gets

$$
\begin{aligned}
k1_{\lambda_2} &= \frac{()}{\lambda_2}, \\
&= \frac{\frac{A}{\rho}\left(B_2 + 2B_3 A + 3B_4 A^2\right) - \frac{\beta Q^2}{A^2}}{\frac{\beta Q}{A} + c}, \\
&= \frac{c^2 - \frac{\beta^2 Q^2}{A^2}}{\frac{\beta Q}{A} + c}, \\
&= \frac{\left(c - \frac{\beta Q}{A}\right)\cancel{\left(c + \frac{\beta Q}{A}\right)}}{\cancel{\left(c + \frac{\beta Q}{A}\right)}}, \\
&= -\lambda_1.
\end{aligned}
$$

Therefore, the row eigenvector corresponding to λ_2 is $\mathbf{l_2} = [-\lambda_1, 1]$.

A.7 Equation (3.90)

$$
\begin{aligned}
&\bar{\mathbf{L}}_\mathbf{n}(\mathbf{U_{n+1}} - \mathbf{U_i}) = \bar{\mathbf{L}}^*_\mathbf{n}(\mathbf{U^*_n} - \mathbf{U^*_i}) + \Delta T \left(\bar{\mathbf{\Lambda}}^*_\mathbf{n} \frac{\partial \bar{\mathbf{L}}^*_\mathbf{n}}{\partial z}(\mathbf{U^*_n} - \mathbf{U^*_i}) - \bar{\mathbf{L}}^*_\mathbf{n}(\mathbf{S^*_{2_n}} - \mathbf{S^*_{2_i}}) \right), \\
&\begin{bmatrix} -\lambda_{2_n}, & 1 \\ -\lambda_{1_n}, & 1 \end{bmatrix} \begin{bmatrix} A_{n+1} - A_i \\ Q_{n+1} - Q_i \end{bmatrix} = \begin{bmatrix} -\lambda^*_{2_n}, & 1 \\ -\lambda^*_{1_n}, & 1 \end{bmatrix} \begin{bmatrix} A^*_n - A^*_i \\ Q^*_n - Q^*_i \end{bmatrix} + ... \\
&...\Delta T \left(\begin{bmatrix} \lambda^*_{1_n}, & 0 \\ 0, & \lambda^*_{2_n} \end{bmatrix} \begin{bmatrix} -\frac{\partial \lambda^*_{2_n}}{\partial z}, & 0 \\ -\frac{\partial \lambda^*_{1_n}}{\partial z}, & 0 \end{bmatrix} \begin{bmatrix} A^*_n - A^*_i \\ Q^*_n - Q^*_i \end{bmatrix} - \begin{bmatrix} -\lambda^*_{2_n}, & 1 \\ -\lambda^*_{1_n}, & 1 \end{bmatrix} \begin{bmatrix} 0 \\ ()_{n^*-i^*} \end{bmatrix} \right).
\end{aligned}
$$

We recall that subscripts n, $n+1$ and i refer to time, i.e., n: $t_n = n\Delta T$, $n+1$: $t_{n+1} = (n+1)\Delta T$ and i: initial time. In addition, variables without superscript are those at the boundary one is considering, while variables with superscript $*$ are those at a distance $c\Delta T$ form the boundary. The term $()_{n^*-i^*}$ is the difference between the second component of vector $\mathbf{S_2}$ (3.71) evaluated at a distance $c\Delta T$ form the boundary, at time t_n and at initial time.

The above system leads to two compatibility equations

1.

$$
\begin{aligned}
&-\lambda_{2_n}(A_{n+1} - A_i) + (Q_{n+1} - Q_i) = ... \\
&... - \lambda^*_{2_n}(A^*_n - A^*_i) + (Q^*_n - Q^*_i) + \Delta T \left(-\lambda^*_{1_n} \frac{\partial \lambda^*_{2_n}}{\partial z}(A^*_n - A^*_i) - ()_{n^*-i^*} \right),
\end{aligned}
$$

2.

$$
\begin{aligned}
&-\lambda_{1_n}(A_{n+1} - A_i) + (Q_{n+1} - Q_i) = ... \\
&... - \lambda^*_{1_n}(A^*_n - A^*_i) + (Q^*_n - Q^*_i) + \Delta T \left(-\lambda^*_{2_n} \frac{\partial \lambda^*_{1_n}}{\partial z}(A^*_n - A^*_I) - ()_{n^*-i^*} \right),
\end{aligned}
$$

where the first equation refers to the first characteristic line (the one with slope λ_1), while the second equation refers to the second characteristic line (the one with slope λ_2). Since at initial state flow rate is set null everywhere ($Q_i = 0$), the two compatibility equations become

1.
$$Q_{n+1} - Q_n^* - \lambda_{2_n}(A_{n+1} - A_i) + \lambda_{2_n}^*(A_n^* - A_i^*)... \\ ... - \Delta T \left(-\lambda_{1_n}^* \frac{\partial \lambda_{2_n}^*}{\partial z}(A_n^* - A_i^*) - ()_{n^*-i^*} \right) = 0,$$

2.
$$Q_{n+1} - Q_n^* - \lambda_{1_n}(A_{n+1} - A_i) + \lambda_{1_n}^*(A_n^* - A_i^*)... \\ ... - \Delta T \left(-\lambda_{2_n}^* \frac{\partial \lambda_{1_n}^*}{\partial z}(A_n^* - A_i^*) - ()_{n^*-i^*} \right) = 0.$$

To solve time t_{n+1}, the unknowns are A_{n+1} and Q_{n+1}, while all the other terms are known. Thus, one can write the two compatibility equations as

1.
$$Q_{n+1} = \lambda_{2_n} A_{n+1} + tn_1,$$

2.
$$Q_{n+1} = \lambda_{1_n} A_{n+1} + tn_2,$$

where

$$\begin{aligned} tn_1 &= Q_n^* - \lambda_{2_n} A_i - \lambda_{2_n}^*(A_n^* - A_i^*) + \Delta T \left(-\lambda_{1_n}^* \frac{\partial \lambda_{2_n}^*}{\partial z}(A_n^* - A_i^*) - ()_{n^*-i*} \right), \\ tn_2 &= Q_n^* - \lambda_{1_n} A_i - \lambda_{1_n}^*(A_n^* - A_i^*) + \Delta T \left(-\lambda_{2_n}^* \frac{\partial \lambda_{1_n}^*}{\partial z}(A_n^* - A_i^*) - ()_{n^*-i^*} \right). \end{aligned} \tag{A.2}$$

When applying a two-steps Runge-Kutta method the terms tn_1 and tn_2 modify with the time step. We have, for the first time step ($t_{n+1/2} = (n + 1/2)\Delta T$),

$$\begin{aligned} tn_1 &= Q_n^{1*} - \lambda_{2_n} A_i - \lambda_{2_n}^{1*}(A_n^{1*} - A_i^{1*}) + \frac{\Delta T}{2} \left(-\lambda_{1_n}^{1*} \frac{\partial \lambda_{2_n}^{1*}}{\partial z}(A_n^{1*} - A_i^{1*}) - ()_{n^{1*}-i^{1*}} \right), \\ tn_2 &= Q_n^{1*} - \lambda_{1_n} A_i - \lambda_{1_n}^{1*}(A_n^{1*} - A_i^{1*}) + \frac{\Delta T}{2} \left(-\lambda_{2_n}^{1*} \frac{\partial \lambda_{1_n}^{1*}}{\partial z}(A_n^{1*} - A_i^{1*}) - ()_{n^{1*}-i^{1*}} \right), \end{aligned} \tag{A.3}$$

and for the second time step (t_{n+1})

$$\begin{aligned} tn_1 &= Q_n^{2*} - \lambda_{2_n} A_i - \lambda_{2_n}^{2*}(A_n^{2*} - A_i^{2*}) + \Delta T \left(-\lambda_{1_{n+1/2}} \frac{\partial \lambda_{2_{n+1/2}}}{\partial z}(A_{n+1/2} - A_i^{2*}) - ()_{n+1/2-i^{2*}} \right), \\ tn_2 &= Q_n^{2*} - \lambda_{1_n} A_i - \lambda_{1_n}^{2*}(A_n^{2*} - A_i^{2*}) + \Delta T \left(-\lambda_{2_{n+1/2}} \frac{\partial \lambda_{1_{n+1/2}}}{\partial z}(A_{n+1/2} - A_i^{2*}) - ()_{n+1/2-i^{2*}} \right). \end{aligned} \tag{A.4}$$

The superscripts $1*$ and $2*$ refer to the points located at a distance from the boundary equal to $c\Delta T/2$ and $c\Delta T$, respectively. Then, subscripts n, $n+1/2$ and $n+1$ refer to times t_n, $t_{n+1/2}$ and t_{n+1}, respectively.

A.8 Resolution of a generic arterial bifurcation

The generic arterial bifurcation, represented in Figure 3.6, is solved by the system

$$\begin{cases} p_1 + \frac{1}{2}\rho\bar{u}_1^2 = p_2 + \frac{1}{2}\rho\bar{u}_2^2, \\ p_1 + \frac{1}{2}\rho\bar{u}_1^2 = p_3 + \frac{1}{2}\rho\bar{u}_3^2, \\ Q_1 = Q_2 + Q_3, \\ Q_1 = \lambda_{1,1}A_1 + tn_{2,1}, \\ Q_2 = \lambda_{2,2}A_2 + tn_{1,2}, \\ Q_2 = \lambda_{2,3}A_3 + tn_{1,3}. \end{cases} \tag{A.5}$$

The first three equations give the physical boundary condition (equation (3.68)), while the last three equations are the compatibility conditions (equations (3.91) and (3.92)) - one per artery - chosen according to the rules in section 3.1.7. The subscripts of variables p, Q and A are 1 for the parent artery and 2/3 for the daughter arteries at the bifurcation. For variables λ and tn, instead, the first subscript refers to the characteristic line (1 for the backward line and 2 for the forward one), and the second subscript to the vessel number as before.

To solve this system, one uses the definition of pressure (equation (3.34)) and approximates $\bar{u}$ as Q/A. With these substitutions, one gets a system of three not-linear equations in A_1, A_2 and A_3. Namely,

$$\begin{cases} B_{1,1} + B_{2,1}A_1 + B_{3,1}A_1^2 + B_{4,1}A_1^3 - \frac{B_{5,1}}{\sqrt{A_1}}\frac{\partial Q_1}{\partial z} + \frac{1}{2}\rho\left(\frac{\lambda_{1,1}A_1 + tn_{2,1}}{A_1}\right)^2 = ... \\ ...B_{1,2} + B_{2,2}A_2 + B_{3,2}A_2^2 + B_{4,2}A_2^3 - \frac{B_{5,2}}{\sqrt{A_2}}\frac{\partial Q_2}{\partial z} + \frac{1}{2}\rho\left(\frac{\lambda_{2,2}A_2 + tn_{1,2}}{A_2}\right)^2, \\ B_{1,1} + B_{2,1}A_1 + B_{3,1}A_1^2 + B_{4,1}A_1^3 - \frac{B_{5,1}}{\sqrt{A_1}}\frac{\partial Q_1}{\partial z} + \frac{1}{2}\rho\left(\frac{\lambda_{1,1}A_1 + tn_{2,1}}{A_1}\right)^2 = ... \\ ...B_{1,3} + B_{2,3}A_3 + B_{3,3}A_3^2 + B_{4,3}A_3^3 - \frac{B_{5,3}}{\sqrt{A_3}}\frac{\partial Q_3}{\partial z} + \frac{1}{2}\rho\left(\frac{\lambda_{2,3}A_3 + tn_{1,3}}{A_3}\right)^2, \\ \lambda_{1,1}A_1 + tn_{2,1} = \lambda_{2,2}A_2 + tn_{1,2} + \lambda_{2,3}A_3 + tn_{1,3}. \end{cases}$$

This latter is rewritten as

$$\begin{cases} f_1 : K_1 + B_{2,1}A_1 + B_{3,1}A_1^2 + B_{4,1}A_1^3 + \dfrac{\rho}{2}\left(\dfrac{tn_{2,1}}{A_1} + \lambda_{1,1}\right)^2 + ... \\ ... - B_{2,2}A_2 - B_{3,2}A_2^2 - B_{4,2}A_2^3 - \dfrac{\rho}{2}\left(\dfrac{tn_{1,2}}{A_2} + \lambda_{2,2}\right)^2 = 0, \\ f_2 : K_2 + B_{2,1}A_1 + B_{3,1}A_1^2 + B_{4,1}A_1^3 + \dfrac{\rho}{2}\left(\dfrac{tn_{2,1}}{A_1} + \lambda_{1,1}\right)^2 + ... \\ ... - B_{2,3}A_3 - B_{3,3}A_3^2 - B_{4,3}A_3^3 - \dfrac{\rho}{2}\left(\dfrac{tn_{1,3}}{A_3} + \lambda_{2,3}\right)^2 = 0, \\ f_3 : K_3 + \lambda_{1,1}A_1 - \lambda_{2,2}A_2 - \lambda_{2,3}A_3 = 0, \end{cases}$$

with

$$K_1 = B_{1,1} - B_{1,2} - \frac{B_{5,1}}{\sqrt{A_1}}\frac{\partial Q_1}{\partial z} + \frac{B_{5,2}}{\sqrt{A_2}}\frac{\partial Q_2}{\partial z}, \quad K_2 = B_{1,1} - B_{1,3} - \frac{B_{5,1}}{\sqrt{A_1}}\frac{\partial Q_1}{\partial z} + \frac{B_{5,3}}{\sqrt{A_3}}\frac{\partial Q_3}{\partial z},$$
$$K_3 = tn_{2,1} - tn_{1,2} - tn_{1,3}.$$

The system above can be written in the form

$$\mathbf{F}(\mathbf{X}) = 0,$$

with

$$\mathbf{F}(\mathbf{X}) = [f_1, f_2, f_3]^T,$$

and

$$\mathbf{X} = [A_1, A_2, A_3]^T.$$

It is solved through the multidimensional Newton method as

$$\mathbf{X^{m+1}} = \mathbf{X^m} - \frac{\mathbf{F}(\mathbf{X^m})}{\mathbf{F'}(\mathbf{X^m})},$$

where $\mathbf{X^m}$ and $\mathbf{X^{m+1}}$ are the old and updated values of vector $\mathbf{X}$, and $\mathbf{F'}(\mathbf{X^m})$, the Jacobian matrix, is defined as

$$\mathbf{F}'(\mathbf{X^m}) = \begin{bmatrix} \frac{\partial f_1}{\partial A_1} & \frac{\partial f_1}{\partial A_2} & \frac{\partial f_1}{\partial A_3} \\ \frac{\partial f_2}{\partial A_1} & \frac{\partial f_2}{\partial A_2} & \frac{\partial f_2}{\partial A_3} \\ \frac{\partial f_3}{\partial A_1} & \frac{\partial f_3}{\partial A_2} & \frac{\partial f_3}{\partial A_3} \end{bmatrix},$$

with

$$\begin{aligned}
&\frac{\partial f_1}{\partial A_1} = B_{2,1} + 2B_{3,1}A_1 + 3B_{4,1}A_1^2 + \rho\left(\frac{tn_{2,1}}{A_1} + \lambda_{1,1}\right)\left(-\frac{tn_{2,1}}{A_1^2}\right), \\
&\frac{\partial f_1}{\partial A_2} = -B_{2,2} - 2B_{3,2}A_2 - 3B_{4,2}A_2^2 - \rho\left(\frac{tn_{1,2}}{A_2} + \lambda_{2,2}\right)\left(-\frac{tn_{1,2}}{A_2^2}\right), \\
&\frac{\partial f_1}{\partial A_3} = 0, \\
&\frac{\partial f_2}{\partial A_1} = B_{2,1} + 2B_{3,1}A_1 + 3B_{4,1}A_1^2 + \rho\left(\frac{tn_{2,1}}{A_1} + \lambda_{1,1}\right)\left(-\frac{tn_{2,1}}{A_1^2}\right), \\
&\frac{\partial f_2}{\partial A_2} = 0, \\
&\frac{\partial f_2}{\partial A_3} = -B_{2,3} - 2B_{3,3}A_3 - 3B_{4,3}A_3^2 - \rho\left(\frac{tn_{1,3}}{A_3} + \lambda_{2,3}\right)\left(-\frac{tn_{1,3}}{A_3^2}\right), \\
&\frac{\partial f_3}{\partial A_1} = \lambda_{1,1}, \quad \frac{\partial f_3}{\partial A_2} = -\lambda_{2,2} \quad \frac{\partial f_3}{\partial A_3} = -\lambda_{2,3}.
\end{aligned}$$

Appendix B

0D models details

This appendix contains additional information on the 0D model of the systemic, heart and pulmonary circulations presented in section 3.2, together with the baroreflex model introduced in section 3.5. Details about the resolution of the boundary condition at the entrance to the aorta and distal arteries are also provided.

B.1 Parameters and initial conditions of RLC models

Table B.1 gives the parameters (according to Liang et al. [181] with adjustments) and initial conditions of the *RLC* models used to represent some portions of the systemic circulation, as introduced in section 3.2.1. Initial conditions are the values of flow rate, Q_j^0, and pressure, p_j^0, for each j-th compartment. Q_j^0 are set null. p_j^0 are calculated from the relationship linking pressure and volume, $p_j^0 = (V_j^0 - V_{j_0})/C_i$, with the initial values of total volumes, V_j^0, and unstressed volumes, V_{j_0}, (unstressed volumes of venules and veins change with time because of the baroreflex action) set in order to have a global blood volume of 5.7 l, and respect the vascular and regional blood volume distribution according to [120, 119, 176].

B.2 Parameters and initial conditions of cardiac chambers

Table B.2 reports the parameters (according to [30, 120, 180, 181] with some variations) and initial conditions used in the 0D models of cardiac chambers, as introduced in section 3.2.2. Initial conditions consist in the values of pressure, p_{ch}^0, within each cardiac chamber. p_{ch}^0 are calculated from the relationship linking pressure and volume, $p_{ch}^0 = E_{ch}^0(V_{ch}^0 - V_{0,ch})$, where E_{ch}^0 is the initial elastance

Table B.1: Parameters of the RLC models representing some portions of the systemic circulation. For the j-th compartment the following data are reported: resistance (R_j), compliance (C_j), inertance (L_j), unstressed volume (V_{j_0}), and initial values of pressure (p_j^0) and total volume (V_j^0).

Cardiovascular region	R_j $\left[\frac{\text{mmHgs}}{\text{ml}}\right]$	C_j $\left[\frac{\text{ml}}{\text{mmHg}}\right]$	L_j $\left[\frac{\text{mmHgs}^2}{\text{ml}}\right]$	V_{j_0} [ml]	p_j^0 [mmHg]	V_j^0 [ml]
Arteries						
Pulmonary	0.08	3.8	-	44.30	526.27	59.30
Arterioles						
Vertebral (6/20)	25.88	0.013	0.019	4.2	40	4.72
Radial (8/22)	17.03	0.014	0.018	3.6	40	4.16
Interosseous (10/24)	393.70	0.0009	0.07	3.6	40	3.64
Ulnar B (11/25)	19.69	0.014	0.018	3.6	40	4.16
Internal Carotid (12/16)	23.60	0.015	0.017	4.2	40	4.80
External Carotid (13/17)	21.85	0.015	0.017	4.2	40	4.80
Intercostals (26)	5.61	0.054	0.009	6.9	40	9.06
Hepatic (31)	16.24	0.021	0.015	30.6	40	31.44
Gastric (32)	8.91	0.033	0.012	9.3	40	10.62
Splenic (33)	21.33	0.014	0.018	11.6	40	12.16
Superior Mesenteric (34)	3.85	0.081	0.007	15.9	40	19.14
Renal (36/38)	4.31	0.068	0.008	5.9	40	8.62
Inferior Mesenteric (40)	30.74	0.011	0.02	11.9	40	12.34
Inner Iliac (43)	23.48	0.014	0.018	3.5	40	4.06
Deep femoral (45)	13.37	0.023	0.014	14.4	40	15.32
Anterior Tibial (47)	14.03	0.023	0.014	14.4	40	15.32
Posterior Tibial (48)	30.44	0.01	0.021	14.4	40	14.80
Capillaries						
HA	0.97	0.03	0.003	74.8	150	79.3
ABD LEGS	0.29	0.1	0.003	202.3	121	214.4
Venules						
HA	0.14	0.5	0.001	288.6	139.4	358.3
ABD LEGS	0.04	1.5	0.001	780.4	125.47	968.6
Veins						
Pulmonary	0.01	20.5	-	232.6	509.88	311.2
HA	0.03	15	0.0005	323.5	8.45	450.2
ABD LEGS	0.009	75	0.0005	1378.9	7.21	1919.3
Venae Cavae						
SVC	0.0005	5	0.0005	4.9	0.44	7.1
IVC	0.0005	15	0.0005	14.8	0.44	21.4

(calculated through the (3.97)), V_{ch}^0 is the initial total volume, and $V_{0,ch}$ is the unstressed volume (unstressed volumes of cardiac chambers are constant with time)

of the generic cardiac chamber. The latter volumes, as before, are set in order to have a global blood volume of 5.7 l, and respect the vascular and regional blood volume distribution according to [120, 119, 176].

Table B.2: Parameters of the 0D models of cardiac chambers. There is an indication of the following data: atrial (T_{ac}/T_{ar}) and ventricular (T_{vc}/T_{vr}) periods of contraction/relaxation, times when atrial start contracting/relaxing (t_{ac}/t_{ar}), amplitude/minimum values of the elastances ($E_{A,ch}/E_{B,ch}$), unstressed volumes ($V_{0,ch}$), and initial values of total volumes (V^0_{ch}) and pressures (p^0_{ch}). RR is the heartbeat duration.

Cardiac chamber	RA	RV	LA	LV
T_{ac} [s]	0.17RR		0.17RR	
T_{ar} [s]	T_{ac}		T_{ac}	
T_{vc} [s]		$0.3\sqrt{RR}$		$0.3\sqrt{RR}$
T_{vr} [s]		$\frac{T_{vc}}{2}$		$\frac{T_{vc}}{2}$
t_{ac} [s]	$0.8RR$		$0.8RR$	
t_{ar} [s]	$t_{ac}+T_{ac}$		$t_{ac}+T_{ac}$	
$E_{A,ch}$ $\left[\frac{\text{mmHg}}{\text{ml}}\right]$	0.06	0.65	0.07	2.75
$E_{B,ch}$ $\left[\frac{\text{mmHg}}{\text{ml}}\right]$	0.14	0.073	0.11	0.083
$V_{0,ch}$ [ml]	6	12	6	7
V^0_{ch} [mmHg]	91.9	116.3	109.9	109.4
p^0_{ch} [mmHg]	16.79	7.61	18.16	8.50

B.3 Parameters and initial conditions of cardiac valves

Table B.3 reports the parameters (according to Blanco et al. [30]) used in the 0D models of cardiac valves, introduced in section 3.2.2. Initial conditions consist in the values of the flow rate through each cardiac valve, Q^0_{va}, and the angle formed by the valve leaflets, θ^0_{va}, both set at 0.

Table B.3: Parameters of the 0D models of cardiac valves. For each cardiac valve there is an indication of the following data: viscous resistance (R_{va}), fluid inertance (L_{va}), turbulent flow separation coefficient (B_{va}), and coefficients to calculate the forces applied to the valve leaflets (k_p/I_{ao}, k_q/I_{ao}, k_f/I_{ao}, and k_v/I_{ao}, with I_{ao} the momentum of inertia of the valve).

Cardiac valve	TV	PV	MV	AV
$R_{va} \cdot 10^{-6}$ $\left[\frac{\text{mmHg s}}{\text{ml}}\right]$	4.5	4.5	4.5	4.5
$L_{va} \cdot 10^{-6}$ $\left[\frac{\text{mmHg s}^2}{\text{ml}}\right]$	3.75	3.75	3.75	3.75
$B_{va} \cdot 10^{-6}$ $\left[\frac{\text{mmHg s}^2}{\text{ml}^2}\right]$	4.8	5.67	4.8	5.67
k_p/I_{ao} $\left[\frac{\text{rad}}{\text{mmHg s}^2}\right]$	5500	5500	5500	55000
k_q/I_{ao} $\left[\frac{\text{rad}}{\text{ml s}}\right]$	2	2	2	2
k_f/I_{ao} $\left[\frac{\text{rad}}{\text{ml s}}\right]$	50	50	50	50
k_v/I_{ao} $\left[\frac{\text{rad}}{\text{ml s}}\right]$	3.5	3.5	3.5	7

B.4 System solving the 0D model of the systemic microcirculation and venous return, with the heart and pulmonary circulation

The 0D circuit representing the systemic microcirculation and venous return, with the heart and pulmonary circulation, is represented in Figure 3.11. It is solved by the system of ordinary differential equations (B.1), with variables in red provided by the boundaries to the 0D model, and the opposite for variables in green.

$$
\begin{cases}
\dfrac{\mathrm{d}\mathbf{p_{art,i\_HA}}}{\mathrm{d}t} = \dfrac{\mathbf{Q_{ter\_art,i\_HA}} - Q_{art,i\_HA}}{C_{art,i\_HA}}, & \forall i_{HA}, \\
\dfrac{\mathrm{d}Q_{art,i\_HA}}{\mathrm{d}t} = \dfrac{\mathbf{p_{art,i\_HA}} - R_{art,i\_HA}Q_{art,i\_HA} - p_{c\_HA}}{L_{art,i\_HA}}, & \forall i_{HA}, \\
\dfrac{\mathrm{d}p_{c\_HA}}{\mathrm{d}t} = \dfrac{\sum_{iHA}(Q_{art,i\_HA}) - Q_{c\_HA}}{C_{c\_HA}}, \\
\dfrac{\mathrm{d}Q_{c\_HA}}{\mathrm{d}t} = \dfrac{p_{c\_HA} - R_{c\_HA}Q_{c\_HA} - p_{ve\_HA}}{L_{c\_HA}}, \\
\dfrac{\mathrm{d}p_{ve\_HA}}{\mathrm{d}t} = \dfrac{Q_{c\_HA} - Q_{ve\_HA}}{C_{ve\_HA}}, \\
\dfrac{\mathrm{d}Q_{ve\_HA}}{\mathrm{d}t} = \dfrac{p_{ve\_HA} - R_{ve\_HA}Q_{ve\_HA} - p_{v\_HA}}{L_{ve\_HA}}, \\
\ldots
\end{cases}
\tag{B.1}
$$

$$
\begin{cases}
\dots \\
\dfrac{\mathrm{d}p_{v\_HA}}{\mathrm{d}t} = \dfrac{Q_{ve\_HA} - Q_{v\_HA}}{C_{v\_HA}}, \\
\dfrac{\mathrm{d}Q_{v\_HA}}{\mathrm{d}t} = \dfrac{p_{v\_HA} - R_{v\_HA}Q_{v\_HA} - p_{svc}}{L_{v\_HA}}, \\
\dfrac{\mathrm{d}p_{svc}}{\mathrm{d}t} = \dfrac{Q_{v\_HA} - Q_{svc}}{C_{svc}}, \\
\dfrac{\mathrm{d}Q_{svc}}{\mathrm{d}t} = \dfrac{p_{svc} - R_{svc}Q_{svc} - p_{ra}}{L_{svc}}, \\
\dfrac{\mathrm{d}\mathbf{p_{art,i\_AL}}}{\mathrm{d}t} = \dfrac{\mathbf{Q_{ter\_art,i\_AL}} - Q_{art,i\_AL}}{C_{art,i\_AL}}, \qquad \forall i_{AL}, \\
\dfrac{\mathrm{d}Q_{art,i\_AL}}{\mathrm{d}t} = \dfrac{\mathbf{p_{art,i\_AL}} - R_{art,i\_AL}Q_{art,i\_AL} - p_{c\_AL}}{L_{art,i\_AL}}, \qquad \forall i_{AL}, \\
\dfrac{\mathrm{d}p_{c\_AL}}{\mathrm{d}t} = \dfrac{\sum_{iAL}(Q_{art,i\_AL}) - Q_{c\_AL}}{C_{c\_AL}}, \\
\dfrac{\mathrm{d}Q_{c\_AL}}{\mathrm{d}t} = \dfrac{p_{c\_AL} - R_{c\_AL}Q_{c\_AL} - p_{ve\_AL}}{L_{c\_AL}}, \\
\dfrac{\mathrm{d}p_{ve\_AL}}{\mathrm{d}t} = \dfrac{Q_{c\_AL} - Q_{ve\_AL}}{C_{ve\_AL}}, \\
\dfrac{\mathrm{d}Q_{ve\_AL}}{\mathrm{d}t} = \dfrac{p_{ve\_AL} - R_{ve\_AL}Q_{ve\_AL} - p_{v\_AL}}{L_{ve\_AL}}, \\
\dfrac{\mathrm{d}p_{v\_AL}}{\mathrm{d}t} = \dfrac{Q_{ve\_AL} - Q_{v\_AL}}{C_{v\_AL}}, \\
\dfrac{\mathrm{d}Q_{v\_AL}}{\mathrm{d}t} = \dfrac{p_{v\_AL} - R_{v\_AL}Q_{v\_AL} - p_{ivc}}{L_{v\_AL}}, \\
\dfrac{\mathrm{d}p_{ivc}}{\mathrm{d}t} = \dfrac{Q_{v\_AL} - Q_{ivc}}{C_{ivc}}, \\
\dfrac{\mathrm{d}Q_{ivc}}{\mathrm{d}t} = \dfrac{p_{ivc} - R_{ivc}Q_{ivc} - p_{ra}}{L_{ivc}}, \\
p_{ra} = E_{ra}(V_{ra} - V_{0,ra}), \\
\dfrac{\mathrm{d}p_{ra}}{\mathrm{d}t} = \dfrac{\mathrm{d}E_{ra}}{\mathrm{d}t}(V_{ra} - V_{0,ra}) + E_{ra}(Q_{svc} + Q_{ivc} + \sum_k (Q_{out,k}) - Q_{TV}), \\
\dfrac{\mathrm{d}Q_{TV}}{\mathrm{d}t} = \dfrac{1}{L_{TV}}\left(-R_{TV}Q_{TV} - B_{TV}|Q_{TV}|Q_{TV} + \dfrac{(1-cos(\theta_{TV}))^4}{(1-cos(\theta_{max}))^4}(p_{ra} - p_{rv})\right), \\
\dfrac{\mathrm{d}\theta_{TV}}{\mathrm{d}t} = f_{TV}, \\
\dfrac{\mathrm{d}f_{TV}}{\mathrm{d}t} = k_{p\_TV}(p_{ra} - p_{rv}) + k_{q\_TV}Q_{TV}cos\theta_{TV} - k_{f\_TV}f_{TV} - k_{v\_TV}Q_{TV}sin(2\theta_{TV}), \quad \text{if} \quad p_{ra} \geq p_{rv}, \\
\dfrac{\mathrm{d}f_{TV}}{\mathrm{d}t} = k_{p\_TV}(p_{ra} - p_{rv}) + k_{q\_TV}Q_{TV}cos\theta_{TV} - k_{f\_TV}f_{TV}, \quad \text{if} \quad p_{ra} < p_{rv}, \\
p_{rv} = E_{rv}(V_{rv} - V_{0,rv}), \\
\dots
\end{cases}
$$

$$
\begin{cases}
... \\
\dfrac{\mathrm{d}p_{rv}}{\mathrm{d}t} = \dfrac{\mathrm{d}E_{rv}}{\mathrm{d}t}(V_{rv} - V_{0,rv}) + E_{rv}(Q_{TV} - Q_{PV}), \\
\dfrac{\mathrm{d}Q_{PV}}{\mathrm{d}t} = \dfrac{1}{L_{PV}}\left(-R_{PV}Q_{PV} - B_{PV}|Q_{PV}|Q_{PV} + \dfrac{(1-cos(\theta_{PV}))^4}{(1-cos(\theta_{max}))^4}(p_{rv} - p_{pa})\right), \\
\dfrac{\mathrm{d}\theta_{PV}}{\mathrm{d}t} = f_{PV}, \\
\dfrac{\mathrm{d}f_{PV}}{\mathrm{d}t} = k_{p\_PV}(p_{rv} - p_{pa}) + k_{q\_PV}Q_{PV}cos\theta_{PV} - k_{f\_PV}f_{PV} - k_{v\_PV}Q_{PV}sin(2\theta_{PV}), \quad \text{if} \quad p_{rv} \geq p_{pa}, \\
\dfrac{\mathrm{d}f_{PV}}{\mathrm{d}t} = k_{p\_PV}(p_{rv} - p_{pa}) + k_{q\_PV}Q_{PV}cos\theta_{PV} - k_{f\_PV}f_{PV}, \quad \text{if} \quad p_{rv} < p_{pa}, \\
\dfrac{\mathrm{d}p_{pa}}{\mathrm{d}t} = \dfrac{Q_{PV} - Q_{pa}}{C_{pa}}, \\
Q_{pa} = \dfrac{p_{pa} - p_{pv}}{R_{pa}}, \\
\dfrac{\mathrm{d}p_{pv}}{\mathrm{d}t} = \dfrac{Q_{pa} - Q_{pv}}{C_{pv}}, \\
Q_{pv} = \dfrac{p_{pv} - p_{la}}{R_{pv}}, \\
p_{la} = E_{la}(V_{la} - V_{0,la}), \\
\dfrac{\mathrm{d}p_{la}}{\mathrm{d}t} = \dfrac{\mathrm{d}E_{la}}{\mathrm{d}t}(V_{la} - V_{0,la}) + E_{la}(Q_{pv} - Q_{MV}), \\
\dfrac{\mathrm{d}Q_{MV}}{vt} = \dfrac{1}{L_{MV}}\left(-R_{MV}Q_{MV} - B_{MV}|Q_{MV}|Q_{MV} + \dfrac{(1-cos(\theta_{MV}))^4}{(1-cos(\theta_{max}))^4}(p_{la} - \mathbf{p_{lv}})\right), \\
\dfrac{\mathrm{d}\theta_{MV}}{\mathrm{d}t} = f_{MV}, \\
\dfrac{\mathrm{d}f_{MV}}{\mathrm{d}t} = k_{p\_MV}(p_{la} - \mathbf{p_{lv}}) + k_{q\_MV}Q_{MV}cos\theta_{MV} - k_{f\_MV}f_{MV} - k_{v\_MV}Q_{MV}sin(2\theta_{MV}), \quad \text{if} \quad p_{la} \geq \mathbf{p_{lv}}, \\
\dfrac{\mathrm{d}f_{MV}}{\mathrm{d}t} = k_{p\_MV}(p_{la} - \mathbf{p_{lv}}) + k_{q\_MV}Q_{MV}cos\theta_{MV} - k_{f\_MV}f_{MV}, \quad \text{if} \quad p_{la} < \mathbf{p_{lv}}, \\
\mathbf{p_{lv}} = E_{lv}(V_{lv} - V_{0,lv}), \\
\dfrac{\mathrm{d}\mathbf{p_{lv}}}{\mathrm{d}t} = \dfrac{\mathrm{d}E_{lv}}{\mathrm{d}t}(V_{lv} - V_{0,lv}) + E_{lv}(Q_{MV} - \mathbf{Q_{aor}}),
\end{cases}
\tag{B.1}
$$

Based on system (B.1), one can define the vector of the complete 0D system

$$
\begin{aligned}
\mathbf{V_{0D}} = [&p_{art,i\_HA}, Q_{art,i\_HA}, p_{c\_HA}, Q_{c\_HA}, p_{ve\_HA}, Q_{ve\_HA}, p_{v\_HA}, Q_{v\_HA}, p_{svc}, Q_{svc}, \\
&p_{art,i\_AL}, Q_{art,i\_AL}, p_{c\_AL}, Q_{c\_AL}, p_{ve\_AL}, Q_{ve\_AL}, p_{v\_AL}, Q_{v\_AL}, p_{ivc}, Q_{ivc}, p_{ra}, \\
&Q_{TV}, \theta_{TV}, f_{TV}, p_{rv}, Q_{PV}, \theta_{PV}, f_{PV}, p_{pa}, Q_{pa}, p_{pv}, Q_{pv}, p_{la}, Q_{MV}, \theta_{MV}, f_{MV}, p_{lv}],
\end{aligned}
$$

and the vector of the variables required by the 0D model at its boundaries.

$$\mathbf{V_{b,0D}} = [Q_{ter\_art,i\_HA}, Q_{ter\_art,i\_AL}, Q_{out,k}, Q_{aor}].$$

$Q_{out,k}$ are the flow rates exiting the microvascular distal districts of terminal coronary arteries. Thus, the term $\sum_k(Q_{out,k})$ in the above system disappears as coronaries are not included in the global model.

Notice that Q_{aor} and $Q_{ter\_art,i\_HA/AL} = Q_{ter\_art,i}$ also belong to the vector of variables required by the 1D model at the boundaries, that is

$$\mathbf{V_{b,1D}} = [Q_{aor}, A_{aor}, Q_{ter\_art,i}, A_{ter\_art,i}].$$

We recall that A_{aor} and $A_{ter\_art,i}$ can be obtained from p_{aor} and $p_{ter\_art,i}$ (which derive from the boundary resolution), respectively, through the constitutive equation of pressure (equation (3.34)).

B.5 Resolution of the entrance to the aorta

The entrance to the aorta is solved by coupling the equation solving the aortic valve (equation (3.100)), representing the physical boundary condition, the constitutive equation of pressure (equation (3.34)), and the compatibility condition (equation (3.91)), which is chosen according to the rules in section 3.1.7. Namely,

$$\begin{cases} \dfrac{\mathrm{d}\mathbf{Q_{aor}}}{\mathrm{d}t} = \dfrac{1}{L_{AV}}\left(-R_{AV}\mathbf{Q_{aor}} - B_{AV}|\mathbf{Q_{aor}}|\mathbf{Q_{aor}} + \dfrac{(1-\cos(\theta_{AV}))^4}{(1-\cos(\theta_{max}))^4}(\mathbf{p_{lv}} - p_{aor})\right), \\ \dfrac{\mathrm{d}\theta_{AV}}{\mathrm{d}t} = f_{AV}, \\ \dfrac{\mathrm{d}f_{AV}}{\mathrm{d}t} = k_{p\_AV}(\mathbf{p_{lv}} - p_{aor}) + k_{q\_AV}\mathbf{Q_{aor}}\cos(\theta_{AV}) = -k_{f\_AV}f_{AV} - k_{v\_AV}\mathbf{Q_{aor}}\sin(2\theta_{AV}), \quad \text{if} \quad \mathbf{p_{lv}} \geq p_{aor}, \\ \dfrac{\mathrm{d}f_{AV}}{\mathrm{d}t} = k_{p\_AV}(\mathbf{p_{lv}} - p_{aor}) + k_{q\_AV}\mathbf{Q_{aor}}\cos(\theta_{AV}) - k_{f\_AV}f_{AV}, \quad \text{if} \quad \mathbf{p_{lv}} < p_{aor}, \\ p_{aor} = B_{1,aor} + B_{2,aor}A_{aor} + B_{3,aor}A_{aor}^2 + B_{4,aor}A_{aor}^3 - \dfrac{B_{5,aor}}{\sqrt{A_{aor}}}\dfrac{\partial Q_{aor}}{\partial z}, \\ Q_{aor} = \lambda_{2,aor}A_{aor} + tn_{1,aor}. \end{cases} \tag{B.2}$$

Notice that variables in red are provided by the boundary resolution to the 0D model, while the opposite for variables in green. Ordinary differential equations are solved through a two steps Runge-Kutta explicit scheme, coherently with the resolution of the 0D model (section 3.2.3). This allows one to update at each time

step Q_{aor}, θ_{AV}, $\frac{\mathrm{d}\theta_{AV}}{\mathrm{d}t}$. A_{aor} and p_{aor} are then updated through the compatibility condition and the constitutive equation for pressure, respectively.

B.6 Resolution of the i-th systemic distal artery

The i-th terminal artery, represented in Figure 3.5, is solved by system

$$\begin{cases} Q_{ter\_art,i} = \dfrac{p_{ter\_art,i} - \mathbf{p_{art,i}}}{Z_{c,i}}, \\ Q_{ter\_art,i} = \lambda_{1,ter\_art,i} A_{ter\_art,i} + tn_{2,ter\_art,i}. \end{cases} \tag{B.3}$$

The first equation is the physical boundary condition (equation (3.67)) and the last equation is the compatibility condition (equation (3.92)), chosen according to the rules in section 3.1.7. All variables are defined at the end of the terminal artery (subscript: $*_{ter\_art,i}$), apart from $\mathbf{p_{art,i}}$, which is provided by the 0D model of the following arteriole. Notice that the flow rate at the i-th terminal artery coincides with the flow rate entering the i-th arteriole. Combining the definition of pressure (equation (3.34)) with the equations of system (B.3), one finds the not-linear equation in $A_{ter\_art,i}$

$$\begin{aligned} f : B_{1,ter\_art,i} + B_{2,ter\_art,i} A_{ter\_art,i} + B_{3,ter\_art,i} A_{ter\_art,i}^2 + B_{4,ter\_art,i} A_{ter\_art,i}^3 + ... \\ ... - \frac{B_{5,ter\_art,i}}{\sqrt{A_{ter\_art,i}}} \frac{\partial Q_{ter\_art,i}}{\partial z} - \mathbf{p_{art,i}} - (\lambda_{1,ter\_art,i} A_{ter\_art,i} + tn_{2,ter\_art,i}) Z_{c,i} = 0. \end{aligned}$$

This latter is solved through the Newton method as

$$A_{ter\_art,i}^{m+1} = A_{ter\_art,i}^{m} - \frac{f(A_{ter\_art,i}^{m})}{f'(A_{ter\_art,i}^{m})},$$

where $f'(A_{ter\_art,i})$, the first derivative of f, is equal to

$$\begin{aligned} f'(A_{ter\_art,i}) = & B_{2,ter\_art,i} + 2B_{3,ter\_art,i} A_{ter\_art,i} + 3B_{4,ter\_art,i} A_{ter\_art,i}^2 + ... \\ & ... + \frac{1}{2} \frac{B_{5,ter\_art,i}}{A_{ter\_art,i}^{3/2}} \frac{\partial Q_{ter\_art,i}}{\partial z} - \lambda_{1,ter\_art,i} Z_{c,i}. \end{aligned}$$

B.7 Resolution of the k-th distal coronary artery

The k-th terminal artery is solved by system

$$\begin{cases} Q_{ter\_art,k} = \dfrac{p_{ter\_art,k} - \mathbf{p_{a,k}}}{Z_{ca,k}}, \\ Q_{ter\_art,k} = \lambda_{1,ter\_art,k} A_{ter\_art,k} + t_{n2,ter\_art,k}. \end{cases} \tag{B.4}$$

The first equation is the physical boundary condition (equation (3.120)) and the last equation is the the compatibility condition (equation (3.92)), which is chosen according to the rules in section 3.1.7. All variables are defined at the end of the terminal artery (subscript: $*_{ter\_art,k}$), apart from $\mathbf{p_{a,k}}$, written in green because provided by the coronary microvascular distal district (system (3.123)). The procedure to solve system (B.4) is the one developed to solve system (B.3).

B.8 Parameters of barorereflex system

Table B.4 indicates the parameters adopted in the 0D model of the baroreflex system according to [256].

Table B.4: Parameters adopted in the 0D model of the baroreflex system. For each efferent organ the following data are given: the time it takes for the efferent response to be fully active (τ_m), the weights of the sympathetic (α_m) and parasympathetic (β_m) activity, the constant (γ_m), and the saturation levels (max and min). All variables apart from τ_m are given in non-dimensional form and are made dimensional by multiplying them for their reference values. The reference HR is 75 bpm, the reference $E_{A,rv-lv}$ are the ones in Table B.2, and the reference R_{art-c}, C_{ve-v} and $V_{0,ve-v}$ are the ones in Table B.1.

Efferent Organ	τ_m [s]	α_m	β_m	γ_m	**min**	**max**
HR	3	0.75	0.75	1	0.25	1.75
$E_{A,rv-lv}$	3	0.40	0	0.80	0.8	1.2
R_{art-c}	15	0.80	0	0.60	0.6	1.4
C_{ve-v}	30	-0.20	0	1.10	0.9	1.1
$V_{0,ve-v}$	30	-0.42	0	1.21	0.79	1.21

Appendix C

Details about the models adopted for the applications in chapter 6

This appendix contains some details about the models adopted for the applications reported in chapters 6 and 7.

C.1 3-elements Windkessel models in chapter 6

Table C.1 indicates the parameters of the 3-elements Windkessel models associated to the simplified version of the model adopted in chapter 6. For each distal artery, R_{w1}, R_{w2} and C_w correspond to the proximal resistance, distal resistance, and compliance of the relative peripheral zone.

C.2 Parameters of the 0D compartments of the model in chapter 7

Table C.2 indicates the parameters of the 0D compartments integrated in the model used in chapter 7 to simulate both the 1G and 0G conditions. For each compartment and configuration, the values of resistance, R [mmHg s/ml], compliance, C [ml/mmHg], inertance, L [mmHg s2/ml], and unstressed volume, V_0 [ml], are provided.

Table C.1: Parameters of the 3-elements Windkessel models closing the terminating 1D arteries in the simplified model adopted in chapter 6. For each distal artery, the following information are reported: name (reference number according to Figure 3.1) (column i), proximal resistance (R_{w1}), distal resistance (R_{w2}) and compliance (C_w).

Distal artery	R_{1w} $\left[\frac{\text{mmHgs}}{\text{ml}}\right]$	R_{2w} $\left[\frac{\text{mmHgs}}{\text{ml}}\right]$	C_w $\left[\frac{\text{ml}}{\text{mmHg}}\right]$
Vertebral (6/20)	11.72	33.36	0.0041
Radial (8/22)	9.27	30.33	0.0070
Interosseous (10/24)	32.37	599.90	0.000441
Ulnar B (11/25)	11.72	27.89	0.0070
Internal Carotid (12/16)	4.37	99.89	0.0018
External Carotid (13/17)	3.93	100.32	0.0018
Intercostals (26)	0.71	9.77	0.027
Hepatic (31)	4.14	23.09	0.010
Gastric (32)	10	30.60	0.0069
Splenic (33)	5.47	11.89	0.016
Superior Mesenteric (34)	1.38	5.60	0.040
Renal (36/38)	3.17	5.30	0.033
Inferior Mesenteric (40)	8.62	42.96	0.0054
Inner Iliac (43)	5.16	54.40	0.0047
Deep femoral (45)	6.17	29.64	0.0078
Anterior Tibial (47)	12.89	29	0.0067
Posterior Tibial (48)	11.72	24.10	0.0078

Table C.2: Parameters of the 0D compartments integrated in the model used in chapter 7 to simulate both the 1G and 0G conditions. For each compartment, the following information are given: resistance R [mmHg s/ml], compliance C [ml/mmHg], inertance L [mmHg s^2/ml], and unstressed volume V_0 [ml], in 1G supine and 0G conditions.

Cardiovascular region	**1G** R, C, L, V_0	**0G** R, C, L, V_0
	Arteries	
Pulmonary	0.08, 3.8, /, 42.80	0.08, 3.97, /, 58.24
	Arterioles	
Vertebral (6/20)	25.88, 0.013, 0.019, 4	28.40, 0.013, 0.019, 2.85
Radial (8/22)	17.03, 0.014, 0.018, 3.40	17.03, 0.014, 0.018, 2.25
Interosseous (10/24)	393.70, 0.0009, 0.07, 3.40	393.70, 0.0009, 0.07, 2.25
Ulnar B (11/25)	19.69, 0.014, 0.018, 3.40	19.69, 0.014, 0.018, 2.25
Internal carotid (12/16)	23.60, 0.015, 0.017, 4	25.90, 0.015, 0.017, 2.85
External Carotid (13/17)	21.85, 0.015, 0.017, 4	23.98, 0.015, 0.017, 2.85
Intercostals (26)	5.61, 0.054, 0.009, 6.60	5.61, 0.054, 0.009, 5.45
Hepatic (31)	16.24, 0.021, 0.015, 29.60	16.24, 0.021, 0.015, 28.45
Gastric (32)	8.91, 0.033, 0.012, 8.90	8.91, 0.033, 0.012, 7.75
Splenic U (33)	127.98, 0.014, 0.11, 11.20	127.98, 0.014, 0.11, 10.05
Splenic L (33)	25.60, 0.014, 0.022, 11.20	23.04, 0.014, 0.022, 10.05
Superior mesenteric (34)	3.85, 0.081, 0.007, 15.40	3.46, 0.081, 0.007, 14.25
Renal U (36/38)	8.62, 0.068, 0.016, 5.70	8.62, 0.068, 0.016, 4.55
Renal L (36/38)	8.62, 0.068, 0.016, 5.70	7.76, 0.068, 0.016, 4.55
Inferior mesenteric (40)	30.74, 0.011, 0.02, 11.50	27.60, 0.011, 0.02, 10.35
Inner iliac (43)	23.48, 0.014, 0.018, 3.4	21.08, 0.014, 0.018, 2.25
Deep femoral (45)	13.37, 0.023, 0.014, 13.90	12, 0.023, 0.014, 12.75
Anterior tibial (47)	5.51, 0.023, 0.014, 13.90	4.95, 0.023, 0.014, 12.75
Posterior tibial (48)	30.44, 0.010, 0.021, 13.90	27.33, 0.010, 0.021, 12.75
	Capillaries	
HA	0.81, 0.03, 0.00045, 72.20	0.81, 0.03, 0.00045, 75
U ABD	0.65, 0.031, 0.00043, 89.80	0.65, 0.031, 0.00043, 89.58
L ABD	0.68, 0.038, 0.00047, 48.10	0.68, 0.038, 0.00047, 27.33
LEGS	0.87, 0.032, 0.00034, 57.20	0.87, 0.032, 0.00034, 35.49
	Venules	
HA	0.26, 0.6, 0.0005, 278.40	0.26, 0.6, 0.0005, 289.21
U ABD	0.21, 0.61, 0.00077, 256.30	0.21, 0.61, 0.00077, 255.68
L ABD	0.22, 0.46, 0.00013, 226.60	0.22, 0.46, 0.00013, 128.77
LEGS	0.28, 0.53, 0.00061, 269.80	0.28, 0.53, 0.00061, 167.40
	Veins	
HA	0.022, 15, 0.00056, 312	0.022, 15, 0.00056, 324.11
SVC	5E-4, 15, 0.0005, 14.30	5E-4, 15, 0.0005, 14.27
IVC	5E-4, 15, 0.0005, 4.80	5E-4, 15, 0.0005, 4.99
Pulmonary	0.01, 20.5, /, 224.60	0.01, 21.47, /, 305.60
U ABD	0.035, 49.35, 0.00084, 427.60	0.035, 49.35, 0.00084, 426.57
L ABD	0.06, 16.78, 0.00094, 412	0.06, 16.78, 0.00094, 234.13
LEGS	0.07, 9.87, 0.00067, 490.60	0.07, 12.53, 0.00067, 304.39

Appendix D

List of symbols

This appendix contains the full list of acronyms and symbols adopted throughout the text in alphabetical order, with Greek letters at the and of the list. Each symbol is taken as a unique word and its subscript is considered as part of the word. Numbers are indicated before letters, letters in lower case are put before letters in upper case, punctuation is neglected, superscripts are taken into account last.

A : Vessel area,
$\overline{A}$: Time-averaged vessel area,
A_0 : Vessel area at p_0,
A_1 : Area at the outlet of the parent artery for an arterial bifurcation,
A_2 : Area at the entrance to the first daughter artery (vessel 2) for an arterial bifurcation,
A_3 : Area at the entrance to the second daughter artery (vessel 3) for an arterial bifurcation,
A_{aor} : Area at the entrance to the aorta,
AD : Average diameter,
AF : Atrial fibrillation,
age : Age,
age_{ref} : Age of the reference subject,
AI : Augementation index,
$\mathrm{AI_{AA}}$: Augementation index at the ascending aorta,
A_{in_0} : Proximal vessel area at p_0,
A_{j_0} : Area at the$j$-th node of the generic artery at p_0,
AL : Abdomen and legs,
A_{n+1} : Vessel area at the $(n+1)$-th time step,
A_{out_0} : Distal vessel area at p_0,
A_p : Pressure-dependent function of the vessel area,
AP : Augemented pressure,
AT : Average thickness,

$A_{ter\_art,i}$: Area at the outlet of the i-th distal artery,
ATV : Atrioventricular,
AV : Aortic valve,
$B_1 \div B_5$: Pressure coefficients,
BMI : Body mass index,
BP : Blood pressure,
BSA : Body surface area,
B_{va} : Turbulent flow separation coefficient of the generic cardiac valve,
c : Pulse wave velocity through the (3.73),
C : Capacitor/Compliance,
$C_{1j,k}$: Compliances of the arterial compartments for the k-th terminal coronary artery,
$C_{1,k}$: Total arterial compliance associated to the k-th terminal coronary artery,
$C_{1,T}$: Total arterial compliance to distribute to the arterial compartments of the terminal coronary arteries,
$C_{3j,k}$: Compliances of the venous compartments for the k-th terminal coronary artery,
$C_{3,k}$: Total venous compliance associated to the k-th terminal coronary artery,
$C_{3,T}$: Total venous compliance to distribute to the venous compartments of the terminal coronary arteries,
CAD : Coronary Haert Disease,
C_A^e : Elastic component of the arterial compliance,
C_{art} : Arteriolar compliance,
$C_{art,i\_HA/AL}$: Compliance of the i-th arteriole belonging to the HA/AL groups,
CBF : Coronary blood flow,
C_c : Capillary complinace,
$C_{ca,k}$: Complinace of the k-th terminal coronary artery,
$C_{c\_HA/AL}$: Compliance of the capillary compartment belonging to the HA/AL groups,
$C_{cv,k}$: Complinace of the venula closing the k-th terminal coronary artery,
CEP : Cavity-induced extracellular pressure,
c_{FTF} : Wave speed through the Foot-to-Foot method,
C_g^e : Geometric-dependent function of C_A^e,
C_{ivc} : Compliance of the inferior vena cava compartment,
C_j : Compliance of the j-th RLC compartment in the 0D model closing the systemic arterial tree,
c_{MK} : Wave speed through the Moens-Korteweg equation,
CO : Cardiac output,
C_{pa} : Compliance of the pulmonary artery compartment,
C_p^e : Pressure-dependent function of C_A^e,
CPP : Coronary perfusion pressure,
C_{pv} : Compliance of the pulmonary vein compartment,
C_{svc} : Compliance of the superior vena cava compartment,
cv : Coeffient of variation
C_v : Venous compliance,
cv_{AF} : Coeffient of variation associated to a variable calculated in AF
C_{vc} : Vena cava compliance,

C_{ve} : Venular compliance,
$C_{ve\_HA/AL}$: Compliance of the venular compartment belonging to the HA/AL groups,
cv_G : cv of τ_G
$C_{v\_HA/AL}$: Compliance of the venous compartment belonging to the HA/AL groups,
C_{v_LEGS} : Compliance of the venous compartment belonging to the LEGS groups,
CVP : Central venous pressure,
cv_{SR} : Coeffient of variation associated to a variable calculated in SR
C_w : Compliance of the generic three-elements Windkessel model,
d : Generic distance,
D : Vessel diameter,
$\overline{D}$: Time-averaged vessel diameter,
D_0 : Vessel diameter at p_0,
d_{art} : Arterial diameters,
D_{in_0} : Proximal vessel diameter at p_0,
D_{out_0} : Distal vessel diameter at p_0,
E : Elastance,
e_a : Atrial e_{ch} function,
$E_{A,ch}$: Amplitude of E_{ch} for the generic cardiac chamber,
$E_{A,lv}$: Amplitude of E_{lv},
$E_{A,rv}$: Amplitude of E_{rv},
$E_{B,ch}$: Minimum of E_{ch} for the generic cardiac chamber,
e_{ch} : Normalised time-varying function of E_{ch},
E_{ch} : Elastance of the generic cardiac chamber,
ECG : Electrocardiogram,
EDV : End-diastolic volume,
EF : Ejection fraction,
E_{la} : Elastance of the left atrium,
E_{lv} : Elastance of the left ventricle,
E_m : Incremental elastic modulus of the vessel wall,
E_{ra} : Elastance of the right atrium,
E_{rv} : Elastance of the right ventricle,
ESV : End-systolic volume,
e_v : Ventricular e_{ch} function,
f : Beat frequency,
$\mathbf{F}$: Vector of the flux terms in the conservative formulation,
F_{bm} : Force acting on the generic valve - the dynamic action of the blood pushing on the valve leaflets,
F_{fr} : Force acting on the generic valve - frictional effect caused by the tissue resistance,
$\mathbf{F_{LF}}$: Internal boundary flux through the Lax-Friedrichs method,
F_{pr} : Force acting on the generic valve - pressure gradient,
F_{vo} : Force acting on the generic valve - effects of the vortexes downstream of the valve,

$\mathbf{g}$: Gravity vector,
G : Gravity condition on Earth; 1G for g_z=9.81 m/s^2, 0G for g_z=0 m/s^2,
$\mathbf{G}$: Vector of known terms in the spatial resolution of the 1D model,
$\mathbf{G_{1/2}}$: $\mathbf{G}$ at nodes 1/2 of the e-th elemental region Ω_e for A and Q,
$\mathbf{G}^n$: $\mathbf{G}$ at the n-th time step
$\mathbf{G}^{n+1/2}$: $\mathbf{G}$ at the $(n+1/2)$-th time step
$\mathbf{G}^{n+1}$: $\mathbf{G}$ at the $(n+1)$-th time step
G_{LV} : Groups of coronary arteries feeding the left ventricle
g_r : Radial component of $\mathbf{g}$,
G_{RV} : Groups of coronary arteries feeding the right ventricle
G_S : Groups of coronary arteries feeding the septum
g_z : Axial component of $\mathbf{g}$,
g_ϕ : Azimuthal component of $\mathbf{g}$,
h : Body height,
$\mathbf{H}$: Vector representing the distance between the generic site and HIP,
$\bar{\mathbf{H}}$: Matrix of the derivatives $\dfrac{\partial \mathbf{F}}{\partial \mathbf{U}}$,
HA : Head and arms,
h_{art} : Arterial thicknesses,
HIP : Hydrostatic indifference point,
HR : Heart rate,
h_{ref} : Body height of the reference subject,
HR$_{ref}$: Heart rate of the reference subject,
h_w : Wall thickness,
h_{w_0} : Wall thickness at p_0,
$\bar{\mathbf{I}}$: Identity matrix,
I_{ao} : Momentum of inertia of the generic cardiac valve,
IPP : Inter-pleural pressure,
ISS : International Space Station,
IVC : Inferior vena cava,
K_{visc} : Effective wall viscosity,
L : Inductor/Inertance,
$\bar{\mathbf{L}}$: Matrix of the eigenvectors for matrix $\mathbf{H}$
$\mathbf{l_{1/2}}$: Row eigenvectors corresponding to $\lambda_{1/2}$,
LA : Left atrium,
L ABD : Lower abdomen,
LAD : Left Anterior Descending coronary artery,
l_{art} : Arterial lengths,
L_{art} : Arteriolar inertance,
$L_{art,i\_HA/AL}$: Inertance of the i-th arteriole belonging to the HA/AL groups,
L_{AV} : L_{va} for the aortic valve,

LBNP : Lower body negative pressure,
L_c : Capillary inertance,
$L_{c\_HA/AL}$: Inertance of the capillary compartment belonging to the HA/AL groups,
l_e : Length of the element Ω_e,
LEGS : Legs,
LEO : Low Earth Orbit,
LH : Left heart,
L_{ivc} : Inertance of the inferior vena cava compartment,
L_j : Inertance of the j-th RLC compartment in the 0D model closing the systemic arterial tree,
L_{MV} : L_{va} for the mitral valve,
$\bar{\mathbf{L}}_\mathbf{n}$: $\bar{\mathbf{L}}$ at the n-th time step
$\bar{\mathbf{L}}_\mathbf{n}^*$: $\bar{\mathbf{L}}$ at the n-th time step and at the point $c\Delta T$ from the boundary
$\bar{\mathbf{L}}_\mathbf{n}^{\mathbf{1}*}$: equal to $\bar{\mathbf{L}}_\mathbf{n}^*$
$\bar{\mathbf{L}}_\mathbf{n}^{\mathbf{2}*}$: $\bar{\mathbf{L}}$ at the n-th time step and at the point $c\Delta T/2$ from the boundary
$\bar{\mathbf{L}}_{\mathbf{n+1/2}}$: $\bar{\mathbf{L}}$ at the $(n+1/2)$-th time step
$\bar{\mathbf{L}}_{\mathbf{n+1}}$: $\bar{\mathbf{L}}$ at the $(n+1)$-th time step
L_{PV} : L_{va} for the pulmonary valve,
L_{spezz} : Lenght of the N_v segments discretizing the generic artery,
L_{svc} : Inertance of the superior vena cava compartment,
L_{TV} : L_{va} for the tricuspid valve,
l_v : Vessel length,
l_{v_0} : Vessel length at p_0,
L_v : Venous inertance,
LV : Left ventricle,
L_{va} : Fluid inertance of the generic cardiac valve,
L_{ve} : Venular inertance,
$L_{ve\_HA/AL}$: Inertance of the venular compartment belonging to the HA/AL groups,
L_{vc} : Vena cava inertance,
$L_{v\_HA/AL}$: Inertance of the venous compartment belonging to the HA/AL groups,
$\bar{\mathbf{M}}$: Mass matrix in the spatial resolution of the 1D model,
MAP : Mean arterial pressure,
MAV : Mean velocity in time and over the cross sectional area,
M_R : Constant linking $R_{s,j,k}$ to $r_{v,k}$,
MV : Mitral valve,
M_w : Constant linking w_k to $r_{v,k}$,
MW : Midwall,
N_4 : Viscous coefficient,
N_e : Number of elements discretizing the whole network of 1D vessels,

n_p : Parasympathetic activity,
n_s : Sympathetic activity,
NSD : Normalised signal difference,
N_t : Total number of ΔT intervals to simulate,
N_v : Number of segments discretizing the generic vessel,
p : Excess pressure: pressure impressed by the left ventricle to the blood during ejection,
$\bar{p}$: Beat-averaged value of excess pressure,
p_0 : Reference pressure,
p_1 : Pressure at the outlet of the parent artery for an arterial bifurcation,
$p_{1j,k}$: Pressure acting on $C_{1j,k}$,
p_{1va} : Pressure at the inlet of the generic cardiac valve,
p_2 : Pressure at the entrance to the first daughter artery (vessel 2) for an arterial bifurcation,
p_{2va} : Pressure at the outlet of the generic cardiac valve,
p_3 : Pressure at the entrance to the second daughter artery (vessel 3) for an arterial bifurcation,
$p_{3j,k}$: Pressure acting on $C_{3j,k}$,
$\overline{p}_{acs}$: Mean aortic-carotid sinus pressure,
$\overline{p}_{acs,ref}$: Reference $\overline{p}_{acs}$,
$p_{a,k}$: Arterial pressure for the k-th coronary microvascular distal districts,
p_{aor} : Pressure at the entrance to the aorta,
$p_{aor_{dia}}$: Diastolic aortic pressure,
$p_{aor_{mean}}$: Mean aortic pressure,
$p_{aor_{sys}}$: Systolic aortic pressure,
p_{art} : Systemic arterial pressure,
$\overline{p}_{art}$: Time-averaged value of the systemic arterial pressure over the cardiac cycle,
P ART : Pulmonary arteries,
$p_{art,i}$: Pressure at the entrance to the i-th arteriole,
$p_{art,i\_HA/AL}$: Pressure at the entrance to the i-th arteriole belonging to the HA/AL groups,
PC : Pulmonary circulation,
p_{ch} : Cardiac chamber pressure,
$p_{c\_HA/AL}$: Pressure at the entrance to the capillary compartment belonging to the HA/AL groups,
$p_{cs,dx}$: Right carotid sinus pressure,
$p_{cs,sx}$: Left carotid sinus pressure,
p_{db} : Diatolic brachial pressure,
PDF : Probability density function,
p_{dia} : Diastolic pressure,
p_e : Elastic pressure component,
p_E : External pressure acting on the vessel walls,
p_{edlv} : End-diastolic left ventricular pressure,
p_{eslv} : End-systolic left ventricular pressure,
p_H : Hydrostatic pressure,
p_{ivc} : Pressure at the entrance to the inferior vena cava compartment,

$p_{j/j+1}$: Pressure at the inlet/outlet of the j-th RLC compartment in the 0D model of the systemic arterial tree,
p_j^{im} : Intramyocardial pressures in the coronary microvascular distal districts,
p_{la} : Pressure in the left atrium,
p_{lv} : Pressure in the left ventricle,
p_{max} : Maximum pressure,
p_{mb} : Mean brachial pressure $p_{db} + pp_b/3$,
$p_{mb_{ref}}$: Mean brachial pressure of the reference subject,
p_{mean} : Mean pressure $(p_{dia} + pp/3)$,
$p_{out,k}$: Pressure at the outlet of the coronary microvascular distal districts,
pp : Pulse pressure,
p_{pa} : Pressure at the entrance to the pulmonary artery,
pp_{aor} : Aortic pulse pressure,
pp_b : Brachial pulse pressure,
$pp_{b_{ref}}$: Brachial pulse pressure of the reference subject,
p_{pv} : Pressure at the entrance to the pulmonary vein,
P_r : Pearson correlation coefficient,
p_{ra} : Pressure in the right atrium,
p_{rv} : Pressure in the right ventricle,
p_{sb} : Systolic brachial pressure,
p_{svc} : Pressure at the entrance to the superior vena cava compartment,
p_{sys} : Systolic pressure,
p_T : Transmural pressure,
$p_{ter\_art,i}$: Pressure at the outlet of the i-th distal artery,
$p_{ter\_art,k}$: Pressure at the outlet of the k-th terminal coronary artery,
PV : Pulmonary valve,
$p_{ve\_HA/AL}$: Pressure at the entrance to the venular compartment belonging to the HA/AL groups,
p_{ve} : Constant venular pressure at the outlet of the generic three-elements Windkessel model,
P VEN : Pulmonary veins,
$p_{v\_HA/AL}$: Pressure at the entrance to the venous compartment belonging to the HA/AL groups,
p_{visc} : Viscous pressure component,
$p_{v,k}$: Venous pressure for the k-th coronary microvascular distal districts,
p_w : Pressure at the entrance of the generic three-elements Windkessel model,
PWV : Pulse wave velocity,
PWV_0 : Pulse wave velocity at p_0,
PWV_{art} : Arterial pulse wave velocity,
q : Mean flow rate per beat,
Q : Flow rate,
$\bar{Q}$: Beat-averaged value of flow rate,
Q_1 : Flow rate at the outlet of the parent artery for an arterial bifurcation,

$Q_{1j,k}$: Flow rates through C_{1j},
Q_2 : Flow rate at the entrance to the first daughter artery (vessel 2) for an arterial bifurcation,
Q_3 : Flow rate at the entrance to the second daughter artery (vessel 3) for an arterial bifurcation,
$Q_{3j,k}$: Flow rates through C_{3j},
$Q_{a,k}$: Arterial flow rate of the coronary microvascular distal districts,
Q_{aor} : Flow rate at the entrance to the aorta,
$Q_{art,i\_HA/AL}$: Flow rate exiting the i-th arteriole belonging to the HA/AL groups,
$Q_{Cca,k}$: Flow rate through $C_{ca,k}$, Q
Q_{ivc} : Flow rate exiting the inferior vena cava compartment,
$Q_{j-1/j}$: Flow rate entering/exiting the j-th RLC compartment in the 0D model of the systemic arterial tree,
$Q_{ja,k}$: Flow rates through $R_{1j,k}$,
$Q_{jm,k}$: Flow rates through $R_{2j,k}$,
$Q_{jv,k}$: Flow rates through $R_{3j,k}$,
Q_{LAD} : LAD flow rate,
$< Q_{LAD} >$: Average LAD flow rate for a given sequence of RR interbeat intervals,
$Q_{LAD,i}$: LAD flow rate at the i-th heartbeat period,
$Q_{max,dia}$: Maximum Q_{LAD} during diastole,
$Q_{max,sys}$: Maximum Q_{LAD} during systole,
Q_{mean} : Mean flow rate over the heartbeat duration,
Q_{min} : Minimum Q_{LAD} throughout the heart cycle,
Q_{MV} : Q_{va} for the mitral valve,
Q_{n+1} : Flow rate at the $(n+1)$-th time step,
$Q_{out,k}$: Flow rate at the outlet of the coronary microvascular distal districts,
Q_{pa} : Flow rate exiting the pulmonary artery compartment,
Q_{pv} : Flow rate exiting the pulmonary vein compartment,
Q_{PV} : Q_{va} for the pulmonary valve,
Q_{svc} : Flow rate exiting the superior vena cava compartment,
$Q_{ter\_art,i}$: Flow rate at the outlet of the i-th distal artery,
$Q_{ter\_art,i\_HA/AL}$: Flow rate at the outlet of the i-th distal artery belonging to the HA/AL groups,
$Q_{ter\_art,k}$: Flow rate at the outlet of the k-th terminal coronary artery,
Q_{TV} : Q_{va} for the tricuspid valve,
$Q_{v,k}$: Venous flow rate of the coronary microvascular distal districts,
Q_{va} : Flow rate through the generic cardiac valve,
$Q_{ve\_HA/AL}$: Flow rate exiting the venular compartment belonging to the HA/AL groups,
$Q_{v\_HA/AL}$: Flow rate exiting the venous compartment belonging to the HA/AL groups,
Q_w : Flow rate at the entrance of the generic three-elements Windkessel model,
r : Radial coordinate,
R : Resistance,
$R_{0,1j,k}$: Reference resistances of the arterial compartments for the k-th terminal coronary artery,

$R_{0,2j,k}$: Reference resistances of the intermediate compartments for the k-th terminal coronary artery,
$R_{0,3j,k}$: Reference resistances of the venous compartments for the k-th terminal coronary artery,
$R_{1j,k}$: Resistances of the arterial compartments for the k-th terminal coronary artery,
$R_{2j,k}$: Resistances of the intermediate compartments for the k-th terminal coronary artery,
$R_{3j,k}$: Resistances of the venous compartments for the k-th terminal coronary artery,
RA : Right atrium,
R_{art} : Arteriolar resistance,
$R_{art,i\_HA/AL}$: Resistance of the i-th arteriole belonging to the HA/AL groups,
R_{AV} : R_{va} for the aortic valve,
R_c : Capillary resistance,
$R_{c\_HA/AL}$: Resistance of the capillary compartment belonging to the HA/AL groups,
Re : Reynolds number,
RH : Right heart,
RI : Reflection index,
R_{ivc} : Resistance of the inferior vena cava compartment,
R_j : Resistance of the j-th RLC compartment in the 0D model closing the systemic arterial tree,
$R_{j,T}$: Total resistance of the j-th layer to distribute to the j-th layer of the terminal coronary arteries,
RM : Reflection magnitude,
R_{MV} : R_{va} for the mitral valve,
R_p : Peripheral resistance,
R_{pa} : Resistance of the pulmonary artery compartment,
RPP : Rate pressure product,
R_{pv} : Resistance of the pulmonary vein compartment,
R_{PV} : R_{va} for the pulmonary valve,
RR : Heartbeat period,
$\mathrm{RR_{AF}}$: AF RR sequence used in the arterial tree study,
RR_{dia} : Diastolic period within RR,
$\mathrm{RR_{SR}}$: SR RR sequence used in the arterial tree study,
RR_{sys} : Systolic period within RR,
$R_{s,j,k}$: Sum of the reference resistances for the j-th layer of the k-th terminal coronary artery,
R_{svc} : Resistance of the superior vena cava compartment,
R_{TV} : R_{va} for the tricuspid valve,
r_v : Vessel radius,
r_{v_0} : Vessel radius at p_0,
R_v : Venous resistance,
RV : Right ventricle,
R_{va} : Viscous resistance of the generic cardiac valve,
R_{vc} : Vena cava resistance,
R_{ve} : Venular resistance,
$R_{ve\_HA/AL}$: Resistance of the venular compartment belonging to the HA/AL groups,

$R_{v\_HA/AL}$: Resistance of the venous compartment belonging to the HA/AL groups,
$r_{v,k}$: Vessel radius of the k-th terminal coronary artery,
R_{w1} : Proximal resistance of the generic three-elements Windkessel model,
R_{w2} : Distal resistance of the generic three-elements Windkessel model,
s : Sex,
$\mathbf{S}$: Vector of the source terms in the conservative formulation,
$\mathbf{S_2}$: Vector of the source terms in the quasi-linear formulation,
$\mathbf{S^*_{2_i}}$: Initial $\mathbf{S_2}$ at the point $c\Delta T$ from the boundary
$\mathbf{S^*_{2_n}}$: $\mathbf{S_2}$ at the n-th time step and at the point $c\Delta T$ from the boundary
$\mathbf{S^{1*}_{2_n}}$: equal to $\mathbf{S^*_{2_n}}$
$\mathbf{S_{2_{n+1/2}}}$: $\mathbf{S_2}$ at the $(n+1/2)$-th time step
SA : Sinoatrial,
$S(f)$: Power spectrum,
SC : Systemic circulation,
SEN : Subendocardium,
$Sens$: Coefficient to determine the sensitivity of output to input parameters,
SEP : Subepicardium,
SIP : Shortening-induced intracellular pressure,
s_{ref} : Sex of the reference subject,
SR : Sinux rhythm,
SV : Stroke volume,
SVC : Superior vena cava,
SV_{LAD} : LAD stroke volume; sum of V_{sys} and V_{dia},
SW : Stroke work,
t : Time,
$\mathbf{t}$: Time vector to simulate,
TCVP : Transmural central venous pressure,
t_n : $n\Delta T$,
$t_{n+1/2}$: $(n+1/2)\Delta T$,
t_{n+1} : $(n+1)\Delta T$,
tn_1, tn_2 : Known terms in the compatibility conditions for $\lambda_{1,2}$,
t_{ac} : Time when atria start contracting,
T_{ac} : Period of contraction for atria,
t_{ar} : Time when atria start relaxing,
T_{ar} : Period of relaxation for ventricles,
TCSA : Total cross sectional area,
$\mathbf{T_H}$: Sequence of heartbeat durations to simulate,
TNV : Total number of vessels,
TPR : Total arterial peripheral resistance,
TTI : Tension time index,

TV : Tricuspid valve,
T_{vc} : Period of contraction for ventricles,
$T_{vc_{ref}}$: Period of contraction for ventricles of the reference subject,
T_{vr} : Period of relaxation for ventricles,
$\mathbf{u}$: Velocity vector,
$\mathbf{U}$: Vector of the dependent variables in the conservative formulation,
$\overline{u}_1$: Q_1/A_1 at the outlet of the parent artery for an arterial bifurcation,
$\overline{u}_2$: Q_2/A_2 at the entrance to the first daughter artery (vessel 2) for an arterial bifurcation,
$\overline{u}_3$: Q_3/A_3 at the entrance to the second daughter artery (vessel 3) for an arterial bifurcation,
U ABD : Upper abdomen,
$\mathbf{U_h}$: Approximated solution of $\mathbf{U}$,
$\mathbf{U_h}^{-/+}$: Approximated solution of $\mathbf{U}$ on the left/right side of the generic internal boundary,
$\mathbf{U_i}$: Initial $\mathbf{U}$
$\mathbf{U_i}^*$: Initial $\mathbf{U}$ at the point $c\Delta T$ from the boundary
$\mathbf{U_n}$: $\mathbf{U}$ at the n-th time step
$\mathbf{U_n^*}$: $\mathbf{U}$ at the n-th time step and at the point $c\Delta T$ from the boundary
$\mathbf{U_n^{1*}}$: equal to $\mathbf{U_n^*}$
$\mathbf{U_n^{2*}}$: $\mathbf{U}$ at the n-th time step and at the point $c\Delta T/2$ from the boundary
$\mathbf{U_{n+1/2}}$: $\mathbf{U}$ at the $(n+1/2)$-th time step
$\mathbf{U_{n+1}}$: $\mathbf{U}$ at the $(n+1)$-th time step
u_r : Radial component of $\mathbf{u}$,
u_z : Axial component of $\mathbf{u}$,
$\overline{u}_z$: Axial velocity within the flat core of the velocity profile $u_z(t, r, z)$,
u_ϕ : Azimuthal component of $\mathbf{u}$,
V : Total volume,
$\bar{V}$: Beat-averaged value of total volume,
V_0 : Unstressed volume,
$V_{0,1j,k}$: Unstressed volumes of the arterial compartments for the k-th terminal coronary artery,
$V_{0,1,T}$: Total unstressed volume to distribute to the arterial compartments of the terminal coronary arteries,
$V_{0,3j,k}$: Unstressed volumes of the venous compartments for the k-th terminal coronary artery,
$V_{0,3,T}$: Total unstressed volume to distribute to the venous compartments of the terminal coronary arteries,
$V_{0,ch}$: Unstressed volume of the generic cardiac chamber,
$\mathbf{V_{0D}}$: Vector containing the variables of the 0D model closing the systemic arterial tree,
$\mathbf{V_{0Dkc}}$: Vector containing the variables of the microvascular distal district closing the k-th coronary artery,
$\mathbf{V_{0D}}^n$: $\mathbf{V_{0D}}$ at the n-th time step,
$\mathbf{V_{0D}}^{n+1/2}$: $\mathbf{V_{0D}}$ at the $(n+1/2)$-th time step,
$\mathbf{V_{0D}}^{n+1}$: $\mathbf{V_{0D}}$ at the $(n+1)$-th time step,
$V_{0,la}$: Unstressed left atrial volume,
$V_{0,lv}$: Unstressed left ventricular volume,
$V_{0,ra}$: Unstressed right atrial volume,
$V_{0,rv}$: Unstressed right ventricular volume,

$V_{0,v}$: Venous unstressed volume,
$V_{0,ve}$: Venular unstressed volume,
$V_{1j,k}$: Stressed volumes of the arterial compartments for the k-th terminal coronary artery,
$V_{3j,k}$: Stressed volumes of the venous compartments for the k-th terminal coronary artery,
$\mathbf{V_{b,0D}}$: Vector containing the variables at the boundaries of the 0D model closing the systemic arterial tree,
$\mathbf{V_{b,0Dc}}$: Vector containing the variables at the boundaries of the coronary microvasculature distal districts,
$\mathbf{V_{b,0D}}^n$: $\mathbf{V_{b,0D}}$ at the n-th time step,
$\mathbf{V_{b,0D}}^{n+1/2}$: $\mathbf{V_{b,0D}}$ at the $(n+1/2)$-th time step,
$\mathbf{V_{b,0D}}^{n+1}$: $\mathbf{V_{b,0D}}$ at the $(n+1)$-th time step,
$\mathbf{V_{b,1D}}$: Vector containing the variables at the boundaries between the 0D and the 1D model,
$\mathbf{V_{b,1Dc}}$: Vector containing the variables at the boundaries coronary microvasculature distal districts-1D model,
$\mathbf{V_{b,1D}}^n$: $\mathbf{V_{b,1D}}$ at the n-th time step,
$\mathbf{V_{b,1D}}^{n+1/2}$: $\mathbf{V_{b,1D}}$ at the $(n+1/2)$-th time step,
$\mathbf{V_{b,1D}}^{n+1}$: $\mathbf{V_{b,1D}}$ at the $(n+1)$-th time step,
V_{ch} : Total volume of the generic cardiac chamber,
V_{dia} : Blood volume through the LAD artery during diastole,
V_{edlv} : End-diastolic left-ventricular volume,
V_{eslv} : End-systolic left-ventricular volume,
VIP : Volume Indifference point,
V_j : Total volume of the j-th RLC compartment in the 0D model of the systemic arterial tree,
V_{j_0} : Unstressed volume of the j-th RLC compartment in the 0D model of the systemic arterial tree,
V_{la} : Total left atrial volume,
V_{lv} : Total left ventricular volume,
V_{ra} : Total right atrial volume,
V_{rv} : Total right ventricular volume,
V_{sys} : Blood volume through the LAD artery during systole,
w : Body weight,
$\mathbf{W}$: Vector of the characteristic variables,
w_k : Portion of the myocardial weight going to the k-th terminal coronary artery,
w_{LV} : Left ventricular weight,
w_{ref} : Body weight of the reference subject,
w_{RV} : Right ventricular weight,
w_S : Septum weight,
x : Variable to define the distance between th heart and a generic arterial site,
x_m : m-th effector organ,
z : Axial coordinate,
Z_c : Characteristic impedance,
$Z_{ca,k}$: Characteristic impedance of the k-th terminal coronary artery,
$Z_{c,i}$: Characteristic impedance of the i-th distal artery,

$Z_{c,i\_HA/AL}$: Characteristic impedance of the i-th distal artery belonging to the HA/AL groups,
$Z_{cv,k}$: Characteristic impedance of the venula closing the k-th terminal coronary artery,
z_e : Coordinate of the e-th elemental region Ω_e,
z_e^l : Left coordinate of the e-th elemental region Ω_e,
z_e^r : Right coordinate of the e-th elemental region Ω_e,
α : Vector of weights for the 1D model
α^0 : Initial α
$\alpha_{1A/Q}$: Weights at node 1 of the e-th elemental region Ω_e for A and Q
$\alpha_{2A/Q}$: Weights at node 2 of the e-th elemental region Ω_e for A and Q
α^n : α at the n-th time step
$\alpha^{n+1/2}$: α at the $(n+1/2)$-th time step
α^{n+1} : α at the $(n+1)$-th time step
α_m : Weight of the sympathetic activity for the m-th efferent organ
α_v : Angle between the apothem and the vessel axis
α_{WN} : Womersley number
β : Coriolis coefficient
β_m : Weight of the parasympathetic activity for the m-th efferent organ
γ : Angle between the axial and horizontal directions
$\gamma_{CEP,j}$: Vector distributing p_{lv}/p_{rv} to the different layers in the definition of CEP
$\gamma_{C,j}$: Vector distributing $C_{1j,k}$ and $C_{3j,k}$ to the different layers
γ_E : Decay rate of the RR PDF in AF
γ_m : Constant in the calculation of the derivative $\dfrac{\mathrm{d}x_m}{\mathrm{d}t}$
$\gamma_{V0,j}$: Vector distributing $V_{0,1j,k}$ and $V_{0,3j,k}$ to the different layers
δ : Boundary layer thickness
δ_{Ω_e} : Boundary of the e-th elemental region,
Δ_p : Pressure gradient through a vessel, Variation in the mean pressure of a generic organ/vascular region,
Δ_Q : Mean flow rate through a vessel,
Δ_t : Time it takes for the minimum of the pressure wave to travel Δ_x,
ΔT : Time interval discretizing time vector $\mathbf{t}$,
Δ_V : Variation in the blood volume of a generic organ/vascular region,
Δ_x : Distance between two generic arterial sites,
θ_{va} : Opening angle of the generic cardiac valve,
θ_{max} : Maximum opening angle of the generic cardiac valve,
$\lambda_{1,2}$: Eigenvalues of matrix $\mathbf{H}$ - slopes of the charcateristic lines
$\lambda_{1n,2n}$: $\lambda_{1,2}$ at the n-th time step,
λ_{max} : Maximum eigenvalue of matrix $\mathbf{H}$,
$\bar{\mathbf{\Lambda}}$: Matrix of the eigenvalues $\lambda_{1,2}$,
$\bar{\mathbf{\Lambda}}_\mathbf{n}^*$: $\bar{\mathbf{\Lambda}}$ at the n-th time step and at the point $c\Delta T$ from the boundary,
$\bar{\mathbf{\Lambda}}_\mathbf{n}^{\mathbf{1}*}$: equal to $\bar{\mathbf{\Lambda}}_\mathbf{n}^*$,

$\bar{\mathbf{\Lambda}}_{\mathbf{n+1/2}}$: $\bar{\mathbf{\Lambda}}$ at the $(n+1)$-th time step,
μ : Dynamic viscosity of blood,
μ_E : Mean value of τ_E,
μ_G : Mean value of τ_G,
$\mu_{(p(t))}$: Average waveform of the pressure signal $p(t)$ over the recorded cardiac cycles,
μ_v : Mean value,
ν : Kinematic viscosity of blood,
ν_b : Parameter to define the steepness of n_s and n_p,
ξ : Non-dimensional form of z_e in the elemental region Ω_e,
ρ : Blood density
σ_E : Standard deviation of τ_E,
σ_G : Standard deviation of τ_G,
$\sigma_{p(t)}$: Standard deviation of the pressure signal $p(t)$ over the recorded cardiac cycles,
σQ_{LAD} : Standard deviation signal of a sequence of LAD flow rate waveforms,
σ_v : Standard deviation,
τ : Non-dimensional beating period,
τ_E : Interbeat time intervals extracted from an uncorrelated white noise-like Exponential distribution,
τ_G : Interbeat time intervals extracted from a pink noise-like Gaussian distribution,
τ_m : The time it takes for the efferent response to fully act,
ϕ : Azimuthal coordinate,
$\phi_{1/2}$: Trial function at node 1/2 of the e-th elemental region Ω_e,
ϕ_{SIP} : Constant in the definition of SIP,
ψ : Arbitrary test functions in the Discontinuous-Galerkin formulation,
$\psi_{\mathbf{h}}$: Discrete arbitrary test functions in the Discontinuous-Galerkin formulation,
ω : Cardiac pulsation,
Ω : Entire domain,
Ω_e : e-th elemental region,

Bibliography

[1] International Space Exploration Coordination Group (ISECG). *The global exploration roadmap*. International Space Exploration Coordination Group (ISECG), 2018.

[2] S.M. Abdullah et al. "Effects of prolonged space flight on cardiac structure and function". In: *Circulation* 128 (2013), A18672.

[3] S.R. Abram et al. "Quantitative circulatory physiology: an integrative mathematical model of human physiology for medical education". In: *Advances in Physiology Education* 31 (2007), pp. 202–210. DOI: 10.1152/advan.00114.2006.

[4] G. Seibert et al. *A world without gravity*. European Space Agency, 2001.

[5] J. Alastruey et al. "Modelling the circle of Willis to assess the effects of anatomical variations and occlusions on cerebral flows". In: *Journal of Biomechanics* 40 (2007), pp. 1794–1805. DOI: 10.1016/j.jbiomech.2006.07.008.

[6] J. Alastruey et al. "Pulse wave propagation in a model human arterial network: Assessment of 1-D visco-elastic simulations against *in vitro* measurements". In: *Journal of Biomechanics* 44 (2011), pp. 2250–2258. DOI: 10.1016/j.jbiomech.2011.05.041.

[7] P. Alboni et al. "Hemodynamics of idiopathic paroxysmal atrial fibrillation". In: *Pacing and Clinical Electrophysiology* 18 (1995), pp. 980–985. DOI: 10.1111/j.1540-8159.1995.tb04738.x.

[8] C.P. Alfrey et al. "Control of red blood cell mass in spaceflight". In: *Journal of Applied Physiology* 81 (1996), pp. 98–104. DOI: 10.1152/jappl.1996.81.1.98.

[9] D. Ambrosi et al. "Growth and remodelling of living tissues: perspectives, challenges and opportunities". In: *Journal of the Royal Socity Interface* 16 (2019), p. 20190233. DOI: 10.1098/rsif.2019.0233.

[10] J. Andrade et al. "The clinical profile and pathophysiology of atrial fibrillation - Relationships among clinical features, epidemiology, and mechanisms". In: *Circulation Research* 114 (2014), pp. 1453–1468. DOI: 10.1161/CIRCRESAHA.114.303211.

[11] E. Anter, M. Jessup, and D.J. Callans. "Atrial fibrillation and heart failure - Treatment considerations for a dual epidemic". In: *Circulation* 119 (2009), pp. 2516–2525. DOI: 10.1161/CIRCULATIONAHA.108.821306.

[12] G. Antonutto and P.E. di Prampero. "Cardiovascular deconditioning in microgravity: some possible countermeasures". In: *European Journal of Applied Physiology* 90 (2003), pp. 283–291. DOI: 10.1007/s00421-003-0884-5.

[13] C. Antzelevitch. "Basic mechanisms of reentrant arrhythmias". In: *Current Opinion in Cardiology* 16 (2001), pp. 1–7. DOI: 10.1097/00001573-200101000-00001.

[14] P. Arbeille et al. "Adaptation of the left heart, cerebral and femoral arteries, and jugular and femoral veins during short- and long-term head-down tilt and spaceflight". In: *European Journal of Applied Physiology* 86 (2001), pp. 157–168. DOI: 10.1007/s004210100473.

[15] P. Arbeille et al. "Cardiovascular adaptation to zero-G during a long-term flight (237 days) on board the Salyut-VII soviet space station (1984)". In: *European Space Agency Public* 271 (1987), pp. 134–146.

[16] V.G. Ardakani et al. "Near-wall flow in cerebral aneurysms". In: *Fluids* 4 (2019), p. 89. DOI: 10.3390/fluids4020089.

[17] A. Diaz Artiles, T. Heldt, and L.R. Young. "Computational model of cardiovascular response to centrifugation and lower body cycling exercise". In: *Journal of Applied Physiology* 127 (2019), pp. 1453–1468. DOI: 10.1152/japplphysiol.00314.2019.

[18] A.E. Aubert, F. Beckers, and B. Verheyden. "Cardiovascular function and basics of physiology in microgravity". In: *Acta Cardiologica* 60 (2005), pp. 129–151. DOI: 10.2143/AC.60.2.2005024.

[19] A.E. Aubert et al. "Towards human exploration of space: the THESEUS review series on cardiovascular, respiratory, and renal research priorities". In: *npj Microgravity* 2 (2016), p. 16031. DOI: 10.1038/npjmgrav.2016.31.

[20] A.P. Avolio. "Multi-branched model of the human arterial system". In: *Medical and Biological Engineering and Computing* 18 (1980), pp. 709–718. DOI: 10.1007/BF02441895.

[21] O. Bailliart et al. "Changes in lower limb volume in humans during parabolic flight," in: *Journal of Applied Physiology* 85 (1998), pp. 2100–2105. DOI: 10.1152/jappl.1998.85.6.2100.

[22] M.P. Baldo et al. "Carotid-femoral pulse wave velocity in a healthy adult sample: The ELSA-Brasil study". In: *International Journal of Cardiology* 251 (2018), pp. 90–95. DOI: 10.1016/j.ijcard.2017.10.075.

[23] E.J. Benjamin et al. “Impact of atrial fibrillation on the risk of death - The Framingham Heart Study”. In: *Circulation* 98 (1998), pp. 946–952. DOI: 10.1161/01.CIR.98.10.946.

[24] H.E. Berg et al. “Hip, thigh and calf muscle atrophy and bone loss after 5-week bedrest inactivity”. In: *European Journal of Applied Physiology* 99 (2007), pp. 283–289. DOI: 10.1007/s00421-006-0346-y.

[25] E. Berglund et al. “Effect of heart rate on cardiac work, myocardial oxygen consumption and coronary blood flow in the dog”. In: *Acta Physiologica Scandinavica* 42 (1958), pp. 185–198. DOI: 10.1111/j.1748-1716.1958.tb01551.x.

[26] D.A. Bertovic et al. “Muscular strength training is associated with low arterial compliance and high pulse pressure”. In: *Hypertension* 33 (1999), pp. 1385–1391. DOI: 10.1161/01.hyp.33.6.1385.

[27] J.G. Betts et al. *Anatomy & Physiology*. Openstax, 2013.

[28] E. Bianconi et al. “An estimation of the number of cells in the human body”. In: *Annals of Human Biology* 40 (2013), pp. 463–471. DOI: 10.3109/03014460.2013.807878.

[29] N. Bjarnegard and T. Länne. “Arterial properties along the upper arm in humans: age-related effects and the consequence of anatomical location”. In: *Journal of Applied Physiology* 108 (2010), pp. 34–38. DOI: 10.1152/japplphysiol.00479.2009.

[30] P.J. Blanco and R.A. Feijóo. “A dimensionally-heterogeneous closed-loop model for the cardiovascular system and its applications”. In: *Medical Engineering and Physics* 35 (2013), pp. 652–667. DOI: 10.1016/j.medengphy.2012.07.011.

[31] P.J. Blanco et al. “On the integration of the baroreflex control mechanism in a heterogeneous model of the cardiovascular system”. In: *International Journal for Numerical Methods in Biomedical Engineering* 28 (2012), pp. 412–433. DOI: 10.1002/cnm.1474.

[32] C.G. Blomqvist. “Regulation of the systemic circulation at microgravity and during redaptation to 1G”. In: *Medicine & Science in Sports & Exercise* 28 (1996), S9–S13. DOI: 10.1097/00005768-199610000-00025.

[33] M. Böhle et al. *Prandtl’s essentials of fluid mechanics*. 2nd ed. Springer, 2004.

[34] D. Du Bois and E.F. Du Bois. “A formula to estimate the approximate surface area if height and weight be known”. In: *Archives of internal Medicine* 17 (1916), pp. 863–871.

[35] C.P. Bolter and J.R. Ledsome. "Effect of cervical sympathetic nerve stimulation on canine carotid sinus reflex". In: *American Journal of Physiology* 230 (1976), pp. 1026–1030. DOI: 10.1152/ajplegacy.1976.230.4.1026.

[36] A. Borlotti et al. "Noninvasive determination of local pulse wave velocity and wave intensity: changes with age and gender in the carotid and femoral arteries of healthy human". In: *Journal of Applied Physiology* 113 (2012), pp. 727–735. DOI: 10.1152/japplphysiol.00164.2012.

[37] L.M. Van Bortel et al. "Expert consensus document on the measurement of aortic stiffness in daily practice using carotid-femoral pulse wave velocity". In: *Journal of Hypertension* 30 (2012), pp. 445–448. DOI: 10.1097/HJH.0b013e32834fa8b0.

[38] S. Boujena, O. Kafi, and N. E.l. Khatib. "A 2D mathematical model of blood flow and its Interactions in an atherosclerotic artery". In: *Mathematical Modelling of Natural Phenomena* 9 (2014), pp. 46–68. DOI: 10.1051/mmnp/20149605.

[39] P. Boutouyrie and S.J. Vermeersch. "Determinants of pulse wave velocity in healthy people and in the presence of cardiovascular risk factors: establishing normal and reference values". In: *European Heart Journal* 31 (2010), pp. 2338–2350. DOI: 10.1093/eurheartj/ehq165.

[40] P. Boutouyrie et al. "Opposing effects of ageing on distal and proximal large arteries in hypertensives". In: *Journal of Hypertension. Supplement: official journal of the International Society of Hypertension* 10 (1992), S87–S91. DOI: 10.1097/00004872-199208001-00023.

[41] M. Broomé et al. "Closed-loop real-time simulation model of hemodynamics and oxygen transport in the cardiovascular system". In: *BioMedical Engineering OnLine* 12 (2013), p. 69. DOI: 10.1186/1475-925X-12-69.

[42] J. Buckey. *Space physiology*. Oxford University Press, 2006.

[43] J.C. Buckey et al. "Central venous pressure in space". In: *Journal of Applied Physiology* 81 (1996), pp. 19–25. DOI: 10.1152/jappl.1996.81.1.19.

[44] J. Buss. "Limitation of body mass index to assess body fat". In: *Workplace Health & Safety* 62 (2014), p. 264. DOI: 10.1177/216507991406200608.

[45] The Society for Cardiovascular Angiography and Interventions. *What is atrial fibrillation (Afib or AF)?* URL: http://www.secondscount.org/heart-condition-centers/info-detail-2/what-is-atrial-fibrillation-afib-af#.XrEriC1aaJ8 (visited on 02/10/2020).

[46] C.G. Caro et al. *The mechanics of the circulation*. 2nd ed. Cambridge University Press, 2012.

[47] J.C. Chancellor, G.B.I. Scott, and J.P. Sutton. "Space radiation: The number one risk to astronaut health beyond low earth orbit". In: *Life (Basel)* 4 (2014), pp. 491–510. DOI: 10.3390/life4030491.

[48] J.B. Charles et al. *Cardiovascular Deconditioning*. URL: https://ntrs.nasa.gov/search.jsp?R=20040201532%202019-09-05T12:28:32+00:00Z (visited on 05/22/2020).

[49] H.Y. Chen et al. "Fluid–structure interaction (FSI) modeling in the cardiovascular system". In: *Computational Cardiovascular Mechanics* (2009), pp. 141–157. DOI: 10.1007/978-1-4419-0730-1_9.

[50] C.P. Cheng, R.J. Herfkens, and C.A. Taylor. "Inferior vena caval hemodynamics quantified in vivo at rest and during cycling exercise using magnetic resonance imaging". In: *American Journal of Physiology - Heart and Circulatory Physiology* 284 (2003), H1161–H1167. DOI: 10.1152/ajpheart.00641.2002.

[51] H.M. Cheng et al. "Measurement accuracy of noninvasively obtained central blood pressure by applanation tonometry: a systematic review and meta-analysis". In: *International Journal of Cardiology* 167 (2013), pp. 1867–1876. DOI: 10.1016/j.ijcard.2012.04.155.

[52] F. Chirillo et al. "Estimating mean pulmonary wedge pressure in patients with chronic atrial fibrillation from transthoracic doppler indexes of mitral and pulmonary venous flow velocity". In: *Journal of the American College of Cardiology* 30 (1997), pp. 19–26. DOI: 10.1016/s0735-1097(97)00130-7.

[53] N. Christensen, C. Drummer, and P. Norsk. "Renal and sympathoadrenal responses in space". In: *American Journal of Kidney Diseases* 38 (2001), pp. 679–683. DOI: 10.1053/ajkd.2001.27758.

[54] S.S. Chugh et al. "Worldwide epidemiology of atrial fibrillation - A global burden of disease 2010 study". In: *Citculation* 129 (2014), pp. 837–847. DOI: 10.1161/CIRCULATIONAHA.113.005119.

[55] D.M. Clark, V.J. Plumb adn A.E. Epstein, and G.N. Kay. "Hemodynamic effects of an irregular sequence of ventricular cycle lengths during atrial fibrillation". In: *Journal of the American College of Cardiology* 30 (1997), pp. 1039–1045. DOI: 10.1016/S0735-1097(97)00254-4.

[56] G. Clement. *Fundamentals of Space Medicine*. 2nd ed. Springer, 2011.

[57] V.A. Convertino, D.F. Doerr, and S.L. Stein. "Changes in size and compliance of the calf after 30 days of simulated microgravity". In: *Journal of Applied Physiology* 66 (1989), pp. 1509–1512. DOI: 10.1152/jappl.1989.66.3.1509.

[58] V.A. Convertino et al. “Changes in volume, muscle compartment, and compliance of the lower extremities in man following 30 days of exposure to simulated microgravity”. In: *Aviation Space and Enviromental Medicine* 60 (1989), pp. 653–658.

[59] R.J. Corliss et al. “Hemodynamics effects after conversion of arrhythmias”. In: *The Journal of Clinical Investigations* 47 (1968), pp. 1774–1786. DOI: 10.1172/JCI105867.

[60] M.Y. Cortez-Cooper et al. “Effects of High Intensity Resistance Training on Arterial Stiffness and Wave Reflection in Women”. In: *American Journal of Hypertension* 18 (2005), pp. 930–934. DOI: 10.1016/j.amjhyper.2005.01.008.

[61] E.F. Cox et al. “Multiparametric renal magnetic resonance imaging: validation, interventions, and alterations in chronic kidney disease”. In: *Frontiers in Physiology* 8 (2017), p. 696. DOI: 10.3389/fphys.2017.00696.

[62] R.H. Cox and R.J. Bagshaw. “Baroreceptor reflex control of arterial hemodynamics in the dog”. In: *Circulation Research* 37 (1975), pp. 772–786. DOI: 10.1161/01.RES.37.6.772.

[63] F.A. Cucinotta et al. “How safe is safe enough? Radiation risk for a human mission to Mars”. In: *Plos One* 8 (2013), e74988. DOI: 10.1371/journal.pone.0074988.

[64] J.S. Dahl et al. “Atrial fibrillation in severe aortic valve stenosis — association with left ventricular left atrial remodeling”. In: *IJC Heart & Vessels* 4 (2014), pp. 102–107. DOI: 10.1016/j.ijchv.2014.06.006.

[65] E.G. Daoud et al. “Effect of an irregular ventricular rhythm on cardiac output”. In: *American Journal of Cardiology* 78 (1996), pp. 1433–1436. DOI: 10.1016/s0002-9149(97)89297-1.

[66] A.E. Davis et al. “Observational study of regional, aortic size referenced to body size: production of a cardiovascular magnetic resonance nomogram”. In: *Journal of Cardiovascular Magnetic Resonance* 16 (2014), p. 9. DOI: 10.1186/1532-429X-16-9.

[67] P. Dorian et al. “The impairment of health-related quality of life in patients with intermittent atrial fibrillation: Implications for the assessment of investigational therapy”. In: *Journal of the American College of Cardiology* 36 (2000), pp. 1303–1309. DOI: 10.1016/s0735-1097(00)00886-x.

[68] A. Dueñas, A.E. Aranega, and F. Diego. “More than just a simple cardiac envelope; cellular contributions of the epicardium”. In: *Frontiers in Cell and Developmental Biology* 5 (2017), p. 44. DOI: 10.3389/fcell.2017.00044.

[69] N.T.L. van Duijnhoven et al. "The effect of bed rest and an exercise countermeasure on leg venous function". In: *European Journal of Applied Physiology* 104 (2008), pp. 991–998. DOI: 10.1007/s00421-008-0854-z.

[70] M. Durante and F. Cucinotta. "Heavy ion carcinogenesis and human space exploration". In: *Nature Reviews Cancer* 8 (2008), pp. 465–472. DOI: 10.1038/nrc2391.

[71] D.L. Eckberg et al. "Human vagal baroreflex mechanisms in space". In: *Journal of Physiology* 588 (2010), pp. 1129–1138. DOI: 10.1113/jphysiol.2009.186650.

[72] P. Eckerbom et al. "Multiparametric assessment of renal physiology in healthy volunteers using noninvasive magnetic resonance imaging". In: *American Journal of Physiology-Renal Physiology* 316 (2019), F693–F702. DOI: 10.1152/ajprenal.00486.2018.

[73] A. Einstein. *Investigation on the theory of the brownian movement*. Dover Publications, 1956.

[74] J.P. Ferreira and M. Santos. "Heart failure and atrial fibrillation: from basic science to clinical practice". In: *International Journal of Molecular Science* 16 (2015), pp. 3133–3147. DOI: 10.3390/ijms16023133.

[75] J. Fish and T. Belytschko. *A First Course in Finite Elements*. John Wiley & Sons, 2007.

[76] D. Fleischmann et al. "Quantitative determination of age-related geometric changes in the normal abdominal aorta". In: *Journal of Vascular Surgery* 33 (2001), pp. 97–105. DOI: 10.1067/mva.2001.109764.

[77] N. Foldager et al. "Central venous pressure in humans during microgravity". In: *Journal of Applied Physiology* 81 (1996), pp. 408–412. DOI: 10.1152/jappl.1996.81.1.408.

[78] I.O. Fomin et al. "[Effect of water immersion on indices of central hemodynamics in subjects older than 45 years]". In: *Kosmicheskaia Biologiia I Aviakosmicheskaia Meditsina* 19 (1985), pp. 37–40.

[79] G.A. Fomina, A.R. Kotovskaya, and E.V. Temnova. "Dynamics of human cardiovascular responses in different periods of long-term exposure to weightlessness". In: *Human Physiology* 38 (2012), pp. 715–720. DOI: 10.1134/S0362119712070080.

[80] L. Formaggia, D. Lamponi, and A. Quarteroni. "One-dimensional models for blood flow in arteries". In: *Journal of Engineering Mathematics* 47 (2003), pp. 251–276. DOI: 10.1023/B:ENGI.0000007980.01347.29.

[81] L. Formaggia et al. “Multiscale modelling of the circulatory system: a preliminary analysis”. In: *Computing and Visualization in Science* 2 (1999), pp. 75–83. DOI: 10.1007/s007910050030.

[82] L. Formaggia et al. “Numerical modeling of 1D arterial networks coupled with a lumped parameters description of the heart”. In: *Computer Methods in Biomechanics and Biomedical Engineering* 9 (2006), pp. 273–288. DOI: 10.1080/10255840600857767.

[83] J.-O. Fortrat et al. “Altered venous function during long-duration spaceflights”. In: *Frontiers in Physiology* 8 (2017), p. 694. DOI: 10.3389/fphys.2017.00694.

[84] O. Frank. “Die Grundform des Arteriellen Pulses”. In: *Zeitschrift für Biologie* 37 (1899), pp. 483–526.

[85] S.S. Franklin et al. “Hemodynamic patterns of age-related changes in blood pressure. The Framingham Heart Study”. In: *Circulation* 96 (1997), pp. 308–315. DOI: 10.1161/01.CIR.96.1.308.

[86] J.M. Fritsch-Yelle et al. “Microgravity decreases heart rate and arterial pressure in humans”. In: *Journal of Applied Physiology* 80 (1996), pp. 910–914. DOI: 10.1152/jappl.1996.80.3.910.

[87] H.M. Frost. “Bone’s mechanostat: a 2003 update”. In: *The Anatomical Record Part A Discoveries in Molecular Cellular and Evolutionary Biology* 275 (2003), pp. 1081–1101. DOI: 10.1002/ar.a.10119.

[88] Q. Fu et al. “Impact of prolonged spaceflight on orthostatic tolerance during ambulation and blood pressure profiles in astronauts”. In: *Circulation* 140 (2019), pp. 729–738. DOI: 10.1161/CIRCULATIONAHA.119.041050.

[89] F.A. Gaffney et al. “Cardiovascular deconditioning produced by 20 hours of bedrest with head-down tilt (-5 degrees) in middle-aged healthy men”. In: *American Journal of Cardiology* 56 (1985), pp. 634–638. DOI: 10.1016/0002-9149(85)91025-2.

[90] K.M. Gallagher et al. “Effects of exercise pressor reflex activation on carotid baroreflex function during exercise in humans”. In: *The Journal of Physiology* 533 (2001), pp. 871–880. DOI: 10.1111/j.1469-7793.2001.t01-2-00871.x.

[91] C. Gallo, L. Ridolfi, and S. Scarsoglio. “A closed-loop multiscale model of the cardiovascular system: application to heart pacing and open-loop response”. In: *IFMBE Proceedings* 76 (2020), pp. 577–585. DOI: 10.1007/978-3-030-31635-8_69.

[92] C. Gallo, L. Ridolfi, and S. Scarsoglio. “Cardiovascular deconditioning during long-term spaceflight through multiscale modeling”. In: *npj Microgravity* 6 (2020), p. 27. DOI: 10.1038/s41526-020-00117-5.

[93] C. Gallo, L. Ridolfi, and S. Scarsoglio. "Effects of atrial fibrillation on the coronary flow at different heart rates: a computational approach". In: *Computing in Cardiology* 45 (2018), pp. 1–4. DOI: 10.22489/CinC.2018.130.

[94] C. Gallo et al. "Testing a patient-specific in-silico model to noninvasively estimate central blood pressure". In: *Cardiovascular Engineering and Technology* ().

[95] I.C. Van Gelder et al. "Lenient versus strict rate control in patients with atrial fibrillation". In: *The New England Journal of Mediine* 362 (2010), pp. 1363–1373. DOI: 10.1056/NEJMoa1001337.

[96] P.J. Gentlesk et al. "Reversal of left ventricular dysfunction following ablation or atrial fibrillation". In: *Journal of Cardiovascular Electrophysiology* 18 (2007), pp. 9–14. DOI: 10.1111/j.1540-8167.2006.00653.x.

[97] National Geographic. *Heart - The heart is one of the body's most essential organs*. URL: https://www.nationalgeographic.com/science/health-and-human-body/human-body/heart/ (visited on 01/28/2020).

[98] B. Gerber et al. "A computer simulation of short-term adaptations of cardiovascular hemodynamics in microgravity". In: *Computers in Biology and Medicine* 102 (2018), pp. 86–94. DOI: 10.1016/j.compbiomed.2018.09.014.

[99] C. Giglioli et al. "Hemodynamic effects in patients with atrial fibrillation submitted to electrical cardioversion". In: *International Journal of Cardiology* 168 (2013), pp. 4447–4450. DOI: 10.1016/j.ijcard.2013.06.150.

[100] A.L. Goldberger et al. "PhysioBank, PhysioToolkit, and PhysioNet: components of a new research resource for complex physiologic signals". In: *Circulation* 101 (2000), E215–220. DOI: 10.1161/01.cir.101.23.e215.

[101] R.A. Gray and P. Pathmanathan. "Patient-specific cardiovascular computational modeling: diversity of personalization and challenges". In: *Journal of Cardiovascular Translational Research* 11 (2018), pp. 80–88. DOI: 10.1007/s12265-018-9792-2.

[102] L.J. Greaney and W.B. Farquhar. "Why do veins stiffen with advancing age?" In: *Journal of Applied Physiology* 110 (2011), pp. 11–12. DOI: 10.1152/japplphysiol.01273.2010.

[103] D.J. Green et al. "Impact of age, sex and exercise on brachial and popliteal artery remodelling in humans". In: *Atherosclerosis* 210 (2010), pp. 525–530. DOI: 10.1016/j.atherosclerosis.2010.01.048.

[104] A.I. Grigoriev, A.R. Kotovskaya, and G.A. Fomina. "The human cardiovascular system during space flight". In: *Acta Astronautica* 68 (2011), pp. 1495–1500. DOI: 10.1016/j.actaastro.2009.11.013.

[105] A.I. Grigoriev et al. "[Clinical and physiological evaluation of bone changes among astronauts after long-term space flights]". In: *Aviakosmicheskaia i Ekologicheskaia Meditsina* 32 (1998), pp. 21–25.

[106] A. Guala, C. Camporeale, and L. Ridolfi. "Compensatory effect between aortic stiffening and remodelling during ageing". In: *PLOS ONE* 10 (2015), e0139211. DOI: 10.1371/journal.pone.0139211.

[107] A. Guala, M. Scalseggi, and L. Ridolfi. "Coronary fluid mechanics in an ageing cardiovascular system". In: *Meccanica* 52 (2015), pp. 503–514. DOI: 10.1007/s11012-015-0283-0.

[108] A. Guala et al. "Modelling and subject-specific validation of the heart-arterial tree system". In: *Annals of Biomedical Engineering* 43 (2015), pp. 222–237. DOI: 10.1007/s10439-014-1163-9.

[109] H.-C. Gunga et al. *Cardiovascular system, red blood cells, and oxygen transport in microgravity*. Springer, 2016.

[110] A.C. Guyton, T.G. Coleman, and H.J. Grancer. "Circulation: overall regulation". In: *Annual Review of Physiology* 34 (1972), pp. 13–44. DOI: 10.1146/annurev.ph.34.030172.000305.

[111] A. Hager et al. "Diameters of the thoracic aorta throughout life as measured with helical computed tomography". In: *Surgery for Acquired Cardiovascular Disease* 123 (2002), pp. 1060–1066. DOI: 10.1067/mtc.2002.122310.

[112] P.B. Halmos and C.G. Patterson. "Effect of atrial fibrillation on cardiac output". In: *British Heart Journal* 27 (1965), pp. 719–723. DOI: 10.1136/hrt.27.5.719.

[113] D.R. Hamilton et al. "On-orbit prospective echocardiography on international space station crew". In: *Echocardiography* 28 (2011), pp. 491–501. DOI: 10.1111/j.1540-8175.2011.01385.x.

[114] F. Hansen et al. "Diameter and compliance in the human common carotid artery - variations with age and sex". In: *Ultrasound in Medicine & Biology* 21 (1995), pp. 1–9. DOI: 10.1016/0301-5629(94)00090-5.

[115] J. Hayano et al. "Spectral characteristics of ventricular response to atrial fibrillation". In: *American Journal of Physiology - Heart and Circulatory Physiology* 273 (1997), H2811–H2816. DOI: 10.1152/ajpheart.1997.273.6.H2811.

[116] M. Heer and W.H. Paloski. "Space motion sickness: Incidence, etiology, and countermeasures". In: *Autonomic Neuroscience* 129 (2006), pp. 77–79. DOI: 10.1016/j.autneu.2006.07.014.

[117] S.T. Heidt et al. “Symptoms in atrial fibrillation: A contemporary review and future directions”. In: *Journal of Atrial Fibrillation* 9 (2016), p. 1422. DOI: 10.4022/jafib.1422.

[118] J. Heijman et al. “Cellular and molecular electrophysiology of atrial fibrillation initiation, maintenance, and progression”. In: *Circulation Research* 114 (2014), pp. 1483–1499. DOI: 10.1161/CIRCRESAHA.114.302226.

[119] T. Heldt. “Computational models of cardiovascular response to orthostatic stress (Ph.D thesis)”. In: (2004).

[120] T. Heldt et al. “Computational modeling of cardiovascular response to orthostatic stress”. In: *Journal of Applied Physiology* 92 (2002), pp. 1239–1254. DOI: 10.1152/japplphysiol.00241.2001.

[121] H.K. Hellerstein and M. Santiago-Stevensos. “Atrophy of the heart: a correlative study of eighty-five proved cases”. In: *Circulation* 1 (1950), pp. 93–126. DOI: 10.1161/01.CIR.1.1.93.

[122] T. Hennig et al. “Exponential distribution of long heart beat intervals during atrial fibrillation and their relevance for white noise behaviour in power spectrum”. In: *Journal of Biological Physics | Home - Springer* 32 (2006), pp. 383–392. DOI: 10.1007/s10867-006-9022-z.

[123] W.L. Henry et al. “Effect of prolonged space flight on cardiac functions and dimensions”. In: *The American Journal of cardiology* 35 (1975), p. 143. DOI: 10.1016/0002-9149(75)90678-5.

[124] S. Herault et al. “Cardiac, arterial and venous adaptation to weightlessness during 6-month MIR space flights with and without thigh cuffs (bracelets)”. In: *European Journal of Applied Physiology* 81 (2000), pp. 384–390. DOI: 10.1007/s004210050058.

[125] S.S. Hickson et al. “The relationship of age with regional aortic stiffness and diameter”. In: *Journal of the American College of Cardiology - Cardiovascular Imaging* 3 (2010), pp. 1247–1255. DOI: 10.1016/j.jcmg.2010.09.016.

[126] H. Hinghofer-Szalkay. “Gravity, the hydrostatic indifference concept and the cardiovascular system”. In: *European Journal of Applied Physiology* 111 (2011), pp. 163–174. DOI: 10.1007/s00421-010-1646-9.

[127] G. Howard et al. “Carotid artery intimal-media thickness distribution in general populations as evaluated by B-mode ultrasound”. In: *Stroke* 24 (1993), pp. 1297–1304. DOI: 10.1161/01.str.24.9.1297.

[128] L.E. Hudsmith et al. “Normal human left and right ventricular and left atrial dimensions using steady state free precession magnetic resonance imaging”. In: *Journal of Cardiovascular Magnetic Resonance* 7 (2005), pp. 775–782. DOI: 10.1080/10976640500295516.

[129] R.L. Hughson, A. Helm, and Durante M. "Heart in space: effect of the extraterrestrial environment on the cardiovascular system". In: *Nature Reviews Cardiology* 15 (2018), pp. 167–180. DOI: 10.1038/nrcardio.2017.157.

[130] R.L. Hughson et al. "Cardiac output by pulse contour analysis does not match the increase measured by rebreathing during human spaceflight". In: *Journal of Applied Physiology* 123 (2017), pp. 1145–1149. DOI: 10.1152/japplphysiol.00651.2017.

[131] R.L. Hughson et al. "Cardiovascular regulation during long-duration spaceflights to the International Space Station". In: *Journal of Applied Physiology* 112 (2012), pp. 719–727. DOI: 10.1152/japplphysiol.01196.2011.

[132] T. Jämsä et al. "Effect of daily physical activity on proximal femur". In: *Clinical biomechanics (Bristol, Avon)* 21 (2005), pp. 1–7. DOI: 10.1016/j.clinbiomech.2005.10.003.

[133] C.T. January et al. "2014 AHA/ACC/HRS Guideline for the management of patients with atrial fibrillation: Executive summary". In: *Circulation* 130 (2014), pp. 2071–2104. DOI: 10.1161/CIR.0000000000000040.

[134] S.S. Jarvis and J.A. Pawelczyk. "Identification of the human electrical impedance indifferent point: a surrogate for the volume indifferent point?" In: *European Journal of Applied Physiology* 107 (2009), pp. 473–480. DOI: 10.1007/s00421-009-1148-9.

[135] S.S. Jarvis and J.A. Pawelczyk. "The location of the human volume indifferent point predicts orthostatic tolerance". In: *European Journal of Applied Physiology* 109 (2010), pp. 331–341. DOI: 10.1007/s00421-009-1336-7.

[136] O. Kafi et al. "Numerical Simulations of a 3D fluid-structure interaction model for blood flow in an atherosclerotic artery". In: *Mathematical Bioscience and Engineering* 14 (2017), pp. 179–193. DOI: 10.3934/mbe.2017012.

[137] V.S. Kaliujnaya and S.I. Kalyuzhny. "The assessment of blood pressure in atrial fibrillation". In: *Computational Cardiology* 32 (2005), pp. 387–390. DOI: 10.1109/CIC.2005.1588093.

[138] H. Kamel et al. "Atrial fibrillation and mechanisms of stroke - Time for a new model". In: *Stroke* 47 (2016), pp. 895–900. DOI: 10.1161/STROKEAHA.115.012004.

[139] A.V. Kamenskiy et al. "Age and disease-related geometric and structural remodeling of the carotid artery". In: *Journal of vascular surgery* 62 (2015), pp. 1521–1528. DOI: 10.1016/j.jvs.2014.10.041.

[140] J.M. Karemaker and J. Berecki-Gisolf. "24-h blood pressure in space: the dark side of being an astronaut". In: *Respiratory Physiology and Neurobiology* 169 (2009), S55–S58. DOI: 10.1016/j.resp.2009.05.006.

[141] M. Kavousi. "Differences in epidemiology and risk factors for atrial fibrillation between women and men". In: *Frontiers in Cardiovascular Medicine* 7 (2020), p. 3. DOI: 10.3389/fcvm.2020.00003.

[142] E.L. Kerstman et al. "Space adaptation back pain: A retrospective study". In: *Aviation Space and Enviromental Medicine* 83 (2012), pp. 2–7. DOI: 10.3357/asem.2876.2012.

[143] F. Khaja and J.O. Parker. "Hemodynamics effects of cardioversion in chronic atrial fibrillation". In: *Archives of Internal Medicine* 129 (1972), pp. 433–440. DOI: 10.1001/archinte.1972.00320030053005.

[144] T. Killip and R.A. Baer. "Hemodynamics effects after reversion from atrial fibrillation to sinus rhythm by precordial shock". In: *The Journal of Clinical Investigations* 45 (1966), pp. 658–671. DOI: 10.1172/JCI105381.

[145] C.S. Kim et al. "Numerical models of human circulatory system under altered gravity: Brain circulation". In: *42nd AIAA Aerospace Sciences Meeting and Exhibit* 42 (2005), pp. 6794–6806. DOI: 10.2514/6.2004-1092.

[146] K.A. Kirsch et al. "Venous pressure in man during weightlessness". In: *Science* 225 (1984), pp. 218–219. DOI: 10.1126/science.6729478.

[147] Y. Kivity and R. Collins. "Nonlinear wave propagation in viscoelastic tubes: application to aortic rupture". In: *Journal of Biomechanics* 7 (1974), pp. 67–76. DOI: 10.1016/0021-9290(74)90071-2.

[148] R.E. Klabunde. *Cardiovascular physiology concepts*. 2nd ed. Lippincott Williams & Wilkins, 2012.

[149] W.M. Klein et al. "Magnetic resonance imaging measurement of blood volume flow in peripheral arteries in healthy subjects". In: *Journal of Vascular Surgery* 38 (2003), pp. 1060–1066. DOI: 10.1016/S0741-5214(03)00706-7.

[150] M. Kobayashi and T. Musha. "1/f Fluctuation of Heartbeat Period". In: *IEEE Transaction on Biomedical Engineering* 29 (1982), pp. 456–457. DOI: 10.1109/TBME.1982.324972.

[151] G.E. Kochiadakis and E.M. Kallergis. "Impact of atrial fibrillation on coronary blood flow: A systematic review". In: *Journal of Atrial Fibrillation* 5 (2012), pp. 161–165. DOI: 10.4022/jafib.458.

[152] G.E. Kochiadakis et al. "Effect of acute atrial fibrillation on phasic coronary blood flow pattern and flow reserve in humans". In: *European Heart Journal* 23 (2002), pp. 734–741. DOI: 10.1053/euhj.2001.2894.

[153] B.M. Koeppen and B.A. Stanton. *Berne & Levy Physiology*. 6th ed. Elsevier, 2009.

[154] I. Kokalari, T. Karaja, and M. Guerrisi. "Review on lumped parameter method for modeling the blood flow in systemic arteries". In: *Journal of Biomedical Science and Engineering* 6 (2013), pp. 92–99. DOI: 10.4236/jbise.2013.61012.

[155] T. Korakianitis and Y. Shi. "A concentrated parameter model for the human cardiovascular system including heart valve dynamics and atrioventricular interaction". In: *Medical Engineering & Physics* 28 (2006), pp. 613–628. DOI: 10.1016/j.medengphy.2005.10.004.

[156] T. Korakianitis and Y. Shi. "Numerical simulation of cardiovascular dynamics with healthy and diseased heart valves". In: *Journal of Biomechanics* 39 (2006), pp. 1964–1982. DOI: 10.1016/j.jbiomech.2005.06.016.

[157] A.R. Kotovskaya and G.A. Fomina. "Human venous hemodynamics in microgravity and prediction of orthostatic tolerance in flight". In: *Human Physiology* 41 (2015), pp. 699–703. DOI: 10.1134/S0362119715070063.

[158] S. Kralev et al. "Incidence and severity of coronary artery disease in patients with atrial fibrillation undergoing first-time coronary angiography". In: *Plos One* 6 (2011), e24964. DOI: 10.1371/journal.pone.0024964.

[159] J. Krejza et al. "Carotid artery diameter in men and women and the relation to body and neck size". In: *Stroke* 37 (2006), pp. 1103–1105. DOI: 10.1161/01.STR.0000206440.48756.f7.

[160] E.J. Kroeker and E.H. Hood. "Comparison of simultaneously recorded central and peripheral arterial pressure pulses during rest, exercise and tilted position in man". In: *Circulation Research* 3 (1955), pp. 623–632. DOI: 10.1161/01.RES.3.6.623.

[161] D.N. Ku. "Blood flow in arteries". In: *Annual Review of Fluid Mechanics* 29 (1997), pp. 399–434. DOI: 10.1146/annurev.fluid.29.1.399.

[162] J.P. Kuhtz-Buschbeck et al. "Rediscovery of Otto Frank's contribution to sciences". In: *Journal of Molecular and Cellular Cardiology* 119 (2018), pp. 96–103. DOI: 10.1016/j.yjmcc.2018.04.017.

[163] W.D. Lakin, S.A. Stevens, and P.L. Penar. "Modeling intracranial pressures in microgravity: the influence of the blood-brain barrier". In: *Aviation Space and Environmental Medicine* 78 (2007), pp. 932–936. DOI: 10.3357/asem.2060.2007.

[164] R. Lampe et al. "Mathematical modelling of cerebral blood circulation and cerebral autoregulation: towards preventing intracranial hemorrhages in preterm newborns". In: *Computational and Mathematical Methods in Medicine* 2014 (2014), p. ID 965275. DOI: 10.1155/2014/965275.

[165] T. Lang et al. “Cortical and trabecular bone mineral loss from the spine and hip in long-duration spaceflight”. In: *Journal of Bone and Mineral Research* 19 (2004), pp. 1006–1012. DOI: 10.1359/JBMR.040307.

[166] C. Langenberg et al. “Influence of height, leg and trunk length on pulse pressure, systolic and diastolic blood pressure”. In: *Journal of Hypertension* 21 (2003), pp. 537–543. DOI: 10.1097/00004872-200303000-00019.

[167] C. Langenberg et al. “Influence of short stature on the change in pulse pressure, systolic and distolic blood pressure from age 35 to 53 years: an analysis using multilevel models”. In: *International Journal of Epidemiology* 34 (2005), pp. 905–913. DOI: 10.1093/ije/dyi071.

[168] D.H. Lau et al. “Modifiable risk factors and atrial fibrillation”. In: *Circulation* 136 (2017), pp. 583–596. DOI: 10.1161/CIRCULATIONAHA.116.023163.

[169] E.M.T. Lau et al. In: *European Respiratory Journal* 47 (2016), pp. 1436–1444. DOI: 10.1183/13993003.01684-2015.

[170] S. Laurent, J. Sharman, and P. Boutouyrie. “Central versus peripheral blood pressure: finding a solution”. In: *Journal of Hypertension* 34 (2016), pp. 1497–1499. DOI: 10.1097/HJH.0000000000001000.

[171] J.S. Lawley et al. “Effect of gravity and microgravity on intracranial pressure”. In: *Journal of Physiology* 595 (2017), pp. 2115–2127. DOI: 10.1113/JP273557.

[172] V. Lebedev. *Diary of a cosmonaut: 211 days in space*. PhytoResource Research, 1988.

[173] A. LeBlanc, L. Shackelford, and V. Schneider. “Future human bone research in space”. In: *Bone* 22 (1998), 113S–116S. DOI: 10.1016/S8756-3282(98)00013-1.

[174] S.M.C. Lee et al. “Orthostatic intolerance after ISS and space shuttle missions”. In: *Aerospace Medicine and Human Performance* 86 (2015), A54–A67. DOI: 10.3357/AMHP.EC08.2015.

[175] P.J. Lees. “Cardiology in space”. In: *Hellenic Journal of Cardiology* 46 (2005), pp. 320–323.

[176] R.W. Leggett and Williams LR. “Suggested reference values for regional blood volumes in humans”. In: *Health Physics* 60 (1991), pp. 139–154. DOI: 10.1097/00004032-199102000-00001.

[177] J.R. Levick. *An introduction to Cardiovascular physiology*. Butterworths, 1991.

[178] B.D. Levine, J.H. Zuckerman, and J.A. Pawelczyk. “Cardiac atrophy after bed-rest deconditioning”. In: *Circulation* 96 (1997), pp. 517–525. DOI: 10.1161/01.cir.96.2.517.

[179] B. Lewandowski et al. “Risk assessment of bone fracture during space exploration missions to the Moon and Mars”. In: *Space Systems Engineering and Risk Management Symposium* (2008).

[180] F. Liang et al. “Multi-scale modeling of the human cardiovascular system with applications to aortic valvular and arterial stenoses”. In: *Medical & Biological Engineering & Computing* 47 (2009), pp. 743–755. DOI: 10.1007/s11517-009-0449-9.

[181] F.Y. Liang et al. “Biomechanical characterization of ventricular–arterial coupling during aging: a multi-scale model study”. In: *Journal of Biomechanics* 42 (2009), pp. 692–704. DOI: 10.1016/j.jbiomech.2009.01.010.

[182] H.-L. Liang. “Doppler flow measurement of lower extremity arteries adjusted by pulsatility index”. In: *American Journal of Roentgenology* 214 (2020), pp. 10–17. DOI: 10.2214/AJR.19.21280.

[183] J. Lighthill. *Mathematical Biofluiddynamics*. Society for Industrial and Applied Mathematics, 1975.

[184] J.M. Linenger. *Off the planet*. McGraw-Hill, 2000.

[185] J. Liu et al. “Patient-specific oscillometric blood pressure measurement”. In: *IEEE Transactions on Biomedical Engineering* 63 (2016), pp. 1220–1228. DOI: 10.1109/TBME.2015.2491270.

[186] V.I. Lobachik et al. “Hemodynamic effects of microgravity and their ground-based simulation”. In: *Acta Astronautica* 23 (1991), pp. 35–40. DOI: 10.1016/0094-5765(91)90097-o.

[187] G.M. London et al. “Influence of sex on arterial hemodynamics and blood pressure: role of body height”. In: *Hypertension* 26 (1995), pp. 514–519. DOI: 10.1161/01.hyp.26.3.514.

[188] A. Lopez-Perez, R. Sebastian, and J.M. Ferrero. “Three-dimensional cardiac computational modelling: methods, features and applications”. In: *BioMedical Engineering OnLine* 14 (2015), p. 35. DOI: 10.1186/s12938-015-0033-5.

[189] C.H. Lorenz et al. “Normal human right and left ventricular mass, systolic function, and gender differences by cine magnetic resonance imaging”. In: *Cardiovascular Magnetic Resonance* 1 (1999), pp. 7–21. DOI: 10.3109/10976649909080829.

[190] C. Loudon and A. Tordesillas. “The use of the dimensionless Womersley number to characterize the unsteady nature of internal flow”. In: *Journal of Theoretical Biology* 191 (1998), pp. 63–78. DOI: 10.1006/jtbi.1997.0564.

[191] C. Luo et al. "Documentation of impaired coronary blood flow by TIMI frame count method in patients with atrial fibrillation". In: *International Journal of Cardiology* 167 (2013), pp. 1176–1180. DOI: 10.1016/j.ijcard.2012.03.118.

[192] C. Luo et al. "Predictive value of coronary blood flow for future cardiovascular events in patients with atrial fibrillation". In: *International Journal of Cardiology* 177 (2014), pp. 545–547. DOI: 10.1016/j.ijcard.2014.08.102.

[193] S.-M. Ma et al. "The age correlation of the carotid intima-media thickness according to sex and side in asymptomatic subjects". In: *Acta Neurologica Taiwanica* 20 (2011), pp. 29–34. DOI: 10.29819/ANT.201103.0005.

[194] B.R. Macias et al. *ntracranial Pressure and Its Effect on Vision in Space and on Earth: Vision Impairment in Space*. World Scientific, 2017.

[195] S. Magder. "Volume and its relationship to cardiac output and venous return". In: *Critical Care* 20 (2016), p. 271. DOI: 10.1186/s13054-016-1438-7.

[196] W.H Maisel and L.W. Stevenson. "Atrial fibrillation in heart failure: epidemiology, pathophysiology, and rationale for therapy". In: *The American Journal of Cardiology* 91 (2003), pp. 2–8. DOI: 10.1016/S0002-9149(02)03373-8.

[197] J. Malmivuo and R. Plonsey. *Bioelectromagnetism - Principles and applications of bioelectric and biomagnetic fields*. Oxford University Press, 1985.

[198] A.W.C. Man and C.M. Wang. "Age-associated arterial remodelling". In: *ECronicon Cardiology* 4 (2017), pp. 137–164.

[199] K. Marshall-Goebel et al. "Assessment of jugular venous blood flow stasis and thrombosis during spaceflight". In: *JAMA Network Open* 2 (2019), e1915011. DOI: 10.1001/jamanetworkopen.2019.15011.

[200] D.S. Martin et al. "Comparison of echocardiographic changes after short- and long-duration spaceflight". In: *Aviation Space and Enviromental Medicine* 73 (2002), pp. 532–536.

[201] D.S. Martin et al. *Comparison of echocardiographic measurements before and after short and long duration spaceflight*. URL: https://ntrs.nasa.gov/search.jsp?R=20100029745 (visited on 05/22/2020).

[202] D.S. Martin et al. "Internal jugular pressure increases during parabolic flight". In: *Physiological Reports* 4 (2016), e13068. DOI: 10.14814/phy2.13068.

[203] R.I.R. Martin and M.G.D. Bates. "Management of atrial fibrillation and concomitant coronary artery disease". In: *Continuing Cardiology Education* 3 (2017), pp. 47–55. DOI: 10.1002/cce2.55.

[204] E.S. Di Martino et al. "Fluid–structure interaction within realistic three-dimensional models of the aneurysmatic aorta as a guidance to assess the risk of rupture of the aneurysm". In: *Medical Engineering & Physics* 23 (2001), pp. 647–655. DOI: 10.1016/s1350-4533(01)00093-5.

[205] K.S. Matthys et al. "Pulse wave propagation in a model human arterial network: Assessment of 1-D numerical simulations against *in vitro* measurements". In: *Journal of Biomechanics* 40 (2007), pp. 3476–3486. DOI: 10.1016/j.jbiomech.2007.05.027.

[206] M.A. McDonald. *Blood flow in arteries*. Edward Arnold, 1974.

[207] C.M. McEniery et al. "Central blood pressure: current evidence and clinical importance". In: *European Heart Journal* 35 (2014), pp. 1719–1725. DOI: 10.1093/eurheartj/eht565.

[208] C.M. McEniery et al. "Central pressure: variability and impact of cardiovascular risk factors: the Anglo-Cardiff Collaborative Trial II". In: *Hypertension* 51 (2008), pp. 1476–1482. DOI: 10.1161/HYPERTENSIONAHA.107.105445.

[209] McGraw-Hill. *McGraw-Hill encyclopedia of science and technology*. 11th ed. McGraw-Hill, 2012.

[210] E. Michniewicz et al. "Patients with atrial fibrillation and coronary artery disease - Double trouble". In: *Advances in Medical Sciences* 63 (2018), pp. 30–35. DOI: 10.1016/j.advms.2017.06.005.

[211] L.R. Mikael et al. "Vascular ageing and arterial stiffness". In: *Arquivos Brasileiros De Cardiologia* 20 (2011), pp. 29–34. DOI: 10.5935/abc.20170091.

[212] D.E. Miller et al. "Effect of ventricular rate on the cardiac output in the dog with chronic heart block". In: *Circulation Research* 10 (1962), pp. 658–663. DOI: 10.1161/01.RES.10.4.658.

[213] M. Miyachi et al. "Greater age-related reductions in central arterial compliance in resistance-trained men". In: *Hypertension* 41 (2003), pp. 130–135. DOI: 10.1161/01.hyp.0000047649.62181.88.

[214] K.D. Monahan et al. "Smaller age-associated reductions in leg venous compliance in endurance exercise-trained men". In: *American Journal of Physiology - Heart and Circulation Physiology* 281 (2001), H1267–H1273. DOI: 10.1152/ajpheart.2001.281.3.H1267.

[215] G.L. Moneta et al. "Duplex ultrasound measurement of postprandial intestinal blood flow: effect of meal composition". In: *Gastroenterology* 95 (1988), pp. 1294–1301. DOI: 10.1016/0016-5085(88)90364-2.

[216] L.D. Montgomery. "Body volume changes during microgravity II: comparison of horizontal and head-down bed rest". In: *Aviation Space and Enviromental Medicine* 64 (1993), pp. 899–904.

[217] L.D. Montgomery, A.J. Parmet, and C.R. Booher. "Body volume changes during simulated microgravity: auditory changes, segmental fluid redistribution, and regional hemodynamics". In: *Annals of Biomedical Engineering* 21 (1993), pp. 417–433. DOI: 10.1007/BF02368634.

[218] S.M. Moore et al. "One-dimensional and three-dimensional models of cerebrovascular flow". In: *Journal of Biomechanical Engineering* 127 (2004), pp. 440–449. DOI: 10.1115/1.1894350.

[219] T.P. Moore and W.E. Thornton. "Space shuttle inflight and postflight fluid shifts measured by leg volume changes". In: *Aviation Space and Enviromental Medicine* 58 (1987), A91–A96.

[220] P.D. Morris et al. "Computational fluid dynamics modelling in cardiovascular medicine". In: *Heart* 102 (2016), pp. 18–28. DOI: 10.1136/heartjnl-2015-308044.

[221] R.D. Mosteller. "Simplified calculation of body surface area". In: *The New England Journal of Medicine* 317 (1987), p. 1098. DOI: 10.1056/NEJM198710223171717.

[222] L.O. Müller and E.F. Toro. "A global multiscale mathematical model for the human circulation with emphasis on the venous system". In: *International Journal for Numerical Methods in Biomedical Engineering* 30 (2014), pp. 681–725. DOI: 10.1002/cnm.2622.

[223] J.P. Murgo et al. "Aortic input impedance in normal man: relationship to pressure wave forms". In: *Circulation* 62 (1980), pp. 105–116. DOI: 10.1161/01.CIR.62.1.105.

[224] J.P. Mynard. "Computer modelling and wave intensity analysis of perinatal cardiovascular function and dysfunction". In: *PhD Thesis, Department of Paediatrics and Heart Research Group, Murdoch Childrens Research Institute, The University of Melbourne* (2011).

[225] J.P. Mynard and P. Nithiarasu. "A 1D arterial blood flow model incorporating ventricular pressure, aortic valve and regional coronary flow using the locally conservative Galerkin (LCG) method". In: *Communications in Numerical Methods and Engineering* 24 (2008), pp. 367–417. DOI: 10.1002/cnm.1117.

[226] J.P. Mynard, D.J. Penny, and J.J. Smolich. "Scalability and in vivo validation of a multiscale numerical model of the left coronary circulation". In: *American Journal of Physiology Heart and Circulatory Physiology* 306 (2014), H517–H528. DOI: 10.1152/ajpheart.00603.2013.

[227] J.P. Mynard and J.J. Smolich. "One-dimensional haemodynamic modeling and wave dynamics in the entire adult circulation". In: *Annals of Biomedical Engineering* 43 (2015), pp. 1443–1460. DOI: 10.1007/s10439-015-1313-8.

[228] J.P. Mynard et al. “A simple, versatile valve model for use in lumped parameter and one-dimensional cardiovascular models”. In: *International Journal for numerical methods in Biomedical Engineering* 28 (2012), pp. 626–641. DOI: 10.1002/cnm.1466.

[229] NASA. *Anthropometric source book - Volume I: anthropometry for designers*. URL: https://ntrs.nasa.gov/search.jsp?R=19790003563 (visited on 05/28/2020).

[230] K. Natarajan et al. “Central blood pressure monitoring via a standard automatic arm cuff”. In: *Scientific Report* 7 (2017), p. 14441. DOI: 10.1038/s41598-017-14844-5.

[231] S. Nattel. “New ideas about atrial fibrillation 50 years on”. In: *Nature* 415 (2002), pp. 219–226. DOI: 10.1038/415219a.

[232] S. Nattel and D. Dobrev. “Controversies about atrial fibrillation mechanisms - Aiming for order in chaos and whether it matters”. In: *Cardiovascular Research* 120 (2017), pp. 1396–1398. DOI: 10.1161/CIRCRESAHA.116.310489.

[233] S. Nattel and D. Dobrev. “Deciphering the fundamental mechanisms of atrial fibrillation: a quest for over a century”. In: *Circulation Research* 109 (2016), pp. 465–466. DOI: 10.1093/cvr/cvw028.

[234] A.V. Naumova et al. “Clinical imaging in regenerative medicine”. In: *Nature Biotechnology* 32 (2014), pp. 804–818. DOI: 10.1038/nbt.2993.

[235] T.D. Nauser and S.W. Stites. “Diagnosis and treatment of pulmonary hypertension”. In: *American Family Physician* 63 (2001), pp. 1789–1799.

[236] E.S. Nelson, L. Mulugeta, and J.G. Myers. “Microgravity-induced fluid shift and ophthalmic changes”. In: *Life* 4 (2014), pp. 621–665. DOI: 10.3390/life4040621.

[237] S. Nicosia and G. Pezzinga. “Mathematical models of blood flow in the arterial network”. In: *Journal of Hydraulic Research* 45 (2007), pp. 188–201. DOI: 10.1080/00221686.2007.9521759.

[238] M.I.M. Noble. “The contribution of blood momentum to left ventricular ejection in the dog”. In: *Circulation Research* 23 (1968), pp. 663–670. DOI: 10.1161/01.RES.23.5.663.

[239] M.I.M. Noble, D. Trenchord, and A. Guz. “Effect of changing heart rate on cardiovascular function in the conscious dog”. In: *Circulation Research* 19 (1966), pp. 206–213. DOI: 10.1161/01.RES.19.1.206.

[240] P. Norsk. “Adaptation of the cardiovascular system to weightlessness: Surprises, paradoxes and implications for deep space missions”. In: *Acta Physiologica* 228 (2020), e13434. DOI: 10.1111/apha.13434.

[241] P. Norsk. "Blood pressure regulation IV: adaptive responses to weightlessness". In: *European Journal of Applied Physiology* 114 (2014), pp. 481–497. DOI: 10.1007/s00421-013-2797-2.

[242] P. Norsk et al. "Fluid shifts, vasodilatation and ambulatory blood pressure reduction during long duration spaceflight". In: *The Journal of Physiology* 593 (2015), pp. 573–584. DOI: 10.1113/jphysiol.2014.284869.

[243] P. Norsk et al. "Vasorelaxation in space". In: *Hypertension* 47 (2006), pp. 69–73. DOI: 10.1161/01.HYP.0000194332.98674.57.

[244] V.B. Noskov. "Redistribution of bodily fluids under conditions of microgravity and in microgravity models". In: *Human Physiology* 39 (2013), pp. 698–706. DOI: 10.1134/S0362119713070128.

[245] F.Q. Nuttall. "Body mass index - Obesity, BMI, and health: a critical review". In: *Nutrition Research* 50 (2015), pp. 117–128. DOI: 10.1097/NT.0000000000000092.

[246] M.F. O'Rourke. "Consequences of arterial stiffening and increase in central blood pressure in hypertension". In: *Mediographia* 37 (2015), pp. 380–390.

[247] M.F. O'Rourke and J. Hashimoto. "Mechanical factors in arterial aging - A clinical perspective". In: *Journal of the American College of Cardiology* 50 (2007), pp. 1–13. DOI: 10.1016/j.jacc.2006.12.050.

[248] M.F. O'Rourke, M. Namasivayam, and A. Adji. "Treatment of hypertension in patients 80 years of age or older". In: *Minerva Medica* 100 (2009), pp. 25–38.

[249] M.F. O'Rourke et al. "Pressure wave transmission along the human aorta - Changes with age and in arterial degenerative disease". In: *Circulation Research* 23 (1968), pp. 567–579. DOI: 10.1161/01.res.23.4.567.

[250] S.O. Oktar et al. "Blood-flow volume quantification in internal carotid and vertebral arteries: comparison of 3 different ultrasound techniques with phase-contrast MR imaging". In: *American Journal of Neuroradiology* 27 (2006), pp. 363–369.

[251] J. Olbers et al. "High beat-to-beat blood pressure variability in atrial fibrillation compared to sinus rhythm". In: *Blood Pressure* 27 (2018), pp. 249–255. DOI: 10.1080/08037051.2018.1436400.

[252] H. Olsen and T. Länne. "Reduced venous compliance in lower limbs of aging humans and its importance for capacitance function". In: *American Journal of Physiology* 275 (1998), H878–H886. DOI: 10.1152/ajpheart.1998.275.3.H878.

[253] R.M. Olson. "Aortic blood pressure and velocity as a function of time and position". In: *Journal of Applied Physiology* 24 (1968), pp. 563–569. DOI: 10.1152/jappl.1968.24.4.563.

[254] M.S. Olufsen et al. "Numerical simulation and experimental validation of blood flow in arteries with structured-tree outflow conditions". In: *Annals of Biomedical Engineering* 28 (2000), pp. 1281–1299. DOI: 10.1114/1.1326031.

[255] J.R. Orlando et al. "Hemodynamics and echocardiograms before and after cardioversion of atrial fibrillation to normal sinus rhythm". In: *Chest* 76 (1979), pp. 521–526. DOI: 10.1378/chest.76.5.521.

[256] J. Ottesen, M. Olufsen, and J. Larsen. *Applied Mathematical Models in Human Physiology*. Society for Industrial and Applied Mathematics, 2004.

[257] N. Pagonas et al. "Impact of atrial fibrillation on the accuracy of oscillometric blood pressure monitoring". In: *Hypertension* 62 (2013), pp. 579–584. DOI: 10.1161/HYPERTENSIONAHA.113.01426.

[258] H-D Panpenfuss and J.F. Gross. "Mathematical Model of the Single-File Flow of Red Blood Cells in Capillaries". In: *Recent Contributions to Fluid Mechanics* (1982), pp. 180–195. DOI: 10.1007/978-3-642-81932-2_19.

[259] K. Passera et al. "Patient-specific model of arterial circulation for surgical planning of vascular access". In: *The Journal of Vascular Access* 14 (2013), pp. 180–192. DOI: 10.5301/jva.5000099.

[260] K. Patel et al. "Effect of postural changes on cardiovascular parameters across gender". In: *Medicine* 95 (2016), p. 28. DOI: 10.1097/MD.0000000000004149.

[261] T.J. Pedley. *The fluid mechanics of large blood vessels*. Cambridge University Press, 1980.

[262] M.A. Perhonen et al. "Cardiac atrophy after bed rest and spaceflight". In: *Journal of Applied Physiology* 91 (2001), pp. 645–653. DOI: 10.1152/jappl.2001.91.2.645.

[263] L.G. Petersen et al. "Mechanisms of increase in cardiac output during acute weightlessness in humans". In: *Journal of Applied Physiology* 111 (2011), pp. 407–411. DOI: 10.1152/japplphysiol.01188.2010.

[264] L.G. Petersen et al. "The hydrostatic pressure indifference point underestimates orthostatic redistribution of blood in humans". In: *Journal of Applied Physiology* 116 (2014), pp. 730–735. DOI: 10.1152/japplphysiol.01175.2013.

[265] N. Petersen et al. "Postflight reconditioning for European Astronauts – A case report of recovery after six months in space". In: *Musculoskeletal Science and Practice* 27 (2017), S23–S31. DOI: 10.1016/j.msksp.2016.12.010.

[266] S. Petrutiu, A.V. Sahakian, and S. Swiryn. "Abrupt changes in fibrillatory wave characteristics at the termination of paroxysmal atrial fibrillation in humans". In: *EP Europace* 9 (2007), pp. 466–470. DOI: 10.1093/europace/eum096.

[267] D.S. Picone et al. "Discovery of new blood pressure phenotypes and relation to accuracy of cuff devices used in daily clinical practice". In: *Hypertension* 71 (2018), pp. 1239–1247. DOI: 10.1161/HYPERTENSIONAHA.117.10696.

[268] SM Pikkujämsä et al. "Determinants and interindividual variation of R–R interval dynamics in healthy middle-aged subjects". In: *American Journal of Physiology - Heart and Circulatory Physiology* 280 (2001), H1400–H1406. DOI: 10.1152/ajpheart.2001.280.3.H1400.

[269] R.N. Pittman. *Regulation of Tissue Oxygenation*. Morgan & Claypool Life Sciences, 2011.

[270] G.K. Prisk et al. "Pulmonary diffusing capacity, capillary blood volume, and cardiac output during sustained microgravity". In: *Journal of Applied Physiology* 75 (1993), pp. 15–26. DOI: 10.1152/jappl.1993.75.1.15.

[271] A. Quarteroni and L. Formaggia. *Mathematical modelling and numerical simulation of the cardiovascular system*. Elsevier, 2003.

[272] A. Quarteroni et al. "Integrated Heart-Coupling multiscale and multiphysics models for the simulation of the cardiac function". In: *Computer Methods in Applied Mechanics and Engineering* 314 (2017), pp. 345–407. DOI: 10.1016/j.cma.2016.05.031.

[273] T. Ramanathan and H. Skinner. "Coronary blood flow". In: *Continuing Education in Anaesthesia Critical Care & Pain* 5 (2005), pp. 61–65. DOI: 10.1093/bjaceaccp/mki012.

[274] S.A. Rashid and S.A. Mahmud. "Correlation between carotid artery intima-media thickness and luminal diameter with body mass index and other cardiovascular risk factors in adults". In: *Sultan Qaboos University Medical Journals* 15 (2015), e344–e350. DOI: 10.18295/squmj.2015.15.03.007.

[275] M.M. Redfield et al. "Age- and gender-related ventricular-vascular stiffening: a community-based study". In: *Circulation* 112 (2005), pp. 2254–2262. DOI: 10.1161/CIRCULATIONAHA.105.541078.

[276] A. Redheuil et al. "Reduced ascending aortic strain and distensibility - Earliest manifestation of vascular aging in humans". In: *Hypertension* 55 (2010), pp. 319–326. DOI: 10.1161/HYPERTENSIONAHA.109.141275.

[277] G. Redlarski, A. Palkowski, and M. Krawczuk. "Body surface area formulae: an alarming ambiguity". In: *Scientific reports* 6 (2016), p. 27966. DOI: 10.1038/srep27966.

[278] L. Resnekov et al. “Electroversion of lone atrial fibrillation and flutter including hemodynamics studies at rest and on exercise”. In: *British of Heart Journal* 33 (1971), pp. 339–350. DOI: 10.1136/hrt.33.3.339.

[279] P. Reymond et al. “Validation of a one-dimensional model of the systemic arterial tree”. In: *American Journal of Physiology-Heart and Circulatory Physiology* 297 (2009), H208–H222. DOI: 10.1152/ajpheart.00037.2009.

[280] P. Reymond et al. “Validation of a patient-specific one-dimensional model of the systemic arterial tree”. In: *American Journal of Physiology-Heart and Circulatory Physiology* 301 (2011), H1173–H1182. DOI: 10.1152/ajpheart.00821.2010.

[281] M. Di Rienzo et al. “Dynamic adaptation of cardiac baroreflex sensitivity to prolonged exposure to microgravity: data from a 16-day spaceflight”. In: *Journal of Applied Physiology* 105 (2008), pp. 1569–1575. DOI: 10.1152/japplphysiol.90625.2008.

[282] B. Rilsky et al. “Gender-related changes in aortic geometry throughout life”. In: *European Journal of Cardio-Thoracic Surgery* 45 (2014), pp. 805–811. DOI: 10.1093/ejcts/ezt597.

[283] D. Robertson. “The pathophysiology and diagnosis of orthostatic hypotension”. In: *Clinical Autonomic Research* 18 (2008), pp. 2–7. DOI: 10.1007/s10286-007-1004-0.

[284] W.J. Rogers et al. “Age-associated changes in regional aortic pulse wave velocity”. In: *Journal of the American College of Cardiology* 38 (2001), pp. 1123–1129. DOI: 10.1016/s0735-1097(01)01504-2.

[285] T. Russomano, G. Dalmarco, and F. Prehn Falcão. *The effects of hypergravity and microgravity on biomedical experiments*. Morgan & Claypool Publishers, 2008. DOI: 10.2200/S00105ED1V01Y200801BME018.

[286] K. Sagawa, R.K. Lie, and J. Schaefer. “Translation of Otto Frank’s paper "Die Grundform des Arteriellen Pulses" Zeitschrift für Biologie 37: 483-526 (1899)”. In: *Journal of Molecular and Cellular Cardiology* 22 (1990), pp. 253–254. DOI: 10.1016/0022-2828(90)91459-k.

[287] P. Samet. “Hemodynamics sequelae of cardiac arrhythmias”. In: *Circulation* 47 (1973), pp. 399–407. DOI: 10.1161/01.CIR.47.2.399.

[288] R. Sankaranarayanan et al. “How does chronic atrial fibrillation influence mortality in the modern treatment era?” In: *Current Cardiology Review* 11 (2015), pp. 190–198. DOI: 10.2174/1573403x10666140902143020.

[289] J.V. Sayson et al. “Back pain in space and post-flight spine injury: Mechanisms and countermeasure development”. In: *Acta Astronautica* 86 (2013), pp. 24–38. DOI: 10.1016/j.actaastro.2012.05.016.

[290] M. Scalseggi. "Modellazione fluidodinamica della circolazione coronarica ed impatto dell'invecchiamento". In: *Tesi di Laurea Magistrale, Politecnico di Torino, Corso di Laurea in Ingegneria Matematica* (2015).

[291] S. Scarsoglio, C. Gallo, and L. Ridolfi. "Effects of atrial fibrillation on the arterial fluid dynamics: a modelling perspective". In: *Meccanica* 53 (2018), pp. 3251–3267. DOI: 10.1007/s11012-018-0867-6.

[292] S. Scarsoglio et al. "Impact of atrial fibrillation on the cardiovascular system through a lumped-parameter approach". In: *Medical & Biological Engineering & Computing* 52 (2014), pp. 905–920. DOI: 10.1007/s11517-014-1192-4.

[293] S. Scarsoglio et al. "Impaired coronary blood flow at higher heart rates during atrial fibrillation: Investigation via multiscale modelling". In: *Computer Methods and Programs in Biomedicine* 175 (2019), pp. 95–102. DOI: 10.1016/j.cmpb.2019.04.009.

[294] S.G. Schultz. "William Harvey and the circulation of the blood: the birth of a scientific revolution and modern physiology". In: *American Physiological Society - Physiology* 17 (2002), pp. 175–180. DOI: 10.1152/nips.01391.2002.

[295] S. Sethi et al. "Aortic stiffness: pathophysiology, clinical implications, and approach to treatment". In: *Integrated Blood Pressure Control* 7 (2014), pp. 29–34. DOI: 10.2147/IBPC.S59535.

[296] W. Shapiro and G. Klein. "Alteration in cardiac function immediately following electrical conversion of atrial fibrillation to normal sinus rhythm". In: *Circulation* 38 (1968), pp. 1074–1084. DOI: 10.1161/01.CIR.38.6.1074.

[297] J.E. Sharman et al. "Validation of non-invasive central blood pressure devices: ARTERY Society task force consensus statement on protocol standardization". In: *European Heart Journal* 38 (2017), pp. 2805–2812. DOI: 10.1093/eurheartj/ehw632.

[298] M.K. Sharp, J.J. Batzel, and J.P. Montani. "Space physiology IV: mathematical modeling of the cardiovascular system in space exploration". In: *European Journal of Applied Physiology* 113 (2013), pp. 1919–1937. DOI: 10.1007/s00421-013-2623-x.

[299] A. Sheidaei et al. "Simulation of abdominal aortic aneurysm growth with updating hemodynamic loads using a realistic geometry". In: *Medical Engineering and Physics* 33 (2011), pp. 80–88. DOI: 10.1016/j.medengphy.2010.09.012.

[300] T.F. Sherman. "On connecting large vessels to small. The meaning of Murray's law". In: *Journal of General Physiology* 78 (1981), pp. 431–453. DOI: 10.1085/jgp.78.4.431.

[301] S.J. Sherwin et al. "One-dimensional modelling of a vascular network in space-time variables". In: *Journal of Engineering Mathematics* 47 (2003), pp. 217–250. DOI: 10.1023/B:ENGI.0000007979.32871.e2.

[302] Y. Shi, P. Lawford, and R. Hose. "Review of zero-D and 1-D models of blood flow in the cardiovascular system". In: *Biomedical Engineering Online* 10 (2011), p. 33. DOI: 10.1186/1475-925X-10-33.

[303] Y. Shi, Y. Zhao, and N.H. Hwhang T.J. Yeo. "Numerical simulation of opening process in a bileaflet mechanical heart valve under pulsatile flow condition". In: *The Journal of Heart Valve Disease* 12 (2003), pp. 245–255.

[304] Y.-T. Shih et al. "Comparison of two generalized transfer functions for measuring central systolic blood pressure by an oscillometric blood pressure monitor". In: *Journal of Human Hypertension* 27 (2013), pp. 204–210. DOI: 10.1038/jhh.2012.17.

[305] Y.-T. Shih et al. "Quantification of the calibration error in the transfer function-derived central aortic blood pressures". In: *American Journal of Hypertension* 24 (2011), pp. 1312–1317. DOI: 10.1038/ajh.2011.146.

[306] A.A. Shoukas and M. Connoly-Brunner. "Epinephrine and the carotid sinus baroreceptor reflex influence on capacitive and resistive". In: *Circulation Research* 47 (1980), pp. 249–257. DOI: 10.1161/01.RES.47.2.249.

[307] B.E. Shykoff et al. "Cardiovascular response to submaximal exercise in sustained microgravity". In: *Journal of Applied Physiology* 81 (1996), pp. 26–32. DOI: 10.1152/jappl.1996.81.1.26.

[308] E.L. Smith and C. Gilligan. "Physical activity effects on bone metabolism". In: *Calcified Tissue International* 49 (1991), S50–S54. DOI: 10.1007/BF02555089.

[309] N. Smith et al. "euHeart: personalized and integrated cardiac care using patient-specific cardiovascular modelling". In: *Interface Focus* 1 (2011), pp. 349–364. DOI: 10.1098/rsfs.2010.0048.

[310] N.P. Smith, A.J. Pullan, and P.J. Hunter. "An anatomically based model of transient coronary blood flow in the heart". In: *Journal of Applied Mathematics* 62 (2002), pp. 990–1018. DOI: 10.1137/S0036139999355199.

[311] S.M. Smith et al. "Benefits for bone from resistance exercise and nutrition in long-duration spaceflight: Evidence from biochemistry and densitometry". In: *Journal of Bone and Mineral Research* 27 (2012), pp. 1896–1906. DOI: 10.1002/jbmr.1647.

[312] H. Smulyan et al. "Influence of body height on pulsatile arterial hemodynamic data". In: *Journal of the American College of Cardiology* 31 (1998), pp. 1103–1109. DOI: 10.1016/s0735-1097(98)00056-4.

[313] M.F. Snyder and V.C. Rideout. "Computer simulation studies of the venous circulation". In: *IEEE Transactions on Bio-Medical Engineering* 16 (1969), pp. 325–334. DOI: 10.1109/tbme.1969.4502663.

[314] N. Someya et al. "Blood flow responses in celiac and superior mesenteric arteries in the initial phase of digestion". In: *American journal of physiology - Regulatory, integrative and comparative physiology* 294 (2008), R1790–R1796. DOI: 10.1152/ajpregu.00553.2007.

[315] M. Sosnowski et al. "Relationship between R–R interval variation and left ventricular function in sinus rhythm and atrial fibrillation as estimated by means of heart rate variability fraction". In: *Cardiology Journal* 18 (2011), pp. 538–545. DOI: 10.5603/CJ.2011.0010.

[316] P. Spiller et al. "Measurement of systolic and diastolic flow rates in the coronary artery system by x-ray densitometry". In: *Circulation* 68 (1983), pp. 337–347. DOI: 10.1161/01.cir.68.2.337.

[317] J.H. Spuhler et al. "3D Fluid-structure interaction simulation of aortic valves using a unified continuum ALE FEM model". In: *Frontiers in Physiology* 9 (2018), p. 363. DOI: 10.3389/fphys.2018.00363.

[318] E. Stein et al. "The relation of heart rate to cardiovascular dynamics". In: *Circulation* 33 (1966), pp. 925–932. DOI: 10.1161/01.cir.33.6.925.

[319] J.H. Stein et al. "Distribution and cross-sectional age-related increases of carotid artery intima-media thickness in young adults - The Bogalusa heart study". In: *Stroke* 35 (2004), pp. 2782–2787. DOI: 10.1161/01.STR.0000147719.27237.14.

[320] J. Steppan et al. "Vascular stiffness and increased pulse pressure in the aging cardiovascular system". In: *Cardiology Research and Practice* 2011 (2011), p. 263585. DOI: 10.4061/2011/263585.

[321] N. Stergiopulos, D.F. Young, and T.R. Rogge. "Computer simulation of arterial flow with applications to arterial and aortic stenoses". In: *Journal of Biomechanics* 25 (1992), pp. 1477–1488. DOI: 10.1016/0021-9290(92)90060-E.

[322] G.S. Stergiou et al. "Automated blood pressure measurement in atrial fibrillation: a systematic review and meta-analysis". In: *Journal of Hypertension* 30 (2012), pp. 2074–2082. DOI: 10.1097/HJH.0b013e32835850d7.

[323] T. Straume. "Space radiation effects on crew during and after deep space missions". In: *Current Pathobiology Reports* 6 (2018), pp. 167–175. DOI: 10.1007/s40139-018-0175-9.

[324] T. Straume et al. "Cosmic-ray interaction data for designing biological experiments in space". In: *Life Sciences in Space Research* 13 (2017), pp. 51–59. DOI: 10.1016/j.lssr.2017.04.002.

[325] H. Suga, K. Sagawa, and A.A. Shoukas. "Load independence of the instantaneous pressure-volume ratio of the canine left ventricle and effects of epinephrine and heart rate on the ratio". In: *Circulation Research* 32 (1973), pp. 314–322. DOI: 10.1161/01.RES.32.3.314.

[326] J. Sugawara et al. "Age-associated elongation of the ascending aorta in adults". In: *Journal of the American College of Cardiology - Cardiovascular Imaging* 1 (2008), pp. 739–748. DOI: 10.1016/j.jcmg.2008.06.010.

[327] R.L. Summers et al. "Computer systems analysis of spaceflight induced changes in left ventricular mass". In: *Computers in Biology and Medicine* 37 (2007), pp. 358–363. DOI: 10.1016/j.compbiomed.2006.04.003.

[328] R.L. Summers et al. "Mechanism of spaceflight-induced changes in left ventricular mass". In: *The American Journal of Cardiology* 95 (2005), pp. 1128–1130. DOI: 10.1016/j.amjcard.2005.01.033.

[329] W. Sun, C. Martin, and T. Pham. "Computational modeling of cardiac valve function and intervention". In: *Annual Review of Biomedical Engineering* 16 (2014), pp. 53–76. DOI: 10.1146/annurev-bioeng-071813-104517.

[330] P.N. Swarztrauber. "On computing the points and weights for Gauss-Legendre quadrature". In: *SIAM Journal on Scientific Computing* 24 (2002), pp. 945–954. DOI: 10.1137/S1064827500379690.

[331] K. Tae-Seok and Y. Ho-Joong. "Role of echocardiography in atrial fibrillation". In: *Journal of Cardiovascular Ultrasound* 19 (2011), pp. 51–61. DOI: 10.4250/jcu.2011.19.2.51.

[332] S. Takayama et al. "Changes of blood flow volume in the superior mesenteric artery and brachial artery with abdominal thermal stimulation". In: *Evidence-Based Complementary and Alternative Medicine* 2011 (2011), p. 214089. DOI: 10.1093/ecam/nep110.

[333] M. Tanabe et al. "Assessment of left ventricular systolic function in patients with chronic atrial fibrillation and dilated cardiomyopathy using the ratio of preceding to prepreceding R-R intervals". In: *International Journal of Cardiology* 108 (2006), pp. 197–201. DOI: 10.1016/j.ijcard.2005.05.001.

[334] H. Tanaka et al. "Carotid artery wall hypertrophy with age is related to local systolic blood pressure in healthy men". In: *Arteriosclerosis, Thrombosis, and Vascular biology* 21 (2001), pp. 82–87. DOI: 10.1161/01.atv.21.1.82.

[335] K. Tateno and L. Glass. "Automatic detection of atrial fibrillation using the coefficient of variation and density histograms of RR and deltaRR intervals". In: *Medical & biological engineering & computing* 39 (2001), pp. 664–671. DOI: 10.1007/BF02345439.

[336] M. Tavassoli. "Medical problems of space flight". In: *The American Journal of Medicine* 81 (1986), pp. 850–854. DOI: 10.1016/0002-9343(86)90357-8.

[337] C.A. Taylor and C.A. Figueroa. "Patient-specific modeling of cardiovascular mechanics". In: *Annual Review of Biomedical Engineering* 11 (2009), pp. 109–134. DOI: 10.1146/annurev.bioeng.10.061807.160521.

[338] S.K. Therkelsen et al. "Atrial and ventricular volume and function evaluated by magnetic resonance imaging in patients with persistent atrial fibrillation before and after cardioversion". In: *American Journal of Cardiology* 97 (2006), pp. 1213–1219. DOI: 10.1016/j.amjcard.2005.11.040.

[339] W.E. Thornton, G.W. Hoffler, and J.A. Rummel. "Anthropometric changes and fluid shifts". In: *The Proceedings of the Skylab Life Sciences Symposium* 2 (1974), pp. 637–658.

[340] W.E. Thornton, T.P. Moore, and S.L. Pool. "Fluid shifts in weightlessness". In: *Aviation Space and Enviromental Medicine* 58 (1987), A86–A90.

[341] W.E. Thornton et al. "Changes in leg volume during microgravity simulation". In: *Aviation Space and Enviromental Medicine* 63 (1992), pp. 789–794.

[342] F.E. Tilton, J.J. Degioanni, and V.S. Schneider. "Long-term follow-up of Skylab bone demineralization". In: *Aviation, Space, and Environmental Medicine* 51 (1980), pp. 1209–1213.

[343] G.J. Tortora. *Introduction to the human body - The essentials of anatomy and physiology*. 3rd ed. HarperCollins College Publishers, 1994.

[344] A. Tosetto et al. "Age-adjusted reference limits for carotid-intima media thickness as better indicator of vascular risk: population-based estimates from the VITA projects". In: *Journal of Thrombosis and Haemostasis* 3 (2005), pp. 1224–1230. DOI: 10.1111/j.1538-7836.2005.01440.x.

[345] N.A. Trayanova, J. Constantino, and V. Gurev. "Electromechanical models of the ventricles". In: *American Journal of Physiology - Heart and Circulatory Physiology* 301 (2011), H279–H286. DOI: 10.1152/ajpheart.00324.2011.

[346] C.B. Upshaw. "Hemodynamic changes after cardioversion of chronic atrial fibrillation". In: *Archives of Internal Medicine* 157 (1997), pp. 1070–1076. DOI: 10.1001/archinte.1997.00440310032003.

[347] M. Ursino and C.A. Lodi. "A simple mathematical model of the interaction between intracranial pressure and cerebral hemodynamics". In: *Journal of Applied Physiology* 82 (1997), pp. 1256–1269. DOI: 10.1152/jappl.1997.82.4.1256.

[348] M. Ursino and E. Magosso. "Acute cardiovascular response to isocapnic hypoxia. I. A mathematical model". In: *American Physiological Society - American Journal of Physiolgy - Heart and Circulatory Physiology* 279 (2000), H149–H165. DOI: 10.1152/ajpheart.2000.279.1.H149.

[349] A.J. Vander, J.H. Sherman, and D.S. Luciano. *Human physiology - The mechanisms of body function*. 4th ed. McGraw-Hill Book Company, 1985.

[350] P. Verdecchia, A. Fabio, and G. Reboldi. "Hypertension and atrial fibrillation - Doubts and certainties from basic and clinical studies". In: *Circulation Research* 122 (2018), pp. 352–368. DOI: 10.1161/CIRCRESAHA.117.311402.

[351] B. Verheyden et al. "Adaptation of heart rate and blood pressure to short and long duration space missions". In: *Respiratory Physiology & Neurobiology* 169 (2009), S13–S16. DOI: 10.1016/j.resp.2009.03.008.

[352] B. Verheyden et al. "Operational point of neural cardiovascular regulation in humans up to 6 months in space". In: *Journal of Applied Physiology* 108 (2010), pp. 646–654. DOI: 10.1152/japplphysiol.00883.2009.

[353] R. Videbaek and P. Norsk. "Atrial distension in humans during microgravity induced by parabolic flights". In: *Journal of Applied Physiology* 83 (1997), pp. 1862–1866. DOI: 10.1152/jappl.1997.83.6.1862.

[354] F. Viola, V. Meschini, and R. Verzicco. "Fluid–Structure-Electrophysiology interaction (FSEI) in the left-heart: A multi- way coupled computational model". In: *European Journal of Mechanics /B Fluids* 79 (2020), pp. 212–232. DOI: 10.1016/j.euromechflu.2019.09.006.

[355] R. Virmani et al. "Effect of aging on aortic morphology in populations with high and low prevalence of hypertension and atherosclerosis". In: *American Journal of Pathology* 139 (1991), pp. 1119–1129.

[356] F.N. van de Vosse and N Stergiopulos. "Pulse wave propagation in the arterial tree". In: *Annual Review of Fluid Mechanics* 43 (2010), pp. 467–499. DOI: 10.1146/annurev-fluid-122109-160730.

[357] O. Vriz et al. "Comparison of sequentially measured Aloka echo-tracking one-point pulse wave velocity with SphygmoCor carotid-femoral pulse wave velocity". In: *SAGE Open Medicine* 1 (2013), p. 2050312113507563. DOI: 10.1177/2050312113507563.

[358] X. Wang et al. "Three-dimensional numerical simulation of blood flow through a modelled aneurysm". In: *Russian Journal of Biomechanics* 1 (1999), pp. 26–36.

[359] Z. Wang, M.J. Golob, and N.C. Chesler. *Viscoelastic properties of cardiovascular tissues*. IntechOpen, 2016. DOI: 10.5772/64169.

[360] D.E. Watenpaugh et al. "Effects of spaceflight on human calf hemodynamics". In: *Journal of Applied Physiology* 90 (2001), pp. 1552–1558. DOI: 10.1152/jappl.2001.90.4.1552.

[361] P. Weismüller et al. "AV nodal pathways in the R-R interval histogram of the 24-hour monitoring ECG in patients with atrial fibrillation". In: *Annals of Noninvasive Electrocardiology* 6 (2001), pp. 285–289. DOI: 10.1111/j.1542-474x.2001.tb00120.x.

[362] J. Werner, D. Böhringer, and M. Hexamer. "Simulation and prediction of cardiotherapeutical phenomena from a pulsatile model coupled to the guyton circulatory model". In: *IEEE Transactions on Biomedical Engineering* 49 (2002), pp. 430–439. DOI: 10.1109/10.995681.

[363] N. Westerhof, G. Elzinga, and P. Sipkema. "An artificial arterial system for pumping hearts". In: *Journal of Applied Physiology* 31 (1971), pp. 776–781. DOI: 10.1152/jappl.1971.31.5.776.

[364] N. Westerhof, J-W. Lankhaar, and B.E. Westerhof. "The arterial Windkessel". In: *Medical & Biological Engineering & Computing* 47 (2009), pp. 131–141. DOI: 10.1007/s11517-008-0359-2.

[365] N. Westerhof, N. Stergiopulos, and M.I.M. Noble. *Snapshots of Hemodynamics*. 2nd ed. Springer, 2010.

[366] T. Wichter. "Impaired myocardial perfusion in atrial fibrillation cause or effect?" In: *Europace* 12 (2010), pp. 611–613. DOI: 10.1093/europace/euq084.

[367] W. Lippincott & Wilkins. *ECG interpretation made incredibly easy*. 5th ed. W. Lippincott & Wilkins, 2005.

[368] B. Williams et al. "Differential impact of blood pressure–lowering drugs on central aortic pressure and clinical outcomes - Principal results of the conduit artery function evaluation (CAFE) study". In: *Circulation* 113 (2006), pp. 1213–1225. DOI: 10.1161/CIRCULATIONAHA.105.595496.

[369] D. Williams et al. "Acclimation during space flight: effects on human physiology". In: *Canadian Medical Association Journal* 180 (2009), pp. 1317–1323. DOI: 10.1503/cmaj.090628.

[370] A. Wolak et al. "Aortic size assessment by noncontrast cardiac computed tomography: normal limits by age, gender, and body surface area". In: *Journal of the American College of Cardiology - Cardiovascular Imaging* 1 (2008), pp. 200–209. DOI: 10.1016/j.jcmg.2007.11.005.

[371] S.E. Wolowacz et al. "The cost of illness of atrial fibrillation: a systematic review of the recent literature". In: *EP Europace* 13 (2011), pp. 1375–1385. DOI: 10.1093/europace/eur194.

[372] J.R. Womersley. "Method for the calculation of velocity, rate of flow and viscous drag in arteries when the pressure gradient is known". In: *The Journal of Physiology* 127 (1955), pp. 553–563. DOI: 10.1113/jphysiol.1955.sp005276.

[373] B. Wozakowska-Kaplon. "Changes in left atrial size in patients with persistent atrial fibrillation: a prospective echocardiographic study with a 5-year follow-up period". In: *International Journal of Cardiology* 101 (2005), pp. 47–52. DOI: 10.1016/j.ijcard.2004.03.010.

[374] G. Wyse. "Lenient versus strict rate control in atrial fibrillation: Some devils in the details". In: *Journal of the American College of Cardiology* 58 (2011), pp. 950–952. DOI: 10.1016/j.jacc.2011.04.028.

[375] H. Xiong et al. "A numerical study of the effect of varied blood pressure on the stability of carotid atherosclerotic plaque". In: *BioMedical Engineering OnLine* 13 (2014), p. 152. DOI: 10.1186/1475-925X-13-152.

[376] J. Xu, J.G. Y. Luc, and K. Phan. "Atrial fibrillation: review of current treatment strategies". In: *Journal of Thoracic Disease* 8 (2016), E886–E900. DOI: 10.21037/jtd.2016.09.13.

[377] Y. Yang et al. 2018. Chap. The noninvasive measurement of central aortic blood pressure waveform. DOI: 10.5772/intechopen.76770.

[378] X. Zhang et al. "Gravitational effects on global hemodynamics in different postures: A closed-loop multiscale mathematical analysis". In: *Acta Mechanica Sinica* 33 (2017), pp. 595–618. DOI: 10.1007/s10409-016-0621-z.

[379] Y. Zhang et al. "Multiscale modeling of the cardiovascular system: disease development and clinical intervention progression". In: *Annals of Biomedical Engineering* 44 (2016), pp. 2642–2660. DOI: 10.1007/s10439-016-1628-0.

[380] L. Zhong et al. "Application of patient-specific computational fluid dynamics in coronary and intra-cardiac flow simulations: challenges and opportunities". In: *Frontiers in Physiology* 9 (2018), p. 742. DOI: 10.3389/fphys.2018.00742.

[381] S. Zhou et al. "A review on low-dimensional physics-based models of systemic arteries: application to estimation of central aortic pressure". In: *BioMedical Engineering OnLine* 18 (2019), p. 41. DOI: 10.1186/s12938-019-0660-3.

[382] H. Zhu, H. Wang, and Z. Liu. "Effects of real and simulated weightlessness on the cardiac and peripheral vascular function on humans: a review". In: *International Journal of Occupational Medicine and Enviromental Health* 28 (2015), pp. 793–802. DOI: 10.13075/ijomeh.1896.00301.

[383] R.S. Zitnik et al. "Continuously recorded changes of thoracic aortic blood flow in man in response to leg exercise in supine position". In: *Circulation Research* 17 (1965), pp. 97–105. DOI: 10.1161/01.RES.17.2.97.

[384] Y. Zócalo et al. "Structural and functional properties of venous wall: relationship between elastin, collagen, and smooth muscle components and viscoelastic properties". In: *International Scholarly Research Notices: Physiology* 2013 (2013), pp. 1–9. DOI: 10.1155/2013/906031.

[385] M. Zoni-Berisso et al. “Epidemiology of atrial fibrillation: European perspective”. In: *Clinical Epidemiology* 6 (2014), pp. 212–220. DOI: 10.2147/CLEP.S47385.

[386] H. Zulkifly, G.Y.H. Lip, and D.A. Lane. “Epidemiology of atrial fibrillation”. In: *The International Journal of Clinical Practice* 72 (2018), e13070. DOI: 10.1111/ijcp.13070.

This Ph.D. thesis has been typeset by means of the TEX-system facilities. The typesetting engine was pdfLATEX. The document class was `toptesi`, by Claudio Beccari, with option `tipotesi=scudo`. This class is available in every up-to-date and complete TEX-system installation.